REPORT DOCUMENTATION PAGE

Public reporting burden for this collection of information is estimated to average 1 hour per response, including the time for reviewing instructions, searching existing data sources, gathering and maintaining the data needed, and completing and reviewing the collection of information. Send comments regarding this burden estimate or any other aspect of this collection of information, including suggestions for reducing this burden, to Washington Headquarters Services, Directorate for Information Operations and Reports, 1215 Jefferson Davis Highway, Suite 1204, Arlington, VA 22202-4302, and to the Office of Management and Budget, Paperwork Reduction Project (0704-0188), Washington, DC 20503.

1. AGENCY USE ONLY (Leave blank)	2. REPORT DATE 06 June 1997	3. REPORT TYPE AND DATES COVERED Technical

4. TITLE AND SUBTITLE
Elastic Properties of Novel Materials using PVDF Film and Resonance Ultrasound Spectroscopy

5. FUNDING NUMBERS
PE 61153N
G N00014-92-J-1186

6. AUTHOR(S)
Philip S. Spoor

7. PERFORMING ORGANIZATION NAME(S) AND ADDRESS(ES)
The Pennsylvania State University
Department of Physics
104 Davey Lab
University Park, PA 16802

8. PERFORMING ORGANIZATION REPORT NUMBER

9. SPONSORING/MONITORING AGENCY NAME(S) AND ADDRESS(ES)
Office of Naval Research
ONR 331
800 North Quincy Street
Arlington, VA 22217-5660

10. SPONSORING/MONITORING AGENCY REPORT NUMBER

11. SUPPLEMENTARY NOTES

12a. DISTRIBUTION/AVAILABILITY STATEMENT

Approved for public release:
Distribution unlimited

12b. DISTRIBUTION CODE

13. ABSTRACT (Maximum 200 words)

Elastic properties are of fundamental interest in condensed matter physics, material science, geoscience, and many branches of engineering. This paper describes the use of a relatively new technique, known as "Resonant Ultrasound Spectroscopy" (RUS), with which the elastic properties of a small sample may be found in a single measurement, by analyzing a sufficient number of the sample's normal modes of free vibration. The present work describes the use of polyvinylidene (PVDF) thin-film transducers to extend the above method to very small ~100 µg, fragile samples. The method is calibrated by measuring the elastic constants of a well-characterized material, cubic silicon. Measurements and analyses of several novel materials, including spherical ceramic particles (``proppants'') and an aluminum alloy "quasicrystal", are subsequently presented. Second-order perturbations of the normal mode frequencies due to minor sample preparation errors are also discussed.

14. SUBJECT TERMS
Acoustics, Solid State Physics, Materials

15. NUMBER OF PAGES
119

16. PRICE CODE

17. SECURITY CLASSIFICATION OF REPORT	18. SECURITY CLASSIFICATION OF THIS PAGE	19. SECURITY CLASSIFICATION OF ABSTRACT	20. LIMITATION OF ABSTRACT
UNCLASSIFIED	UNCLASSIFIED	UNCLASSIFIED	

Elastic Properties of Novel Materials Using PVDF Film and Resonant Ultrasound Spectroscopy

P. S. Spoor

Department of Physics, the Pennsylvania State University, University Park, Pennsylvania 16802
(July 6, 1997)

Elastic properties, or the ways in which solids (particularly crystalline solids) respond to stress, are of fundamental interest in condensed matter physics, material science, geoscience, and many branches of engineering. This paper describes the use of a relatively new technique, variously known as "Resonant Acoustic Spectroscopy" or "Resonant Ultrasound Spectroscopy", with which the elastic properties of a small sample in any one of many simple analytic shapes (parallellepiped, sphere, cylinder, *etc.*) may be found in a single measurement, by analyzing a sufficient number of the sample's normal modes of free vibration. In contrast to previous work using this technique, the present work describes the use of polyvinylidene fluoride thin-film transducers to extend the above method to very small (~ 100 μg), fragile samples. The method is calibrated by measuring the elastic constants of a well-characterized material, cubic silicon. Measurements and analyses of several novel materials, including spherical ceramic particles ("proppants") and an aluminum alloy "quasicrystal", are subsequently presented. Second-order perturbations of the normal mode frequencies due to minor sample preparation errors are also discussed.

I. INTRODUCTION

Elastic properties, or the ways in which materials respond to stress, are of fundamental interest in engineering and condensed matter physics. The elastic constants of a crystal describe structure at the atomic level (the nature of the potential well for atoms in the lattice), and so are invaluable for studying the thermodynamics of a solid; yet they also manifest themselves in macroscopic properties such as sound speed and tensile strength. Given that elastic properties are of such importance, it is not surprising that many ingenious ways have been devised to measure them, including the use of static loads with strain gauges, Brillioun scattering, inelastic neutron scattering, X-ray scattering under different conditions of stress, and, of course, acoustic methods such as surface acoustic waves (SAW), vibrating reed, torsional pendulum, and ultrasonic pulse time-of-flight. Pulse techniques in particular have enjoyed a certain preeminence due to their ability to measure accurately all the elastic moduli of an anisotropic substance (at least in principle) [1]. Even for materials that are available as large, single crystals of high purity, the reputed accuracy of pulse ultrasonic methods is apparently not very robust, for if one examines the literature, one finds that the published values of elastic constants vary considerably. Sizeable discrepancies are common, particularly for the "off-diagonal" moduli such as c_{12} (α-quartz is a good example) [47]. The difficulties in performing an accurate pulse measurement on an anisotropic sample are greatly exacerbated if the sample is small (≤ 1 mm), lossy, inhomogeneous, or lacks parallel faces. Given the increasing interest in engineered materials, thin films, and novel substances such as quasicrystals and high-temperature oxide superconductors (of which the only available single-domain samples are very small), such limitations are significant.

1. Resonant ultrasound spectroscopy

This paper describes the use of an alternate approach, which is to recognize that if the normal modes of free vibration of an object are determined by its geometry and material properties, it is reasonable to suppose that one could find some or all of the desired material properties by examining the normal modes. Resonant Acoustic Spectroscopy or Resonant Ultrasound Spectroscopy (RUS) is the name given to the use of mechanical resonance spectra to determine material properties. [45]. This method is distinguished from its predecessors such as the torsion pendulum and vibrating bar [12] in that it actually treats the normal mode problem rigorously, rather than idealizing the modes to be entirely torsional, longitudinal, or whatever. The sample need not be long and skinny, but can have almost any shape. Among the advantages of this technique are:

1. the normal modes of a sample are well-defined even if it is oddly shaped or highly anisotropic;

2. frequency is the perhaps the easiest quantity to measure accurately in the laboratory;

3. since the sample is resonating, not the transducer, one may use very weakly coupled transducers for excitation and measurement, thereby eliminating transducer loading and ringing;

4. the fact that the sample is driven at resonance also enables measurements on lossy materials, for which the attenuation of an ultrasonic pulse would be too rapid to obtain an accurate time-of-flight reading, and

5. the frequencies of resonance for the lower modes of a sample are much lower than the frequencies

required to produce a well–localized pulse, so much smaller samples can be investigated.

This last point is of particular importance when new, novel materials are discovered, since the best single-crystal samples are often only a few hundred microns in size. The main contribution of the author is to adapt and apply this method to very small samples of novel materials; where others have measured samples of a few milligrams in mass [43], [45], the author has had good success with samples as small as $70\mu g$. Thus, the precise measurement of elastic properties of superconducting wafers, decagonal quasicrystals, *etc.* is within reach.

A. Purpose

The purpose of this paper is twofold: first, it attempts to demonstrate the usefulness and effectiveness of RUS in general, and the specific techniques of this work in particular, for measuring accurately the elastic constants of small samples. Second, the method is applied to small samples of novel materials which are particularly well suited to investigation by RUS. In the process of carrying out one of these investigations, a method is developed for assessing the effects of sample preparation errors on the confidence in a measurement; this has not been done previously.

B. Organization and synopsis

The organization of the paper is as follows: Section II develops the analytic and computational tools needed to analyze the data, after first reviewing (in some detail) basic elasticity theory as it applies to RUS. In the process of this review, several results are derived which are of significance in later sections. Section III describes in detail the actual experimental techniques used in this paper, so the motivated reader will hopefully have enough information to carry out his or her own successful RUS measurements. The descriptions are done in the context of an actual measurement, that of finding the elastic constants of cubic silicon for calibration purposes.

Section IV describes the use of RUS to find the elastic constants and internal friction of tiny, spherical ceramic particles known as "proppants", used in fossil fuel recovery and, ironically, in some new kinds of experimental solar receivers. Section V details a measurement of the elastic properties of a new phase of matter, an icosahedral AlCuLi quasicrystal [80], and compares these properties with those of a cubic crystalline phase of the same alloy. In particular, the prediction of quasicrystal elastic isotropy is tested and the effects of defects unique to quasiperiodic systems ("phasons") are discussed.

Testing a prediction of isotropy requires especially high precision, so for the measurements in Section V it became necessary to consider the effects of small boundary perturbations (caused by sample preparation errors) on the frequencies of free vibration. This work is summarized in Section VI. While the task is not entirely trivial, a reasonable solution is obtained that allows one to quantify with what precision samples need to be prepared to ensure a desired accuracy.

As the last element in the paper, an appendix is provided that includes the source code for FORTRAN 77 programs used to perform the various calculations.

1. Synopsis

Resonant ultrasound spectroscopy uses measured values of a sample's normal mode frequencies (and, occasionally, resonance peakwidths) to find elastic properties (or, occasionally, other material properties). This method has certain advantages, enumerated in section I 1, over conventional methods such as pulse-echo techniques. The chief obstacle to such an approach is that no straightforward relationship exists between the frequencies and the elastic constants, as there does in the case of a plane wave pulse traveling in a sample fashioned into an ultrasonic waveguide. In practice it is found that to determine the elastic properties from the frequencies, one must be able to calculate theoretical frequencies based on some assumed values for the elastic constants (the forward problem), and then adjust the constants until the calculated spectrum matches the observed one (the inverse problem). In the past, it has been impossible to calculate the normal mode frequencies of finite elastic objects for all but a few special cases. With the advent of modern high-speed digital computers, however, this ancient problem in applied physics is easily solved with the aid of a simple variational principle.

a. Normal modes by Rayleigh-Ritz If it is assumed that during the execution of a normal mode, the maximum potential and kinetic energies associated with the motion are equal (Rayleigh's principle), then for an elastic solid:

$$\omega^2 = \frac{\int_V c_{ijkl} \frac{\partial \psi_i}{\partial \psi_j} \frac{\partial \psi_k}{\partial \psi_l} \, dV}{\int_V \rho \, \psi \cdot \psi \, dV} , \qquad (1)$$

where ψ is the displacement and c_{ijkl} is the linear elastic tensor from the stress-strain relation $\sigma_{ij} = c_{ijkl}\epsilon_{kl}$. If the displacement is expanded in a basis ϕ_n with unknown coefficients $a_{n,i}$ according to $\psi_i = \sum_{n=1}^N a_{n,i}\phi_n$, then requiring ω^2 to be a stationary value (a minimum) for the corresponding eigenfunction results in a matrix eigenvalue solution for ω^2 (the Ritz method).

In order to get accurate solutions for the eigenvalues, many basis functions must be used, resulting in large matrices. This was a problem in the past, but brute force now succeeds where subtlety and ingenuity failed.
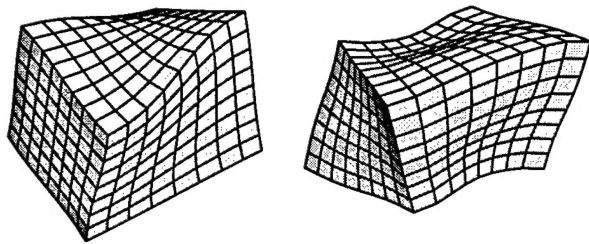
EV-1 (3.296 MHz)   **OZ-2 (6.146 MHz)**

FIG. 1. Two normal mode shapes of an isotropic parallelepiped, computed by the Rayleigh-Ritz method. Mode labels refer to eigenfunction symmetries and mode types (*e.g.* EV is torsion, *etc.*).

TABLE I. Selected nondimensional resonance frequencies $\eta = \omega a/v_s$ of an elastically isotropic, homogeneous sphere. The η_0 are the zeroes of the analytic solution, and the η_{xyz} are calculated using the Rayleigh-Ritz method, with $x^l y^m z^n$ as the basis set. The maximum order of the basis functions is $l + m + n = 12$. Because the frequencies of a sphere are highly degenerate, the Ritz mode numbers grow much faster than the analytic ones.

	Analytic sol'n		Rayleigh-Ritz		
	Mode	η_0	mode #	η_{xyz}	$\Delta\eta$ (%)
1	$T_{2,0}$	2.5011326	1	2.5011326	0.000
2	$S_{2,0}$	2.6398693	6	2.6398693	0.000
4	$T_{3,0}$	3.8646998	14	3.8646998	0.000
6	$S_{0,1}$	4.4399982	28	4.4399982	0.000
9	$T_{4,0}$	5.0946156	50	5.0946156	0.000
13	$S_{3,1}$	6.4543693	77	6.4543693	0.000
16	$T_{2,1}$	7.1360088	100	7.1360096	0.000
26	$T_{8,0}$	9.6209991	200	9.6233328	0.024
32	$S_{0,2}$	10.4939244	260	10.4939248	0.000
37	$S_{4,2}$	11.0390581	300	11.0931275	0.489

Tables I and II show comparisons between frequencies of vibration calculated using Rayleigh-Ritz (approximately 200 basis functions per mode) and "exact" solutions, for two cases for which there is an analytic equation for the frequencies (the homogeneous, isotropic sphere and the Lamé modes of a rectangular parallelepiped). Figure 1 shows a couple of the eigenfunctions calculated for an isotropic rectangular parallelepiped (these are taken from Fig. 8 in Section II).

b. The basic measurement setup Figure 2 shows a generic resonant ultrasound schematic, for making a measurement of a sample's normal mode frequencies. A sample to be investigated, usually polished into the shape of a rectangular parallelepiped, is held very lightly between two transducers (piezoelectric film, lithium niobate disks, *etc.*); one is connected to a tunable frequency source and is used as a driver, and the other is connected to a detector (such as a lock-in amplifier) and is used as a re-

TABLE II. Two of the Lamé modes of an elastic parallelepiped, for which there is an exact solution, calculated by the exact formula and numerically with Rayleigh-Ritz. The basis functions used in the Rayleigh-Ritz calculation are products of Legendre polynomials $P_i(x/l_x)P_j(y/l_y)P_k(z/l_z)$, where the maximum order $i + j + k$ of the basis functions is 12.

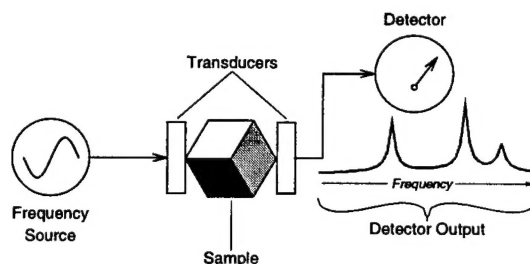| Lamé modes $f_m = (m/4a)\sqrt{2\mu/\rho}$				
	Analytic sol'n	Rayleigh-Ritz		
m	f (MHz)	mode	f (MHz)	Δf (%)
1	6.8981983	15 OD-3	6.8981983	0.000
2	13.7963966	83 OZ-11	13.7964015	0.000

FIG. 2. A basic schematic for experimentally determining the natural resonances of an elastic solid, in this case, a cube.

ceiver. As the drive frequency is swept, peaks appear in the detector output, corresponding to sample resonances. The locations of the peaks give the resonance frequencies, while the Q's (frequency $\div$ peakwidth) of the resonances may give information about internal friction in the sample. In the author's thesis work, polyvinylidene fluoride (PVDF) strips of 9μm thickness are used; the thin film does a minimum of damage to fragile samples and contributes negligible transducer loading; also, the film is extremely lossy, with a Q of about 10. This ensures that all resonances observed will be those of the sample.

In order for one to successfully fit measured data to a calculated spectrum, a sample must have a well-defined geometry (although there is great freedom in what type of shape is used). Therefore, even small samples must be prepared very carefully, which can be challenging.

2. Calibration with cubic silicon

In order to satisfy ourselves (and the reader) that RUS really does work, we perform what may be considered a sort of calibration measurement on a sample of single-crystal cubic silicon. Silicon is perhaps the best characterized material in the world today, and can be grown in crystals so pure and perfect that there has been serious talk of using silicon to replace water as the standard of density and specific gravity [4]. We therefore assume that the published values of the elastic constants of Si can be

TABLE III. The observed and calculated frequencies, in MHz, for the 1 mg cubic silicon sample.

	Mode	f_{obs}	f_{calc}	Δf	|% error|
1	EV-1	2.84189	2.84029	0.00159	0.056
5	EV-2	4.32065	4.31954	0.00111	0.026
10	EX-2	4.69970	4.69880	0.00090	0.019
15	OZ-2	5.45274	5.45630	−0.00356	0.065
20	EZ-3	5.73738	5.73829	−0.00090	0.016
25	EZ-5	6.47913	6.47586	0.00327	0.050
31	OD-6	7.11800	7.12043	−0.00243	0.034
				Avg.	0.04%

TABLE IV. Elastic constants of cubic silicon, in units of 10^{12} dyne/cm^2.

	Author	Literature[1]	Δ(%)
C_{11}	1.6568±0.001	1.6564	0.02
C_{12}	0.6385±0.001	0.6394	-0.14
C_{44}	0.7963±0.0002	0.7951	0.15

[1]From [6].

taken as the "true" values, and should be very consistent from sample to sample.

A rectangular parallelepiped of cubic Si is prepared, with approximate dimensions $0.6 \times 0.7 \times 0.9$ mm^3, and mass approximately 1 mg. The lowest 32 modes of this sample were measured, and a version of the Levenberg-Marquart [39] optimization method was used to find the elastic constants, using the average of the values given in the Landolt-Börnstein Tables [5] as starting values; a "Monte Carlo" simulation based on the rms error was used to find the uncertainties in the elastic constants. Table III shows the fit for some of the modes (not necessarily the best ones); the mode labels will correspond roughly to the mode shapes of the isotropic sample shown in Figs. 1 and 8. Table IV shows the resulting elastic constants, compared with values from the literature measured by pulse-echo methods on much larger samples. The full details of this measurement are presented in Section III.

C. Novel materials

Two uses of this method on novel materials are presented; first, the measurement of the elastic constants and internal friction of tiny, spherical ceramic particles (proppants) as a function of heat treatment temperature, and second, the verification of quasicrystal elastic isotropy.

a. Proppants In an interesting irony, tiny ($\simeq 600\mu$m) electrically fused ceramic particles developed for fossil fuel recovery (known as "proppants" for their role in propping open cracks in hydraulically fractured wells)
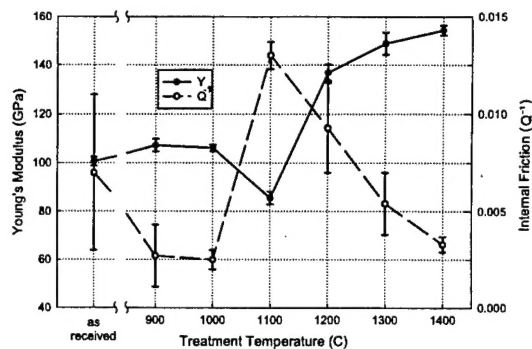

FIG. 3. A summary of the elastic properties of Zirprop Z126 proppants as a function of heat treatments in air for 150 hours at various temperatures.

became the focus of an effort to design a solar receiver using a *solid* thermal transfer medium. In order to optimize these particles for the solar application, they needed to be precisely characterized as a function of heat treatment, including the elastic constants. It would obviously be impossible to use a pulse-echo technique on an individual proppant; but since the particles are nearly spherical, their normal mode frequencies can be compared with those of an elastic sphere to determine the elastic constants. Rather than account for any asphericity in the computer code, we chose to measure a large number of samples for each case, and average the results. These are shown in Fig.3. As the figure shows, the particles get softer and lossier up to a certain temperature, and then begin to stiffen. This seems to be related to the growth, and subsequent healing at high temperatures, of internal microcracks.

b. Quasicrystals Quasicrystals were discovered in 1984 when Dany Shechtman and colleagues observed that certain melt-spun alloys had non-crystallographic five-fold symmetry in the diffraction pattern. As quasicrystal growing improved, many samples exhibited facets reminiscent of the Penrose rhombuses that make up two-dimensional quasiperiodic tilings. It has been suggested that these materials are three-dimensional versions of these two-dimensional tilings: solids with long-range, non-crystallographic rotational symmetry, but without periodic structure (hence without translational symmetry). The overall three-dimensional symmetry of "Shechtmanite" and other quasicrystals appears to be icosahedral; interestingly, this implies elastic isotropy. Icosahedral symmetry is very similar to cubic symmetry, and indeed there are cubic crystals ("approximants") that almost have icosahedral symmetry. These would not have to be isotropic, but could be very close. As a test of these theories, we measured the elastic constants of two quasicrystals and an approximant; we discovered that while the anisotropy of the approximant was indeed tiny, it was easily measureable with the precision of RUS and could be distinguished from the quasicrystal. Fig.4 shows these results. Sample QX2 is the 70μg sam-
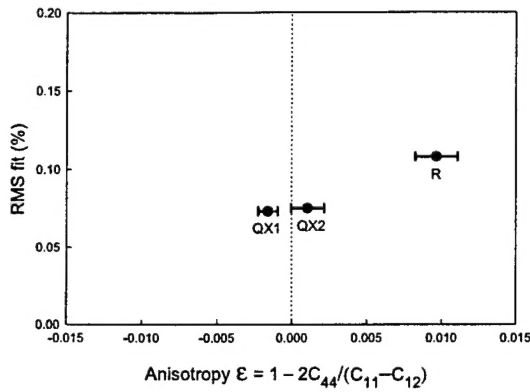
4

FIG. 4. The anisotropies for three samples of aluminum-lithium copper: QX1 and QX2 are icosahedral phases, while R is an R-phase cubic approximant.

ple alluded to earlier. Whether the quasicrystal samples posess anisotropy is not entirely clear—the very small anisotropies of QX1 and QX2 from 4 may be due to the presence of a type of defect unique to quasiperiodic systems ("phason strain"). This is discussed in the conclusions of Section V.

The existence of these very small but apparently real quasicrystal anisotropy results prompted a search for possible sources of bias error. One likely candidate was thought to be errors in rectangular parallelepiped sample preparation, specifically sides that are not quite parallel or perpendicular. A FORTRAN 77 program (npr.f) was developed that would allow one to find the approximate frequency shifts due to arbitrary (but small) tilts in all 6 sides. Results using this program indicate that a sample whose sides are parallel within 0.3° and perpendicular within 0.5° can be safely approximated as a rectangular parallelepiped in a RUS measurement. The details of developing and testing this program are given in Section VI, and the source code itself is given in the Appendix.

D. Some background, and a little history

The study of linear elasticity may be said to have begun in 1678 with CEIIINOSSSTTUV, a Latin cryptogram published by English physicist Robert Hooke [9]. The solution, UT TENSIO SIC VIS ("as the extension, so the force"), is known as Hooke's law, mathematically expressed as $F = K\Delta x$ for a simple spring, or $\sigma_{ij} = c_{ijkl}\varepsilon_{kl}$ for three dimensional stress as a function of strain in an elastic solid (see Section II).

The earliest methods of measuring elastic constants consisted of direct tests of Hooke's law. For a modulus of extension this entails measuring the extension (or compression) of a bar in response to a static axial load; for a shear modulus, one may measure the angular deflection of a circular rod under the influence of an applied torque.

1. Dynamic methods for measuring elastic properties

It was recognized from the very beginning of elasticity theory that the restoring forces caused by elastic stiffness, plus the intertial properties of a body, determine its natural frequencies of vibration. Thus, frequencies of vibration could be used to find elastic constants. This principle is exemplified by the torsion pendulum, first used by Charles Coulomb in 1787 to find the modulus of rigidity (shear modulus) of metal wires [10]. It is thus interesting to note that these experiments predate Young's famous investigations of extensional stiffness [11].

This approach became widely applied to the vibration of bars, which can undergo longitudinal, flexural, and torsional vibrations, all having different relationships to the elastic moduli. For instance, if a "fixed-fixed" or "free-free" bar is undergoing longitudinal vibrations, its resonance frequencies are given by

$$f_n = \frac{nv_p}{2l} = \frac{n}{2l}\sqrt{\frac{E}{\rho}},$$

where E is Young's modulus, l is the length of the bar, v_p is the velocity of longitudinal (pressure) waves, and ρ is the mass density, in exact analogy with waves on a string. Particularly useful is the fact that the speed of flexural and torsional disturbances is much slower than the speed of longitudinal disturbances, so frequencies corresponding to one or the other category may be easily distinguished.

Some of these dynamic methods were described in a 1935 paper by J. M. Ide [12]. One important result that he reported was that the natural resonance frequencies of a bar were extremely robust, noting that "[t]he same longitudinal natural frequencies (to 0.2%) are obtained for test specimens regardless of whether they are supported vertically or horizontally, or whether they are set into vibration by electrostatic traction, piezoelectric crystal drive, magnetostriction, or by resonating with an acoustic field." [12]

These methods were found to be very useful, but limited in scope because the sample sizes had to be fairly large, the techniques were effective only for isotropic materials, and the samples had to be precisely shaped long rods or reeds, to satisfy the approximate equations of motion.

a. Pulsed ultrasonic methods As mentioned in the beginning of this section, the traditional method for finding elastic constants of single crystals has been to measure the time-of-flight of an ultrasonic pulse; most sets of elastic constants currently in the literature have been measured in this fashion. The method first became practical in the early 1930's [13], when electronics for generating and detecting acoustic vibrations in the megahertz range became available.

If the elastic constants c_{ijkl} are denoted by the reduced notation c_{ij} (see Section II), then, for instance, constant
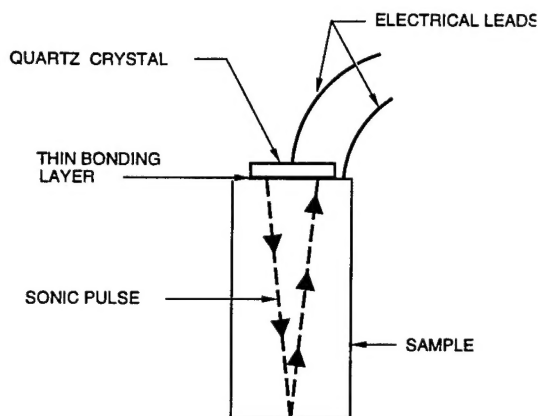
FIG. 5. A basic pulse-echo experimental setup (adapted from [7]).

c_{11} can be obtained by a measurement of the longitudinal sound velocity in the proper crystal direction; in the case of a cubic crystal, this would be the $\langle 100 \rangle$ or equivalent direction. The longitudinal velocity is then:

$$v_p \langle 100 \rangle_{\text{cubic}} = \sqrt{\frac{c_{11}}{\rho}}.$$

The elastic constant dependence may be slightly more complicated in other directions, but always has the form $v = \sqrt{\frac{a_{ij} c_{ij}}{\rho}}$; if the sound velocities, both longitudinal and shear, are measured in enough directions, a complete set of elastic constants can be obtained by solving a set of simultaneous equations.

One of the most popular setups for performing a sound-velocity measurement in a crystal is shown in Fig. 5. In this setup, the sound pulse is generated and its echo received by the same transducer, thus doubling the transit time of the pulse. In order for this measurement to succeed, the crystal must be oriented so that the tensor equations of motion in the solid uncouple, to ensure that the sample functions essentially as a plane waveguide for a single mode of propagation. Furthermore, the opposite faces must be parallel, or else wave motion of one type will be converted into other types. If the sample is highly anisotropic, the sample would have to be cut and polished with sides parallel to several different crystal directions, and transducers would have to be remounted for each direction, resulting in a possible loss of relative accuracy. In many cases, separate transducers are used to excite shear versus longitudinal (pressure) waves, so there are even more opportunities for error.

Perhaps most importantly, it is necessary that the properties of the transducer and bonding do not mask the properties of the sample one is measuring, which is of particular concern with small samples. For instance, the acoustic impedance of transducer materials is similar to many materials which one might wish to investigate;

if the transducer is a significant part of the system, it becomes difficult to define precisely where the pulse begins and ends. Some researchers consider this to be a problem even with large samples, and attempt to eliminate it by polishing a 'kink' or shoulder in the sample, which creates additional reflections of the pulse [89]. Other problems that can occur with pulse-echo experiments on small samples, such as ultrasonic beam diffraction and sidewall reflections, are discussed in [8].

b. Progress on the normal mode problem Despite its shortcomings, ultrasonic pulse-echo remained the only viable technique for most anisotropic single-crystal investigations through the 1960's. Resonant techniques were limited to special cases, because the problem of an oscillating finite elastic solid was unsolved in general. However, progress was being made on this front, although a connection with the measurement of elastic properties was not foreseen by all of the innovators.

A partial chronology of the developments in solving the normal mode problem since the 1930's might be as follows:

1951— R. D. Mindlin extends the theory of flexural motion of isotropic plates to anisotropic crystal plates [14].

1956— Ekstein and Schiffman [15] apply the Rayleigh-Ritz method to finding the free vibrations of isotropic cubes, using the Lamé modes as trial functions, and solve the resulting matrix eigenvalue problem analytically; their paper includes the first graphics depicting the normal modes of an elastic cube. Mindlin [16] finds exact solutions for certain modes of crystalline cubes and parallelepipeds, in analogy with the Lamé modes.

1962— Satô and Usami solve numerically the transcendental equation for the normal modes of an elastically isotropic sphere, given by Lamb and others in the 1880's. This paves the way for better understanding of the Earth's structure by enabling analysis of normal mode frequencies of the Earth extracted from seismic data.

1964— Fraser and Lecraw [69] duplicate Satô and Usami's results and apply them to the determination of the elastic constants of isotropic spherical specimens, performing what could be considered the earliest RUS measurement. The technique used in Section IV for finding the elastic constants of spherical ceramic particles is essentially the same as theirs, with differences in instrumentation and transduction.

1968— Holland [36] applies the Rayleigh-Ritz method to the problem of the vibration of piezoelectric rectangular parallelepipeds, using sinusoids as basis functions; he is the first to use large numbers of basis functions and solve the resulting matrix problem

6

on a computer. Unfortunately, his choice of basis is not general enough and his results are not especially accurate.

1971— Demarest [42] applies the Rayleigh-Ritz method to the problem of the free vibrations of an elastic parallelepiped, using an appropriate basis (Legendre polynomials). He calculates the frequencies of a cube of fused quartz, and compares the calculated values with measured values, and for the special case of the Lamé modes, the analytic solution; he obtains excellent agreement. He also uses the lowest 12 modes of the cube to determine the isotropic moduli graphically, in a manner similar to Fraser and Lecraw.

1992— Visscher [103] uses the Rayleigh-Ritz method to find the normal modes of elastic solids, using simple powers of cartesian coordinates as a basis (the "xyz" method). This deceptively minor innovation enables a numerical solution for the natural frquencies of a wide variety of shapes, including rectangular parallelepipeds, spheres, ellipsoids, eggs, hemispheres, cylinders, bells, cones, pyramids, and many other analytic shapes. Even more importantly, the calculations are rendered no more difficult if the above objects are highly anisotropic or (to an extent) inhomogeneous.

c. Modern history of RUS The modern history of RUS may be said to have begun in 1976 with a seminal paper by Ichiro Ohno [43], in which he extends the methods of Demarest to crystals of general symmetry, and applies the method to some orthorhombic specimens. He explains in detail how to set up the Rayleigh-Ritz problem and obtain the matrix solution, how to block-diagonalize the matrix using object and crystal symmetries, and the effect of matrix size on the accuracy of the calculations. He also provides a fairly detailed account of the experimental procedure.

Ohno's was also the first paper to address the issue of the inverse problem, when a graphical solution for the elastic constants is not possible and one must use an iterative method to converge on the correct values. Among the issues he addressed were mode identification, including the trick of polishing a side between measurements and using the length derivatives of the frequencies to identify modes, and the relative sensitivity of the data to different linear combinations of elastic moduli (a subject more recently reviewed by Avery and Sachse [17] in the context of pulse-echo measurements). Even 20 years later, Ohno's paper is an excellent introduction to RUS.

One additional detail of interest (which is, incidentally, not included in Ohno's review paper but in a related paper by a colleague in the same journal [23]), is Ohno and colleagues' treatment of the problem of perturbation of the natural frequencies by the transducers. Demarest [42] states that "An elastic force on the surface of a vibrating body must raise the frequency", and indeed the frequencies he measured were in general higher than the calculated ones. Ohno *et al.* attempted to circumvent this problem by mounting one transducer on an arm of a balance; in this way, the force on the specimen could be controlled by the amount of mass placed on the other arm of the balance. The measurement of the frequencies was repeated several times with decreasing amounts of mass; the results were extrapolated to zero, to obtain the frequencies of free vibration. Interestingly, the rms errors from least-squares fits of these extrapolated frequencies are much larger than the typical errors encountered in modern measurements, which generally use no such correction (compare the present work plus results in [45,41] to results in [43], [23]).

A consideration of an elastic bar terminated with a spring may convince the reader that the frequencies are raised not so much due to a static force on the body, but by an extra restoring force altering the boundary condition. Plotting the frequencies of the bar versus spring constant show that the plot is approximately linear around zero, so one can conceivably extrapolate to zero if one's experimental points have a good linear correlation. The author's experience has been that the frequencies of a RUS sample as a function of transducer contact force show no such correlation; the frequency shifts seen by Ohno *et al.* are probably due to high drive levels, rather than mere transducer contact, and are not seen by most modern experimenters [45].

Despite its promise, resonant ultrasound languished in obscurity for a number of years, limited almost exclusively to use by a small community of geoscientists. In the 1980's, the discovery of high-temperature superconductors provided an especially compelling motivation to find a method for measuring the elastic constants of anisotropic, small specimens. Albert Migliori of Los Alamos National Laboratory and J. D. Maynard of the Pennsylvania State University collaborated on developing such a method for the high-T_c application. Eventually, Dr. Migliori discovered the papers of Demarest and Ohno, and subsequently found that Demarast's Ph.D. thesis advisor, Orson L. Anderson, was still actively using RUS for geoscience applications at nearby UCLA.

The resulting collaborations brought resonant ultrasound into the larger physics community, with the computational techniques refined by William Visscher of Los Alamos, and the experimental methods updated by Maynard and Migliori. Some of these advances are summarized in Maynard's 1992 JASA paper [47], and Migliori's excellent review article in Physica B [45], where the term "resonant ultrasound spectroscopy" is officially introduced to the literature.

Despite the enormous progress that has been made in making RUS a viable technique, virtually all results have been on samples of several mm^3. Many of the best specimens of interest are only a few hundred microns in size; examples are single crystals of some high-temperature superconductors, icosahedral and decagonal quasicrystals, C_{60} crystals, and so on; the spherical ceramic particles

studied in Section IV have an average diameter of about 700 μm. It is therefore hoped that the present work will establish RUS as a practical choice for measuring the elastic properties of many new and novel materials, which might currently be thought out of reach of any other precise method.

II. GENERAL PRINCIPLES

A. Introduction

Resonant Ultrasound Spectroscopy (RUS) is the general term given to the measurement of a system's material properties by analyzing the normal mode (mechanical resonance) frequency spectrum of that system. This may include anything from an investigation of thermodynamic derivatives at a phase transition, to the nondestructive testing of ball bearings; one may also use the term "resonant *acoustic* spectroscopy" to include such things as the study of the free oscillations of the Earth caused by earthquakes. Since this paper involves only the measurement of elastic properties at room temperature, the scope of this section will be limited to the theoretical subjects essential to such a measurement. These would include:

- Basic elasticity theory, including wave propagation in elastic solids.

- The "forward problem", or the calculation of an object's resonance spectrum from known material properties.

- The "inverse problem", or the determination of elastic properties from measured resonances (this always presumes the ability to solve the forward problem).

Given the fundamental nature of elastic properties in so many areas of science and engineering, it is not surprising that many ingenious ways have been devised to measure them. As was noted in Section I, the idea that one should be able to extract elastic constants from measured resonance frequencies has been around for quite a long time; but it is only with the gradual improvement of instrumentation and computing power that this approach has become feasible. In addition, progress has been hastened by some key mathematical insights (as also mentioned in Section I); it is a purpose of this section to review them, and allow an evaluation of the theoretical foundation upon which rests the modern practice of RUS.

B. Theory of Elasticity

A brief review of some of the concepts of the linear theory of elasticity will provide the necessary background for a discussion of the measurement of elastic properties, and provide an opportunity to establish notation. To begin,
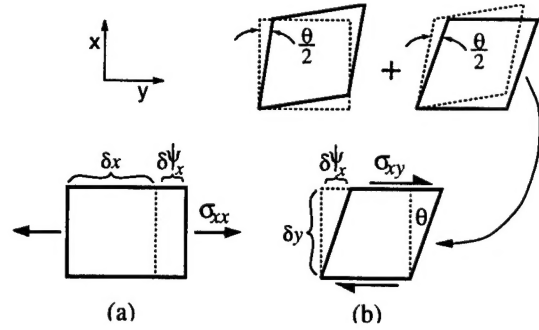

FIG. 6. A differential element of an elastic solid, showing (a) axial strain, and (b) shear strain. The drawings at top right show the shear strain (b) to be a combination of a symmetric strain and a rigid-body rotation.

one may imagine a spring, with a mark at position x and another a small distance away at $x+dx$. If a uniform, constant tensile force F is applied to the spring, the spring will stretch such that the marks on it are displaced according to some function $\psi(x)$. The amount of stretching can be quantified by looking at the change in separation of these neighboring points, *i.e.* $\psi(x + dx) - \psi(x)$. If we define the strain ϵ to be the *fractional* amount of stretch, then

$$\epsilon \equiv \frac{\psi(x + dx) - \psi(x)}{dx} = \frac{d\psi}{dx} . \tag{2}$$

If the spring is linear, *i.e.* obeys Hooke's law, then the force and strain are related by a simple constant of proportionality, *e.g.*

$$F = C\frac{d\psi}{dx} ;$$

if the spring has length l, then the familiar spring constant K is given by $K = \frac{C}{l}$.

Suppose instead of a spring, an elastic solid is deformed. One may imagine a deformation analagous to that of the spring, where the solid is extended (or compressed) by axial forces; or, due to the extra degrees of freedom, a deformation where the solid is distorted by *shearing* forces, without changing the volume (see Fig. 6). In Fig. 6(a), the solid is extended in the x-direction by a force in the x-direction, so the strain is $\epsilon_{xx} = \delta\psi_x/\delta x$. In 6(b), the solid is not extended, but only distorted, the distortion being characterized by an angle θ. If θ is small, it can be approximated by its tangent, or $\theta \simeq \delta\psi_x/\delta y$. There is a rotation hidden in 6(b), however; the two drawings on the top right of Fig. 6 show how the deformation in 6(b) can be decomposed into a symmetric shear strain and a solid-body rotation (note this only works for small angles). Thus, to eliminate the solid body rotation, the small strain tensor is defined:

$$\epsilon_{ij} = \frac{1}{2}\left(\frac{\partial\psi_i}{\partial x_j} + \frac{\partial\psi_j}{\partial x_i}\right) ; \tag{3}$$

note that $\epsilon_{ij} = \epsilon_{ji}$.

8

The total force normal to any differential surface element is $\mathbf{F}_n = \mathbf{t} \cdot \mathbf{n}\, dS$ and the total shear force is $\mathbf{F}_s = \mathbf{t} \times \mathbf{n}\, dS$, where $\mathbf{n}$ is the unit normal to the surface and $\mathbf{t}$ is the *traction*, given by:

$$t_i = \sigma_{ij} n_j, \qquad (4)$$

where σ_{ij} is the stress tensor. The σ_{ij} have units of force per unit area, and are defined such that the first index indicates its direction, and the second index indicates the plane on which it acts (see the examples of σ_{xx} and σ_{xy} in Fig.6). A consideration of the stress components on a differential volume element show that in order for the element to be in equilibrium, the stress tensor must also be symmetric, *i.e.*, the shear stresses must balance so that $\sigma_{ij} = \sigma_{ji}$. Otherwise, there would be a net torque on the element[1].

For small deformations, it is assumed that the stresses are a linear combination of the strains. In general, each stress will be coupled to all the strains (for instance, a bar shrinks in the x and y directions when pulled in the z direction). Thus, an 81-component tensor is needed to relate the two 9-component tensors, and Hooke's law for a general solid becomes:

$$\sigma_{ij} = c_{ijkl} \epsilon_{kl}, \qquad (5)$$

where the c_{ijkl} are the elastic constants, in units of force per unit area.

In the absence of body forces such as torques produced by magnetic fields, σ_{ij} is symmetric in the above formula (this may not be true for special materials such as ferromagnetics). Since ϵ_{ij} is symmetric, there are actually only six independent components of stress and six independent components of strain, reducing the number of independent c_{ijkl} to 36. This number can be further reduced by noting that the elastic energy should be quadratic in the strains; in analogy with the potential energy of a stretched spring, $U = \frac{1}{2}K(\Delta x)^2$, one may write for an elastic solid:

$$U = U_0 + \frac{1}{2} c_{ijkl} \epsilon_{ij} \epsilon_{kl}. \qquad (6)$$

Now the pairs of indices ij and kl may be interchanged, without affecting the result; this reduces the number of independent constants to 21. For most crystals, there are additional symmetries that further reduce the number of independent constants, and make many of the elements zero. For instance, a cubic crystal has three independent constants, a hexagonal (or transversely isotropic) material has five, and an orthorhombic crystal has nine.

---

[1]Obviously, in many cases of interest, the object is not actually in equilibrium, *e.g.*, if it is oscillating; but if the deformations are "small" then the stresses are also small, and any asymmetry in the stress tensor will be second-order in smallness.

Since there are now six strains and six stresses that can be related by 21 elastic constants, it is common practice to use a reduced notation [18]:

$$\sigma_i = c_{ij}\epsilon_j, \; i,j = 1,6 \qquad (7)$$

where ij and kl from (5) are collapsed to i and j according to the substitutions

$$
\begin{array}{ll}
11 \rightarrow 1 & 23 \rightarrow 4 \\
22 \rightarrow 2 & 13 \rightarrow 5 \\
33 \rightarrow 3 & 12 \rightarrow 6
\end{array} \qquad (8)
$$

and $c_{ij} = c_{ji}$. The fact that there are actually 9 elements of stress and strain is accounted for by letting $\epsilon_j = \epsilon_{jj}$ ($j \le 3$), but $\epsilon_4 = 2\epsilon_{23}$, $\epsilon_5 = 2\epsilon_{13}$, and $\epsilon_6 = 2\epsilon_{12}$.

Most published elastic constants are these latter c_{ij}; however, there are many instances when it is more convenient to work with the original tensor c_{ijkl}. Both notations will be used in this paper, with a remark if there is any possiblility of confusion.

1. The atomic view

The above analyses assume an elastic continuum; this may be complemented by briefly considering atoms in a lattice. A simple monatomic lattice is often modeled in one dimension as a chain of balls and springs. Propagation of disturbances (phonons) in such a lattice is dispersive; at long wavelengths (low wavenumber $k = \omega/c$), the dispersion relation $d\omega/dk$ approaches a constant slope. This is the phase velocity of a sound wave in this lattice; sound velocities are of the form (elastic constant/mass density)$^{1/2}$; thus the connection between the atomic lattice, sound propagation, and elasticity.

The springs in this model are unlike ideal springs, however, in that the atoms sit in a decidedly asymmetric potential well. At large separation distances (*e.g.* the 'rarified' portion of a sound wave) the restoring forces are weaker than at smaller distances (the compressed part of a sound wave). For small disturbances, the well is approximately quadratic, and the free energy of the crystal is:

$$U(\epsilon) = U_0 + \frac{1}{2}U_0''\epsilon^2 + \frac{1}{6}U_0'''\epsilon^3 \ldots$$

where ϵ is the strain. The second derivative(s) of the free energy with respect to strain may be identified with the linear elastic constant(s). The higher-order derivatives may be identified as higher-order elastic constants, and are evidently derivatives of the linear c_{ijkl} with respect to strain. Thus at least some can be found by measuring changes in the c_{ijkl} as a function of some quantity that produces a finite background strain, such as hydrostatic pressure. These higher-order constants may be linked to such thermodynamic quantities as the Debye temperature, the Grunheissen parameter, and the coefficient of thermal expansion [19].

9

a. Adiabatic vs. isothermal The above treatment makes the implicit assumption that the atom is at rest in the absence of a sonic disturbance, *i.e.*, it is at zero temperature. For real substances at room temperature, the presence of thermal agitation means one can have isothermal disturbances or adiabatic disturbances, hence isothermal or adiabatic elastic constants. The usual assumption in acoustics is that sound waves are adiabatic; we may use aluminum as an example to check this assumption for ultrasound in solids. "Adiabatic" means that the distance between hot and cold regions in a sound wave is too long for heat to conduct between cycles, *i.e.* the thermal penetration depth δ_κ is much less than $\lambda/2$ (note that for a thin rod or bar vibrating in flexure, the distance between hot and cold regions would be the half-width of the cross-section). We want

$$\frac{\lambda}{2} \gg \delta_\kappa = \sqrt{\frac{\kappa}{\rho c_p \omega}},$$

where κ is the thermal conductivity, ρ is the mass density, c_p is the specific heat at constant pressure and $\omega = 2\pi f$. This leads to

$$f \ll \frac{\rho c_p \pi c^2}{4\kappa}. \tag{9}$$

For bulk aluminum, the RHS of (9) is approximately $2.5 \times 10^{14} s^{-1}$, so ultrasonic propagation in the MHz range would appear to be adiabatic.

Most of the elastic constants published are, in fact, adiabatic constants, measured by dynamic methods. Isothermal moduli could be measured by static methods, *e.g.*, using a static load with a strain gauge. One can use a fairly simple derivation to compare adiabatic and isothermal moduli; let the adiabatic Young's modulus of aluminum be E_S, and the isothermal modulus be E_T. Then their ratio is [20]:

$$\frac{E_T}{E_S} = 1 - \frac{\alpha^2 \theta}{9c_p} E_T;$$

where θ is the temperature in °K, and α is the coefficient of thermal expansion. For $\theta = 300$°K, $E_T/E_s \simeq 0.998$. Thus (for aluminum, at least) the difference is not great.

b. Frequency dependence and anelastic effects Dynamic methods of measuring moduli may use frequencies that vary greatly with the size of the sample; this suggests that frequency dependence of elastic constants might be of concern. From the last example, we see that δ_κ is frequency dependent, although any ultrasonic propagation in the MHz range is most likely completely adiabatic. Of more importance could be frequency dependence of internal friction. With internal friction, hence some mechanism of relaxation, the dynamics of deformation are altered; one simple model, described by Zener in his *Elasticity and Anelasticity of Metals* [21], indicates that the elastic modulus will vary between a "relaxed" value for oscillations slow compared to a characteristic

relaxation time τ and an unrelaxed value when $\omega \gg 1/\tau$. At $\omega\tau \simeq 1$, the internal friction is at a maximum, and the elastic modulus changes most rapidly. Kolsky (1963) adds:

> [Internal friction] of plastics and dielectrics is generally much higher than in metals, and the elastic modulus often changes very rapidly with frequency [22].

While this may be of concern when dealing with very lossy materials, it is probably not much a factor in most resonant ultrasound investigations. One indication is given by the cubic silicon "calibration" measurement detailed in the next section. The elastic moduli are in excellent agreement with moduli measured by pulse-echo methods on much bigger samples.

This issue is mentioned mainly in the interests of full disclosure; it will not be considered in the rest of the paper. While the mathematics that follow will exclude attenuation, a development of the variational principles used in resonant ultrasound, including attenuation, has been put forth by Sumino, Goto, Ohno, and Kumazawa [23] and Oda, Anderson, and Suzuki [24].

2. Examples of elastic symmetry

To round out the above discussions, two elastic tensors with high symmetry will be discussed (the cubic and isotropic tensors), which will be of importance in Section V.

Cubic symmetry is a subset of orthorhombic symmetry, where the crystal lattice unit cell has three mutually orthogonal mirror planes. It is simple to ascertain the effect on the elastic symmetry of one mirror plane (say, the xy plane); we simply require that c_{ijkl} be invariant under the transformation $z \to -z$. The matrix of direction cosines a_{ij} (where $v_i' = a_{ij}v_j$) is:

$$a_{ij} = \begin{array}{c} \\ x' \\ y' \\ z' \end{array} \begin{array}{ccc} x & y & z \\ \left[\begin{array}{ccc} 1 & 0 & 0 \\ 0 & 1 & 0 \\ 0 & 0 & -1 \end{array}\right] \end{array}.$$

Then $c'_{ijkl} = a_{im}a_{jn}a_{ko}a_{lp}c_{mnop} = c_{ijkl}$; since $a_{ij} = 0$ if $i \neq j$, this reduces to

$$c'_{ijkl} = a_{ii}a_{jj}a_{kk}a_{ll}c_{ijkl} = c_{ijkl} \quad \text{(no summation)}.$$

Since $a_{33} = -1$, it is clear that if the index 3 is present an odd number of times, that value of c_{ijkl} will change sign; hence, if the elastic tensor is to remain invariant under reflection, all c_{ijkl} with the subscript 3 occuring 1 or 3 times must be zero, *e.g.* $c_{1113} = c_{1131} = c_{1311} = c_{3111} = c_{15} = 0$. Hence, for one plane of symmetry (monoclinic),

using the collapsed indices:

$$c_{ij} = \begin{bmatrix} c_{11} & c_{12} & c_{13} & 0 & 0 & c_{16} \\ c_{12} & c_{22} & c_{23} & 0 & 0 & c_{26} \\ c_{11} & c_{13} & c_{33} & 0 & 0 & c_{36} \\ 0 & 0 & 0 & c_{44} & c_{45} & 0 \\ 0 & 0 & 0 & c_{45} & c_{55} & 0 \\ c_{16} & c_{26} & c_{36} & 0 & 0 & c_{66} \end{bmatrix} \quad \text{(monoclinic)}$$

There are 13 independent elastic constants.

A similar argument can be used for mirror planes in the other two directions, so that for an orthorhombic crystal, any elastic constant where any index appears an odd number of times is zero. The resulting matrix of elastic constants is:

$$c_{ij} = \begin{bmatrix} c_{11} & c_{12} & c_{13} & 0 & 0 & 0 \\ c_{12} & c_{22} & c_{23} & 0 & 0 & 0 \\ c_{11} & c_{13} & c_{33} & 0 & 0 & 0 \\ 0 & 0 & 0 & c_{44} & 0 & 0 \\ 0 & 0 & 0 & 0 & c_{55} & 0 \\ 0 & 0 & 0 & 0 & 0 & c_{66} \end{bmatrix} \quad \text{(orthorhombic)}$$

Here there are nine independent constants.

A cubic crystal has orthorhombic symmetry, and in addition has four axes of threefold rotational symmetry (the body diagonals of the cubic unit cell). Requiring the elastic tensor c_{ijkl} to be invariant under a rotation of $2\pi/3$ about a body diagonal ([111], for instance), which amounts to interchanging the x, y, and z axes according to $x \to y \to z \to x$ (i.e. $c_{1133} = c_{2211}$, etc.), shows that there are only three independent constants; the resulting reduced elastic tensor is:

$$c_{ij} = \begin{bmatrix} c_{11} & c_{12} & c_{12} & 0 & 0 & 0 \\ c_{12} & c_{11} & c_{12} & 0 & 0 & 0 \\ c_{12} & c_{12} & c_{11} & 0 & 0 & 0 \\ 0 & 0 & 0 & c_{44} & 0 & 0 \\ 0 & 0 & 0 & 0 & c_{44} & 0 \\ 0 & 0 & 0 & 0 & 0 & c_{44} \end{bmatrix} \quad \text{(cubic)} \quad (10)$$

a. Isotropy An elastically isotropic substance is one whose elastic properties are independent of direction; thus isotropy is characteristic of (but not limited to) glassy, amorphous substances. An isotropic substance has at least cubic symmetry; in addition, the elastic tensor is unaltered by an arbitrary rotation. If one gives the cubic tensor an arbitrary rotation, setting the result equal to the original, one obtains a set of equations in c_{11}, c_{12}, and c_{44}; some are identities, but the rest are redundant statements of the equation, $c_{12} = c_{11} - 2c_{44}$. Thus an isotropic substance has two independent constants; these may be related in various ways with familiar bulk properties such as the bulk modulus, shear modulus, Poisson's ratio, and Young's modulus. Using the familiar Lamé moduli λ and μ for c_{12} and c_{44}, one obtains:
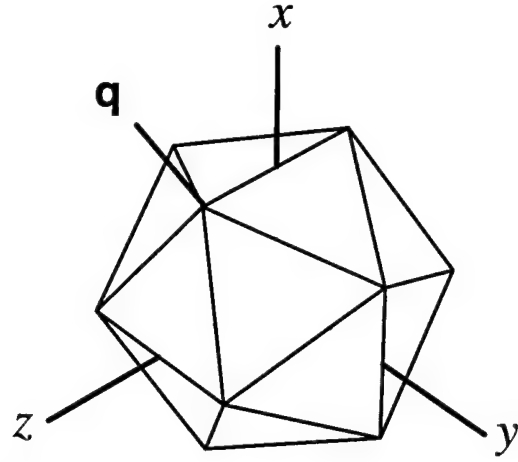

FIG. 7. A regular icosahedron, with twofold axes aligned with an orthogonal coordinate system. There is threefold symmetry about the center of each triangular facet; four of the threefold axes are the same as those for a cube aligned with the coordinate axes (its body diagonals). One of the fivefold axes is labeled **q**.

$$c_{ij} = \begin{bmatrix} \lambda + 2\mu & \lambda & \lambda & 0 & 0 & 0 \\ \lambda & \lambda + 2\mu & \lambda & 0 & 0 & 0 \\ \lambda & \lambda & \lambda + 2\mu & 0 & 0 & 0 \\ 0 & 0 & 0 & \mu & 0 & 0 \\ 0 & 0 & 0 & 0 & \mu & 0 \\ 0 & 0 & 0 & 0 & 0 & \mu \end{bmatrix} \quad \text{(isotropic)}$$

$$(11)$$

Then, for instance, Young's modulus of extension E and the shear modulus G are given by:

$$E = \frac{\mu(3\lambda + 2\mu)}{\lambda + \mu} \; ; \quad G = \mu \, .$$

It is significant that the isotropic tensor is essentially a special case of the cubic tensor; it means that a cubic crystal could have an elastic tensor that is numerically very close to isotropic, even though the lattice itself is not isotropic. This will be of importance in the study of AlCuLi quasicrystals presented in Section V.

b. Isotropy of icosahedral solids The discovery of icosahedral quasicrystals in 1984 [26], and the subsequent discovery of dodecagonal and octagonal quasicrystals, makes these non-crystallographic symmetries of interest. Consider an icosahedron, as shown in Fig. 7: it has numerous twofold, threefold and fivefold axes; moreover, a cube may be oriented so that its threefold and twofold axes coincide with those of the icosahedron. The elastic properties of an icosahedral solid must therefore have at least cubic symmetry (another way of expressing this is to note that the icosahedral point groups 235 and $m35$ both contain the cubic subgroup 23). Furthermore, the elastic tensor for icosahedral symmetry should be invariant under a rotation about any of the fivefold axes; one of these (labeled **q** in Fig. 7) is at an angle of $\tan^{-1}(1/\tau)$

from the x-axis in the xy plane, where τ represents the golden mean, or $(\sqrt{5}+1)/2$. This number has interesting properties, including $\tau - 1 = 1/\tau$, and $\tau + 1 = \tau^2$. Using these properties, a rotation of $2\pi/5$ about axis $\mathbf{q}$ can be represented by the direction cosines:

$$a_{ij} = \frac{1}{2}\begin{bmatrix} \tau & -1/\tau & 1 \\ -1/\tau & 1 & \tau \\ -1 & -\tau & 1/\tau \end{bmatrix} .$$

Requiring the cubic elastic tensor to be invariant under this transformation leads to the equation

$$\frac{1}{16}(\tau^4 + 1/\tau^4 + 1)c_{11} + \frac{1}{8}(1 + \tau^2 + 1/\tau^2)c_{12} +$$
$$\frac{1}{4}(1 + \tau^2 + 1/\tau^2)c_{44} = c_{11} ; \quad (12)$$

using various properties of τ, one may reduce this to the expression $c_{12} = c_{11} - 2c_{44}$. In other words, an icosahedral solid must be isotropic in the linear elastic constants. This is a curious sort of isotropy, because the solid itself has long-range order, and may be anisotropic in other properties, such as the higher-order elastic constants [27].

3. Wave propagation in solids

The force balance on a small element of an elastic solid obtains:

$$\frac{\partial \sigma_{ij}}{\partial x_j} = \rho \frac{\partial^2 \psi_i}{\partial t^2} ;$$

Using Hooke's law (5) as the constitutive relation,

$$\frac{1}{2}c_{ijkl}\frac{\partial}{\partial x_j}\left(\frac{\partial \psi_k}{\partial x_l} + \frac{\partial \psi_l}{\partial \psi_k}\right) = \rho\frac{\partial^2 \psi_i}{\partial t^2} .$$

Since the summation extends over all k, l, and $c_{ijkl} = c_{ijlk}$, this is equivalent to:

$$c_{ijkl}\frac{\partial^2 \psi_k}{\partial x_j \partial x_l} = \rho\frac{\partial^2 \psi_i}{\partial t^2} , \quad (13)$$

the equation of motion for a linear elastic solid.

It is not obvious from the above equation that traveling wave solutions are possible, or what their velocities will be. The Christoffel equations [1] are an equivalent and more convenient expression of (13). Let u, v, and w be the displacements in the x, y, and z directions, respectively. Let the direction of wave propagation have direction cosines p, q, and r. A distance along this direction can be expressed as $s = px + qy + rz$.

Then

$$\rho\frac{\partial^2 u}{\partial t^2} = \gamma_{11}\frac{\partial^2 u}{\partial s^2} + \gamma_{12}\frac{\partial^2 u}{\partial s^2} + \gamma_{13}\frac{\partial^2 u}{\partial s^2} ;$$

$$\rho\frac{\partial^2 v}{\partial t^2} = \gamma_{12}\frac{\partial^2 v}{\partial s^2} + \gamma_{22}\frac{\partial^2 v}{\partial s^2} + \gamma_{23}\frac{\partial^2 v}{\partial s^2} ;$$

$$\rho\frac{\partial^2 w}{\partial t^2} = \gamma_{13}\frac{\partial^2 w}{\partial s^2} + \gamma_{23}\frac{\partial^2 w}{\partial s^2} + \gamma_{33}\frac{\partial^2 w}{\partial s^2} ;$$

$$(14)$$

where the γ_{ij} are functions of the elastic constants c_{ij} and the direction cosines p, q, and r. From these, one may obtain a determinant equation for three velocities and another for direction cosines of particle velocity (the details may be found in [1]).

a. Limits of pulse measurements It is evident from 14 that one cannot expect in general that the particle velocities will be in or perpendicular to the direction of propagation. For a pulse-echo measurement to succeed, it is neccessary that the tensor equations uncouple and provide mutually orthogonal modes of propagation, so that samples can be treated as one-dimensional waveguides, supporting only that mode which is excited. This turns out to be true in general only for specific orientations of a crystal lattice. Hence one of the advantages of RUS—a sample can be expected to have well-defined normal modes regardless of the orientation of the lattice with regard to the sample geometry.

As an example, consider a crystal with cubic symmetry. Solving the Christoffel equations shows that there are only three distinct directions along which a longitudinal and two shear waves can be transmitted; these are the crystal directions $\langle 100 \rangle$, $\langle 110 \rangle$, and $\langle 111 \rangle$ [1]. For instance, if a sample is cut and polished so that one pair of sides is normal to the $\langle 110 \rangle$ direction, another normal to the $\langle 1\bar{1}0 \rangle$ direction, and the third pair normal to $\langle 001 \rangle$ (the z-direction), then a transducer placed on a face normal to $\langle 110 \rangle$ can excite longitudinal waves along $\langle 110 \rangle$ with velocity $V_l = [(c_{11} + c_{12} + 2c_{44})/\rho]^{1/2}$, and shear waves along $\langle 1\bar{1}0 \rangle$ and $\langle 001 \rangle$ with velocities $v_s = [c_{44}/\rho]^{1/2}$ and $v_s = [(c_{11} - c_{12})/\rho]^{1/2}$. Thus all three elastic constants of a cubic crystal can be measured from velocity data along $\langle 110 \rangle$. In the $\langle 100 \rangle$ or $\langle 111 \rangle$ direction, however, shear wave propagation is isotropic, so measurements in either of these directions alone is insufficient.

Lower symmetry crystals present even more difficulty, since at most only three velocities (hence three constants) can be measured in any one direction. Again, the normal mode approach is attractive, because measuring the resonances of a highly anisotropic sample is no more difficult than measuring the resonances of an isotropic sample. The chief difficulty with this approach is that there exists no simple relationship between the resonance frequencies and the elastic constants, as between the elastic constants and the velocities of propagation. In general, one must be able to calculate theoretical values of the normal mode frequencies based on some assumed values for the elastic constants (the forward problem), and then

adjust these until the calculated spectrum matches that which is observed (the inverse problem). The forward problem, finding the normal modes of vibration of a finite elastic solid, is one of the great problems of applied physics. As will be shown in the next section, the existence of modern high-speed computers renders the problem easily solvable for many important cases, with the use of a simple variational principle.

C. The forward problem

Since no straightforward relationship between resonance frequencies and elastic constants exists, to find the constants from the frequencies one must be able to calculate frequencies from nominal values of elastic constants, subsequently adjusting them until, hopefully, the measured and observed spectra coincide. Finding the natural resonance freqencies of a finite elastic solid, the "forward problem", is of intrinsic interest as one of the oldest and most intractable problems of applied physics. The classic approach to solving a boundary-value problem of this type is to write down the differential equation of motion, find a time-harmonic solution, and use the boundary conditions to obtain an analytic expression for the natural frequencies; few solutions of this type exist for finite elastic solids. Important exceptions include:

- The homogeneous, elastically isotropic sphere [64].

- Certain shear modes of isotropic and crystalline parallelepipeds, with the ratio of two sides being a ratio of integers (the Lamé modes) [16].

Both these solutions will be utilized in this section; as a more general, numerical method for finding the normal modes is sought, the exact solutions for these cases can be used for comparison.

1. Analytic solutions

Two analytic solutions will be used in this work; that of the free vibrations of an elastic sphere, and the Lamé modes of an elastic parallelepiped.

a. Radial modes of an oscillating elastic sphere As an illustration of an analytic solution of the free vibration of a finite elastic solid, an expression will be derived for the frequency of the lowest dilatational mode, the "breathing" mode, of an isotropic sphere.

The equation of motion for an elastic continuum is

$$c_{ijkl}\frac{\partial^2\psi_k}{\partial x_j \partial x_l} = \rho\frac{\partial^2\psi_i}{\partial t^2},$$ (15)

and the condition that the surface remain traction-free, where $t_i = \sigma_{ij}n_j$, is expressed as

$$c_{ijkl}\frac{\partial\psi_k}{\partial x_l}n_j = 0.$$ (16)

These Cartesian component forms are not useful for a problem in spherical coordinates; if one writes out the components for the isotropic case, using a few vector identities, one can obtain the vector forms:

$$(\lambda + 2\mu)\nabla(\nabla\cdot\psi) - \mu\nabla\times(\nabla\times\psi) = \rho\frac{\partial^2\psi}{\partial t^2};$$ (17)

$$\lambda(\nabla\cdot\psi)\hat{n} + 2\mu\vec{\nabla}\psi\cdot\hat{n} - \mu(\vec{\nabla}\psi - \psi\overleftarrow{\nabla})\cdot\hat{n} = 0;$$ (18)

the reader may recognize that the rightmost terms on the l.h.s. of both 17 and 18 are zero if the motion is irrotational. Using this fact, along with the vector identity $\nabla\times(\nabla\times\psi) = \nabla(\nabla\cdot\psi) - \nabla^2\psi$, one can extract two equations for plane waves, which are:

$$(\lambda + 2\mu)\nabla^2\psi = \rho\frac{\partial^2\psi}{\partial t^2} \quad \text{(irrotational)}$$ (19)

$$\mu\nabla^2\psi = \rho\frac{\partial^2\psi}{\partial t^2} \quad \text{(equivoluminal)}$$ (20)

Thus the speed of dilatational, or pressure, waves is $v_p = \left((\lambda + 2\mu)/\rho\right)^{1/2}$, and the speed of pure shear waves is $v_s = (\mu/\rho)^{1/2}$.

For the case of the vibrating sphere, we note that the "breathing" mode of a sphere is spherically symmetric and purely radial, so the rotational terms are zero. Converting to spherical coordinates, with no θ or ϕ dependence, where $\nabla\cdot\psi\hat{n} = 1/r^2\partial/\partial r(r^2\psi)$, $\vec{\nabla}\psi\cdot\hat{n} = \partial\psi/\partial r$, and $\nabla(\nabla\cdot\psi) = \partial/\partial r(1/r^2\partial/\partial r(r^2\psi))$, we obtain:

$$(\lambda + 2\mu)\left[\frac{\partial^2\psi}{\partial r^2} + \frac{2}{r}\frac{\partial\psi}{\partial r} - \frac{2}{r^2}\right] = \rho\frac{\partial^2\psi}{\partial t^2};$$ (21)

$$(\lambda + 2\mu)\frac{\partial\psi}{\partial r} + \frac{2\lambda}{r}\psi = 0.$$ (22)

The first equation is the equation of mation, and the second is the boundary condition.

Note that even in the purely radial, spherically symmetric case, it is not necessary that $\vec{\nabla}\psi\cdot\hat{n}$ be zero at a free boundary, as it would for a string, membrane, or for acoustic (air) waves in a spherical cavity. This has some important consequences when constructing a numerical approach to the boundary value problem.

The equation of motion may be recast by assuming a time harmonic solution, *i.e.* $\partial^2/\partial t^2 \to -\omega^2$, and letting $k^2 = \rho\omega^2/(\lambda + 2\mu) = (\omega/v_p)^2$ and $\xi = kr$. Then the equation of motion can be written

$$\xi^2\frac{\partial^2\psi}{\partial\xi^2} + 2\xi\frac{\partial\psi}{\partial\xi} + (\xi^2 - n(n+1))\psi = 0, n = 1;$$ (23)

this has the form of the spherical Bessel equation, with $n = 1$. The solution is then a combination of spherical

13

Bessel and spherical Neumann functions of first order, j_1 and y_1; y_1 blows up at $kr = 0$, so the solution is of the form

$$\psi(r) = A j_1(kr) = A \frac{1}{kr} \left(\frac{\sin kr}{kr} - \cos kr \right) . \quad (24)$$

Applying the boundary condition at $r = a$, and using the properties of the spherical Bessel functions [30], the following transcendental equation for the ka is obtained:

$$ka(\lambda + 2\mu) j_0(ka) = 4\mu j_1(ka) , \quad (25)$$

where $j_0(ka) = \sin ka/ka$, and j_1 is given in (24) above.

The presence of both λ and μ in (25) shows that the solutions depend on the ratio λ/μ, or equivalently, on Poisson's ratio $\nu = \lambda/2(\lambda + \mu)$, the ratio of lateral shrink to longitudinal stretch under an axial stress. This distinguishes the breathing mode from the pure shear modes, which depend only on μ.

To obtain a solution for ka, we set $\lambda = \mu$, or $\nu = 0.25$. The lowest root of (25) is found to be $ka = 2.563$. It will turn out to be convenient to normalize the nondimensional frequencies of free oscillation to the shear wave velocity; if $\lambda = \mu$, then $v_s = v_p/\sqrt{3}$, and for the lowest breathing mode of a freely oscillating isotropic sphere we have $\omega a/v_s = 4.440$.

The general solution for all the modes of vibration of a freely oscillating isotropic sphere is obtainable, and is discussed in Section IV in the context of studying spherical samples.

b. *Lamé modes* The Lamé modes [28], [16] occur when shear waves propagating in directions orthogonal to one another, but parallel to the surface of a rectangular parallelepiped or plate, interfere in such a way as to break the solid up into traction-free prisms. If the sides whose normals are in the direction of propagation are in an integer ratio, then the boundaries of the parallelepiped can become stress-free. Such modes exist for isotropic, cubic, hexagonal, and some tetragonal symmetries. For an isotropic rectangular parallelepiped with sides $2a$, $2b$, and $2c$, where $a/m = b/n$ and m, n are integers, the Lamé modes are given by:

$$\omega_m = \frac{m\pi}{2a} \sqrt{\frac{\mu}{\rho}} . \quad (26)$$

Thus these modes form a harmonic series, which is not usually the case for modes of vibration of elastic objects.

The Lamé modes and the sphere modes will both be used to check the accuracy of numerical calculations later in this section.

2. Solution using the Rayleigh-Ritz method

One of the main obstacles to solving the free-vibration problem for elastic solids is the vector nature of the differential equation of motion. This naturally suggests that a more fruitful approach might be to formulate an equivalent variational principle based on scalar quantities, like the kinetic and potential energies. This is accomplished using the variational form of Hamilton's principle, in which the eigenfunctions of the elastic solid make the Lagrangian stationary.

A very simple way of introducing this concept is to consider a mass-spring oscillator, with a mass m hanging on a spring of stiffness k. If the displacement of the mass from equilibrium is ψ, the potential energy of the spring is $U = \frac{1}{2}k\psi^2$; the kinetic energy of the mass is $T = \frac{1}{2}m(\partial\psi/\partial t)^2$. If the system is in harmonic oscillation, then $(\partial\psi/\partial t)^2 = \omega^2\psi^2$; if $\psi(t) = A_0 \cos\omega t$, say, then the time-averaged energies are $\langle U \rangle = \frac{1}{4}kA_0^2$ and $\langle T \rangle = \frac{1}{4}m\omega^2 A_0^2$. However, the motion is such that the energy is continually being changed from all potential (when the spring is maximally stretched) to all kinetic (when the mass is at maximum velocity as it passes through $\psi = 0$). If there are no losses, then these maximum values must be equal; it follows that the time-averaged quantities must also be equal (this is a special result of the *virial theorem* [29], which states that if a system has a potential energy of the form $U = Kr^{n+1}$, then the time-averaged kinetic energy $\langle U \rangle = \frac{1}{2}(n + 1)\langle U \rangle$).

It follows that $\omega^2 = \langle U \rangle/\frac{1}{4}mA_0^2$, or

$$\omega = \sqrt{\frac{k}{m}} .$$

This is the well-known result for a mass-spring oscillator that one normally derives from solving the equation of motion. Although this system is extraodinarily simple, the principle applies equally well to elastic solids. If a vibrating elastic solid is executing a normal mode, it still oscillates between extremes of maximum strain and zero velocity, where potential energy is a maximum and kinetic energy is zero, and zero strain but maximum particle velocity, where kinetic energy is a maximum and potential energy is zero; and if energy is conserved, these maximum quantities must be equal. If the elastic potential energy density is given by

$$U = \tfrac{1}{2}c_{ijkl}\epsilon_{ij}\epsilon_{kl} = \tfrac{1}{2}c_{ijkl}\frac{\partial\psi_i}{\partial x_j}\frac{\partial\psi_k}{\partial x_l} ,$$

and the kinetic energy density is

$$T = \tfrac{1}{2}\rho\omega^2\psi\cdot\psi ,$$

then it is expected that

$$\omega^2 = \frac{\displaystyle\int_V c_{ijkl}\frac{\partial\psi_i}{\partial x_j}\frac{\partial\psi_k}{\partial x_l}\, dV}{\displaystyle\int_V \rho\,\psi\cdot\psi\, dV} . \quad (27)$$

This is actually a simplified statement of Rayleigh's principle [31], for the case of an elastic solid.

This would not seem to create any advantage at first sight, since it assumes that ψ is known. However, if one can guess at the form of ψ, then it turns out that the resulting estimate for ω^2 can be quite accurate. Furthermore, if the form for ψ is unknown, one can use an expansion for ψ in terms of basis functions with unknown coefficients as the guess, and (27) becomes transformed into a matrix eigenvalue problem (this is the Ritz method [32]).

To put this on more formal footing, consider Hamilton's principle, that the motion is such that the difference between the kinetic and potential energies is stationary:

$$\delta \int_{t_1}^{t_2} \int_V (U - T)\, dV dt = 0 \,. \qquad (28)$$

This is variational integral in four independent variables $\{x, y, z, t\}$, and must be stationary in all 4. The integrand is referred to as the Lagrangian, and the variational principle is equivalent to the corresponding Lagrangian equations of motion.

For the present case of an elastic solid, one may examine the requirement that $(T - U)$ be stationary in time by assuming that $\psi(\vec{r}, t)$ is separable, so that $\psi(\vec{r}, t) = \psi(\vec{r}) q(t)$, and $\delta\psi(\vec{r}, t) = \varepsilon\psi(\vec{r})\eta(t)$, where ε is a small constant and η is an arbitrary function of time, except that it vanishes at t_1 and t_2 and is differentiable in that interval. Requiring $\eta(t) = 0$ at the endpoints is not a serious constraint, because t_1 and t_2 are themselves arbitrary. Then

$$\delta \int_{t_1}^{t_2} \int_V c_{ijkl} \frac{\partial \psi_i}{\partial x_j} \frac{\partial \psi_k}{\partial x_l}\, dV dt - \rho \left(\frac{\partial \psi}{\partial t} \right)^2 dV dt \ =$$

$$\left. \frac{\partial}{\partial \varepsilon} \right|_{\varepsilon=0} \int_{t_1}^{t_2} \int_V c_{ijkl} \frac{\partial(\psi_i + \delta\psi_i)}{\partial x_j} \frac{\partial(\psi_k + \delta\psi_k)}{\partial x_l}$$

$$- \rho \left(\frac{\partial(\psi + \delta\psi)}{\partial t} \right)^2 dV dt = 0 \,.$$

Only the terms that are first order in $\delta\psi$ will survive, since the zeroth order terms have no ε dependence and the second order terms will be first order after the differentiation, and hence zero for $\varepsilon = 0$. One obtains

$$\int_{t_1}^{t_2} \int_V c_{ijkl} \frac{\partial \psi_i}{\partial x_j} \frac{\partial \psi_k}{\partial x_l} q(t)\eta(t) - \rho\, \psi \cdot \psi\, \ddot{q}(t)\eta(t)\, dV dt = 0 \,;$$

for brevity a step has been omitted. If one integrates the second term in the integrand by parts, recalling that $\eta(t_1) = \eta(t_2) = 0$, then it is found that

$$\int_{t_1}^{t_2} \left(\int_V c_{ijkl} \frac{\partial \psi_i}{\partial x_j} \frac{\partial \psi_k}{\partial x_l} q(t) - \rho\, \psi \cdot \psi\, \ddot{q}(t)\, dV \right) \eta(t)\, dt = 0 \,;$$

since η is arbitrary except at the endpoints, the expression in braces vanishes and we have

$$\frac{\ddot{q}}{q} = -\frac{\displaystyle\int_V c_{ijkl} \frac{\partial \psi_i}{\partial x_j} \frac{\partial \psi_k}{\partial x_l}\, dV}{\displaystyle\int_V \rho\, \psi \cdot \psi\, dV} = \text{constant.} \qquad (29)$$

Therefore $\ddot{q}/q = -\omega^2$, $q = \hat{A}\cos\omega t$, and we have the result of Eq. (27), Rayleigh's principle for an elastic solid.

Now the consequences of requiring the Lagrangian to be stationary in space are considered. The variational principle is

$$\delta \int_V c_{ijkl} \frac{\partial \psi_i}{\partial x_j} \frac{\partial \psi_k}{\partial x_l} - \rho\omega^2 \psi \cdot \psi\, dV = 0 \,; \qquad (30)$$

If $\delta\psi = \varepsilon\eta(\vec{r})$, then

$$\left[\frac{\partial}{\partial \epsilon} \int_V c_{ijkl} \frac{\partial(\psi_i + \epsilon\eta_i)}{\partial x_j} \frac{\partial(\psi_k + \epsilon\eta_k)}{\partial x_l} \right.$$

$$\left. - \rho(\psi + \epsilon\eta) \cdot (\psi + \epsilon\eta)\, dV \right]_{\epsilon=0} =$$

$$\int_V c_{ijkl} \left(\frac{\partial \psi_i}{\partial x_j} \frac{\partial \eta_k}{\partial x_l} + \frac{\partial \psi_k}{\partial x_l} \frac{\partial \eta_i}{\partial x_j} \right) - 2\rho\omega^2 \psi_i \eta_i dV = 0 \quad (31)$$

Using the symmetry of the elastic tensor, ($c_{ijkl} = c_{klji}$), and integrating the first term by parts with respect to x_j leads to

$$2 \int_V \left(c_{ijkl} \frac{\partial^2 \psi_k}{\partial x_l \partial x_j} + \rho\omega^2 \psi_i \right)$$

$$- 2 \int_S \left[\left(c_{ijkl} \frac{\partial \psi_k}{\partial x_l} \eta_j \right) \eta_i \right] dS = 0$$

Due to the arbitrariness of $\eta(\vec{r})$, both integrals must vanish independently. This not only gives the constant-frequency equation of motion, but also a boundary condition, although which boundary condition depends on the constraints placed on $\eta(\vec{r})$ at the boundary. If $\eta(\vec{r})$ is allowed to be arbitrary on the boundary, then the surface traction must vanish and this corresponds to a free surface. On the other hand, one could specify that $\eta(\vec{r})$ vanish on the boundary, which would then fix the displacement $\psi(\vec{r})$ to be zero at the boundary.

a. The Ritz method The condition that the Lagrangian be stationary with respect to perturbations of the spatial eigenfunction is equivalent to the original differential equation (plus a boundary condition); it can also be used to formulate the problem as a matrix eigenvalue equation, when a sum of basis functions with unknown coefficients is used as the trial function for $\psi(\vec{r})$, *i.e.* the Ritz method [32]. First,

$$\psi(\vec{r}) \approx \sum_{i=1}^{3} \sum_{\mu=1}^{N} a_{\mu,i}\, \phi_\mu(\vec{r})\, \hat{e}_i \,, \qquad (32)$$

where the ϕ_μ are a set of basis functions that one reasonably expects can be combined to approximate the spatial eigenfunctions. Next, the above is substituted into (30); for this purpose, an alternate notation can be used, that cuts down on the number of subscripts. Let

$$\psi(\vec{r}) \approx \sum_{m=1}^{3N} a_m \phi_m \, \hat{e}(m) \,, \quad \phi_m \in \phi_\mu \,. \tag{33}$$

Then the Lagrangian becomes

$$L \approx \int_V c_{i_m j k_n l} \frac{\partial \left(\sum a_m \phi_m\right)}{\partial x_j} \frac{\partial \left(\sum a_n \phi_n\right)}{\partial x_l}$$
$$- \rho \omega^2 \left(\sum a_m \phi_m\right)\left(\sum a_n \phi_n\right) \delta_{i_m k_n} \, dV. \tag{34}$$

This is equivalent to

$$L \approx \sum \sum a_m a_n \Gamma_{mn} - \omega^2 \sum \sum a_m a_n E_{mn} \,,$$

where

$$\Gamma_{mn} = \int_V c_{i_m j k_n l} \frac{\partial \phi_m}{\partial x_j} \frac{\partial \phi_n}{\partial x_l} \, dV \tag{35}$$

and

$$E_{mn} = \int_V \rho \phi_m \phi_n \delta_{i_m k_n} \, dV. \tag{36}$$

In matrix form, this equals

$$L \approx \mathbf{a}^{\mathrm{T}} \left(\mathbf{\Gamma a} - \omega^2 \mathbf{E a}\right)$$

Requiring $\delta L = 0$ means that L is stationary with respect to small perturbations of the eigenfunction, which in this case is equivalent to small perturbations of the basis function coefficients (the a_m). Therefore, $\partial/\partial a_m(L) = 0$, which leads to:

$$\mathbf{\Gamma a} - \lambda \mathbf{E a} = 0 \,, \tag{37}$$

where $\lambda \approx \omega^2$ (note that λ here refers to an eigenvalue, and not a Lamé constant or a wavelength). Therefore, approximate values for the frequencies can be obtained by solving the above eigenvalue problem.

Ohno [43] suggested that if the sample was homogeneous ($\rho = $ constant) that it would be better to find eigenvalues $\lambda = M\omega^2$, where M is the mass of the sample, by solving

$$\bar{\mathbf{\Gamma}} \mathbf{a} - \lambda \bar{\mathbf{E}} \mathbf{a} = 0 \,, \tag{38}$$

where $\bar{\Gamma}_{mn} = V \Gamma_{mn}$ and $\bar{E}_{mn} = \int_V \phi_m \phi_n \delta_{i_m k_n} \, dV$. This takes ρ completely out of the equation, which is more convenient if the sample may be measured under conditions under which the density may change, such as changing temperature and pressure.

b. Cauchy's inequality With some effort, the approximation $\lambda \approx \omega^2$ can be made more meaningful, given certain important assumptions. As an example, we consider the lowest value of ω^2 that makes the Lagrangian L stationary; call it ω_1^2, with a corresponding eigenfunction ψ_1. Let the trial function, or guess, for ψ_1 be ψ_g. Assuming that L is Hermitian, that is, its stationary values are all ≥ 0 and the corresponding eigenfunctions form a complete, orthogonal set, the ith component of ψ_1 can be written:

$$_i\psi_1 = {}_i\psi_g + \sum_{m=2}^{\infty} {}_ic_m \, {}_i\psi_m \,,$$

where the $_ic_m$ are small constants (assuming ψ_g is a good guess). Substituting into (27), integrating the numerator by parts (with respect to x_j), and normalizing the $_i\psi_m$ so that

$$\int_V \rho (_i\psi_m)(_i\psi_m) \, dV = 1 \,,$$

leads to

$$\lambda_g = -\int_V (_i\psi_g + {}_ic_m \, {}_i\psi_m) \, c_{ijkl} \frac{\partial^2 (_k\psi_g + {}_kc_n \, {}_k\psi_n)}{\partial x_l \partial x_j} \, dV,$$

where $\lambda_g \approx \omega_1^2$ is the approximate eigenvalue. Noting that

$$c_{ijkl} \frac{\partial^2 {}_k\psi_n}{\partial x_l \partial x_j} = -\rho \omega_n^2 \, {}_i\psi_n \quad \text{and} \quad \int_V \rho \psi_m \psi_n dV = \lambda_m \delta_{mn} \,,$$

after some algebra, one obtains

$$\lambda_g = \omega_1^2 + \sum_{m=2}^{\infty} \sum_{i=1}^{3} {}_ic_m^2 \left(\omega_m^2 - \omega_1^2\right) + O(c_m^4) \,; \tag{39}$$

since ω_1^2 is the lowest eigenvalue, $\omega_m^2 - \omega_1^2$ is always ≥ 0. This yields two important results: one, that the approximate eigenvalue is always higher than the exact value; and two, that if the error in the eigenfunction is of order one in smallness, the error in the eigenvalue is of order two. In other words, a so-so guess for the eigenfunction could still yield an accurate eigenvalue. The news is even better if frequency is the quantity of interest, since $f \propto \omega$ and the error will be half again as large. Similar results are obtainable for the higher eigenvalues [33].

c. Choice of basis The clear advantage to using the Rayleigh-Ritz method, as outlined here, is that one can obtain approximate values for the frequencies of free vibration of an elastic solid without having to solve the differential equation of motion, or use the boundary conditions explicitly. All one need do is approximate the displacement ψ as a sum of basis functions with unknown coefficients, and solve a matrix eigenvalue problem. The basis functions themselves need not satisfy the original differential equation; however, there are some important criteria for choosing an appropriate basis:

16

1. *Completeness.* The basis functions should form a complete set, so one can expect that any possible eigenfunction can be built up from them.

2. *Analytic E_{mn} and Γ_{mn}.* If high accuracy is desired, the matrices in (37) may have to be quite large; this in turn means that the one wants very much to be able to evaluate the integrals in (36) analytically. This usually means using a relatively simple basis set.

3. *Compatibility with boundary conditions.* If the displacement is clamped at the surface, the basis functions must be also. If the surface is free, the basis functions must not impose any important restrictions on the displacement at the boundary [37].

In the "old days" before high-speed digital computers, one of the most important criteria for selecting a basis was how much its members looked like known solutions, or looked like solutions to similar problems. This was necessary in order to keep the number of terms in the expansion to a minimum. Ekstein and Schiffman [34], in their landmark 1956 paper, used some longitudinal modes of a parallelepiped with zero Poisson's ratio, along with the Lamé modes, as the trial functions in a Ritz calculation of simple modes of an isotropic cube; about 10 basis functions were used for each mode. Nearly all the basis functions of this type were simple combinations of sines and cosines; this may have been what motivated Holland [36] in 1968 to use a basis of the form:

$$\phi_{pqr} = \sin\left(\frac{p\pi x}{2a}\right)\sin\left(\frac{q\pi y}{2b}\right)\sin\left(\frac{r\pi z}{2c}\right),$$

for a rectangular parallelepiped of dimensions $2a \times 2b \times 2c$, with the origin at the center of the object. Holland was not limited to 10 basis functions, and so did not attempt to tailor the basis set to each mode type. However, even with nearly 100 basis functions, Holland obtained 10% error in some modes whose exact solutions are known. To understand why, consider criterion 3 above, the compatibility with boundary conditions. Recall from the derivation of the radial vibrations of an elastic sphere that even in that case, it was not necessary that $\nabla\psi\cdot\hat{\mathbf{n}}$ be zero at the boundary; yet this condition is satisfied for trial functions of the type Holland used.

This fact was appreciated by Demarest [3], who in 1969 performed what could be the first accurate calculations of the resonance spectrum of a finite elastic object other than a sphere, by using normalized Legendre polynomials as a basis. Subsequently, Visscher *et al.* [103] have used an even simpler basis set, powers of cartesian coordinates, to find the resonance spectra of a wide variety of objects.

d. Boundary conditions As mentioned earlier, the boundary condition implied in a Rayleigh-Ritz calculation depends on what restrictions are placed on the variation $\delta\psi$ in the derivation; the range of admissible boundary conditions may be limited to those which gaurantee that the Lagrangian be a Hermitian operator [70].

The question arises: How does Rayleigh-Ritz know what the boundary condition is? As discussed above, this information is entirely encoded in the basis functions; it is therefore of great importance to ensure that the basis is compatible with the desired conditions. It is for this reason that it is said that a "lapse in Murphy's vigilance" [103] must have occurred in this area, because if no restrictions at all are put on the basis set, one obtains the "natural boundary conditions" [37], which correspond to a traction-free boundary, just the boundary condition of most interest to RUS researchers. In other words, one get the desired boundary condition "for free".

As an example, the interested reader may wish to carry out a simple Rayleigh-Ritz calculation for a vibrating string. If one uses as a basis $\psi(x) = a_0 + a_1 x + a_2 x^2 \ldots$, the eigenvalue problem yields the frequencies of a free–free string; if one uses instead $\psi(x) = a_1 x + a_2 x^2 + a_3 x^3 \ldots$, omitting the constant term, then the displacement is clamped at $x = 0$, and one obtains the frequencies of a fixed–free string.

This may not seem to have any immediate application to problems in elasticity, for a fixed boundary would require two elastic solids with impedances different by orders of magnitude. This is unusual, but one possible candidate is a piece of aerogel stuck to a metal support. The aerogel is a resisting solid, and yet is over 99% empty space, giving it a low acoustic impedance. M. H. W. Chan [35] has performed experiments on aerogel plugs confined in tubes, and has reported some effects that may be due to normal mode activity in the aerogel. The normal modes of the aerogel in this configuration could perhaps be analyzed successfully by using the Ritz method with a basis set clamped at $r = a$.

More general boundary conditions may be expressed by adding constraints to the stationary Lagrangian, in the manner of Lagrangian multipliers [38].

3. Examples of forward calculations

When a sample is a rectanglar parallelepiped, the most popular choice of basis has been that of Demarest, *i.e.*

$$\phi_{pqr} = \sum P_p(x/a)P_q(y/b)P_r(z/c). \qquad \text{(Demarest, 1969)}$$

$$(40)$$

The Legendre polynomials are normalized in the interval $-a$, a etc., so the matrix $\mathbf{E}$ in (37) becomes the identity matrix, simplifying the subsequent calculations. The details for calculating matrix $\mathbf{\Gamma}$ for this basis set are given in Ohno's seminal 1976 paper [43], as well as rules for using the symmetry of the basis functions along with the crystal symmetry and object symmetry to block-diagonalize this matrix. This latter procedure will be considered briefly here.

a. Block-diagonalizing Γ Although it is not necessary to tailor the basis set for each mode type, as it was before the days of high-speed computers, considerable advantages in computation time can be realized by recognizing that if the basis functions are either odd or even in x, y, or z, then if different displacement mode types of an object are also odd or even about the center, not all basis functions are needed to describe each mode type. Thus, by arranging the basis functions in the proper order, the matrix Γ is broken up into smaller blocks. As an example, consider a rectangular parallelepiped with orthorhombic symmetry and dimensions $2a \times 2b \times 2c$, centered on the origin and with its faces parallel to the crystal mirror planes; it has 21 non-zero elastic constants c_{ijkl}, nine of them independent. If we use u, v, w for ψ_1, ψ_2, ψ_3, then the potential energy term (from which Γ is derived) can be written:

$$\frac{1}{2}\int_V c_{ijkl} \frac{\partial \psi_i}{\partial x_j} \frac{\partial \psi_k}{\partial x_l}\, dV =$$

$$\frac{1}{2}\int_{-a}^{a}\int_{-b}^{b}\int_{-c}^{c} \left[c_{1111} \frac{\partial u}{\partial x}\frac{\partial u}{\partial x} + 2c_{1122}\frac{\partial u}{\partial x}\frac{\partial v}{\partial y} \right.$$

$$\left. + 2c_{1133}\frac{\partial u}{\partial x}\frac{\partial w}{\partial z}\ldots \right] dx\, dy\, dz\,.$$

Due to the symmetry of the integration limits, any odd terms in the brackets will not contribute. Suppose that $u(x,y,z)$ is of the form in (40); suppose further that it is even in x, y, and z, that is, it has the parity *eee*. Then after a differentiation by x it will have the parity *oee*, and the second term in brackets will be nonzero only if $\partial v/\partial y$ has the parity *oee* also; hence, v must have the parity *ooe*. Likewise, by examining the third term in the brackets, w must have the parity *oeo*. Depending on the elastic symmetry, it is possible that u_{eee} could couple to v and w with other parities as well; in the case of orthorhombic symmetry, it doesn't, and one can therefore group the basis functions into a block according to:

$$\begin{array}{c|cccc} & x & y & z & i \\ \hline u & e & e & e & 1 \\ v & o & o & e & 2 \\ w & o & e & o & 3 \end{array} \qquad . \tag{41}$$

When calculating the matrix Γ, one has a "global index" m to identify each basis function ϕ_m, which in turn specifies, in this case, a set of integers p, q, and r, which are the orders of the Legendre polynomials, and a fourth integer i, which identifies the component of displacement. According to the above table, then, one would group together (*i.e.* assign consecutive values of m to) all combinations of four integers that are even, even, even, 1, with those that are odd, odd, even, 2, and odd, even, odd, 3.

If one repeats this procedure for all possible parities of u, one finds that there are eight separate "parity groups",

TABLE V. Ohno's designations for the eight mode types of an oriented orthorhombic rectangular parallelepiped (or object with similar symmetries), according to the parity of displacement vectors (see Eq. 41).

o	e	e	1			e	e	e	1	
e	o	e	2	OD (dilatation)		e	o	o	e	2	EX (flexure)
e	e	o	3			o	e	o	3	
o	o	o	1			o	o	e	1	
e	e	o	2	OX (shear)		e	e	e	2	EY (flexure)
e	o	e	3			e	o	o	3	
e	e	o	1			o	e	o	1	
o	o	o	2	OY (shear)		e	o	o	2	EZ (flexure)
o	e	e	3			e	e	o	3	
e	o	e	1			e	o	o	1	
o	e	e	2	OZ (shear)		o	e	o	2	EV (torsion)
o	o	o	3			o	o	e	3	

each corresponding to a mode type and a matrix block. Table V gives the parity groups along with the designations given them by Ohno [43]. The descriptions in parentheses are only approximate and are more applicable, in general, to the lower modes.

b. The xyz method   The normalized Legendre polynomials are an ideal basis for the displacements of a rectangular parallelepiped; Γ_{mn} is only slightly awkward to compute, and E_{mn} is made the identity matrix. But for other shapes, obtaining Γ_{mn} and E_{mn} is considerably messier, or impossible analytically. Visscher [103] noted in 1991 that if simple powers of cartesian coordinates $x^p y^q z^r$ are used as a basis, then the Γ_{mn} and E_{mn} integrals both have exactly the same form, and are simple to compute for a wide variety of shapes. Furthermore, Γ is (not suprisingly) block-diagonalized into the very same parity groups as before. The author has found that the matrix conditioning is improved if this basis set is scaled according to

$$\phi_m = \left(\frac{x}{a}\right)^{p_m}\left(\frac{y}{b}\right)^{q_m}\left(\frac{z}{c}\right)^{r_m} = \hat{x}^{p_m}\hat{y}^{q_m}\hat{z}^{z_m}\,. \tag{42}$$

Since differentiating a function of this type, or multiplying two such functions together, does no more than change the exponents and/or multiply the function by a constant (thereby leaving the form the same), the Γ_{mn} and E_{mn} integrals are all of the form $\int_V \phi\, dV$. Using the scaled basis set on a rectangular parallelepiped centered on the origin leads to:

$$\int_V \phi\, dV = abc \int_{-1}^{1}\int_{-1}^{1}\int_{-1}^{1} \hat{x}^p \hat{y}^q \hat{z}^z\, d\hat{x}\, d\hat{y}\, d\hat{z} \tag{43}$$

$$= \begin{cases} 8\dfrac{abc}{(p+1)(q+1)(r+1)} & p,\ q,\ r\ \text{even}; \\[2mm] 0 & \text{otherwise.} \end{cases}$$

TABLE VI. The properties of an elastic rectangular parallelepiped conjured up for example calculations. Its properties are made to be similar to those of a quasicrystal studied in Section V.

$c_{11} = 1.1$ Mbar	$2l_x = 0.4221$ mm	
$c_{12} = 0.3$ Mbar	$2l_y = 0.4221$ mm	$\rho = 2.359$ g/cc
$c_{44} = 0.4$ Mbar	$2l_z = 0.5761$ mm	

Using the xyz basis, Visscher was able to calculate the normal mode frequencies of elastic parallelepipeds, spheres, eggs, potatoes, bells, cones, sandwiches, and more, essentially solving one of the great problems of applied physics with a simple variational principle. Computer programs to calculate natural frequencies of elastic objects using the xyz method are given in the Appendix and in [103]. The simplicity and generality of this method will be exploited in Section VI, when the effects on the frequencies of imperfect sample preparation is considered.

c. Effects of matrix size on calculations As discussed earlier, the frequencies found by the Rayleigh-Ritz method are always higher than the "true" values, asymptotically approaching them with increasing matrix size (assuming that the basis set meets the stated criteria). There are many conceivable ways one could control the matrix size; the most straightforward way is to specify a maximum basis function order, *e.g.* the functions in each block are chosen from the set of all $x^p y^q z^r$ for which $p+q+r \leq R$. The equation $p+q+r = R$ is a plane which bounds a corner prism, or one-sixth of the volume of a cube volume R^3. If p, q, and r start at zero (signifying a zeroth order polynomial, or a constant), then the overall matrix size is

$$3N = \frac{3(R+3)(R+2)(R+1)}{6} = \frac{(R+3)(R+2)(R+1)}{2}.$$

Choosing the maximum basis function order might proceed from an *a priori* judgement about the number of overtones that one might measure of the various mode types, and how many "wiggles" will be necessary to well approximate the mode shapes. The rigorous criterion is, how many basis functions are needed before the eigenvalues converge to an accuracy sufficiently close to the ideal values. This can best be discovered by carrying out calculations for various values of R.

d. Calculated frequencies vs. basis function order Presented in this section are frequencies of free oscillation for an isotropic rectangular parallelepiped, calculated using the Rayleigh-Ritz method discussed above. The properties of the object are given in Table VI; it is made to be similar to an actual quasicrystal sample that is considered in Sections V and VI. The frequencies of free vibration versus maximum basis function order are shown in Table VII; for clarity, the differences between the corresponding frequencies in neighboring columns are given in a separate table, Table VIII. In practice, the first 40 or so modes may be measured, and agreement between calculated and measured frequencies is expected to

TABLE VII. Calculated resonance frequencies of an elastically isotropic parallelepiped (in MHz) versus maximum basis function order R. Bold type indicates a mode that is out of order.

Mode	$R = 8$	$R = 9$	$R = 10$	$R = 12$
EV-1	1, 3.2695	1, 3.2695	1, 3.2687	1, 3.2686
EY-1	2, 4.2135	2, 4.2135	2, 4.2131	2, 4.2131
EX-1	3, 4.2135	3, 4.2135	3, 4.2131	3, 4.2131
EV-2	4, 4.8076	4, 4.8076	4, 4.8052	4, 4.8050
OY-1	5, 5.2368	5, 5.2344	5, 5.2344	5, 5.2344
OX-1	6, 5.2368	6, 5.2344	6, 5.2344	6, 5.2344
OD-1	7, 5.3891	7, 5.3891	7, 5.3891	7, 5.3891
OZ-1	8, 5.8848	8, 5.8772	8, 5.8772	8, 5.8762
OZ-2	9, 6.1501	9, 6.1457	9, 6.1457	9, 6.1454
EZ-1	10, 6.2704	10, 6.2704	10, 6.2700	10, 6.2699
OD-2	11, 6.3220	11, 6.3216	11, 6.3216	11, 6.3215
EX-2	12, 6.3822	12, 6.3822	12, 6.3814	12, 6.3813
EY-2	13, 6.3822	13, 6.3822	13, 6.3814	13, 6.3813
OZ-3	14, 6.4782	14, 6.4538	14, 6.4538	14, 6.4486
OD-3	15, 6.8982	15, 6.8982	15, 6.8982	15, 6.8982
OY-2	16, 6.9233	16, 6.9178	16, 6.9178	16, 6.9171
OX-2	17, 6.9233	17, 6.9178	17, 6.9178	17, 6.9171
EZ-2	18, 7.1209	18, 7.1209	18, 7.1201	18, 7.1199
OD-4	19, 7.2259	19, 7.2249	19, 7.2249	19, 7.2246
EV-3	20, 7.6688	20, 7.6688	20, 7.6625	20, 7.6621
OD-5	21, 7.7609	21, 7.7607	21, 7.7607	21, 7.7606
EZ-3	22, 7.8622	22, 7.8622	22, 7.8606	22, 7.8605
EX-3	23, 7.9061	23, 7.9061	23, 7.8959	23, 7.8946
EY-3	24, 7.9061	24, 7.9061	24, 7.8959	24, 7.8946
EY-4	25, 8.1708	25, 8.1708	25, 8.1625	25, 8.1622
EX-4	26, 8.1708	26, 8.1708	26, 8.1625	26, 8.1622
EZ-4	27, 8.3614	27, 8.3614	27, 8.3594	27, 8.3592
OY-3	28, 8.4149	28, 8.3888	28, 8.3888	28, 8.3816
OX-3	29, 8.4149	29, 8.3888	29, 8.3888	29, 8.3816
EZ-5	30, 8.4948	30, 8.4948	30, 8.4943	30, 8.4943
OY-4	31, 8.7990	31, 8.7755	31, 8.7755	31, 8.7705
	⋰			
EV-5	40, 10.0054	41, 10.0054	41, 9.9837	41, 9.9793
	⋰			
OD-10	**55**, 11.8228	50, 11.3376	**51**, 11.3376	50, 11.2791

TABLE VIII. Percentage change in calculated frequency f_R from Table VII, where R is the maximum basis function order.

Mode	$f_8 - f_9$ (%)	$f_9 - f_{10}$ (%)	$f_{10} - f_{12}$ (%)
EV-01	0.00	0.03	0.00
EY-01	0.00	0.01	0.00
EX-01	0.00	0.01	0.00
EV-02	0.00	0.05	0.00
OY-01	0.05	0.00	0.00
OX-01	0.05	0.00	0.00
OD-01	0.00	0.00	0.00
OZ-01	0.13	0.00	0.02
OZ-02	0.07	0.00	0.00
EZ-01	0.00	0.01	0.00
OD-02	0.01	0.00	0.00
EX-02	0.00	0.01	0.00
EY-02	0.00	0.01	0.00
OZ-03	0.38	0.00	0.08
OD-03	0.00	0.00	0.00
OY-02	0.08	0.00	0.01
OX-02	0.08	0.00	0.01
EZ-02	0.00	0.01	0.00
OD-04	0.01	0.00	0.00
EV-03	0.00	0.08	0.01
OD-05	0.00	0.00	0.00
EZ-03	0.00	0.02	0.00
EX-03	0.00	0.13	0.02
EY-03	0.00	0.13	0.02
EY-04	0.00	0.10	0.00
EX-04	0.00	0.10	0.00
EZ-04	0.00	0.02	0.00
OY-03	0.31	0.00	0.09
OX-03	0.31	0.00	0.09
EZ-05	0.00	0.01	0.00
OY-04	0.27	0.00	0.06
⋱			
EV-05	0.00	0.22	0.04
⋱			
OD-10	4.10	0.00	0.52

be around 0.1% rms. It is evident from these tables that basis functions on the order of 10 or perhaps even 12 are needed for such accuracy. This gives an overall matrix size of about 1400×1400. Such a calculation typically takes about 20 seconds on an IBM mainframe using ESSL subroutines; if the eight submatrices above are used, the maximum block size is about 200×200, and the solution of all 8 takes about 5 seconds.

e. Eigenfunctions Once the eigenvalue problem has been solved, the eigenvectors can be used to plot the displacements of the various modes. This can be informative as well as entertaining. Animations may also be produced, simply by adding a factor $\cos \omega t$ to the displacement. Everyone has their favorite environment for plotting functions; for those acquainted with *Mathematica*, the Appendix provides a routine (fumarp) for producing *Mathematica*–ready ASCII files for eigenfunction plots. Fig. 8 shows such plots of the mode shapes corresponding to the frequencies in Table VII. As one can see, many of the mode shapes, especially the higher ones, are nontrivial. This makes them hard to compute analytically, but also makes them depend on the elastic constants in a sufficiently complicated way that every elastic constant couples to at least a few modes. In the lowest modes can be seen the motivation behind the informal names given the mode types; in particular, modes EV-1, EY-1, OX-1, and OD-1 seem to be described adequately by the labels "torsion", "flexure", "shear", and "dilatation". It is also useful to note that modes such as OD-1 have relatively little motion at the corners, and so may be hard to detect by a corner-to-corner mounting. Of additional interest is mode OD-3, the lowest Lamé mode; notice its prismatic shape and sinusoidally curved sides (compare with figures in [16]).

f. How do we know it's right? The best test of the Rayleigh-Ritz forward calculation is to compare its results to exact calculations, where available. Two types are used here: the nondimensional frequencies $\omega a / v_s$ of an isotropic, homogeneous sphere (discussed further in Section IV), and the Lamé modes of a rectangular parallelepiped. Comparisons for the sphere are shown in Table IX; note that many of the frequencies of a sphere are multiply degenerate, and the Ritz method finds separate frequencies (eigenvalues) for all the modes, degenerate or not. Therefore the mode numbers in the Ritz column get bigger faster than those for the exact solution. The mode numbers in the Ritz column are important, however, because the higher numbered eigenvalues are expected to be less accurate, and it is useful to discover what the effective cutoff is. For the sphere, even modes in the hundreds seem to be plenty accurate.

A sharp-edged object like a rectangular parallelepiped might be expected to experience slower convergence than a rounded object like a sphere, so a comparison of some modes of an RP is included as well, in Table X. Here as well, it would seem from this small sampling that the eigenvalues are accurate to parts per million, for modes higher than those typically used in a RUS measurement.
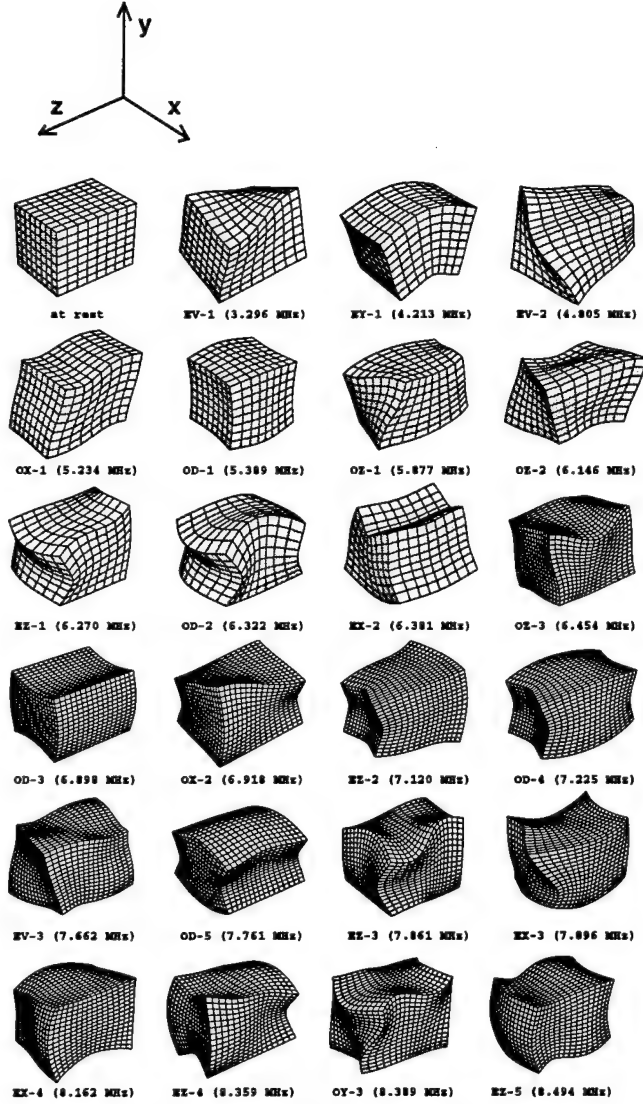
20

y

z   x

at rest	EV-1 (3.296 MHz)	EY-1 (4.213 MHz)

FIG. 8. An array of eigenmode plots.

(The figure contains an array of eigenmode plots with the following labels:)

at rest — EV-1 (3.296 MHz) — EY-1 (4.213 MHz) — EV-2 (4.805 MHz)

OX-1 (5.234 MHz) — OD-1 (5.389 MHz) — OZ-1 (5.877 MHz) — OZ-2 (6.146 MHz)

EZ-1 (6.270 MHz) — OD-2 (6.322 MHz) — EX-2 (6.381 MHz) — OZ-3 (6.454 MHz)

OD-3 (6.898 MHz) — OX-2 (6.918 MHz) — EZ-2 (7.120 MHz) — OD-4 (7.225 MHz)

EV-3 (7.662 MHz) — OD-5 (7.761 MHz) — EZ-3 (7.861 MHz) — EX-3 (7.896 MHz)

EX-4 (8.162 MHz) — EZ-4 (8.359 MHz) — OY-3 (8.389 MHz) — EZ-5 (8.494 MHz)

TABLE IX. Selected nondimensional resonance frequencies $\eta = \omega a / v_s$ of an elastically isotropic, homogeneous sphere. The η_0 are the zeroes of the analytic solution (Eq. (54)), and the η_{xyz} are calculated using the Rayleigh-Ritz method, with $(x/a)^p (y/b)^q (z/c)^r$ as the basis set. The maximum order of the basis functions is $p + q + r \leq 12$.

	Analytic sol'n		Rayleigh-Ritz		
	Mode	η_0	mode #	η_{xyz}	$\Delta\eta$ (%)
1	$T_{2,0}$	2.5011326	1	2.5011326	0.000
2	$S_{2,0}$	2.6398693	6	2.6398693	0.000
4	$T_{3,0}$	3.8646998	14	3.8646998	0.000
6	$S_{0,1}$	4.4399982	28	4.4399982	0.000
9	$T_{4,0}$	5.0946156	50	5.0946156	0.000
13	$S_{3,1}$	6.4543693	77	6.4543693	0.000
16	$T_{2,1}$	7.1360088	100	7.1360096	0.000
26	$T_{8,0}$	9.6209991	200	9.6233328	0.024
32	$S_{0,2}$	10.4939244	260	10.4939248	0.000
37	$S_{4,2}$	11.0390581	300	11.0931275	0.489

TABLE X. Two of the Lamé modes of an elastic parallelepiped, for which there is an exact solution, calculated by the exact formula and numerically with Rayleigh-Ritz. The basis functions used in the Rayleigh-Ritz calculation are products of Legendre polynomials $P_i(x/l_x)P_j(y/l_y)P_k(z/l_z)$, where the maximum order $i + j + k$ of the basis functions is 12.

Lamé modes $f_m = (m/4a)\sqrt{2\mu/\rho}$					
	Analytic sol'n		Rayleigh-Ritz		
m	f (MHz)		mode	f (MHz)	Δf (%)
1	6.8981983	15	OD-3	6.8981983	0.000
2	13.7963966	83	OZ-11	13.7964015	0.000

21

One may see from Table VIII, however, that the convergence of the Lamé modes is among the fastest, so other modes may not be quite as accurate. It is the combination of the results in Tables IX and X, plus the convergence apparent in Tables VII and VIII (plus, of course, the excellent agreement with experimentally measured values, *e.g.* the results for cubic silicon in Section IV) which convinces the author that accurate results are being obtained.

The frequencies from the analytic solution for the sphere were found using *Mathematica* on a Pentium 120 PC, with a program given in Section IV. The Rayleigh-Ritz calculations for the sphere were accomplished with a version of Bill Visscher's *xyz* algorithm [103], while those for the rectangular parallelepiped were done by a program called rprmrq, which is given in the Appendix and discussed in the next section. All Rayleigh-Ritz calculations were carried out on an IBM 3270 mainframe computer, using ESSL subroutines DSYGV or DSPEV in double precision. Since the floating-point arithmetic on these mainframes is known to be less accurate than on other comparable machines, some calculations were carried out in quadruple precision for comparison. No differences were observed in the first 6 decimal places, so it is concluded that the floating-point accuracy of the IBM is not a factor.

D. The inverse problem

While solving the direct problem takes a fair amount of computing power and occasionally some ingenuity, it is still straightforward; that is, given an object's shape, density, and elastic tensor, a unique set of eigenvalues (frequencies) is determined. The reverse is not necessarily true; for instance, if the density of an object is doubled and its elastic constants are doubled, the frequencies stay the same ($f \propto \sqrt{c_{ij}/\rho}$). Likewise, if the dimensions of a rectangular parallelepiped are all doubled and the elastic constants are quadrupled, the frequencies stay the same ($f \propto \sqrt{c_{ij}}/l$). One might suppose, however, that given the shape and the density, one could determine the elastic constants, or given the density and elastic constants, one could determine the shape. If one measures many more frequencies than elastic constants, then the problem is overdetermined and one might suppose that one could find the elastic constants and the relative geometry (*e.g.* aspect ratios), as well as other parameters (such as orientation angles).

This inverse proposition is not rigorously true, even for a simple system such as an elastic membrane [105], [106]. On the other hand, as will be seen in Section IV, global searches of parameter space show that the spectrum of an isotropic sphere uniquely determines its Poisson's ratio, which can be used with the radius and dimensions to find the elastic constants; if the radius and density were unavailable, one could still know the ratio of the elastic

constants. This leads to the following conjecture:

Conjecture 1 *For homogeneous objects with sufficiently simple geometries and elastic tensors, the elastic tensor can be uniquely determined from the mechanical resonance spectrum.*

Even if this conjecture is true, there is no computational mechanism for directly converting frequencies into elastic constants (except in a few special cases). One must instead use some nominal values for the elastic constants in a forward calculation to produce a theorectical spectrum, which one then compares with the measured spectrum. This process is then iterated, adjusting the elastic constants until the computed spectrum matches the observed one. If the number of constants or other parameters to be determined is small, one can do a global search through parameter space to find the best fit. If the number of parameters is large, this may not be practical; it may also be unnecessary, if information is available that can put reasonable bounds on the parameters (for instance, pulse measurements on a polycrystalline sample of some material may yield a reasonable guess for the single-crystal bulk modulus). Thus if some or all the "nominal values" that one starts with are good initial guesses, then the problem becomes one of local rather than global optimization. Good initial guesses might come from pulse-echo or Brillioun scattering measurements, from measurements on similar materials, or in rare cases, from calculations.

Thus it is apparent that RUS will not put practitioners of pulse-echo ultrasound or other methods out of business; rather, complimentary measurements are extremely helpful in successfully fitting RUS data. Nevertheless, there are situations where RUS is the only method available that can obtain the necessary precision in the final measurement; the experiments detailed in Sections IV and V are examples.

1. Local least-squares minimization

If one is in a local minimum, then any method that searches for the minimum should obtain the same or nearly the same result, so precise methodology is less crucial than efficiency. One of the most efficient methods for finding local minima is the *Levenberg-Marquart* method [39]; a brief hand-waving description of this method is as follows. Suppose one has a set of observed frequencies $f_{o,n}$ and a set of calculated frequencies $f_{c,n}(\mathbf{c})$, where $\mathbf{c}$ is a vector of parameters one is trying to estimate. One seeks the optimum set of parameters $\mathbf{c}_{opt}$ that makes

$$\sum_i \left(f_{o,i} - f_{c,i} \right)^2 = \sum_i \left(\Delta f_i \right)^2$$

a minumum. If one is very close to the minimum, then the surface of $\sum_i \left(\Delta f_i \right)^2$ is approximately quadratic, and the frequencies are approximately linear functions of $\mathbf{c}$.

If it is assumed that the model is a pretty good one, then $f_{c,i}(\mathbf{c}_{opt})$ ought to be very close to $f_{o,n}$. Hence $f_{o,i} \approx f_{c,i} + \Delta c_j \frac{\partial f_i}{\partial c_j}$, or

$$\Delta f_i \approx \Delta c_j \frac{\partial f_i}{\partial c_j} .$$

Multiplying both sides by $\partial f_i / \partial c_k$,

$$(\Delta f_i)\frac{\partial f_i}{\partial c_k} \approx \Delta c_j \frac{\partial f_i}{\partial c_j}\frac{\partial f_i}{\partial c_k} .$$

The quantity $\left[\frac{\partial f_i}{\partial c_j}\frac{\partial f_i}{\partial c_k}\right]$ is a square $n \times n$ matrix, where n is the number of parameters, so we may write

$$\Delta c_j \approx \left[\frac{\partial f_i}{\partial c_j}\frac{\partial f_i}{\partial c_k}\right]^{-1}(\Delta f_i)\frac{\partial f_i}{\partial c_k} = [\alpha]^{-1}(\Delta f_i)\frac{\partial f_i}{\partial c_k} . \quad (44)$$

This is the same result as that obtained by expanding $\sum_i (\Delta f_i)^2$ in a Taylor series, differentiating with respect to $\mathbf{c}$, and discarding higher order derivatives. Good discussions of these higher order terms, and why they are customarily discarded, are given in [39] and [45]. Perhaps the most important reason, to quote [39], is that

> [M]inor (or major) fiddling with $[\alpha]$ has no effect at all on what final set of parameters is reached, but affects only the iterative route that is taken in getting there.

Equation (44) works fine near the minimum, but what about far from the minimum? If we assume that we are still in the correct "well", just far from the bottom, then the best strategy is to take a step downhill. Noting that $\nabla\left(\sum_i (\Delta f_i)^2\right) = -2(\Delta f_i)\frac{\partial f_i}{\partial c_j}$, this is equivalent to saying

$$\Delta c_j \sim K(\Delta f_i)\frac{\partial f_i}{\partial c_j} , \quad (45)$$

where K is a positive constant with units $(\mathbf{c}/f)^2$, large enough to make a difference but not so large that it causes Δc_j to overshoot the minimum.

The insight of Marquart was to combine (44) and (45) into one method, that smoothly varies between one case and the other. The definition of $[\alpha]$ guarantees that its diagonal elements will be positive; therefore, let

$$\alpha'_{jk} = \alpha_{jk} + \Lambda \alpha_{jj} , \quad (46)$$

and solve

$$\Delta c_j \approx [\alpha']^{-1}(\Delta f_i)\frac{\partial f_i}{\partial c_k} . \quad (47)$$

If Λ is small, then $\alpha'_{jk} \approx \alpha_{jk}$, and one has (44). If Λ is large, then $[\alpha']$ is nearly diagonal, so its inverse will be close to $[\mathrm{diag}(1/\alpha'_{jj})]$ (no summation). Each term

$(1/\alpha'_{jj})$ then plays the role of K in (45): a positive constant that can be made arbitrarily small by increasing Λ. In this way, one can use the linear approximation to start, and if that doesn't improve the fit, increase Λ to cut down the step size until the fit does improve. Then one can gradually move back to the linear approximation, *etc.* Reference [39], the well-known *Numerical Recipes*, contains a program called `mrqfit` that implements the Marquart method, and detailed instructions on its use. The author has used this program as the core of a RUS data-fitting routine called `rprmrq`, to be discussed shortly.

Since an analytic expression for the frequencies is not available, the $\frac{\partial f_i}{\partial c_j}$ must be obtained from one or more forward calculations. The author simply uses a finite-difference routine; Migliori *et al.* [45] give an expression for calculating the derivatives in terms of the eigenvectors and eigenvalues of one forward calculation. The latter may offer a computational advantage.

a. Inverting $[\alpha']$ using SVD The authors of *Numerical Recipes* advise that one use Singular Value Decomposition (SVD) as the means to invert $[\alpha']$ in (47). In SVD, a matrix $\mathbf{A}$ is decomposed into three matrices according to

$$\mathbf{A} = \mathbf{U}[\mathrm{diag}(s_j)]\mathbf{V}^{\mathrm{T}} ,$$

where the s_j are the so-called "singular values". IF $\mathbf{A}$ is square, its inverse is

$$\mathbf{A}^{-1} = \mathbf{V}[\mathrm{diag}(1/s_j)]\mathbf{U}^{\mathrm{T}} ;$$

if $\mathbf{A}$ is nearly singular, one or more of the s_j will be small compared to the others. If some of the $\partial f_i/\partial c_j$ are small, they may dominate $[\alpha']^{-1}$ and make it difficult to find accurate values for the remaining c's. In other words, the data are insensitive to these parameters, so they can't be determined accurately. If one uses SVD to do the inversion, the insensitive parameters will show up as small singular values, so one can counter their ill effects by setting the offending $(1/s_j)$ to zero. This will allow the remaining parameters to be optimally adjusted, although the "zeroed" parameters will not be adjusted at all.

Monitoring the singular values during the evolution of a fit can be useful in itself. In practice, it is found that a bad "condition number" $(s_{min}/s_{max} \ll 1)$ often occurs when the initial guesses are poor. The Levenberg-Marquart method is also used in the next section to find the center frequency, *etc.* of resonance peaks containing phase shifts, and the singular values are especially helpful here in flagging bad guesses.

2. Accuracy of determined parameters

Because frequency can be measured with such great accuracy in the laboratory, one might expect that the error

23

in a RUS measurement would be limited to the (hopefully random) errors in each resonance peak caused by transducer contact, slight temperature variations during measurement, sample preparation errors, and the like. However, since the frequencies alone cannot uniquely determine the elastic constants, the overall accuracy depends on how well the other physical parameters, namely density and geometry, are known. Density can be measured with fair accuracy in many cases, but of course this may change with temperature or pressure. If a sample is homogeneous, a better strategy is to measure the mass and use the matrices $\bar{\Gamma}$ and $\bar{E}$ from Eq. (38). Precision balances exist that can measure mass of small samples to within tiny fractions of a milligram, such as the Sartorius Supermicro balance used in Section III.

a. Overall accuracy The real limiting factor in overall accuracy is usually knowledge of the sample geometry. If a sample is a rectangular parallelepiped, then knowing the geometry amounts to knowing the edge lengths. Using a micrometer or microscope can normally get edge lengths only within a few microns at best; for a sample less than a millimeter on a side, this could be as much as a percent error in each side. This can cause not only an overall bias in the elastic constants, but relative errors between them.

One possible solution is to let the edge lengths themselves be free parameters in the fit. One cannot let all three vary independently, of course (as mentioned earlier), so one may vary the two shorter lengths (presumably measured less accurately) while keeping the longest constant. Thus the two aspect ratios may be determined to better accuracy than the original length measurement. If the density is also known, one can use it with the mass to determine the correct volume. By properly scaling the edge lengths after each iteration, the volume may be kept constant, making the overall accuracy independent of the length measurements. This strategy is used in the cubic silicon measurement in Section III.

Sample preparation errors such as nonparallel sides may contribute to both the absolute and relative error in the measurement; such effects are considered in detail in Section VI.

b. Relative accuracy The quantification of the relative accuracy, or random error, in a nonlinear least-squares fit of this type is not always completely straightforward. A couple of different approaches will be mentioned.

First, the quantity that is minimized to find the optimum parameters is not literally the least squares, but actually a "figure of merit" F, defined as

$$F = \sum_i \left(\frac{f_{o,i} - f_{c,i}}{f_{o,i}} \right)^2 , \qquad (48)$$

so that each individual error represents a fractional deviation. Since the frequencies may span a large range (say, 3–5 MHz), this prevents the higher frequencies from dominating the fit. In a classic least squares problem, one minimizes χ^2, which in this case would be

$$\chi^2 = \sum_i \left(\frac{f_{o,i} - f_{c,i}}{\sigma_i} \right)^2 ,$$

where σ_i is the uncertainty in measuring $f_{o,i}$. Hence, in (48), the $f_{o,i}$ play the role of the σ_i above.

If, instead of our $[\alpha]$, matrix $[\gamma]$ is defined as $\gamma_{jk} = \frac{1}{\sigma_i^2} \left[\frac{\partial f_i}{\partial c_j} \frac{\partial f_i}{\partial c_k} \right]$, then $[\gamma]^{-1} = G$, the covariance matrix of the fit, and the uncertainty in parameter c_1, say, is given by [40]

$$\delta c_1 = \pm \sqrt{\Delta \chi^2} \sqrt{G_{11}} ,$$

assuming the errors are normally distributed (which they may not be). Here $\Delta \chi^2$ is the amount by which χ^2 exceeds its minimum value, for a perturbation in parameter c_1. For a 68.3% confidence level (standard deviation), $\Delta \chi^2 = 1$.

The difficulties with using this method for finding errors in a RUS measurement are (1) we don't know if the errors really are normally distributed, and (2) we don't know how to assign a meaningful value to the σ_i in the definition of χ^2.

Migliori *et al.* [45], [46] have arrived at an empirical method in which the "error surface" curvature, given by the covariance matrix mentioned above, is explored in several directions to find the largest changes that can be made in the free parameters without the resulting overall fit error F increasing by more than 2%, which they have found consistently to be the repeatability of F for a given sample, based on many scores of RUS measurements.

c. Errors by Monte Carlo simulation Not having the extensive experience of Migliori *et al.*, we resort to another approach, which is generate a large number of synthetic data sets by small random perturbations of the measured frequencies; the scatter in the parameters obtained by fitting each set is used to get the errors. The size of the perturbations that should be used may not be obvious; one formula is to use each individual residual error to define the width of a distribution for the perturbation in each frequency. This issue is discussed in more detail in Section III, in the context of an actual measurement.

3. Some considerations

The subtleties in the inverse calculation are many; what follows is a discussion, by no means exhaustive, of the experiences of the author and others.

a. Ambiguity in elastic constant determination The relative uncertainties in the fitted parameters represent the "sharpness" of the minimum in F in different directions, which can vary quite a bit. In a measurement on cubic silicon in the next section, the uncertainty in c_{12} is over 5 times greater than the uncertainty in c_{44}.

24

This ratio is nearly identical to that found in the literature from pulse measurements. Hence one concludes that frequencies of vibration (or sound speeds) are relatively insensitive to c_{12} (and indeed all off-diagonal constants in general). This has led some researchers to fit for a set of bulk moduli and shear moduli instead of the standard elastic tensor, since the former presumably have more connection with distinct physical processes than the elements of the latter. Ohno [43] reports that the overall ambiguity in the measurement is reduced as a result.

b. How many data are enough? The sharpness of the minimum is obviously related to the size of the $\frac{\partial f_i}{\partial c_j}$; for each free parameter, one wants at least one mode that depends strongly on it, to reduce its ambiguity. The broadening of the minimum in F as a result of missing a mode with a large $\frac{\partial f_i}{\partial c_j}$ is illustrated graphically in Section IV (Fig. 35). Thus it is not enough to measure more modes than free parameters; one must make sure (by looking at a matrix of the $\frac{\partial f_i}{\partial c_j}$ if necessary) that one has at least one strong derivative for each parameter, and that the strong derivative terms are reasonably independent of one another. In general, this translates to about three or four times as many frequencies as number of free parameters, preferably more.

c. Mode identification The preceding discussions all assume that each frequency measured is identified with the correct normal mode. In fact, mode identification is often the most difficult part of a RUS measurement. One cannot simply assign the frequencies measured to those calculated in order. Some of the calculated frequencies may be out of order, especially if one's initial guesses aren't terribly good. Worse, some modes (especially those with little motion at the corners) may have gone undetected, hence are missing from the list of observed frequencies.

No simple prescription exists for guaranteeing correct mode identification. There are, however, several things one can do to improve the odds:

- *Examine actual displacement of sample.* Since the eigenfunctions are known, the displacement of any part of the sample can help identify it. Stekel *et al.* [41] devised a method whereby the receive transducer in a RUS pair is mounted on an XY stage, so that the orientation of the sample's corner with respect to the transducer can be changed systematically. By making a "grid" of measurements for each mode, they were able to identify orientations which would produce a null reading, signifying (for these transducers) that the motion of the sample was parallel to the transducer surface. By comparing the observed direction with that calculated for different modes, the modes could be identified. This method has been used with success; the main drawbacks are that it greatly increases the amount of data needed, and requires that the sample be

moved either manually or automatically between each measurement in the "grid", resulting in either increased labor or mechanical complexity.

The author has proposed that a similar method could be implemented, where one or both transducers are shear transducers with variable polarization. In this case, the sample remains still while the transducer polarization vector is rotated electronically; there should be maxima (minima) in the detector output corresponding to where the (2D projection of the) sample's displacement vector is parallel (perpendicular) to the transducer polarization. Unfortunately, this idea has yet to be tested in practice.

- *Remount and remeasure sample several times.* This does not by itself identify modes, but it can help insure that all of them have been measured. If necessary, the sample can be mounted by the edges or even by faces to find missing modes. The frequencies will most likely not be as accurate, but it may help identify which mode is which. For instance, one might expect that mode EZ-2 (from Fig. 8) would give a stronger response when mounted by the two small faces ($\parallel$ to xy plane) than would mode OD-3.

- *Remeasure after polishing a little off a side.* Some mode frequencies will go up, others down. By examining the $\frac{\partial f_n}{\partial L_i}$, they may be identified. This trick was used by Ohno *et al.* [43].

- *Examine the phase of the resonance curve with respect to the background.* This technique has been used extensively by Migliori *et al.*; its proper description requires jumping ahead to the details of experimental measurement of the resonance spectrum, which are contained in Section III. When a small sample is measured in the manner shown in Fig. 2, the signal from the receive transducer contains considerable electrical crosstalk from the nearby drive transducer. The phase of this crosstalk changes with frequency much more slowly than does the phase of a resonance peak with a decent Q, which shifts by 180° near the peak's center frequency. If the amplitude of the crosstalk is similar to or greater than the amplitude of the resonance peaks, the peaks will interfere constructively and destructively with the background, producing a "phase-shifted" Lorentzian lineshape (see Fig. 28). The particular lineshape will depend on the phase of the background, but more importantly, on the relative phase of the motion of opposing corners (by which the sample is mounted). One can guess roughly at the relative phase of the corners by looking diagrams of the eigenmodes, such as those in Fig. 8. For instance, one would guess

25

that the modes EZ-2 and OD-4 would have opposite phases, since in mode EZ-2 the opposing corners are moving in more or less the same direction, while in mode OD-4 they are moving in opposite directions. This may be confirmed by looking at the actual data obtained on a sample of cubic silicon (which has dimensions similar to those of the sample in Fig. 8); modes OD-4 (5.54 MHz) and EZ-2 (5.65 MHz) do indeed have opposite phases (see Fig. 27 and Table XII).

- *Identify frequencies that are likely to cross.* If all the modes have been measured, the greatest ambiguity may come from modes that are likely to cross due to small (or large, depending) perturbations of the free parameters; one may examine the $\frac{\partial f_i}{\partial c_j}$ to find them. Maynard [47] has suggested that these pairs may be identified by looking for the smallest values of the quantity:

$$\Delta f = f_n - f_m - \left[\Delta^2 \sum_j \left(\frac{\partial f_n}{\partial c_j} - \frac{\partial f_m}{\partial c_j} \right)^2 \right]^{1/2} ,$$

where $\Delta^2 = \sum_j (\Delta c_j)^2$ is a limited change in the free parameters, and $f_n > f_m$. When the pairs have been identified, the fit should be tried several times, switching the mode assignments in each pair.

- *Trial and Error.* If all or almost all the modes have been measured, then often a bit of trial and error, using different trial constants and switching the mode assignments of frequencies that are closely spaced, will identify whether a given mode assignment leads to a robust minimum, or is just one of many shallow local minima.

- *Look at more than one sample.* Finally, the obvious suggestion—compare results of two different samples of the same material, when available.

Fortunately for this paper, the PVDF transducers seem exceptionally good at finding all or nearly all the modes. In addition, the "initial guesses", where needed, are quite good in the present work, so most of the above tricks are not necessary.

d. RUS for misoriented samples The reader may have anticipated one of the greatest advantages of RUS, from the section on elastic symmetry. If the stress-strain relations are considered from the point of view of a coordinate system rotated with respect to the crystal lattice axes, the result is a transformed elastic tensor. If a rectangular parallelepiped is polished so that its faces are out of alignment with the lattice, plane waves may not propagate along the axes of the parallelepiped, but there is nothing to inhibit the existence of well-defined normal modes. Therefore, misorientation in a sample can perhaps be corrected by letting the orientation angles be

free parameters. Perhaps even more useful is simply the ability to take and analyze data on a sample, no matter what the orientation. This is used in Section V, on samples of quasicrystalline and cubic AlCuLi. The author cut and polished them before he learned about transmission Laue diffraction, and was unable, because of poor surface properties, to orient them with reflection Laue diffraction. Therefore the samples have essentially random crystal orientation with respect to the parallelepiped axes (subsequently determined with transmission Laue).

Note that if the crystal lattice is randomly oriented with respect to the sample's geometric axes, the block-diagonalization tricks from section a won't work, and one has to perform the inversion on a much bigger matrix. However, if the elasticity and density are homogeneous, and the sample is, say, a rectangular parallelepiped, then all the displacements of the sample must either be symmetric or antisymmetric about the center, so the basis functions can be grouped into two blocks, depending on whether they are symmetric or antisymmetric with respect to inversion.

e. `rprmrq` Most of the fitting of data in this paper was done with a FORTRAN 77 program named `rprmrq` (for **r**ectangular **p**arallelepiped **r**esonance using the **marq**uardt method), or its offshoots. It calculates the derivatives $\frac{\partial f_i}{\partial c_j}$ by a finite difference method, and uses a modified version of the *Numerical Recipes* routine `mrqfit` to accomplish the fitting. In addition, the matrix inversions in the inverse calculation are done with SVD, making use of *Numerical Recipes* routine `svdcmp`. The forward eigensystem solution is done with the ESSL [104] subroutine DSPEV. Any eigensystem routine could be substituted in its place, to make the program portable to other platforms than the IBM 3270 mainframe, for which it was written.

This program is given in the Appendix, along with other programs and routines used in this paper.

III. EXPERIMENTAL METHOD

A. Overview

Although a room-temperature RUS measurement is, at bottom, a fairly simple experiment, there are naturally many tricks and techniques for maximizing success. In particular, this work will, of course, emphasize those techniques associated with making measurements using PVDF film transducers on particularly small, fragile samples. This section will include detailed discussions of:

- Sample preparation and characterization

- Transducer design and fabrication

- Sample cell design

- Data acquisition

• Data analysis

The section on data analysis will examine some of the numerical issues raised in the previous section, especially the determination of standard errors for elastic constants measured using RUS.

1. Calibration using single-crystal silicon

In order to better illustrate the methods discussed here, they will be presented in the context of applying them to a specific measurement, that of determining the room-temperature single-crystal elastic constants of cubic (undoped) silicon. In addition to furnishing as an example, this measurement will serve to "calibrate" the technique, in a manner of speaking.

Chronologically, the determination of the room-temperature elastic constants of cubic silicon was the last experiment performed in the present work—but logically, it should be presented prior to the other experiments, to establish the basic efficacy of the experimental method before the reader is asked to accept results on new, novel materials. One may inquire as to whether such a "calibration" is necessary; indeed, this is certainly not the first attempt to confirm or quantify the accuracy of RUS, as many investigations, particularly early ones [43], [42], [44] have compared pulse data and RUS data on common substances. In addition, the results of Lin [56], as will be examined subsequently, seem to indicate that the transduction mechanism, at least, should not affect the frequencies that one measures by more than 0.03%. Still, there are good reasons to perform the present "calibration":

• We wish to establish the effectiveness of the specific techniques used in this paper.

• Since the sample sizes are considerably smaller in the present work than in previous RUS investigations, we want to check for size-dependent effects.

• We wish to test RUS on an especially well-characterized material, whose properties are consistent from one sample to another, to set an appropriate "benchmark" for future work. Many materials which we suppose to be well charaterized and consistent are in fact neither, or are not as good as silicon in these respects[2]

• The results of our measurements can be compared with those of other contemporary researchers, to

_____

[2]For instance, it was thought that α-quartz would be a good candidate for a benchmark measurement; however, one finds that the values in the literature vary as much as 50% in the off-diagonal constants such as c_{12} (see [47]).

establish a "state of the art" elastic-constant measurement standard. The accuracy of some early RUS work may have suffered from, for example, the high drive levels used to compensate for the unavailability of modern signal-detection electronics [45]. With modern electronics, transducers, computers, and meticulous crystal growth and sample preparation, we may demonstrate that RUS is capable of greater overall accuracy than the venerable pulse time-of-flight methods.

The analysis and final results on the cubic Si data will be presented at the conclusion of this section.

a. Handling of small samples Throughout subsequent sections, many manipulations of specimens are detailed, and it may be necessary to perform these on very small samples of a few hundred microns. It is very easy to lose or damage them, so some basic care should be taken in their handling. One of the main problems is that they can easily build up a static charge and "jump" from point to point. This and other difficulties are dealt with as follows:

1. A small tray with raised edges (about 1.5 inches) is lined with kimwipes, and a glass plate with a smooth, unscratched surface is placed in the bottom. Whenever possible, the sample is placed in this tray for examination or cleaning, or when gluing it to a sample holder.

2. The sample is only touched by (a) fine tweezers with thin teflon tubing fitted over the ends, (b) small artist's paintbrushes, and (c) hypodermic needles attached to small vacuum pumps.

3. The needle and pump are used mainly for placing the sample on holders (or in the measurement cell, as will be detailed in Section III E 1), on micrometers, or other locations that require a certain orientation. The brushes are used for cleaning, and for gently teasing the sample about on the glass to put it in a needed position. This is not difficult but takes practice, which is best done on a sample that is expendable. For instance, if the sample is sitting on one side and one wishes to rotate it 90° so it is sitting on an adjacent side, very carefully tugging on the sample with a single brush hair is enough to gently lift it up so it can resettle. If the sample has a static charge, it may stick and then suddenly jump, so the samples are frequently cleaned with methanol to neutralize charge (as well as to remove dust and films).

4. Many of the manipulations are easier to accomplish if done under a stereoscope such as a Nikon SMZ-10, equipped with a fiberoptic ringlight. The Nikon is adjustable from about 1× to 60× magnification.

B. Sample preparation and characterization

If a mathematical model used in a RUS inverse calculation assumes a rectangular parallelepiped single crystal (usually with one or more crystal axes aligned with the parallelepiped axes), it is imperative that the samples used in data acquisition be as close to this ideal as possible. There are a number of ways of preparing such samples; the methods detailed here have been demonstrated to work well for small specimens of fragile materials.

In order to prepare a sample, one must first obtain a specimen from which to prepare it; if one has a choice, one should choose a specimen that has no obvious cracks or grain boundaries. Sometimes chemically staining the surface of a specimen will reveal such boundaries. One should also strive to get the largest single-grain specimens available, as long as crystal quality is not compromised. Although samples as small as 70 μg have been successfully investigated, for best results the finished sample should probably be closer to 0.25–0.5 mg.

Depending on the size of the initial specimen, it may be cut with a diamond saw into a parallelepiped, or some approximation thereof, before final polishing. The parallelepiped axes should be aligned with the crystal axes if possible, and any crystal morphology such as facets, grain boundaries, or cleavage planes may be useful in guiding the initial cutting. Often, however, one has an irregularly shaped piece of some material with unknown lattice orientation, so X-rays or some other scattering probe must be used to determine the crystal axes.

1. Laue diffraction

For purposes of illustration, we will consider an irregular piece of crystalline Si obtained from Prof. Moises Levy of the University of Wisconsin at Milwaukee. The specimen has no obvious crystal morphology, so we first use Laue transmission photography (a form of X-ray scattering) to determine the lattice orientation and at the same time evaluate the quality of the crystal, making sure it is a single grain with a minimum of defects.

Fig. 9 shows a schematic of the specimen mounted on a goniometer, with an X-ray beam passing through it; below it, a reproduction of an actual Laue photograph of the specimen. When the orientation is complete, one hopes that such a photograph will show features that indicate a high-quality single crystal aligned with the atomic lattice: single, sharp spots, clearly showing the correct (in this case, 4-fold rotational) symmetry of the cubic crystal. Multiple spots might indicate multiple grains; diffuse or smeared spots could indicate defects. An excellent guide to the interpretation of Laue photographs is given in *The Laue Method*, by J. L. Amoros, M. J. Buerger, and M. C. Amoros [49]. Other scattering probes may be used for the purposes of orientation (such as Laue reflection), but Laue transmission is one of the
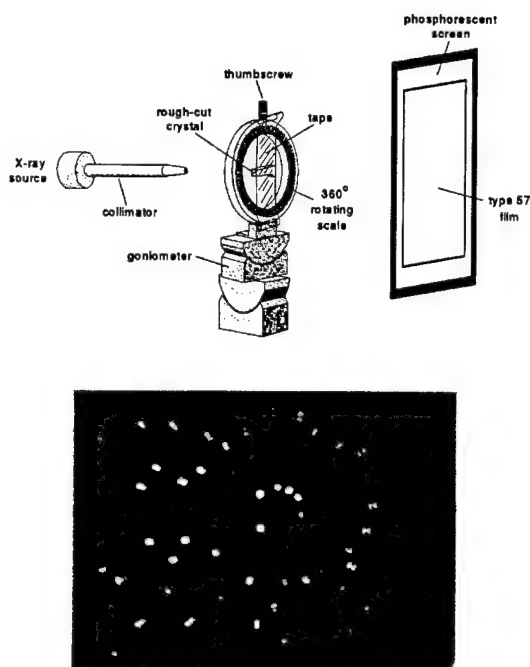

FIG. 9. A setup for making a Laue transmission photograph. The goniometer shown is mounted on a base that rotates freely (not shown). Note that the goniometer consists of two orthogonal sections, that can rotate up to about 20–25 degrees in either the clockwise or counterclockwise directions; the top section has been modified with the addition of a freely rotating scale, to allow orientation at any angle. An actual transmission photograph of the "raw" silicon sample is also shown.

few scattering methods that probes the *inside* of a specimen, and not just the surface. Thus it is one of the methods of choice for determining sample quality. Also, there are many materials such as ductile metals that often have poor surface properties, even after careful polishing and etching. There are, of course, materials such as heavy metals (lead, bismuth, *etc.*) which are very opaque to X-rays, so Laue transmission cannot be used these cases.

a. Orienting "from scratch" The specimen in Fig. 9 must now be oriented, so that it may be cut and polished. Laue transmission is very sensitive to small changes in orientation, and unless the crystal is very close to being aligned with the X-ray beam, the spot pattern may be largely unintelligible. There are a number of solutions. One may attempt to analyze the spot patterns and calculate what the correct orientation should be (such methods are detailed in [49]). Commercial systems are available for this purpose that will digitize spot patterns and analyze them automatically (although such systems are rather pricey). One may also align a crystal by a process of trial and error, which may in fact be the most convenient option once one gains some experience.

First, it is required that the specimen be mounted in a goniometer that allows free rotation in 2 planes. Most only allow free rotation of one plane (the base may rotate freely) but the other two angles may only vary by $\pm 20°$ or so. If the orientation of the crystal is completely unknown, these limits are inconvenient. A standard goniometer head may be modified to allow the necessary rotation, as shown in Fig. 9. Ordinary Scotch tape may be used to hold the specimen to the rotating top dial, as shown. This will allow a rough orientation, so that the sample may be cut approximately along crystal planes with the diamond saw (after cutting, reflection Laue photography will be used to make a more precise orientation before polishing, as will be detailed in the next section).

Second, one must have a systematic approach to finding the lattice orientation. The usual procedure is to look at several different orientations of the object, and examine the spot patterns for possible mirror planes. Then one must manipulate the adjustments to align the mirror plane with the axis of one of the adjustments that has free rotation; then one can conveniently change that one adjustment without losing the mirror plane, until another is found (for the case of $2mm$ symmetry or higher). It is actually quite feasible, once some experience has been gained. A system employing a phosphorescent screen and an image intensifier, to render the Laue images in real time, is of immense assistance in this process. It is also important to remember that until the crystal is perfectly aligned, only the spot *positions* can be relied upon to show the symmetries; the spot *intensities* are very unreliable.

Fig. 10 shows several steps along the way to roughly aligning the Si specimen with the ⟨100⟩ axis. The final picture shows the fourfold symmetry of the cubic lattice; the spot quality is not the best but it is deemed worth continuing. The next step is to cut a piece from this large
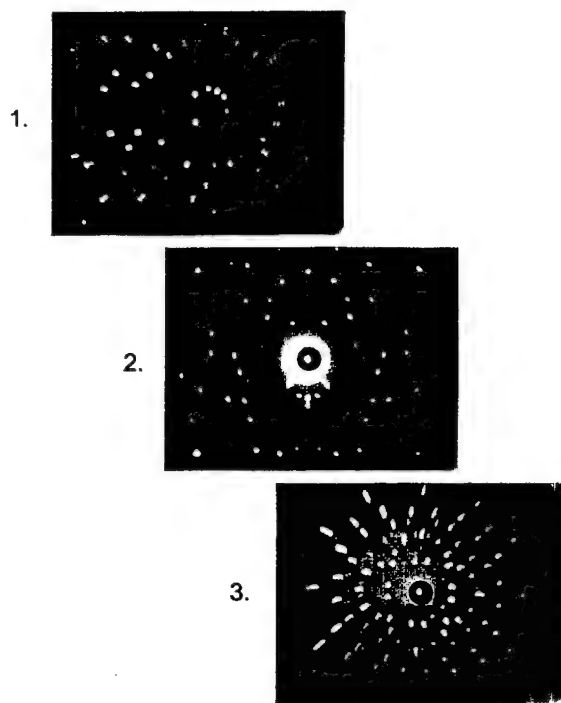

FIG. 10. Several steps in orienting the cubic Si sample for polishing. The reader may be able to identify a distorted axis of twofold symmetry in the first photo; in the second this axis has been aligned so that a second, perpendicular one may be found. Eventual success in this endeavor is shown in the third photo. At this stage in sample preparation, the sample was about 3 mm thick.

specimen, from which a sample on the order of 1 mm will be polished. If an unmodified goniometer head had been used, the specimen could be cut directly, without removing it from the holder. In this case, the goniometer readings must be noted, and replicated on a unmodified unit suitable for use with the diamond saw. If the angles are too large for the standard goniometer head, then one may simply mount the specimen on a block machined at a 45° angle, to extend the range.

Once mounted, the specimen is then cut with a diamond-impregnated blade on a South Bay Technology model 850 wire saw with a model 85022 cross-feed and a model 85016 indexing table. A cleaner cut may be achieved by encasing the sample within a blob of sample mounting wax such as Quickstick 135 [50]. This remarkable wax melts at a relatively low temperature (52 °C), is reasonably hard at room temperature, and dissolves completely in acetone, making it ideal for cutting and polishing RUS parallelepipeds. Once the sample has been cut to a size closer to the desired final size, with at least one face aligned with the crystal lattice, the polishing phase may begin.

Before any actual polishing is done, the sample must be oriented more precisely. For this purpose, it is extremely useful to have a polishing jig that has a built-
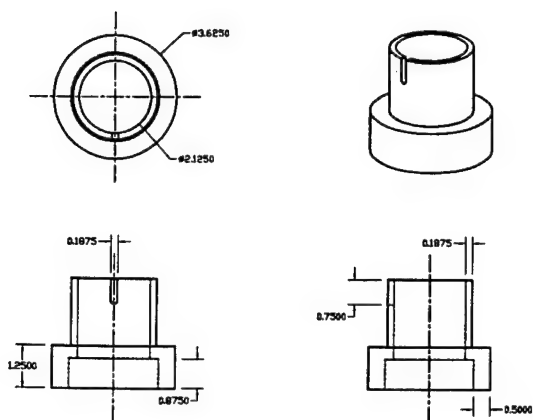
FIG. 11. The outer bell of the polishing jig described in the text. The material is bearing bronze; the dimensions are in inches (1 inch = 2.54 cm).
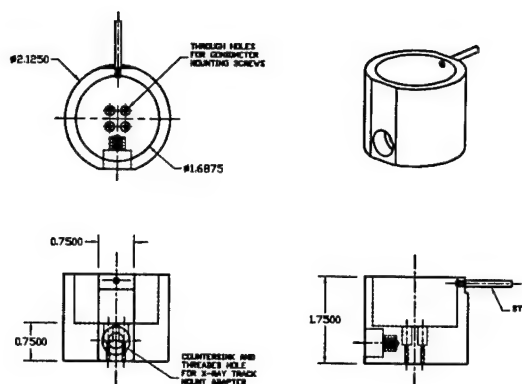

FIG. 12. The inner shaft of the polishing jig described in the text. The material is aluminum, except for the stop, which is cut from a piece of partially threaded steel rod. The dimensions are in inches (1 inch = 2.54 cm). The threads for the track mount adapter, and the size of the through holes for the goniometer mounting screws, will vary depending on what sort of X-ray equipment and goniometer one has.

in goniometer, which can itself be mounted in an X-ray machine. This way, when the sample is oriented, the goniometer may be replaced in the polisher without disturbing the position of the sample. Commercial units are available for this, but may be very expensive— for instance, South Bay Technologies has a multi-axis polishing unit and Laue track mount which together cost almost $10,000! [50]. As an alternative, such a jig may be constructed inexpensively, if one has an extra goniometer lying around (the author was fortunate enough to be given several by a colleague who was cleaning out one of her labs).

b. Making a polishing jig A polishing jig is constructed to use an available goniometer as a sample holder, for the preparation of precision X-ray oriented parallelepipeds. First, the outer bell is machined, making sure that the inner bearing is of sufficient diameter to allow the goniometer to pass. The bell may be made of brass, although ideally one should make it from some material that will not wear down easily. Since stainless steel is somewhat difficult to machine, bearing bronze is used as a compromise. Fig. 11 shows the completed bell. Next, the inner shaft is machined. It is also desirable that this shaft not wear; however, it is also desireable that it be light, so that the amount of force on a sample being polished can be minimized, if desired. Therefore aluminum is chosen as the material, with the idea that if the bearing becomes loose, a new shaft can be made. The specific design of this shaft would, of course, be different for a different goniometer and X-ray mount. Fig. 12 shows the completed shaft. It is very important to make the shaft just small enough to slide freely in the bearing when a little oil is added, and no smaller. Any "play" in the bearing will wear it and cause the sample to wobble as it is being polished, resulting in rounded surfaces. Note the hollow inside of the shaft, in which weights can be placed to increase the pressure on a sample. At this point the jig could be considered useable, but there is one major improvement that can be easily added. The

bottom of the bell will be in constant contact with abrasives, and will naturally wear down. It is quite possible that the bearing-bronze surface (or even stainless steel) will not wear evenly, ruining the alignment of the shaft with the vertical. It is extremely desireable to have a hard surface for the bottom of the bell, to prevent wear.

The author's solution[3] is to line the bottom of the bell with used titanium-alloy tool bits, of the sort used in fly cutters and the like. The trick is to attach the tool bits to the bell in such a way that the bottom surfaces of the tool bits all lie in the same plane, normal to the shaft. This is accomplished by first drawing two concentric circles on a glass plate with a permanent marker, according to the outer diameter and inner diameter of the bell bottom, using the bell itself as a template. The glass plate is then turned over, so the circles are on the bottom. The tool bits are then all arranged on the top of the plate in between these circles, and stuck to the glass with Duco cement thinned out with acetone. After the cement has dried, a new layer of thinned cement is spread on the glass inside the "tool-bit circle"; the polishing bell with shaft inside, but minus goniometer, is lowered onto the tool bits so that the bottom fits over them, as it will when they are attached. The shaft is pressed down so it is stuck to the glass plate. The "stop" is not attached to the shaft in this case, so when the glue dries, the bell can be lifted off without disturbing the shaft. Finally, the top surface of the tool bits and the bottom of the polishing bell are coated with PC-7 epoxy, and the two are pressed together. Since both the shaft and the tool bits are glued to the glass with a very thin coat, it will

---

[3]Due to a suggestion by Sam Condo, foreman of the P.S.U. physics machine shop.
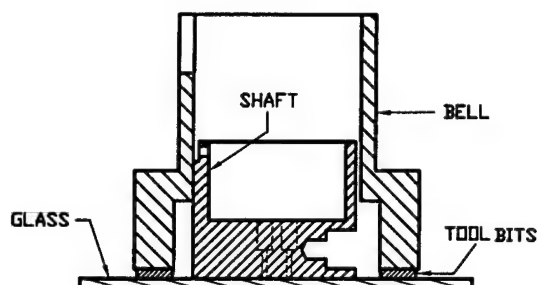
FIG. 13. Schematic of setup for gluing tool bits to the bottom of polishing jig bell, as described in the text. There is a film of thinned-out Duco cement between the tool bits and the glass, as well as between the shaft and the glass. There is a thin layer of PC-7 epoxy between the bottom surface of the bell and the tool bits.
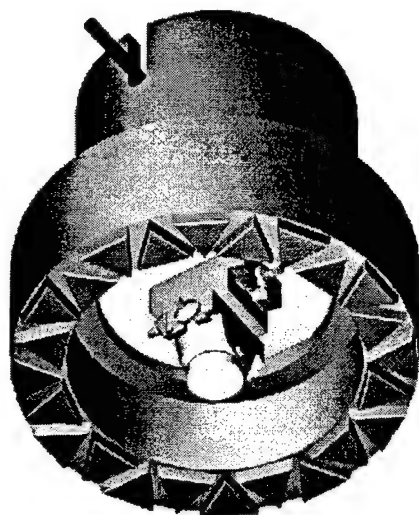

FIG. 14. The completed polishing jig, with goniometer mounted, described in the text. The goniometer is mounted by four screws on the bottom of the inner shaft.

guarantee that the polishing surface of the bell will be normal to the shaft, if the front surface of the shaft has been made square. Fig. 13 shows a schematic of the "final gluing". When the epoxy hardens, the arrangement may be placed in a glass tray and immersed in a shallow bath of acetone. This loosens the tool bits and shaft from the glass, as well as loosening the excess epoxy between the tool bits, without loosening the tool bits from the bell. Fig. 14 shows the completed polishing jig.

c. Final orientation before polishing In order to begin final polishing, at least one surface, and usually two, must be aligned with the lattice, to use as reference surfaces. This is accomplished by gluing one of the sample faces cut normal to a crystal axis to the mounting block at the end of the goniometer; the goniometer is mounted on the shaft and the shaft is attached to the X-ray track mount. Again, acetone with a small amount of Duco cement dissolved in it makes a perfect bonding agent for
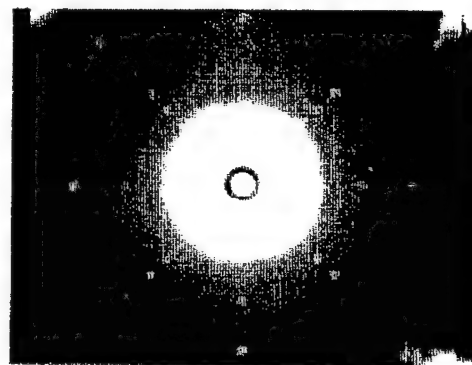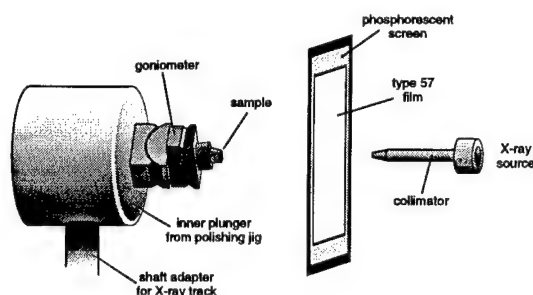

FIG. 15. A schematic arrangement for making a reflection Laue photograph, using the special polishing jig described in the text. On the bottom is shown an actual photograph of the Si sample in progress.

this task. Fig. 15 shows how this assemblage can be used to take a reflection Laue photograph. Since the sample is mounted by a surface that should already be nearly normal to a crystal axis, only minor adjustments should be necessary to achieve precise orientation. Reflection Laue photography is superior to transmission in this instance (if one does not have a real-time system) because unlike a transmission photo, the center of the spot pattern is deflected from the main beam, and simple trigonometry may be used to determine the proper goniometer adjustments (the horizontal deflection of the pattern center is the tangent of twice the angle of deflection times the crystal-to-film distance, *etc.*). The final Laue photograph of the Si ⟨100⟩ surface to be polished is shown on the bottom of Fig. 15; it clearly shows the fourfold symmetry, and the spots are single and symmetric, a good sign.

The orientation of the surface should be accurate within a few tenths of a degree or better, but this is only guaranteed if the proper precautions have been taken to assure that the X-ray beam is running parallel to the track, and that the mounting surface of the goniometer is initially normal to the track. One can ensure this by doing the following:

(a) Place the goniometer/shaft/track mount assembly on a track similar to the one in the X-ray machine, and use a laser beam parallel to the track to check the orientation of the goniometer sample mount

31

(the surface of which should be polished smooth and shiny).

(b) Prepare a glass slide by smearing a portion of it with phosphorescent paint, and after the paint dries, carefully scratch out a pair of perpendicular "crosshairs" near the center of the slide. Attach this slide to the modified goniometer of Fig. 9 so that the slide is more or less normal to the X-ray beam. By first centering the X-ray beam in the crosshairs, and then moving the goniometer up and down the track, any deviation of the beam should be visible; the track may be adjusted until no deviation is observed. **Caution:** always turn the X-ray shutter off before putting one's hand near the beam or track!

2. Polishing by hand

Once the sample is oriented properly, the shaft is removed from the track and the goniometer is detached from the shaft. The goniometer is then placed on a hot plate (or in an aluminum dish on a hot plate, if the hot plate surface is grimy or cruddy). The hot plate is heated to about 60–70 degrees C, and some pieces of Quickstick wax are placed on top of and around the sample. Once the wax has melted and completely covered the sample, the goniometer is removed from the hot plate and allowed to cool at room temperature. The cooling process may be accelerated by placing the goniometer on a large piece of metal to act as a heat sink. The hardened wax will serve as a protective support for the sample during polishing.

With the above step completed, the final polishing can begin. The goniometer is reattached to the shaft, and the two together are replaced in the polishing bell. A piece of abrasive film is placed on a flat piece of plate glass, which in turn is placed on a flat surface (such as a steel surface plate). The polishing jig is placed on the film, and with the addition of an appropriate lubricant such as WD-40, the polishing can commence, with a gentle, smooth figure-8 hand motion. The following tricks have been found to help achieve good results.

1. Start the polishing with 600 grit wet/dry paper. Water may be used as a lubricant for this stage unless the sample is hydrophilic or dissolves in water or some other such thing. The sandpaper will wear down the wax covering quickly, so one can begin the polishing of the actual sample surface that much sooner. The polished wax surface should be checked frequently under a microscope, so one can stop just before reaching the sample surface. If for some reason the sample surface is at a severe angle, or a large amount of material needs to be removed, one may continue polishing with the sandpaper. Note: the sandpaper quickly becomes gummed up with the wax, so the part of the sandpaper used for polishing should be changed frequently.

2. Once the sample surface is exposed or nearly exposed, lapping film should be used, such as that available from Charles Supper Co. or South Bay Technologies [50], with a film thickness of no more than 3 mils, starting with a grit size of 9–15 μm. One may subsequently switch to 5, then 3, and perhaps even 1 μm film to get a smooth, shiny finish. An optically perfect finish is not necessary for this work, so any finer polishing or etching would be excessive.

3. Sometimes when using this film, dust particles are attracted to the bottom of the film and cause slight "bumps" when it is placed on the glass, which can cause scratching and even cracking of delicate samples. To avoid this, the film may be rinsed thoroughly under a vigorous stream of water; while holding the wet and dripping film, the glass plate surface is cleaned with methanol and Kimwipes. The still-wet film is then laid quickly on the plate. The water tends to keep the film from slipping on the glass; in addition, there is less opportunity for dust to settle on the film if it is not dried first.

4. If one is attempting to remove a large amount of material or wax, then it is helpful to put some weight on the inner shaft. With the "homemade" polishing jig this is quite easily done by putting weights in the hollow inner shaft (along with some balled-up tissue paper or whatever so the weights don't move around). With a commercial jig such as the South Bay Technologies model 151, weights may be screwed into a threaded hole at the top of the shaft. In fact, the SBT-151 is weight-balanced by an internal spring, so some weight must be added to the shaft in any case. Small weights of several grams are made especially for the unit, and are useful for final polishing of sample surfaces. For taking off large amounts of material, one may want to make a somewhat heavier weight, with a peice of rod of the proper thread in its center so it can be attached to the unit in the same manner as the smaller weights.

5. Commercial polishing lubricants are generally to be avoided—many of them contain alcohol, which tends to degrade the wax and make it gummy.

Once a surface is finished, the sample may be removed from the mounting block by first removing the shaft from the polishing bell, and placing it goniometer-side down in a beaker of a size large enough to admit the goniometer but small enough so the shaft bottom rests on the beaker rim. Enough acetone is put in the beaker to just cover the sample holder and dissolve all the wax. Eventually, the sample will detach from the holder and float gently to the bottom of the beaker, from which it can be removed, cleaned with acetone and methanol, and replaced on the sample holder with the polished side in contact with the holder, so that the opposite side may be polished parallel.

Normally, we use a smaller, more compact polishing jig (South Bay Technologies model 151 mentioned previously) for polishing all sides except those that must be X-ray oriented. In this case, there is no goniometer, only a stainless-steel sample holder on the end. To remove a sample from this holder, it should be placed sample-side-up in a small container, such as a beaker, and covered with acetone, until the wax completely dissolves. It is helpful in this process to cover the top of the container so the acetone doesn't evaporate before dissolving the wax.

a. Squaring up the sample For a cubic crystal such as the present Si sample, a side perpendicular to the two finished sides may be obtained by X-ray orientation as detailed above (there are three mutually perpendicular fourfold axes). Other orthorhombic crystals may be handled in a similar manner. Once two perpendicular sides have been obtained, a third may be obtained by the following procedure:

1. Two pieces of steel shim are prepared with polished faces that are painstakingly made to be perpendicular with the unpolished ones. At least two surfaces on one of the shims must be polished. Any burrs on the shims are removed carefully with a razor blade.

2. The shims are arranged on a sample mounting block as shown in Fig. 16(a), and fixed with Duco thinned with acetone. Extra Duco may be added to the back side of the shims to keep them from moving in the following steps. The two adjacent shim surfaces that form a corner, as well as the shim surfaces in contact, must be polished. Once the glue dries, the arrangement should be examined carefully under a stereoscope, or a microscope with low magnification, to make sure the shims meet flush and sit flush on the mounting block surface, with no gaps.

3. The sample is then placed in this corner, with the already-polished faces in contact with the polished shim surfaces, and with the sample side to be polished extending slightly above the top of the shims. The sample is stuck to the corner with acetone that has a very slight amount of Duco cement dissolved in it. One way of accomplishing this is to first use a small brush to "paint" a bit of thinned-out Duco in the corner; it will dry to a very thin film, at which point the sample may be placed in the corner, and a small amount of pure acetone added to redissolve the glue. For very small samples, this can be a delicate operation. The sample may tend to be pulled down due to surface tension, and may have to be gently teased back up as the acetone evaporates (which happens rather quickly). Usually this is best done under the stereoscope. Once the acetone has dried, the corner should be examined very carefully under high (60×) magnification,
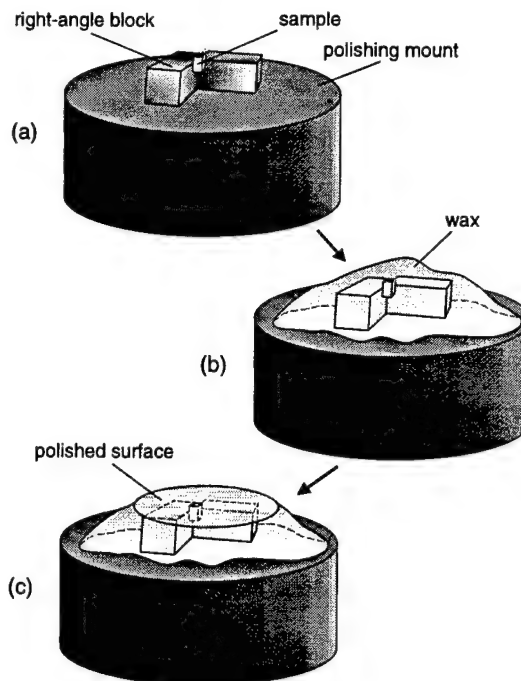
FIG. 16. Three stages in polishing a side of a small sample so it is square with two (or optionally, one) of the other sides, as described in the text. The polishing mount is of the sort that would go on a SBT model 151 jig, and is about 2 cm in diameter.

to make sure the edges of the sample are flush with the shim all around.

4. Once the sample is fixed in place, it is encased in a protective blob of Quickstick, the mounting block is placed in a polishing jig, and the side is polished down to the desired finish. The wax supports the sample sides and helps keep the surface flat and the corners sharp (see Figs. 16(b), 16(c)).

Migliori [45] has detailed an alternate sample-preparation approach which involves supporting the sample on all sides by 4 interlocking shims that are held to a glass plate by a magnet, sealing the whole thing with wax, and then simply turning it over and polishing down to the shims. Supporting the sample on all sides by steel shims results in even sharper corners and edges, although it is not clear that this is necessary. Also, in this method the force on the sample as it is being polished cannot be controlled, which may destroy small, fragile specimens. Still, it may be worth trying, or adapting for use with a polishing jig, if very sharp corners or extremely flat faces are deemed necessary (this might be especially useful with very hard materials, which wear down more slowly than the supporting wax).

b. Final preparation With three mutually perpendicular sides, the sample can be completed by polishing the opposite sides parallel. Since the sides do not have to be polished to optical precision, there are usually some

characteristic patterns of fine scratches on the surface of a finished side that one can see under the microscope; it can be very useful to sketch each of these as one progresses, so one knows which sides have been completed.

Depending on how brittle or prone to cleavage a material is, it may take extroadinary patience to prepare a successful sample, as cracks appear and must be polished out. It is helpful to make sure that lapping film of the appropriate grit size is being used (smaller than the defects one is attempting to polish out, but not so small that progress is too slow), that not too much force is being put on the sample, and that the film and the polishing jig are kept free from dust and dirt as much as possible, cleaning each frequently.

c. How accurate must the parallelepiped be? Exactly how well the sample must approximate a rectangular parallelepiped for a successful RUS measurement is not entirely known, but there is good reason to believe that (a) these methods, when carefully used, yield a sample where each side is accurate to a couple tenths of a degree or perhaps better, and (b) this is good enough so the deviations have no detectable effect, except in some unusual circumstances. This issue is discussed in detail in Section VI, "Effects of Sample Preparation Errors". One thing (perhaps not surprising) that is discovered is that if all sides are parallel, then the parallelepiped can be considerably skewed from perpendicular without the normal mode frequencies being noticeably affected. The reader might gather from the preceding discussions that making the sides parallel is in fact the easiest part of preparation. One should be able to polish two sides parallel within the accuracy of the polishing jig bearing (regardless of whether it is perpendicular to the polishing bell bottom). Thus it is quite reasonable to expect that samples can be prepared which have sufficient geometric accuracy so that the details of the exact geometry can be ignored during a normal measurement.

3. Final characterization and the finished sample

The finished Si sample is $0.93 \times 0.69 \times 0.64$ mm^3, with a mass of approximately 1 mg. Before the sample is used for a measurement, it is desireable to check the sample quality once more using Laue transmission. At this point, the sample is small enough that it will fit entirely within an X-ray beam, so the whole sample may be examined for multiple grains, *etc.*

a. Final characterization Since the sample now has faces which are aligned with the crystal lattice, they should be used as references when setting up the sample on the goniometer. A simple procedure has been developed to assist in this process; this procedure is also useful if one is doing an initial characterization of a sample with natural cleavage planes, or looking at a sample which was polished into a parallelepiped prior to being oriented. First, a small piece of 1/16″ (1.6 mm) steel
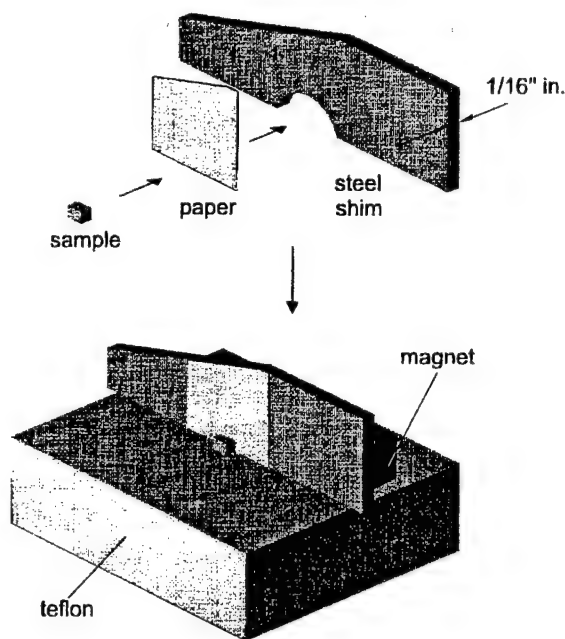

FIG. 17. An adapter for enabling a transmission Laue photograph to be taken of a small sample, so that the beam surrounds the whole sample and is not blocked or diffusely scattered by a sample holder. The sample and paper are stuck to the shim adapter as described in the text, and the whole assembly is then attached to the rotating scale atop the goniometer of Fig. 9.

shim is machined, that can be mounted in the modified (free-rotating) goniometer head, with a small semicircle cut out to let the X-ray beam pass. Next, the steel piece is placed edgewise on a glass plate, and a magnet underneath the glass holds the steel fast. A small piece of tracing paper soaked in Duco thinned out with acetone is stuck to the shim, covering the semicircle, with the edge of the paper flush with the glass.

When the glue dries, the shim and paper are placed on a flat piece of Teflon, and a square magnet behind the shim holds it upright; the sample is then placed in the corner formed by the paper and the Teflon (see Fig. 17). A little acetone is squirted on the sample, and when it dries the shim can be lifted off the Teflon. The sample will (usually) tend to stick to the paper rather than the Teflon. When the shim is attached to the goniometer dial, the sample's parallelepiped axes will be, at least very nearly, the same as the default axes of the goniometer. Thus a properly oriented Laue photograph can be taken with a minimum of adjustment, and the entire sample may be placed within the beam (without some of the beam hitting a sample holder and being blocked or causing diffuse scattering that may wash out the photograph).

b. The finished sample A photograph of the finished Si parallelepiped is shown in Fig. 18, along with a final Laue transmission photograph made by mounting
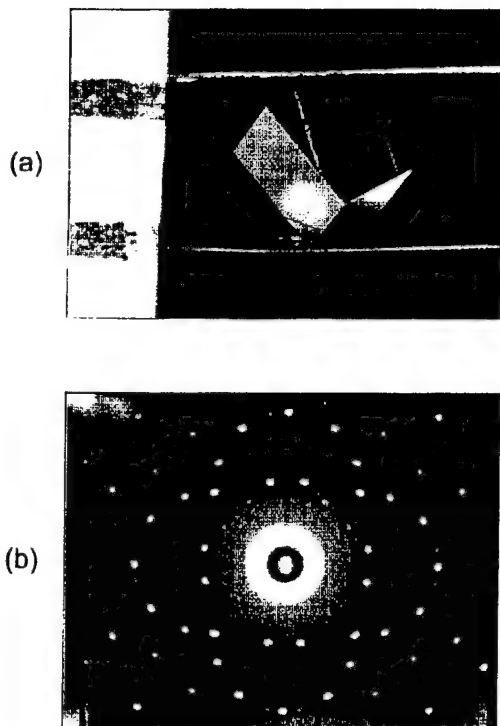
34

FIG. 18. The finished 1 mg silicon parallelepiped described in the text, along with a Laue transmission photograph showing the crystal symmetry and quality. The dark horizontal smudges on the left side of the top photograph are millimeter markings on a piece of plastic ruler. The sample itself is held by its corners between two PVDF film transducers, described in Section III C.

the sample as described above and immersing the entire sample in the beam. In contrast to earlier photos, this one indicates excellent crystal quality, with single, sharp spots, that show very clearly the fourfold symmetry. This is the kind of sample quality and preparation that should be strived for in making a successful RUS measurement. The sample is mounted by its corners between two thin film transducers in a measurement cell (as described briefly in the introduction); the scale is in millimeters. The photograph was taken through the Nikon stereoscope, by placing the camera directly over one of the eyepieces (without the eyeguard), with a shroud to eliminate scattered light, and a blue tungsten filter. Extra fiberoptic lights were employed to illuminate the sample, and an iris diaphragm was placed between the cell and the stereoscope objective, to "F down" the image and improve focusing. Film speed was 25, and exposure time was 1 second.

The Laue photo was made using a Rigaku model CN4037A1 unit equipped with a Siemens FK60-A0 2.4 kW X-ray tube containing a molybdenum (Mo) target, together with a Polaroid Land XR-7 diffraction cassette accepting type 57 Polaroid film. The X-ray tube settings were 40 kV and 25 mA, the crystal-to-film distance was

5.5 cm, and the exposure time was 25 sec.

C. Transducer design and fabrication

The photograph at the end of the preceding section shows a finished sample, mounted by the corners between two 9 μm PVDF film transducers used for measurement. Considerable success has been experienced with these transducers in performing RUS measurements on small samples, and they are relatively easy to prepare. How they work is not entirely understood, however, and it is possible that the present simple design could be improved or optimized, as most of the current design parameters are somewhat arbitrary.

1. Vacuum deposition of aluminum leads

The transducers are essentially capacitors made from vacuum depositing a layer of aluminum on either side of a thin film of polyvinylidene fluoride (PVDF), a piezoelectric film that is sold under the brand name Kynar [51]. The as-received film comes with a predeposited metal coating of aluminum and nickel on either side, which we have found not to be robust enough for our use.

To make the transducer strips, the steps below are carried out:

1. First, a sheet of PVDF is cleaned to remove the factory metallization. For the RUS transducers, we use the 9 μm thickness film. The film is placed gently in a tray containing a 5:1 by weight solution of NaOH, to dissolve the aluminum in the factory metallization; this process is repeated in a 5:1 by volume solution of nitric acid to remove the factory-deposited nickel. Once the metal is loose from the PVDF, the film may be rinsed with distilled water, and placed in a beaker containing a solution of Alconox; the beaker is then put in an ultrasonic cleaner for a few minutes. After a second, thorough rinsing in distilled water, the clean film is then hung to dry.

2. When the film is clean and dry, a section approximately 1″ by 2″ is cut from the larger sheet. The section is cut to be longer along the direction in which the PVDF is stretched during polarization [52]; this direction is marked on the bottom of each large sheet with an arrow. This piece is then placed in a special dual knifedge mask, which may be "flipped" between evaporations; the knife edges are positioned so that the evaporations will overlap in a small region.

3. The mask is placed on one of the shelves in a Veeco VE-300 evaporator unit equipped with a Kronos QM-301 quartz oscillator thickness monitor. A

second shelf below is rotated so that the mask is shielded from the filament below, but a small hole leaves the thickness monitor uncovered. A tungsten filament wound evenly with aluminum wire is hooked up to the electrical leads. The bell jar is pumped out to about 1 micron pressure, and a high voltage probe may be applied to the feedthru to ionize the rarified air as the pumping progresses, to further clean the PVDF surface.

4. The current is then slowly increased through the filament, until the aluminum wets the filament and begins to evaporate. A used ("pre-wetted") filament will wet more easily than a new one; a common difficulty is that the aluminum wire comes apart while melting on a new filament, and the filament gets hot in the spots with higher resistance, and the aluminum melts unevenly and drops off without evaporating.

5. Once the aluminum begins evaporating, the current should be increased so that the deposition rate is several hundred Å/sec. Once this has been achieved, the lower shelf is quickly rotated so that the mask is exposed, and aluminum can begin depositing on the PVDF. A robust coating of aluminum is found to be beneficial, so the evaporation should continue until three or four thousand angstroms have been deposited.

The main difficulty in this process is that heat from the filament will cause the PVDF to wrinkle and wither. It has been found that fast evaporation rates and short evaporation times are preferable to slower evaporation rates (hence less current) and longer times, although one should experiment with different settings, filaments, and filament winding techniques to find those combinations that allow the greatest deposition rates with the least current. It also helps to put the film on the highest shelf possible in the evaporator, to maximize the filament-to-film distance.

Some success has also been experienced using a "cold finger" inside the evaporator, or a copper plate attached to copper refrigeration tubing which is fed through to the outside of the evaporator. The mask in this case is affixed to the copper plate, and liquid nitrogen circulating through the tubing keeps the mask and film from overheating during the deposition. It is important to remember when using a cold finger to completely evacuate the bell jar *before* letting the liquid nitrogen flow through the finger—otherwise, moisture will condense and freeze on the tubing, and slowly "outgas" as the jar is evacuated, preventing a low pressure from being reached.

6. Once the desired amount of aluminum has been deposited, the lower shelf is rotated to shield the
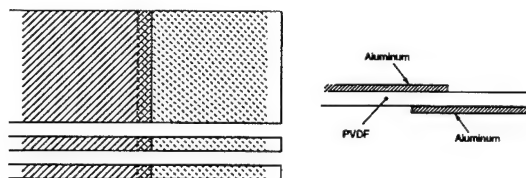

FIG. 19. Schematic of PVDF film used for making RUS transducers, after an evaporation as described in the text. On the left is a top view of a finished sheet of film, and below it some thin strips cut from this sheet. The aluminum depositions are shown by hatching, and the "active area" is the crosshatched section in the middle where the depositions on either side overlap. On the right is a side view of the center of a strip, showing the layers (thicknesses exaggerated).

mask, the chamber is allowed to cool and then vented. The mask is then flipped, exposing the other side. The chamber is reevacuated and the evaporation process repeated.

7. After the chamber has cooled and been vented a second time, the mask is removed and the finished PVDF removed from the mask, taking care not to crease it. If the evaporation has been successful, the aluminum surface should have a bright, silvery appearance (not smoky), and opaque unless held up to bright light. The boundaries of the evaporation should be clearly delineated.

For those desiring a more detailed account of this process using the Veeco evaporator, one is given in a master's thesis by T. M. Slawecki [53]; among other things, this paper contains a diagram of the mask used in these evaporations.

2. Transducer fabrication

The finished piece of film has layers of aluminum on both sides, forming a capacitor with the PVDF as the dielectric. The evaporations have a small overlap region, which can be varied but is typically about 0.5 mm–1 mm. From this piece thin strips are cut, typically 0.5 mm–1 mm wide. The finished film is shown schematically in Fig. 19. The strips are then affixed with silver epoxy to brass tabs which are in turn attached to Bakelite mounting blocks, as shown in Figs. 20 and 21; the aluminum depositions serve as electrical leads from the overlap region to the tabs. Wire leads are then attached to the rear screws on each block. The brass tabs are reenforced with beryllium copper tabs underneath, and small rubber wedges (cut with a razor blade from a pencil eraser, for instance) are placed in between the tabs and the block to maintain tension in the transducer strips. The blocks and tabs do not have formal design criteria, other than being small enough to fit in a measurement cell designed to be mounted in a dewar. Bakelite is an excellent material for low-temperature experiments; but for the room

temperature experiments of this paper, it was found that Plexiglas is preferable, as 0-80 threads in this material do not wear out as quickly.

Most of the transducer blocks used in the present work were, in fact, a bit narrower than those shown in Fig. 21. The strips have to be put under tension in order to work properly, and since the film is so thin, it is easy to strain it beyond its elastic limit. This appears to be less of a problem when the length of strip between the tabs is shorter. One drawback of a narrower block is that the small 0-80 screws that hold the tabs on the block must be filed down to make them shorter than their manufactured thread length of about 1/8 inch. One easily overlooked consequence of not making the screws short enough for the narrower blocks is that the rear screws may come into contact with the rear vertical screw holding the block to the brass base. If the screw holding the tab attached to the positive lead comes in contact with the rear vertical screw holding the block to the brass base, this will create a short circuit if the cell is grounded.

The process of attaching the PVDF strips to the tabs can be a challenge, since the strips pick up a static charge easily and one has to take care not to allow the surfaces to get scratched, lest the continuity of the leads be destroyed. The author has had some luck with the following procedure: A PVDF strip is taped down on a glass plate, with the tape at the extreme ends (where there is no aluminum). Next, a set of tabs is attached to one of the Bakelite blocks with only the rear screws, and the block is placed in a small vise. A small strip of paper is stretched over the tabs in the manner of a transducer strip, at an appropriate tension, and a mark is made at the center of the strip (where the PVDF active area will go), as well as at locations where the strip could be epoxied to the brass tabs. This paper strip is then placed under the glass plate, to serve as a guide for attaching the real transducer. The active (overlap) area of the actual PVDF strip is positioned over the center dot marked on the paper strip; small strips of packing tape (very sticky!) are placed across the PVDF strip 2–3 mm behind the locations marked on the paper where the transducer should be epoxied to the tabs. Pressure is applied to the tape with a pointed instrument only in the small region over the PVDF strip, so that the tape sticks to the PVDF more readily than the glass. The transducer strip is cut with a razor behind these tape sections, and the strip is then teased off the glass, perhaps with two pairs of tweezers, one on each end. Then the strip is stretched over the tabs so that the active area is centered between them, and so that the strip is centered vertically on each tab, and the pieces of tape are pressed down on the tabs to hold the strip. Once the strip is in place, silver epoxy may be applied to the strip and tabs, and the assembly is left overnight for the epoxy to cure. It is helpful if the tabs are well polished on the ends, so that the strips are not scratched by rubbing against them, and if the area on the brass tab where the silver epoxy is to be applied has been roughened a little.
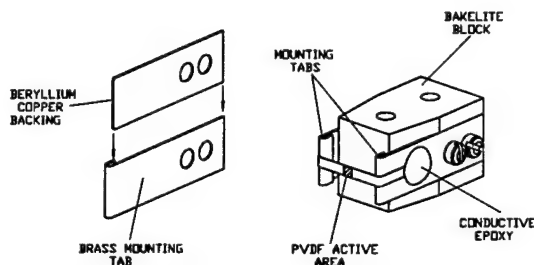
FIG. 20. An assembled transducer of the type used in this work. A narrow PVDF strip, as described in the text, is affixed to brass tabs, which are attached to a Bakelite or plexiglas block (shown below) with 0-80 screws. The brass tabs are reenforced with beryllium copper tabs, which behave like springs. Wire leads would be attached to the tabs by the rear screws.
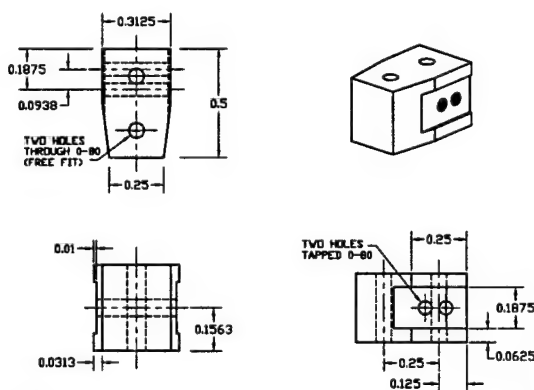
FIG. 21. A bakelite block of the type shown in Fig. 20. Dimensions are in inches (1 in. = 2.54 cm).

37

3. Transducer operation

When voltage from a signal generator is applied across the leads on one of the completed transducers, an electric field is induced across the thickness of the film in the active area. This, in turn, couples to the piezoelectric coefficients d_{31} and d_{32}, where direction 3 is perpendicular to the thickness of the film, causing strain in the 1 and 2 directions. During manufacture, the film is stretched in the 1 direction while it is being polarized, making it anisotropic. Coefficient d_{31} is thus made to be much higher than d_{32}, by almost a factor of 10 [54]; the strips are therefore cut along the 1 direction, to maximize their response. Thus, shear modes may be excited (and hence detected) quite effectively. The transducers only work properly when they are under tension, so they must be attached to the brass tabs described above with a certain amount of "bias tension", so the transducers don't go slack during one half of each cycle when being driven sinusoidally.

Since the film is so thin, the thickness resonance of the film is around 100 MHz. It may result that the thickness mode is unimportant in the operation of these transducers; indeed it has been found that the "breathing" mode (dilatation) of a spherical sample is difficult to detect, compared to the shear modes (see Section IV). The optimum thickness of film, transducer strip width, overlap area, and length are all unknown, as well as whether anything could be gained by using a PVDF "sandwich" and/or a nearby FET preamp, as some have suggested.

Unlike other transducer designs, the transducer resonances have not been carefully considered here. The reason is that PVDF has extremely high internal damping, and any resonances of the transducer strips tend to have a Q in the range of 10–20. Most samples that are studied have Q's of at least several hundred, so there is no danger of mistaking a transducer resonance for a sample resonance. Any vibrations in the surrounding structure would have to travel through the PVDF to get to the sample, so they would be highly damped as well. Some broad spectral features, that could well be transducer resonances, are considered in Section IV, where samples with high internal friction are studied.

Due to the small samples used in this work, the transducers wind up in very close proximity, and there can be several millivolts of crosstalk between them if the drive signal is several volts PP. This can be minimized by placing a conducting barrier or shield between them, with a small hole cut out for the sample to fit.

a. Transducer testing One would like to have a convenient method for testing the transducer strips before going to the trouble of mounting them on the blocks. However, one also wants to handle the strips as little as possible. Therefore, the author has settled for testing the transducers only after they are mounted and in the measurement cell, by using a test sample that has a known response. The test sample most commonly used is a 1/16″

(1.6 mm) Pyrex sphere; it has strong resonances which are virtually independent of mounting. The sphere, since it lacks sharp corners, also does a minimum of damage to the PVDF strips, keeping them in good shape for the "real" measurement.

If the transducers are arranged in the cell (described below) so that the transducers have a separation distance on the order of 1 mm, and there is a conducting shield with a opening of about 1 mm² between them, then with a 5V PP signal on the drive transducer the receive transducer typically develops about 100–300 µV of crosstalk (it varies with frequency somewhat—see Section IV, section IV B 4). Using a PAR 5202 lock-in amplifier as a detector, the first resonance of the sphere, at 1.72 MHz, gives a peak with a height of about 80–100 µV. The corresponding noise level is around 1 µV or less, when the time constant on the lock-in is 0.1 second. The variance in these numbers is considerable, however. One factor which obviously affects the height of the resonance peak (and hence the S/N ratio of the measurement) is the coupling between the transducer and the sample. The above description assumes "light" to "moderate" transducer force on sample (see Section IV).

b. Shift in frequency due to transducers It is important to consider the effect the transducer may have on the resonance frequencies, since any contact with the surface perturbs the natural (free) boundary condition. Demarest [42] states that "...an elastic force on the surface of a vibrating body must raise the frequency", implying that all the measured resonances will be higher than the true ones. Indeed, this seems to be the case for early RUS researchers, who compensated by having one of the transducers on one arm of a balance, taking several measurements with different amounts of weight on the other balance arm, and extrapolating to zero [23]. The data thus obtained show shifts which are roughly linear with contact force; this is consistent with treating the problem as similar to a spring-loaded bar, and assuming the effective "spring constant" coupling the transducer and sample is proportional to contact force. It is important to note that the shift in frequency comes not from the static force but from the change in the boundary condition, and the frequency shifts seen by the early researchers seems to be a result of high drive levels [45]. High drive levels would result in a strong dynamic interaction with the transducer; for a weaker coupling and low drive level, the change in the boundary condition may be unpredictable. However, the associated shifts in frequency should be smaller as well.

The development in our laboratory of resonant photoacoustic (PA) methods for measuring optical absorption by transparent materials [55,56] offers as a side benefit a good test of the effects of transducers on the natural frequencies of a solid. Three different transduction methods have been used in the work, for various applications: non-contact transduction where the sample is simply supported at nodes of vibration by sapphire spheres; thin-film PVDF transducers similar to those

TABLE XI. Resonant frequency and Q for a longitudinal bar mode of a $4 \times 1 \times 1$ cm^3 quartz parallelepiped, measured with three different tranduction mechanisms.

Transduction mechanism	f_0 (Hz)	Q
Non-contact (simp. supp.)	134411	8.4×10^5
LiNbO$_3$ disk	134428	2.0×10^5
PVDF film	134384	1.7×10^5

used in the present work, and standard LiNbO$_3$ disk transducers. The samples studied in the resonant PA work were rectangular parallelepipeds of very high-purity quartz, and for measurements using the latter two transduction mechanisms, the sample was mounted by the corners, as they would be for a RUS measurement of the sort featured in this paper. The quartz samples have intrinsically high Q's ($> 10^5$) so even a very small shift in frequency is observable.

The frequency and Q of what is essentially a longitudinal bar mode of one of these samples, measured by all three methods, is shown in Table XI. The results show that for this mode, the frequency shifts by 0.03% between the different methods. One point of interest is that using the LiNbO$_3$ disks gives a higher frequency (by 0.01%) than the presumably more accurate non-contact result, in accordance with Demarest's observation, but the PVDF film *lowers* the frequency (by 0.02%). This is in accordance with the author's observations that clamping a sample tightly between PVDF transducers actually lowers the frequency relative to light contact. The LiNbO$_3$ evidently acts like a spring load, while the PVDF acts more like a mass load. One also notices that the Q of the sample when simply supported at the nodes is a bit higher than when the sample is supported at the more active corners, which is to be expected. These results give some indication of how corner-contact transducers perturb the resonances of a sample, and also how repeatable a corner-contact resonance measurement is.

Other relevant results from the photoacoustic experiments would include tests on the effects of air loading on the resonances of the PA samples. For instance, one sample's frequency was found to go from 115121 Hz at atmospheric pressure to 115117 in a vacuum (a change of 0.003%), while the Q went from 0.4×10^5 in air to 2.2×10^5 in a vacuum. Thus the effect on the frequency of the air is negligible, but the effect on the Q is quite large (probably because the Q is so high to begin with).

Since these experiments were not temperature controlled, one might wonder how much of the change in frequency from one case to another may be due to a change in temperature. The thermal expansion coefficient of quartz (fused) is $\alpha = 5.5 \times 10^{-7} (°C)^{-1}$ [48]; as the temperature θ changes, the dimensions of a rectangular parallelepiped will all change by a factor of $1 + \alpha\theta$, and the volume will change as $(1 + \alpha\theta)^3$. Since frequency is inversely proportional to length but inversely proportional to the square root of density (hence proportional to the square root of volume if the mass remains constant), we get

$$f_0 \propto \frac{(1+\alpha\theta)^{3/2}}{(1+\alpha\theta)} \propto (1+\alpha\theta)^{1/2}.$$

Hence for a temperature variation of, say, 10 °C, the frequency would shift by only about $\Delta f \simeq 0.0003\%$, which would not account for the effects seen here. For materials with larger thermal expansions, these effects may not be negligible and may contribute to the RMS error if the temperature is not controlled.

It would be of great value to do a very systematic check of the repeatability of spectra on small samples such as those used in this work, especially since the surface-to-volume ratio of small samples is greater than that of large samples. Any surface effects, such as the condensation of moisture with changing temperature, would be more important. Thus all the more reason to do all room-temperature measurements with an evacuated, temperature-controlled cell. Regrettably, this was not done in the present work.

D. Sample cell design

The sample cell used in this work was designed to be small enough to fit through the opening in the top of a helium storage dewar ($\sim$1 inch, or 2.54 cm), and at the same time allow the transducer blocks to be conveniently mounted and removed. It was important to make the space between the transducers accessible to allow samples to be mounted and removed; also, the distance between the transducers had to be easily adjustable.

The bare cell, without transducers, is shown in Fig. 3.14; it is designed to accomodate two 1/16″ (1.6 mm) rods along its length, to guide brass base supports for the transducer blocks of Figs. 20 and 21. The position of the "rear" base (left side in the figure) is adjusted by means of a 2-56 screw that fits through the slot on the bottom left of the cell, from below; the position of the "front" base is adjusted by a piece of 0-80 threaded rod attached to a thubscrew. These bases are shown in Fig. 23. The assembled cell is shown in Fig. 24. Note the beryllium copper crosstalk shield. The position of the transducer block on one side of this shield is adjusted by means of a screw underneath, as mentioned above; the other block is adjusted by the thumbscrew. If the first block can be positioned very closely to the crosstalk shield, without the tabs touching it, then the hole in the shield can be made smaller than the sample, since only the corner need pass through.

39

FIG. 22. The "naked" RUS test cell, before any hardware is added. The material is brass, and dimensions are in inches (1 in. = 2.54 cm).

FIG. 23. The base supports for the transducers of Fig. 20. The material is brass, and dimensions are in inches (1 in. = 2.54 cm). The isometric view shows how the transducers are to be mounted on these bases; the bases in turn are shown with the guide rods and threaded adjusting rod in place, as when mounted in the measurement cell.

FIG. 24. The assembled RUS test cell, with the transducers and a sample in place. The distance between the transducers is mainly controlled by turning the thumbscrew (located on the left end of the unit).

E. Data acquisition

The acquisition of RUS data is fairly straighforward; as summarized in Section I, it consists of mounting the sample between two transducers, driving one with a swept sinusoid and using the other to detect resonances.

1. Mounting the samples

When the samples are only a few hundred microns in size, mounting them can be somewhat tricky. A sample must be mounted so that it is held lightly (by the corners if a rectangular parallelepiped) between the PVDF strips, without any oil or bonding agent, and without getting the sample dirty, damaging it, or damaging the delicate transducers.

The basic strategy is to put the sample on the end of a hypodermic needle hooked up to a small vacuum pump (Telvac k-150); the needle itself is attached to a small fixture which is mounted in the arm of an Emerson micromanipulator (J. H. Emerson Co., Cambridge, MA). This is shown schematically in Fig. 25. The sample is transferred to the end of the hypodermic needle by means of a second, hand-held needle hooked up to a separate pump. The sample may be picked up from a glass plate, clean sheet of paper, or other surface and brought into close proximity with the stationary needle; when one surface of the sample is nearly flush with the end of the stationary needle, the suction on the hand held needle is released. The sample will be pulled against the stationary needle and held by the suction. With practice, this can be done confidently without losing the samples or damaging them. Having the sample attached to a micromanipulator in this fashion allows complete freedom to move the sample precisely in 3D, thus allowing one to position the sample between the transducer strips. To allow one to orient the sample such that the corners line up with the transducer active areas, it is helpful to have a needle with an angled end. The end should also be very smooth and flat around the hole, to avoid scratching the sample and to help maintain suction. Any of the standard needles may be modified for this purpose, by melting a blob of Quickstick around them and then polishing the blob at the desired angle. Finishing with 9μm lapping film will produce a flat, smooth surface. For mounting especially small samples, a very thin (0.01 in. OD) needle is prepared in the above manner, and then bent in the middle at a 90° angle (after first inserting a piece of magnet wire inside to prevent the hollow needle from buckling). This allows the sample to be brought between the transducers from below, without the needle getting in the way or bumping into the crosstalk shield. The sample may be teased into the correct orientation with gentle prodding from an appropriate probe, such as a dentist's tool with a piece of thin teflon tubing inserted over the end.
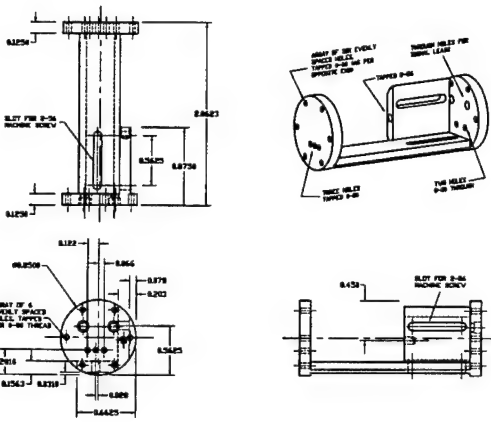
40

FIG. 25. Apparatus used to mount RUS samples between the PVDF transducer strips in the test cell. In (a), the sample is held at the end of one hypodermic needle backed by suction, and is moved toward the end of a second needle, which is mounted permanently on a micromanipulator arm, as shown at the bottom. In (b), the sample has been brought sufficiently close to the second needle that the suction on the first can be turned off, causing the sample to jump onto the second needle. If the suction on the second needle is made stronger than that on the first, the sample will automatically jump to the second when brought close enough.

When the sample is in position, with the corners over the PVDF active area and the body diagonal of the sample more or less normal to the transducer surface, the transducers are brought together by turning the thumbscrew, thus gripping the sample by the corners. The suction on the hypodermic needle is then turned off, and the needle is gently moved away.

a. Some considerations The amount of force exerted on the sample when mounted in this way obviously varies with how tightly the sample is held. Our approach is to hold the sample as lightly as possible, so long as the sample doesn't fall out. The exact amount of force required to do this is not known, but one may suppose that it is on the order of the weight of the sample, or several times the weight of the sample. Since the samples in this work are almost all less than a milligram in mass, it is believed that this system produces less perturbative force on the samples than most other known RUS transduction/mounting schemes (that of Migliori *et al.* uses a known force of several dynes to hold the samples in place [45]).

The obvious reasons for using a light contact force are to maintain point contact, maintain high Q, and to not perturb the natural resonances. There is another reason that is not immediately obvious, when using thin film PVDF transducers. If the samples have been well prepared, they will have sharp edges and corners, which can easily poke through the transducers. This is especially problematic if the samples themselves are conducting, as
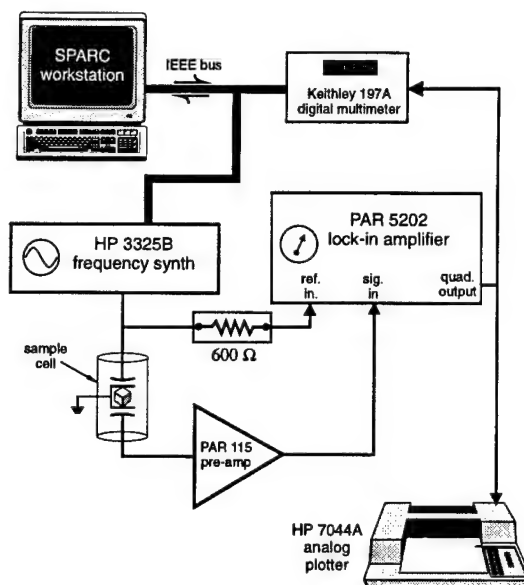
FIG. 26. Signal chain for room-temperature RUS experiment. The sample cell is that shown in Figs. 22 and 24.

they may short out the front and back leads.

The possibility of conducting or semiconducting samples also motivates another design detail: since the sample is in direct contact with the aluminum leads on either transducer, it is important that the transducers and wiring be arranged so 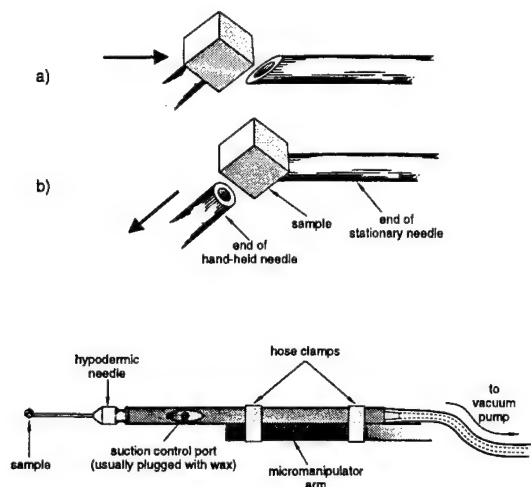that the two transducer leads that face each other are ground, not "hot", so a low-resistance path between them is not a problem.

F. Measuring a spectrum

Once a sample is in place, the cell is sealed and a spectrum may be obtained. The room temperature setup is quite simple, as shown in Fig. 26. A sinusoidal signal from the HP 3325 signal generator excites the drive transducer in the cell, while the signal from the pickup transducer goes first into a Princeton Applied Research (PAR) model 115 broadband preamplifier, and then into a PAR model 5202 two-phase high-frequency lock-in amplifier. The lock-in amplifier also receives a reference from the HP 3325; the output of the 3325 is split and a resistor is added between the 3325 and the lock-in to help balance the circuit, since the lock-in has low (50Ω) input impedance, whereas the cell has very high input impedance, even at high frequencies. As with all RF work, superior results may be achieved by experimenting with different cabling arrangements, *etc.*

The output from the lock-in is also split, to a Keithley 197A multimeter, and to a HP 7044A analog plotter. The HP 3325 and Keithley 197A are both hooked up to an IEEE-HPIB interface on a Sun workstation, so that data acquisition may be controlled by computer and the results stored digitally. One must be very careful not to

41

disturb any of the equipment or cables during a run, as this can change the phase of the RF background (this includes merely touching buttons on the instruments!).

The manner of digital data acquisition used in this work is one area which could use improvement. The software and hardware used in the acquisition were copied from a setup intended for acquisition of data on high-Q systems at lower frequencies, where there is considerable ringdown time. Consequently, not a lot of attention was paid to speed, since the limiting factor was the system being studied. At megahertz frequencies, ringdown times are very short, so data acquisition can be speedy; as it is, the present system takes on the order of 0.5 seconds to acquire one data point, so a complete exploratory spectrum of a new sample could take several hours.

Therefore, the following procedure is used when acquiring a spectrum:

1. The analog plotter and the built-in sweep functions on the HP 3325 are used to scan the spectrum for resonances.

2. When resonances have been located, the computer is programmed to do a series of fine scans around these peaks. This is the actual data that will be used in the analysis.

1. An actual measurement

Fig. 27 shows analog scans of the spectrum of our 1 mg Si test sample. Since the sample is small and the contact force is low, one does not typically see the same S/N that is seen in other RUS data. The resonances interfere constructively and destructively with the background crosstalk, introducing a phase-shift into the Lorentzian line shapes. The Q's are perhaps not as high as one would expect for a single crystal with a minumum of defects; there are several around 10^4 but most are around 3000 to 5000. One might suspect this to be a consequence of the lossy PVDF. On the other hand, Migliori [46] has suggested that the process of preparing a Si parallelepiped, in a manner such as that described previously, leads to surface cracking which lowers the Q.

Fortunately, there are no features seen in the spectrum other than noise and sample resonances (this is not entirely obvious until the data has been analyzed, however). Systems employing non-resonant, high-Q transducers commonly exhibit features in their spectra which are not sample resonances and it is sometimes unclear which features to include as data and which to discard. This would tend to be more of a problem for smaller samples and weaker signals.

G. Data Analysis

When the fine-scanned resonance data have been obtained, they must be turned into a list of frequencies before they can be analyzed. Because the agreement between experiment and theory in RUS is generally very precise, and because the resonance curves are not standard symmetric Lorentzian peaks, one cannot simply use the top of the peak or some other simple visual criterion to find the center frequency. One must actually fit the data to a proper mathematical model that includes the phase shifts.

1. Center frequencies from resonance peaks

To obtain the correct description of the resonance line shapes, we consider the operation of the PAR 5202 lock-in amplifier.

The PAR 5202 lock-in is a two-phase lock-in, meaning it can measure the portion of an incoming signal that is in phase with a reference and that which is in quadrature. If we let the signal due to mechanical vibration of the transducer be $S(t)$ and the electrical crosstalk be $X(t)$, then we have:

$$\text{in-phase} = \frac{1}{T} \int_{\tau-T}^{\tau+T} (S(t) + X(t) + N(t)) \cos \omega t \, dt$$

$$\text{quad} = \frac{1}{T} \int_{\tau-T}^{\tau+T} (S(t) + X(t) + N(t)) \sin \omega t \, dt, \quad (49)$$

where $N(t)$ is noise. We can think of the in-phase output as essentially being the "real part" of the input as a function of frequency, and the quadrature output as being the "imaginary part". If we write the crosstalk as

$$X(t) = \hat{X}(f)e^{i\omega t} = |X|(f)e^{i\varphi_x}e^{i\omega t},$$

then the in-phase crosstalk will be $X_0 = |X|(f) \cos \varphi_x$, and that in quadrature will be $X_{\frac{\pi}{2}} = |X|(f) \sin \varphi_x$.

One conclusion that might be drawn already is that if the crosstalk is more or less in phase with the reference, then the quadrature output should contain a smaller amount of it; indeed this is observed. The mechanical resonance signal is expected to look like a Lorentzian with some arbitrary phase shift; it may be written as:

$$S(t) = A \frac{(f/f_0) + \left(1 - (f/f_0)^2\right) Q i}{(f/f_0)^2 + \left(1 - (f/f_0)^2\right)^2 Q^2} e^{i(\omega t + \varphi_s)}, \quad (50)$$

where A is a dimensionless constant, f is frequency, f_0 is the resonance frequency, Q is the quality factor, and φ_s is the phase angle of the resonance signal with respect to the reference. Since the quadrature output is expected to have less crosstalk, it is used for measurement purposes; we therefore consider what the form of the resonance curve should be for that output. For this purpose, a new phase angle $\phi = \pi/2 - \varphi_s$ may be defined (the significance of this is evident in the next section). The imaginary part of $S(t)$, hence the portion appearing at the lock-in quadrature output, is
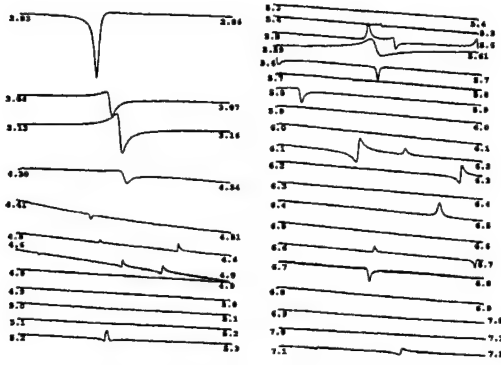
FIG. 27. A collection of scans showing the peaks in the resonance spectrum of the 1 mg Si test sample described in the text. Some traces are double (or triple) runs to check reproducibility of small peaks. The numbers at the ends of each trace are frequencies in MHz.

$$\psi(f) = A \frac{(f/f_0)\cos\phi + \left(1 - (f/f_0)^2\right)Q\sin\phi}{(f/f_0)^2 + \left(1 - (f/f_0)^2\right)^2 Q^2}, \quad (51)$$

or, with a background due to crosstalk:

$$\psi(f) = a_0 + a_1 f + a_2 f^2 + a_3 f^3 \dots$$

$$+A\frac{(f/f_0)\cos\phi + \left(1 - (f/f_0)^2\right)Q\sin\phi}{(f/f_0)^2 + \left(1 - (f/f_0)^2\right)^2 Q^2}. \quad (52)$$

This latter model is the one used to fit the resonances in this work. Some of the possible lineshapes as a function of phase angle are shown in Fig. 28; one can use these to approximate the center frequency of peaks such as those in the spectrum of Fig. 27. Precise values for the frequencies are obtained by fitting the spectral data to the model of (52), using a standard Levenberg-Marquardt algorithm [39]. The Levenberg-Marquardt algorithm is a nonlinear optimization scheme that requires initial guesses for all the free parameters to be fit; this may be done automatically (in some cases), by inspection, or by visual curvefitting. The latter is the preferred method, especially when there are overlapping modes. With a graphics program that displays the data along with a curve calculated from the current guesses, and which updates the curve as the parameters are "tweaked", one may use the brain's powerful pattern recognition capability to obtain very good initial guesses for all the parameters. Such programs are available commercially (such as Jandel Scientific's *Peakfit*™), although with some knowledge of computer graphics one may design one's own, which may be preferable.

a. Guessing Q from the resonance peaks Whether one fits the peaks by eye or with the computer, it is helpful to know how a resonant peak's appearance depends on the relevant parameters (center frequency, peakwidth, amplitude, phase angle). Plots such as Fig. 28 are helpful, but
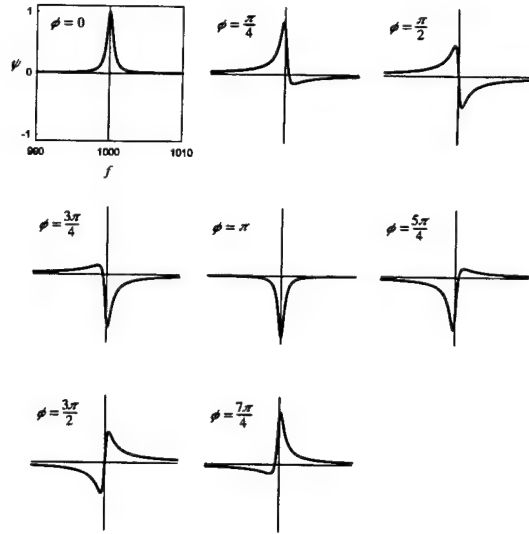
FIG. 28. The resonance curve of Eq.(51), with $A = 1$, $f_0 = 1000$, and $Q = 1000$, for various phase shifts ϕ. The resonance data in this work may have any of these shapes, depending on the phase of the sample's mechanical vibration compared to the reference going into the phase-sensitive detector. Note that the extremum of the peak is only at the center frequency for $\phi = 0$ and $\phi = \pi$.

in order to obtain a first guess for Q, one must know how Q depends on peakwidth. The resonances seen in this work are the "imaginary part" of a complex vector, and Q is the center frequency divided by the peakwidth of this vector's magnitude at the half-power points, which occur at $1/\sqrt{2}$ of the maximum (since the transducers in this work respond essentially to displacement). The Q does not necessarily depend on the peakwidth the same way in the "real" and "imaginary" (in-phase and quadrature) components, however. If ϕ is taken to be zero, then for sufficiently high Q the functional form in (51) will appear as a symmetric peak with its maximum at the center frequency, *i.e.*,

$$\psi_0 = A\frac{(f/f_0)}{(f/f_0)^2 + \left(1 - (f/f_0)^2\right)^2 Q^2}.$$

Hence we may define a quantity Δf as the full width at half maximum (FWHM). The maximum amplitude of this curve occurs near $f = f_0$; it is not exactly at $f = f_0$, since the curve represents an amplitude resonance. If $g \equiv f/f_0$, then ψ_0/A may be written as

$$\psi_0/A = \hat{\psi}_0 = \frac{g}{g^2 + (1 - g^2)^2 Q^2},$$

and hence

$$\frac{d\hat{\psi}_0}{dg} = \frac{g^2 + (1 - g^2)^2 Q^2 - g(2g + (4g^3 - 4g)Q^2)}{(g^2 + (1 - g^2)^2 Q^2)^2}.$$

It follows that $d\hat{\psi}_0/dg = 0$, and ψ_0 is maximum, when $1 + (2 - 1/Q^2)g^2 - 3g^4 = 0$. For large Q, this equation

43

is nearly satisfied by $g = 1$, which is equivalent to saying $f = f_0$. One can then approximate with

$$\psi_{max} \simeq \psi|_{f=f_0} = A.$$

The half-maximum points will occur at $\psi = A/2$; hence one can write an equation for the frequencies at these points:

$$A\frac{(f/f_0)}{(f/f_0)^2 + \left(1 - (f/f_0)^2\right)^2 Q^2} = A/2.$$

Rewriting this equation in terms of $g \equiv f/f_0$,

$$g^2 + (1 - g^2)^2 Q^2 = 2g,$$

or

$$Q = \frac{|2g - g^2|^{1/2}}{|1 - g^2|}.$$

Multiplying top and bottom of the right side by f_0^2,

$$Q = \frac{|2ff_0^3 - f^2 f_0|^{1/2}}{|f_0^2 - f^2|}.$$

If the peak is nearly symmetric, then the frequencies at the half-maximum points can be approximated as $f = f_0 \pm \Delta f/2$. Substituting, one obtains

$$Q = \frac{\left|2(f_0 \pm \Delta f/2)f_0^3 - (f_0 \pm \Delta f/2)^2 f_0^2\right|^{1/2}}{\left|f_0^2 - (f_0 \pm \Delta f/2)\right|};$$

simplifying, this becomes

$$Q = \frac{\left|f_0^4 - f_0^2(\Delta f/2)^2\right|^{1/2}}{\left|\Delta f f_0 - (\Delta f/2)^2\right|}.$$

Since $f \simeq f_0 \gg \Delta f$ if $Q \gg 1$, we discard higher order terms in Δf to finally obtain

$$Q \simeq \frac{|f_0^4|^{1/2}}{|\Delta f f_0|} = \frac{f_0}{\Delta f}.$$

Thus it is concluded that if one is to guess the Q of a peak in the quadrature output graphically, one should divide the center frequency by the FWHM, not the peakwidth at the $1/\sqrt{2}$ point (as one would for the magnitude of the vector addition of the in-phase and quadrature components).

b. Fitting the resonance data Once one has initial guesses for f_0, A, Q, and ϕ, one may fit the data with a nonlinear optimization technique such as the Levenberg-Marquardt scheme mentioned previously. This makes it possible to obtain accurate values for center frequency of peaks that are very weak and hence noisy, or for peaks that overlap. Since the functional form of the mathematical model is known analytically, the necessary derivatives can also be done analytically. This points to one advantage to doing one's own curvefitting as opposed to using a commercial package, as some, like Jandel's Peakfit™, will not allow you to define analytic derivatives of a user-defined function. Another advantage is that one can use singular value decomposition, as mentioned in Section II, to guard against the solution going awry because the fit is insensitive to one or more parameters.

A FORTRAN program for fitting the resonances using the Marquart method, `lrnzmrq.f`, is included in the Appendix. Along with values for the fitted parameters, this program returns standard errors based on the covariance matrix of the fit. From [39] we have:

$$\delta a_i = \pm\sqrt{\Delta \chi_1^2}\sqrt{C_{ii}},$$

where a_i is a fitted parameter, $\Delta \chi_1^2$ is a change in the chi-square statistic of the fit (with a single degree of freedom), and C is the covariance matrix, or the inverse of the Hessian matrix $\alpha_{kl} = 1/2(\partial^2 \chi^2/\partial a_k \partial a_l)$. A 100% change in χ^2 corresponds to a 68.3% confidence level, or the usual standard deviation (if we assume the errors are normally distributed), so we may write $\delta a_i = \pm\sqrt{C_{ii}}$ for this case. This is how errors are calculated in the program `lrnzmrq`, with one slight difference. The formal definition of the chi-square is:

$$\chi^2 = \sum_{i=1}^{N} \frac{[y_i - y(x_i, \mathbf{a})]^2}{\sigma_i^2},$$

which presupposes a knowledge of the σ_i, the uncertainty in the measurement of each point y_i. If it is assumed that the uncertainty in measuring the y_i is dominated by (normally distributed) noise, then this uncertainty is reflected in the minimum rms fit. It may be reasonably assumed that if the model used to fit the data is an appropriate one, that the uncertainty in all the y_i is essentially the same and equal to the variance of the noise:

$$\sigma_i = \sigma \simeq \text{rms} = \frac{\left(\sum_{i=1}^{N}[y_i - y(x_i, \mathbf{a})]^2\right)^{\frac{1}{2}}}{N}$$

Since in this approximation the σ_i are all equal, one can use $F = \sum_{i=1}^{N}[y_i - y(x_i, \mathbf{a})]^2$ as a figure-of-merit, and the resulting covariance matrix $\tilde{C}$ will be off by a constant. This can be corrected in the final calculation of the δa_i:

$$\delta a_i \simeq \text{rms} \cdot \sqrt{\tilde{C}_{ii}}.$$

44
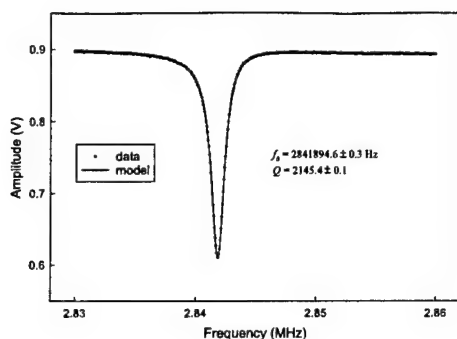
FIG. 29. A fine scan of the lowest peak in the resonance spectrum of the 1 mg Si sample, along with the curve predicted by nonlinear curvefitting using Eq.(52) as a model.
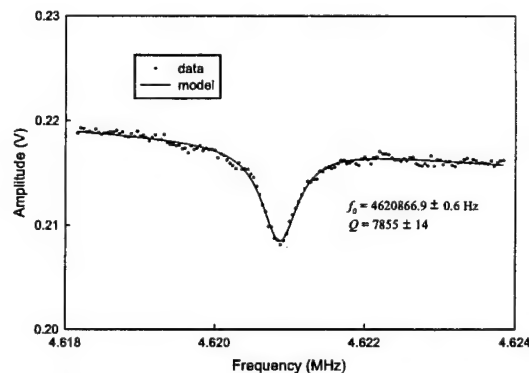
It is found that the errors thus obtained, even for somewhat noisy data, are small enough to determine f_0 to within a part per million and Q to within a part per thousand. These errors are much smaller than the other errors in the measurement of the frequencies, and are therefore not used in the determination of the elastic constants. The order of magnitude of these errors may be verified by generating some synthetic data according to the model in Eq.(52) with the addition of some random numbers to simulate noise, and using lrnzmrq to fit this synthetic data using some appropriate "guesses". It is found that when the variance in the "noise" is 10% of peak amplitude, with 100 data points and a Q of 1000, the original value of f_0 used to calculate the synthetic data is recovered within about a part per million. We may conclude that with enough data, this curvefitting procedure ensures that despite phase-shifted or even overlapping peaks, the frequencies may be determined well enough so that errors in determining frequency from the measured data may be ignored.

The following figures show fine scans of some of the peaks from the the spectrum of Fig. 27, along with the curves fit to these data. Fig. 29 shows the first peak at 2.8419 MHz. This peak has a relatively high signal-to-noise ratio, and so both f_0 and Q are very accurately determined (along with the amplitude, phase, and crosstalk parameters). This graph may be compared to Fig. 30, where the S/N ratio is much lower. Still, f_0 is determined to within a part per million. Fig. 31 shows how even two completely overlapping peaks can be resolved. It should also be remarked that the elastic constants determined from the resonance data are usually not all that sensitive to how the center frequencies are determined; RUS is robust enough so that if one simply guesses by eye where the center frequency of each peak is, the elastic constant results will not usually differ significantly from those corresponding to the frequencies determined by precise curvefitting. Nevertheless, in the interests of thoroughness, the curvefitting procedure is used in most

FIG. 30. Same as Fig. 29, for a somewhat higher, noiser mode.
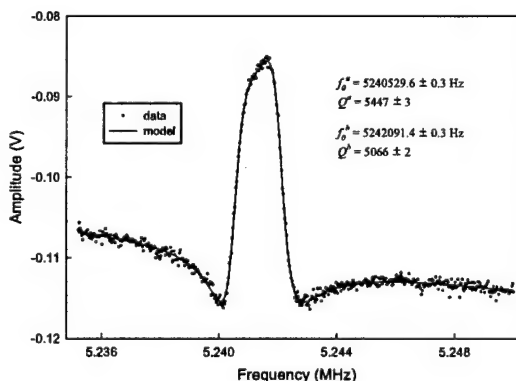
FIG. 31. Same as Fig. 29, for two overlapping peaks.

45

instances.

2. *Elastic constants of single-crystal silicon from the resonance spectrum*

The center frequencies of all the resonance peaks in the spectrum of Fig. 27 are used to determine the room-temperature elastic constants of single-crystal cubic silicon. Here again, the Levenberg-Marquardt method is used to find the optimum elastic constants that will minimize the sum of the squared errors, given some initial guesses. In this case, since silicon is a well-characterized material, the initial guesses may simply be values from the literature. However, one might also want to try other initial guesses to see how they affect the result, *e.g.*, to test how far off one can be in one's initial guess and still wind up in the global minimum, with the correct elastic constants.

Table XII shows the results of a Levenberg-Marquardt least-squares fit of the Si frequency data, using the average of the c_{ij} given in the Landolt-Börnstein tables [5] as starting values. The agreement between experiment and theory is impressive; the average deviation is only 0.04%. The elastic constants (and edge lengths) corresponding to this fit are given in Table XIV; they are in very good agreement with the literature values, with the largest deviation being only 0.15%.

a. Error bars by Monte Carlo simulation The standard errors given in Table XIV merit some discussion. Exactly how to assign uncertainties to quantities determined by least-squares minimization is not always clear. Some common formulas assume that the errors are normally distributed, which may not always be valid. Migliori [45] has chosen an empirical approach, based on years of experience with RUS measurements. In this approach, the curvature of the error surface (the error being the sum of the squares of the frequency residuals) is examined in the vicinity of the minumum, and a perturbation of a free parameter sufficient to increase the error by 2% is taken to be the confidence interval. The idea is that "a change in this error of 2% is larger than all reproducibility and other error sources occurring in the measurement." [45] In other words, the corresponding change in the free parameter should be experimentally detectable.

In this work, a somewhat different approach has been chosen: error bars are generated by analyzing synthetic data sets generated by introducing a random scatter with a variance determined by the frequency residuals, and the width of the corresponding scatter in the determined free parameters is taken to be the confidence interval. The idea is to see how random errors in the frequency data propagate through to the final results. The scheme for randomizing the frequencies is to assume that if there is a discrepancy between a calculated frequency and an observed one, the "true" frequency is probably somewhere

TABLE XII. The observed and calculated frequencies, in MHz, for the 1 mg cubic silicon sample.

	Mode	f_{obs}	f_{calc}	Δf	$|\% \text{ error}|$
1	EV-1	2.84189	2.84029	0.00159	0.056
2	EX-1	3.05334	3.05314	0.00020	0.006
3	EY-1	3.14475	3.14480	−0.00005	0.002
4	OD-1	3.81788	3.82030	−0.00242	0.063
5	EV-2	4.32065	4.31954	0.00111	0.026
6	OX-1	4.44465	4.44729	−0.00264	0.059
7	OD-2	4.53877	4.53941	−0.00063	0.014
8	OY-1	4.57567	4.57670	−0.00132	0.029
9	EZ-1	4.62087	4.62251	−0.00164	0.035
10	EX-2	4.69970	4.69880	0.00090	0.019
11	OZ-1	4.73698	4.73425	0.00272	0.058
12	OD-3	——	4.95494	——	—
13	EY-2	5.24055	5.24140	−0.00085	0.016
14	OY-2	5.24211	5.24285	−0.00074	0.014
15	OZ-2	5.45274	5.45630	−0.00356	0.065
16	OD-4	5.54635	5.54410	0.00225	0.041
17	OX-2	5.55925	5.55995	−0.00070	0.013
18	OZ-3	5.60008	5.59863	0.00145	0.026
19	EZ-2	5.64963	5.65000	−0.00037	0.007
20	EZ-3	5.73738	5.73829	−0.00090	0.016
21	OD-5	5.81184	5.80926	0.00258	0.044
22	EX-3	6.13987	6.13743	0.00244	0.040
23	EY-3	6.16313	6.15971	0.00342	0.056
24	EZ-4	6.28983	6.29106	−0.00123	0.020
25	EZ-5	6.47913	6.47586	0.00327	0.050
26	EV-3	6.64701	6.64955	−0.00254	0.038
27	OX-3	6.69616	6.69598	0.00019	0.003
28	EY-4	6.70767	6.71098	−0.00331	0.049
29	OY-3	6.74415	6.74355	0.00060	0.009
30	EX-4	——	6.88899	——	—
31	OD-6	7.11800	7.12043	−0.00243	0.034
32	OY-4	7.15950	7.15654	0.00296	0.041
				Avg.	0.04%

TABLE XIII. The derivatives of frequency with respect to elastic constants and edge lengths, for the 1 mg cubic silicon sample, in units of MHz/Mbar.

Mode	f_{calc}	$\frac{\partial f_n}{\partial c_{11}}$	$\frac{\partial f_n}{\partial c_{12}}$	$\frac{\partial f_n}{\partial c_{44}}$	$\frac{\partial f_n}{\partial L_1}$	$\frac{\partial f_n}{\partial L_2}$
1 EV-1	2.8387	0.02	-0.02	1.76	1.40	2.80
2 EX-1	3.0525	1.20	-1.04	0.26	1.97	4.01
3 EY-1	3.1440	1.23	-1.05	0.26	3.68	2.29
4 OD-1	3.8194	1.82	-1.72	0.00	2.28	2.72
5 EV-2	4.3169	0.15	-0.14	2.52	0.12	-1.27
6 OX-1	4.4450	0.35	-0.31	2.30	0.31	3.28
7 OD-2	4.5381	2.16	-2.12	0.05	-0.40	1.35
8 OY-1	4.5747	0.61	-0.56	2.06	2.67	1.02
9 EZ-1	4.6212	2.02	-1.94	0.25	-2.01	1.34
10 EX-2	4.6980	1.59	-1.08	0.51	-4.55	5.46
11 OZ-1	4.7323	0.97	-0.85	1.63	0.22	2.21
12 OD-3	4.9535	2.42	-2.40	0.00	-0.43	0.50
13 EY-2	5.2400	1.82	-1.30	0.56	5.17	-5.09
14 OY-2	5.2412	1.34	-1.02	1.33	-1.61	3.58
15 OZ-2	5.4532	0.13	-0.01	3.18	0.13	0.40
16 OD-4	5.5432	2.07	-1.31	0.22	1.57	-1.05
17 OX-2	5.5580	1.80	-1.52	0.96	3.82	-2.69
18 OZ-3	5.5955	0.29	-0.26	3.13	4.55	2.38
19 EZ-2	5.6487	2.09	-1.53	0.41	1.66	-1.71
20 EZ-3	5.7365	2.45	-2.40	0.43	2.15	2.28
21 OD-5	5.8083	2.43	-1.80	0.04	0.91	-0.47
22 EX-3	6.1351	1.73	-1.55	1.49	1.11	1.22
23 EY-3	6.1574	1.93	-1.78	1.27	1.24	0.73
24 EZ-4	6.2894	2.46	-2.13	0.54	3.14	2.38
25 EZ-5	6.4742	2.12	-1.56	0.91	2.22	1.06
26 EV-3	6.6464	0.57	-0.27	3.20	1.93	2.33
27 OX-3	6.6934	1.87	-1.73	1.70	1.94	3.21
28 EY-4	6.7081	0.98	-0.69	2.72	0.95	3.97
29 OY-3	6.7407	1.61	-1.49	2.09	2.25	1.78
30 EX-4	6.8857	0.85	-0.61	3.05	4.50	1.17
31 OD-6	7.1209	1.98	0.16	0.21	1.79	-0.27
32 OY-4	7.1539	1.38	-0.98	2.41	2.52	4.33

TABLE XIV. Fitted parameters for the 1 mg cubic silicon sample (note that Mbar = 10^{12} dyne/cm^2).

Elastic constants (Mbar)			Dimensions (mm)		
Author	Accepted[1]	Δ (%)	Fitted	Measured	Δ (%)
C_{11} 1.6568±0.001	1.6564	0.02	L_1 0.6394	0.638±0.005	0.2
C_{12} 0.6385±0.001	0.6394	-0.14	L_2 0.6928	0.687±0.005	0.8
C_{44} 0.7963±0.0002	0.7951	0.15	L_3 0.9335	0.931±0.005	0.3

[1]From [6].
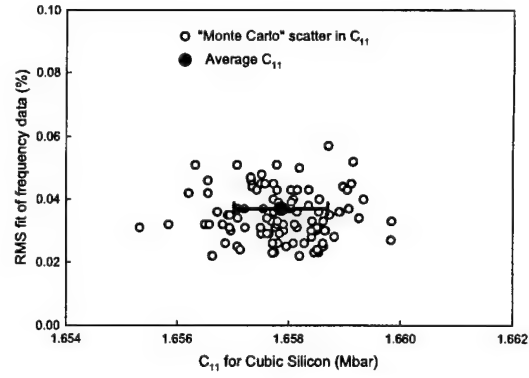
FIG. 32. The uncertainty in measuring c_{11} of cubic Si, by use of Monte Carlo simulations. The circles all represent different values of c_{11} converged upon for various random perturbations of the frequency data; the error bar represents the center and width (standard deviation) of the distribution.

between the two (assuming that the current solution is at or near the minumum of the correct "error well"). There is some probability, of course, that the "true" frequency is somewhere else. Synthetic data sets are then generated by perturbing each measured frequency with a random number from a Gaussian distribution about the median between the measured and calculated frequency, with a width (standard deviation) equal to half the frequency residual $|f_{obs} - f_{calc}|$. The frequency residual is taken to represent in some way the total uncertainty in each frequency (due to random errors).

Each synthetic data set is subsequently analyzed in the same manner as the original data, and the 68% confidence limit on the resulting scatter in each determined parameter is taken to be the standard deviation of that parameter. Figure 32 shows the results of this process for c_{11}.

b. Systematic errors Systematic errors in any measurements are difficult to account for, and so the best approach is to minimize them. In this respect, RUS is a very "clean" measurement, having few if any sizeable bias errors. Some have already been discussed, such as the contact force of the transducers. Sample preparation errors are discussed in detail in Section VI, and are found to be negligible in most cases. The most important source of bias in a RUS measurement is, in fact, not associated with the measurement of the frequencies but in the determination of dimensions and mass. An incorrect measurement of mass or dimensions will sytematically shift all or some of the calculated frequencies artificially, likewise affecting the fit. For small samples, this can be the limiting factor in the overall accuracy.

In the present case of the cubic Si sample, no especially accurate method for measuring the dimensions was at hand; some difficulties were encountered using a micrometer, so a microscope with 100× magnification was used, with a scale posessing divisions of 72 to the millimeter. The sample was found to measure 67.0 × 49.5 × 45.9

47

units^3, which translates to $0.931 \times 0.687 \times 0.638$ mm^3. The uncertainty in each dimension is about 5μm, which leads to an uncertainty of over 2% in the volume. The mass was measured on a Sartorius Supermicro microbalance accurate to at least a thousandth of a milligram, and was found to be 0.9631 mg. The density determined by dividing the measured mass by the volume based on the measured dimensions is 2.356 g/cc; the accepted "book value" [4] for cubic Si is 2.329 g/cc. The error between the two densities is about 1%, and could therefore be due to inaccuracy in measuring the dimensions.

For a completely new material for which only very small samples are available, this could be a serious impediment to measuring elastic constants to an absolute accuracy better than 1%. In the present case, since the sample quality appears to be excellent, the density of Si is well established, and the mass has been measured to great accuracy, there is a way out. If one assumes that the sample has the "book density" of 2.329 g/cc, then the mass can be used to determine the correct volume, which will then be held constant. The correct aspect ratios of the sides may be obtained by including them as free parameters in the fit, using the measured values as the starting guesses. It is this procedure that leads to the dimensions in Table XIV. Because the measurement no longer depends on the measured dimensions (except as seed values that must not be strayed from more than a few tenths of a percent), the absolute accuracy of this measurement is that of the mass, or about 0.1%.

Since the temperature was not controlled, the density could have been slightly different than the book value (although probably by less than 0.1%), which could also lead to systematic error; the measurement was also made in air, which can acoustically couple to the vibrating sample surfaces and shift the resonances; in addition, moisture could have condensed on the sample surface. These problems are fairly easily dealt with, however, by putting the cell in a can, pumping it out, and placing the can in a temperature-controlled bath.

H. Conclusion

It has been demonstrated that in a single fairly straightforward measurement, one may measure the elastic constants of an anisotropic crystal such as cubic Si to high relative accuracy, using a sample less than 1 mg; the absolute accuracy is limited only by one's ability to measure the dimensions, mass, and/or density of the sample. The present results on Si are in close agreement with the accepted values; so it may be concluded that the specific techniques used in this work are reliable.

Even without doing the measurement in a vacuum or with precise temperature control, the RMS error for the measurement (the average of the residual frequency errors) was only 0.04%, which may be the state-of-the-art for small samples. Certainly this experimen-

tal/theoretical agreement in the frequencies is much better than that seen in early RUS investigations such as those by Demarest [42] and Ohno [43] using much bigger samples, and is on par with that achieved by Migliori and colleagues for an isotropic precision 5/16-inch ball-bearing (0.02%) [45]. Thus, while there may be some legitimate concern that a film transducer might not provide as good point contact as a conventional piezoceramic, the overall perturbative effect of the film transducers in a carefully done experiment may be less than that of the conventional transducers.

IV. INVESTIGATION OF CERAMIC PROPPANTS

A. Introduction

The measurements detailed in this section are, in some sense, in sharp contrast to the previous measurement detailed in Section III (calibration using single-crystal silicon). That experiment sought to establish the efficacy of RUS and PVDF film transducers by a single measurement of high precision and accuracy on one very high-quality sample. The work in this section concerns measurements where only limited accuracy and precision are needed, on a fairly large number of samples with variable quality. In this case, it is not the precision of RUS that is desired but rather the ability to do many rapid elastic-constant measurements on samples without parallel sides.

In the 1970's, oil companies began to develop materials that could be used to prop open cracks in bedrock surrounding natural gas deposits, as hydraulic fracturing of deep wells became commonplace as a means of increasing well productivity [57]. These materials became known as "proppants," and included several varieties of small, spherical ceramic particles that could easily flow over each other, in the nature of the hypothetical water atoms of Democritus.

Ironically, these same proppants became the focus of a new solar energy technology, a solar receiver that used a *solid* thermal transfer medium [58], [59]. To better understand the use of proppants in solar receivers, Dr. John R. Hellmann of the Pennsylvania State University began a thorough study of all their relevant physical characteristics. He found that he could measure most or all of them by conventional means, with the notable exception of the elastic constants. Measuring the elastic constants of a single ceramic bead a few hundred microns in diameter is indeed a daunting task with traditional methods such as ultrasonic pulse-superposition; but it turns out to be ideal for RUS, since in RUS normal modes of vibration are analyzed, not overlapping echoes. This created a perfect opportunity to showcase RUS in a novel application as part of a collaboration between Dr. Hellmann and Dr. J. D. Maynard (the author's advisor). One impor-

tant feature of this measurement is that the samples were not prepared for RUS, and therefore were not necessarily ideal samples individually; but because the samples are produced in such mass quantities, there is no shortage of samples with which to check the repeatability of one's results. This makes the present measurement somewhat similar to the measurements on spherical moon "rocks" done by Anderson *et al.* in the late 1960's [71].

c. *Zirprop*™ One of Dr. Hellmann's projects was to characterize proppants as a function of heat treatment temperature, in an attempt to simulate the thermal stresses the proppants might encounter as they are cycled through a solar receiver. Our laboratory was given the task of measuring the elastic constants and the ultrasonic attenuation of a fused-zircon proppant manufactured by Quartz Products Corporation under the brand name Zirprop™ [60], as a function of heat treatment temperatures from 900°C to 1400°C. These proppants are formed by fusing a powder composed mainly of zircon ($ZrSiO_4$), with minor amounts of aluminum and titanium, in the form of α-Al_2O_3 and rutile (TiO_2) [59] as it falls through an electric arc, thereby forming nearly spherical "droplets" of ceramic. The composition of the fused particles is mainly monoclinic zirconia (ZrO_2) in a matrix of amorphous silica (SiO_2) [59]. Their external morphology is shown in Fig. 33. As one can see, many of the particles appear nearly spherical; this allows an analytic solution for the normal mode frequencies. An analytic solution is not necessary, but its use does add a bit of historic flair to the experiment, as will be discussed shortly.

B. RUS for spheres

Although most of the work in this paper concerns rectangular parallelepiped samples, most other analytic shapes, and particularly spheres, are appropriate for use with RUS. As discussed in Section I, much of the earliest work that laid the foundation for RUS was in geoscience; because of their interest in the Earth and its oscillations (associated with earthquakes, for instance), geoscientists have devoted considerable attention to the problem of the normal modes of elastic spheres and ellipsoids (see, for instance, [61], [62], [63]).

1. Solution to the normal-mode problem

An analytic solution for the normal modes of free vibration of a homogeneous, elastically isotropic sphere was first solved in the late nineteenth century, by Horace Lamb and others [64], [65], [66]; this work was reviewed by Love in his *Treatise on the Mathematical Theory of Elasticity* [67]. The solution takes the form of a complicated transcendental equation, so without modern computers, Lamb and his colleagues could make only limited
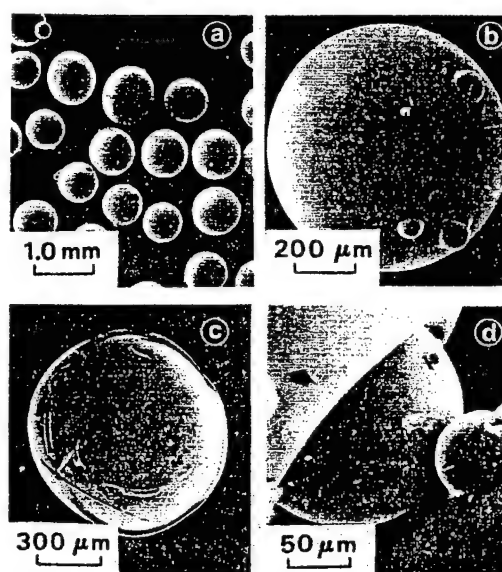
FIG. 33. Characteristics of Quartz Products Corporation Zirprop™ Z126 proppant particles (from [59]). Pictures show (a) the general particle morphology, (b) a closeup showing secondary particles, and (c) a closeup showing "stringers". Picture (d) is intended to show a fine surface dimpling due to dendritic growth of zirconia crystallites, but this is barely visible in the present reproduction.

use of it. It was only in the early 1960's that Sato and Usami [68] solved the problem on a computer and used the result as a first approximation to understanding the oscillations of the heterogeneous, spheroidal Earth. As mentioned in Section I, this work caught the attention of researchers working on systems of much smaller dimension; the ability to precisely calculate the normal mode frequencies of a finite elastic object created the possibility of using these modes to experimentally determine elastic properties, using samples which could in principle be much smaller than those typically needed for accurate pulse-echo work.

The elastically isotropic sphere is perhaps the only finite elastic body for which a general analytic solution can be obtained for the normal modes of vibration; in the 60's when computers were still comparatively slow and the variational approach was not well worked out, the analytic solution was of great value. Fraser and Lecraw [69] used this analytic solution to compare measured and predicted normal-mode frequencies of small garnet spheres, and used these comparisons to obtain the Lamé constants, performing what could be considered the earliest RUS measurement.

Sato and Usami took the results of Lamb for the natural oscillations, and expressed them in a computationally convenient form. There are two distinct transcendental equations, corresponding to two broad classes of normal modes: those that are pure shear, with no compression or extension (torsional oscillations) and those that do in-

volve compression and extension, such as bending modes and radial modes ("spheroidal" oscillations). The characteristic equation for the torsional oscillations is

$$(n-1)J_{n+1/2}(\eta) - \eta J_{n+3/2}(\eta) = 0, \qquad (53)$$

and that for the spheroidal oscillations is

$$\frac{2\xi}{\eta}\left[\frac{1}{\eta} + \frac{(n-1)(n+2)}{\eta^2}\left(\frac{J_{n+3/2}(\eta)}{J_{n+1/2}(\eta)} - \frac{n+1}{\eta}\right)\right]$$

$$J_{n+3/2}(\xi) + \left[-\frac{1}{2} + \frac{(n-1)(2n+1)}{\eta^2} + \right.$$

$$\left. \frac{1}{\eta}\left(1 - \frac{2n(n-1)(n+2)}{\eta^2}\right)\frac{J_{n+3/2}(\eta)}{J_{n+1/2}(\eta)}\right]J_{n+1/2}(\xi) = 0, \qquad (54)$$

where

$$\eta = \frac{\omega a}{v_s} \quad \text{and} \quad \xi = \frac{\omega a}{v_p}; \qquad (55)$$

the frequency of oscillation is $f = \omega/2\pi$, a is the radius of the sphere, v_s is the speed of shear waves, v_p is the speed of dilatational (pressure) waves, and $J_{n+1/2}$ etc. are half-order Bessel functions. Both equations are given in [68]. The wave speeds can of course be expressed in terms of elastic constants; assuming elastic isotropy,

$$v_s = \sqrt{\frac{\mu}{\rho}} \quad \text{and}$$

$$v_p = \sqrt{\frac{\lambda + 2\mu}{\rho}}, \qquad (56)$$

where ρ is the density and λ, μ are the familiar Lamé constants.

Fraser and Lecraw gave the torsional and spheroidal modes the labels $T_{n,m}$ and $S_{n,m}$ respectively, where n is the mode index (from (53) and (54)), and m is the overtone index, for indexing each member of the series of solutions corresponding to a given n. Different values of n correspond to different mode types; for instance, solutions of (53) with $n = 1$ correspond to what Love called "rotatory vibrations" [67], that is, every spherical surface defined by constant r moves as a unit through some small angle about the same axis through the center of the sphere. There is no $T_{1,0}$ mode, since this corresponds to pure rotation.

2. Finding elastic constants by global minimization

It would be possible to use this solution as part of an iterative minimization scheme, improving upon initial guesses for λ and μ, according to the methods discussed

in Sections II and III. However, because of the small number of parameters involved, it is possible to do a global search through parameter space, thereby avoiding any possiblility of falling into a local minimum. In fact, by defining ξ above in terms of η, the minimization problem may be made essentially one-dimensional, making the global search very efficient.

From Eq. (55) and Eq. (56), we have

$$\xi = \eta\left(\frac{v_s}{v_p}\right) = \eta\sqrt{\frac{\mu}{\lambda + 2\mu}};$$

noting that Poisson's ratio is $\nu = \lambda/2(\lambda + \mu)$, one may obtain

$$\xi = \eta\sqrt{\frac{1-2\nu}{2-2\nu}}. \qquad (57)$$

Thus, one may plot the solutions η to (53) and (54) as a function of Poisson's ratio ν, to obtain on a single graph the non-dimensional solution space to the free vibration problem. One need only solve (53) and (54) for various values of ν.

No doubt the reader has her or his favorite method of solving transcendental equations; one "quick and dirty" approach that will work for the present case is to solve the equations for some special case, say, $\nu = 0$, by brute force search or whatever, and use these values as starting values in Newton's method [70] for the next increment of ν; recall that in Newton's method, if x_0 is an initial guess for a zero of a function, then an improved guess x_1 is $x_1 = x_0 - f(x_0)/f'(x_0)$. Since we expect the solutions to behave smoothly, Newton's method should converge very quickly to the correct roots. Then, these roots are used for the next iteration, and so on. Newton's method is, of course, very treacherous when the behavior of the functions is not known, especially if the inital guesses are not very good. However, here we can guarantee that the initial guesses are superb, and the functions are smooth, so convergence is virtually assured. One may also confirm the results by comparing with previously published graphs [69].

A Mathematica program to calculate the $S_{0,1}$ spheroidal breathing mode using Newton's method, and write the results to a file, is as follows:

```
spheq =
  BesselJ[1/2 + n, (eta*(1 - 2*nu)^(1/2))/
     (2 - 2*nu)^(1/2)]*
     (-1/2 + ((-1 + n)*(1 + 2*n))/eta^2 +
     ((1 - (2*(-1 + n)*n*(2 + n))/eta^2)*
     BesselJ[3/2 + n, eta])/
     (eta*BesselJ[1/2 + n, eta])) +
  (2*(1 - 2*nu)^(1/2)*(eta^(-1) +
     ((-1 + n)*(2 + n)*(-((1 + n)/eta) +
     BesselJ[3/2 + n, eta]/
     BesselJ[1/2 + n, eta]))/eta^2)*
  BesselJ[3/2 + n, (eta*(1 - 2*nu)^(1/2))/
     (2 - 2*nu)^(1/2)])/
```

```
(2 - 2*nu)^(1/2);

dspheq = D[spheq, eta];

(* initialize for S_0,1 *)
n = 0
root = 2.94379 (* the solution at nu = 0 *)

 Do[loopeq = spheq/. nu->0.001i;
  dloopeq = dspheq/. nu->0.001i;
  While[(Abs[loopeq/.eta->root])>10^-7,
   root = root-(loopeq/.eta->root)/
   (dloopeq/.eta->root)];
  Write["sph01.dat", OutputForm[i],
  OutputForm[","], OutputForm[0.001i],
   OutputForm[","], OutputForm[root]],
   {i, 0., 450., 1.}]
```

Here nu refers to Poisson's ratio ν. The particular mode and overtone (n and m in $S_{n,m}$) that is calculated is controlled by one's choice of n and the starting root. Obviously, the precision can be controlled by changing the loop constants; here the solution is calculated for values of Poisson's ratio between 0 and 0.45 in increments of 0.001; this turns out to be sufficient for the present work.

3. An example

An example is presented, in which the normal mode frequencies of a Zirprop bead in the "as-received" condition (no heat treatment) are used to determine the elastic constants of that bead. The bead is chosen from a collection of several hundred, for its spherical shape, and absence of "stringers". Several small secondary particles were observed on this sample, on the order of 10 μm. It has a density $\rho = 3.21$ g/cc, determined by helium pycnometry [59]; the diameter is $d = 882 \pm 10$ μm, from inspection under a microscope.

a. *The naming of proppants* In order to adequately characterize the proppants at all the different heat treatments considered in this study, it is necessary to measure over 40 different samples. Therefore, a systematic scheme for naming the samples is desireable. Each proppant shall be given a label of the type: Z$xxyy$, where xx refers to the heat treatment and yy is a number that identifies the sample. The sample to be considered in this section is in the "as-recieved" condition (AR); it happens to be the third AR sample measured, so it is given the label "ZAR03" (Zirprop As-Received # 3). The proppants subjected to various heat treatments are given similar labels: sample # 2 from the 900°C batch would be labeled "Z0902", sample # 10 from the 1100°C batch would be labeled "Z1110", and so on.

b. *A measurement* The normal mode frequencies of ZAR03 are determined in the manner described in Section III, placing the bead between two transducers, driving with one while sweeping frequency, and picking up resonances with the second; there are, however, some complications, which will be discussed shortly. These frequencies are then converted to nondimensional frequencies, and are compared with those calculated for an ideal sphere to see which value of ν gives the best fit. Once ν is known, the elastic constants can be found. The "best fit" may be specified as that which minimizes the sum of the errors squared; if we let the non-dimensional frequencies corresponding to the observed frequencies f_m be denoted as ζ_m, while those calculated for the ideal sphere are η_m, then the sum of the squared errors is:

$$\Sigma(\Delta\eta)^2 = \sum_{i=1}^{N}(\zeta_i - \eta_i)^2 \; ; \tag{58}$$

the optimum value of ν is that which minimizes this quantity.

The first step, converting the f_m to ζ_m, may be accomplished by identifying any of the torsional modes, since they depend only on μ and hence do not change with Poisson's ratio. In all the experience of this laboratory, it appears that seldom or never is the first torsional mode not observed if any modes are observed; and the first torsional mode, not suprisingly, always has the lowest frequency of any mode of an isotropic sphere. Thus we at least begin with the assumption that the lowest mode observed corresponds to $T_{0,2}$, the lowest theoretical mode. We may then convert all the f_m to ζ_m with the simple formula:

$$\zeta_m = f_m \left(\frac{T_{2,0}}{f_1}\right) = f_m \left(\frac{2.50113}{f_1}\right) \; . \tag{59}$$

When the optimum ν has been found, one may find the elastic constants; first, recall that $\eta \equiv 2\pi f a/v_s$, where v_s is the speed of shear waves, and a is the radius of the sphere. Then

$$v_s = \frac{2\pi a f_1}{T_{2,0}} = \frac{\pi d f_1}{2.50113} \; , \tag{60}$$

where d is the diameter and 2.50113 is the theoretical value for $T_{2,0}$. Then, since $v_s = \sqrt{\mu/\rho}$,

$$\mu = \rho v_s^2 \; . \tag{61}$$

The other elastic constants can be obtained using the value found for ν:

$$\lambda = \frac{2\nu\mu}{1 - 2\nu} \tag{62}$$

and

$$E = \frac{\mu(3\lambda + 2\mu)}{\lambda + \mu}, \tag{63}$$

where E is Young's modulus. When f is given in MHz, ρ in g/cc, and d in cm, the resulting elastic constants are

TABLE XV. The observed and calculated frequencies of the Zirprop particle ZAR03 ($d = 0.0882$ cm, $\rho = 3.21$ g/cc).

Mode	f_{obs}	ζ	η	$\zeta - \eta$	% error
$T_{2,0}$	3.2570	2.5027	2.5011	0.0016	0.06
$S_{2,0}$	3.4290	2.6349	2.6367	-0.0018	-0.07
$S_{1,1}$	4.3960	3.3779	3.3732	0.0047	0.14
$T_{3,0}$	5.0360	3.8697	3.8674	0.0023	0.06
$S_{3,0}$	5.0960	3.9158	3.9057	0.0101	0.25
$S_{0,1}$	5.4990	4.2254	4.2314	-0.0059	-0.14
$S_{2,1}$	6.2500	4.8025	4.7972	0.0053	0.11
$S_{4,0}$	6.4910	4.9877	4.9910	-0.0033	-0.07
$T_{4,0}$	6.6180	5.0853	5.0946	-0.0093	-0.18

TABLE XVI. The physical properties of the Zirprop particle ZAR03, determined from the fit in Table XV.

Properties of ZAR03 $d = 0.0882$ cm, $\rho = 3.21$ g/cc		
ν	0.226	
v_s	3607	m/s
μ	41.8	GPa
λ	34.5	GPa
E	102.4	GPa

in units of 10^{12} dyne/cm^2, or Mbar; Mbar may converted to the popular engineering units of GPa by multiplying Mbar by 100.

In order to get the best fit possible to the data, it is of course not ideal to assume that $\zeta_1 \equiv 2.50113$. There is likely to be a small error in measuring the lowest mode, as in every other mode. One may readily account for this by introducing a parameter γ, such that $\zeta \to \gamma\zeta$. Then, the optimum γ for any given value of ν can be found by calculating the ζ_i in a first iteration using Eq.(59), and assuming:

$$\frac{\partial}{\partial \gamma} \sum_i^N [\gamma\zeta_i - \eta_i]^2 = 0,$$

which in turn leads to

$$\gamma = \frac{\sum_i^N \eta_i \zeta_i}{\sum_i^N \zeta_i^2}. \tag{64}$$

Thus γ represents the optimum scale factor that produces the best fit (without changing the relative spacings of any of the observed frequencies). Typically, γ is found to be very close to 1 (for instance, in the measurement described below, $\gamma = 1.00064$ for the optimum ν).

Nine modes of the Zirprop particle ZAR03 were measured, and are given in Table XV, along with the corresponding ζ, η, and errors; the physical properties determined from this fit are summarized in Table XVI. Fig. 34 shows the lowest 10 nondimensional frequencies η of a homogeneous, elastically isotropic sphere, versus Poisson's ratio ν. The non-dimensional frequencies of ZAR03 are also plotted on this graph, at the point where $\Sigma(\Delta\eta)^2$ from (58) is minimized. The reader should be able to satisfy his or herself by looking at Fig. 34 that only in the vicinity of $0.20 \geq \nu \leq 0.25$ is a sensible mode assignment even possible, and the best fit is near 0.23. Numerically, the optimum choice for ν is found to be

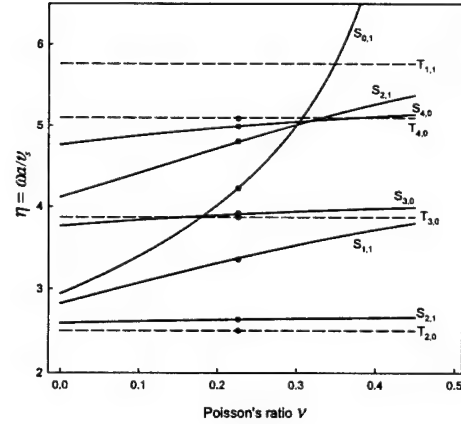FIG. 34. The nondimensional frequencies $\eta \equiv \omega a/v_s$ of a homogeneous, elastically isotropic sphere as a function of Poisson's ratio ν. The solid lines represent spheroidal modes, while the dotted lines represent torsional modes, which depend only on the shear modulus μ; hence they have no dependence on ν. The solid dots are the observed nondimensional frequencies of the Zirprop particle ZAR03.
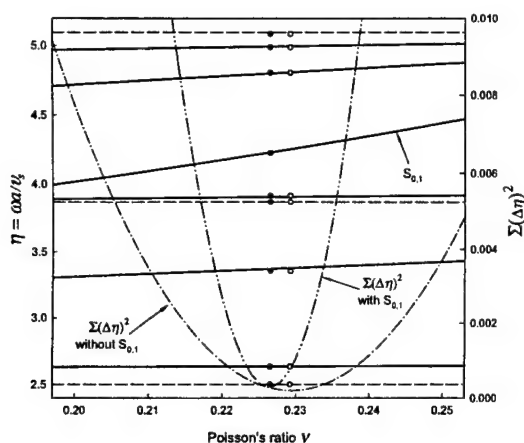
52

FIG. 35. The "error wells" for the determination of ν from the ZAR03 data. The solid dots are the data aligned with the center of the well that results from using all the modes; the open circles are the same data excluding the sharply-varing $S_{0,1}$ "breathing" mode, positioned over the center of the much broader well which results from fitting the data without this mode.

0.226; this corresponds to a true global minimum in the error. It is evident from Fig. 34 that the small number of modes measured is more than sufficient to determine ν, and hence the elastic constants (using the sample's mass and radius, and the method given on the previous pages).

c. *The effect of missed modes* The present case offers an opportunity to examine some of the issues raised in Sections II and III, for instance, the consequences of missing a mode during a RUS measurement. It is not enough to measure a certain number of modes, but they must be identified correctly, and for each elastic constant there must be at least one frequency, preferably several, with strong dependence on it. One might give special attention to modes of dilatation, since they depend strongly on the important bulk modulus. The primary mode of this type in the present case, the sphere "breathing mode" $S_{0,1}$, has the strongest dependence of any mode on Poisson's ratio. Missing it will result in a more ambiguous measurement. Fig. 35 shows how much broader the "error well" becomes when $S_{0,1}$ is excluded from the fit of the ZAR03 data. Unfortunately, in practice, it is found that $S_{0,1}$ does not produce a strong signal in the PVDF transducers, and is somewhat hard to detect. This is one piece of evidence which indicates that the PVDF transducers described in Section III act more like shear devices than pressure devices. One may recall from the last section that in the Si measurement, one of two missed modes was of the "OD" classification, a dilatational mode. Missed modes when measuring rectangular parallelepipeds can often be corrected by remounting the sample, as the corner will meet the transducer at a slightly different angle. With spheres, remounting has very little effect.

Furthermore, as will be discussed shortly, the present proppant samples have a high degree of internal friction,

which is especially high for certain heat treatments. This makes some modes impossible to see in some samples, and leads to a fair amount of mode overlap at higher frequencies. Thus the amount of data one can collect on any one sample is limited; this provides further justification for using a global "brute force" search to find the optimum elastic constants for each sample. Further, many samples are studied to establish repeatability and to obtain confidence intervals for the elastic constants (a luxury not usually available in a RUS measurement!).

One may notice that the errors in the fit, shown in Table XV, are larger than those observed in the Si measurement from Section III, but still quite small. The increase in the fit errors may be partially attributed to asphericity and possibile anisotropy, and other imperfections, in the proppant. These issues are examined in the next section.

4. Effects of imperfections in the samples

The actual proppant particles, as evidenced by Fig. 33, are not perfect spheres; the most spherical ones may be chosen for study, but they will probably still have some degree of eccentricity. Furthermore, the proppants may have some small degree of anisotropy and/or inhomogeneity, which cannot be detected by visual inspection. The result is that the degenerate modes of the sphere split into several different modes. Calculations of the lowest modes of a sphere show that mode $T_{2,0}$ is fivefold degenerate, while $S_{1,1}$ is threefold degenerate. The breathing mode $S_{0,1}$ is, of course, nondegenerate (a fact that may be of help in mode identification!). Thus when detecting mode $T_{2,0}$ we might expect to see as many as five different peaks.

A further complication is that the proppants themselves are not particularly high-Q resonators. As described in [59], "Analysis of polished sections revealed the presence of a severely microcracked crystalline phase which appears to be continuously distributed within a glassy matrix ... Microcracking in zirconia based ceramics is a commonly observed phenomenon and may contribute to enhanced thermal shock damage resistance and fracture toughness." The presence of a network of fine cracks would be expected to contribute greatly to internal friction during oscillations, and indeed the line shapes of the resonances are rather broad. Thus, the nearly degenerate modes all overlap, making it somewhat difficult to resolve them by casual inspection. However, the curve-fitting methods discussed in Section III may be used to successfully separate the peaks into a sum of phase-shifted Lorentzians.

This broadness in the resonance peaks has another consequence—the peaks may be broad enough so that the frequency dependence of the crosstalk is apparent in a given data record. The proppants are so small (only a few hundred microns) that the transducers wind up being very close together, so the crosstalk is rather strong.
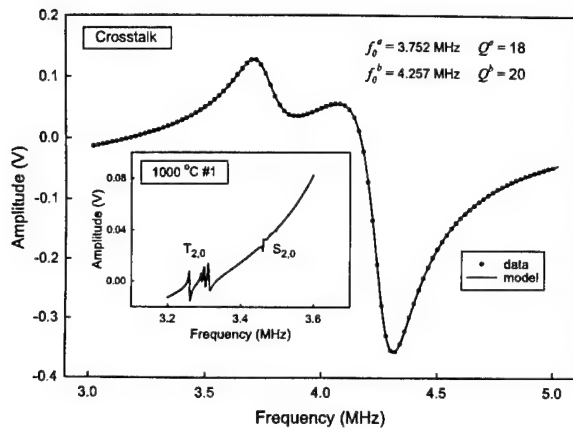
FIG. 36. The crosstalk between two PVDF RUS transducers, at the separation distance appropriate for measuring proppants. No sample was mounted for this measurement. The inset graph shows the same frequency range as the beginning of the crosstalk plot, when a proppant is in the cell.

Fortunately, the variations in the crosstalk are still much broader than the sample resonances, so there is no danger of confusing one for the other.

An interesting aspect of the crosstalk features is that they too may be modeled as phase-shifted Lorentzians. It is suspected that these may represent mechanical resonances in the transducers; were this the case, the crosstalk features might be useful as a means of gauging transducer tension. However, this has not been investigated.

Fig. 36 shows the crosstalk in the frequency range of the proppant measurements; the inset graph shows peaks superimposed on the crosstalk, including the $T_{2,0}$ mode from one of the samples treated at 1000°C (Z1001). The following graph, Fig. 37, shows a closeup of this mode; indeed it appears to be split into at least four, possibly five modes.

The question arises: can one usefully ascribe a single frequency to this clump of peaks, so that the ideal sphere analysis may be used? The answer is aided by the fact that there are many samples over which to average the results, and it turns out that the variations from sample to sample drown out any effects of mode splitting. Still, the question remains, *how* should one assign the frequency? Should one use a weighted average of all the observed peaks, or should one place the frequency at the halfway point between the highest and lowest peaks in the clump, or something else?

In his naïvete, the author decided to assume the frequency should be "around the middle" of each clump, when making the proppant measurements. With the aid of Visscher's xyz method [103], as described in Sections III and VI, we may observe the splitting of sphere modes as a result of a spheroidal perturbation, to see if this assumption was justified. Fig. 38 shows the center frequen-
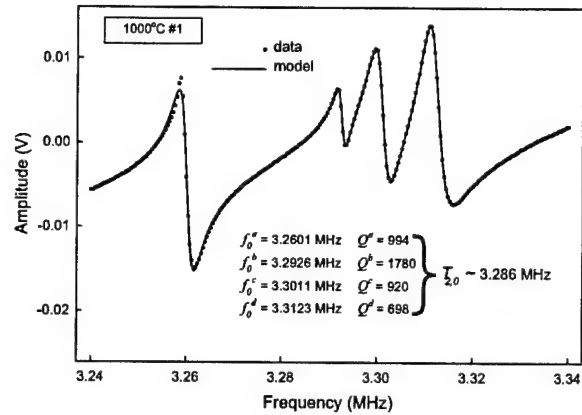
FIG. 37. The lowest mode of Z1001, the first sample studied from the 1000°C heat-treatment batch. It is split into at least four modes; the agreement between the measured data and the predicted curve may be off on the first peak due to the presence of a fifth, very narrow peak, which is too narrow to be modeled at the present resolution.
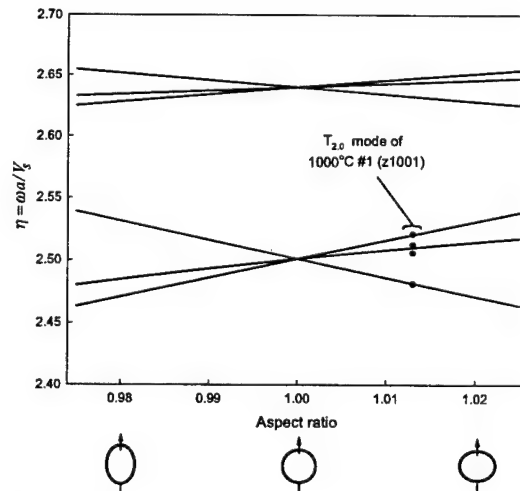
FIG. 38. Nondimensional frequency η versus aspect ratio of a spheroid, for the lowest two sphere modes. The dots represent the non-dimensional frequencies corresponding to the peaks in Fig. 37.

54
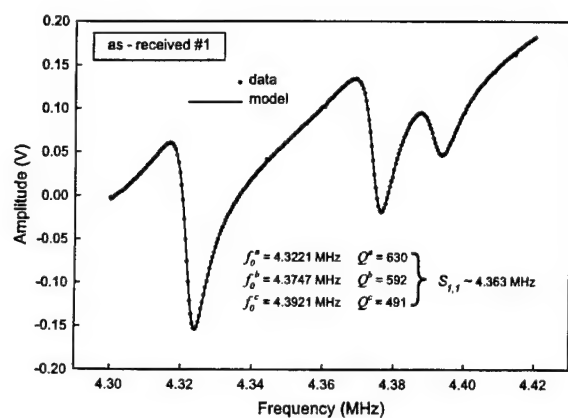
FIG. 39. A cluster of resonance peaks roughly correspond-
ing to the $S_{1,1}$ mode of a sphere, for a proppant particle in
the as-received condition. The frequency used in analysis is
the center of the cluster, around 4.363 MHz.

FIG. 40. Nondimensional frequency η versus aspect ratio
of a spheroid, for the sphere mode $S_{1,1}$. The dots represent
the non-dimensional frequencies corresponding to the peaks
in Fig. 39.

cies of the peaks modeled in Fig. 37 plotted on a graph
showing the nondimensional frequencies η of a spheroid
with $\lambda = \mu$, or $\nu = 0.25$, as a function of aspect ratio (the
volume is kept constant.) The $T_{2,0}$ mode indeed splits in
such a way that the highest and lowest frequencies are
symmetric about the original, and the observed points
seem to fit best in such a way that the median of the
cluster is aligned with the unperturbed frequency. The
frequency obtained by averaging the highest and lowest
fitted peaks is 3.286 MHz; the frequency originally ob-
tained by the author from graphical "guesstimation" is
3.287 MHz. The best fit appears to coincide with an
aspect ratio of 1.013, not an unreasonable number, al-
though it could not be easily confirmed by examining
the sample under a microscope.

Not all the peaks will split in such a symmetric way,
necessarily. Fig. 39 shows the $S_{1,1}$ mode of an as-received
proppant, and Fig. 40 shows the nondimensional peak
frequencies for this mode plotted on a graph similar to
that in Fig. 38. The splitting due to asphericity is de-
cidedly asymmetric; however, the actual sample has an
additional splitting, possibly due to eccentricity in a sec-
ond plane, and the cluster appears to fit the curve best
when its center is again aligned with the unperturbed
frequency. Thus it is concluded that graphically guess-
ing the appropriate frequencies from the center of the
peak clusters is accurate enough for the present purpose.
The frequencies used in the above example analysis of an
as-received bead to find its elastic properties, were deter-
mined in this approximate manner (with no foreknowl-
edge of what exactly the frequencies "ought" to be), and
as has been observed, they gave excellent results. Still,
it is apparent that it would be possible in principle to
use the exact nature of the mode splittings to charac-
terize the proppants further in terms of anisotropy, for
instance, which could be of interest.

C. Properties of proppants as a function of heat treatment

As stated earlier, the main purpose of this work was
to characterize the effects of heat treatment on the me-
chanical properties of the ceramic proppants. As a means
of simulating the kind of thermal stress they might en-
counter in various solar-receiver designs, separate batches
of as-received proppants were subjected to heat treat-
ments in air at temperatures of 900, 1000, 1100, 1200,
1300, and 1400°C, for 150 hours. Samples from each heat
treatment were then measured in the manner described
previously, to determine how the elastic constants change
with treatment temperature. The internal friction was
also monitored by recording the Q's of the spheroidal
mode $S_{1,1}$. At least 5 samples from each of the 7 cate-
gories (AR + 6 treatment temps.) were measured, and
the average and standard deviation of the 5 were used as
the final result. The standard deviations thus obtained
were typically much larger than the uncertainty in any
individual measurement, so only the former errors are
reported.

a. Effects of transducer contact on results Although
this subject was explored in the previous section, it is per-
haps more relevant here. One can achieve nearly point
contact when suspending a rectangular parallelepiped be-
tween two PVDF transducers; but with a sphere, it is
difficult to avoid having a larger contact area. This may
not be bad, in the present case of measuring very small,
highly damped samples; however, it could be if it biases
the results.

It is difficult, as has been mentioned, to quantify the
tension in the PVDF strips or the force exerted on a
sample. Nevertheless, an attempt was made to correlate
the two, by subjecting a Pyrex test sphere to increas-

TABLE XVII. The physical properties of a 0.0625-inch Pyrex sphere, $\rho = 2.24$ g/cc, determined by measurements made under increasing contact force.

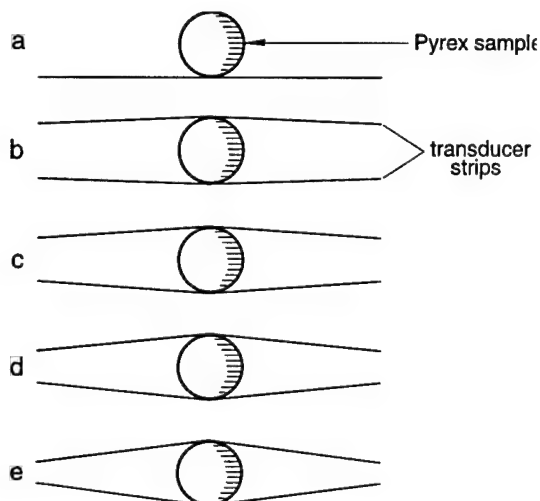| force[1]	$T_{2,0}$ (MHz)	$S_{1,1}$ (MHz)	rms (%)	ν	E (GPa)
a	1.7062	2.2832	0.05	0.2168	62.94
b	1.7049	2.2841	0.05	0.2168	62.88
c	1.7049	2.2840	0.05	0.2168	62.88
d	1.7050	2.2858	0.10	0.2168	62.86
e	1.7042	2.2829	0.11	0.2171	62.78

[1]See Fig 41

FIG. 41. A schematic representation of the manner in which increasing transducer contact force is applied to a Pyrex specimen in the RUS test cell. The movable transducer block (from Fig. 24) is advanced approximately one half of a screw turn between each measurement, except that there are one-and-a-half turns between (d) and (e).

ing force, that could be roughly gauged by the angle of the transducer strip compared to a line perpendicular to the transducer mounting tab. A Pyrex bead rather than a proppant was used for this test because Pyrex glass has less internal friction; the Pyrex beads also have less flaws, so the degenerate sphere modes are not split nearly as much. Frequency can be confidently measured to 5 significant digits, as opposed to 4 with the proppants. With two torsional and four spheroidal modes measured for each tension, the elastic constants can be very precisely determined.

Table XVII shows the results, while Fig. 41 shows a facsimile of the sample at each different tension, based on drawings of the mounted sample as seen through a microscope. The configurations shown in Fig. 41 show more variation in the distension of the transducer strips than is actually used from one measurement to another; in general, the strips appear as in cases (a), (b), or (c), with little or no discernable angle. Presumably the force exerted on the sample varies greatly from (a) to (c), but perhaps more importantly, the area of transducer contact increases as the strips bend around the spherical sample. Nevertheless, the thin PVDF strips do not have a large perturbative effect on the frequencies (as seen in the example modes shown in Table XVII, and there is no significant change in the determined values for the elastic properties. Thus it is concluded that in the present work, the variation in force or area of transducer contact from one measurement to another is not important, at least for frequency measurement. Amplitude and Q are not nearly so consistent, with the Q decreasing at the highest loading by a factor of 2 or so from the lightest loading; amplitude is still more sensitive, increasing by a factor of 5 between minimum contact force and light contact force (positions a and b). Interestingly, no further gain in signal amplitude is obtained by increasing the loading, as the increased damping apparently cancels out the increased coupling strength.

b. Internal friction from resonance data In addition to measuring the elastic constants of the proppants as a function of heat treatment, the internal friction was also considered. As previously mentioned, the proppants are rather lossy resonators (by the standards of elastic objects), most likely due to a high degree of internal microcracking. Thus it is of interest to monitor the internal friction as a function of heat treatment, and hopefully correlate it with some change in the microstructure.

The Q's of the resonances (Q = resonance frequency ÷ peakwidth) do not have the same degree of repeatability as the frequencies, and so no precise treatment of the internal friction, such as using complex frequencies in the analysis, was attempted. Rather, the Q of one mode, spheroidal mode $S_{1,1}$, was used to give an indication of the overall internal friction. The frequencies used in the previous analysis to determine the elastic constants were approximated graphically, as described earlier; this was not possible in the case of the Q's, as the complex line shapes made a peakwidth difficult to determine.

Since only one mode per sample was to be considered, it was cost-effective to curve-fit the resonance peak clusters corresponding to these modes. The results of one of these curve-fittings was shown in Fig. 39, giving the Q's of some modes for the as-received proppant ZAR01. Most of the actual visual curvefitting for this particular task was carried out using the commercial program Peakfit™ by Jandel Scientific, due to the many features incorporated to make visual curvefitting of multiple peaks more convenient. The numerical curvefitting, however, was finished using the author's own software based on Numerical Recipes routines; it was found that Peakfit did not always converge to the optimum solution even when an excellent visual curvefit was achieved prior to initiating the numerical process. The literature for Peakfit indicates that it also uses the Levenberg-Marquardt method; it is not clear why it did not successfully converge for many cases. More recent versions of this software may have improved its handling of user-defined functions, so perhaps these problems have cleared up.
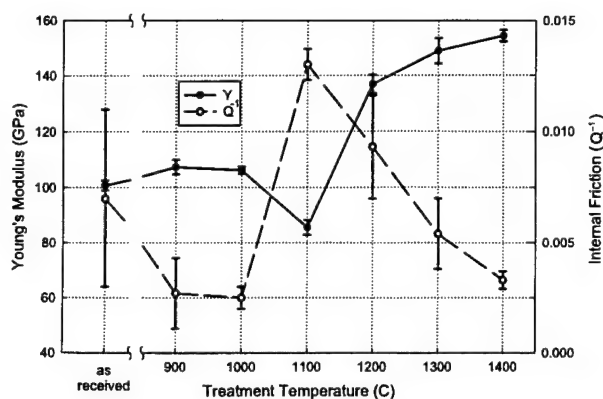
FIG. 42. A summary of the elastic properties of Zirprop Z126 proppants as a function of heat treatments in air for 150 hours at various temperatures. The values and error bars are from the average values of several samples in each category.

1. Summary of results

Figure 42 gives an overall summary of the results obtained for the Zirprop proppant particles. Five samples from each category were used to get the average values and standard errors. Right away one may notice a softening near 1100°C, with a corresponding increase in internal friction. These trends are then reversed at higher temperatures. This is consistent with observations that the microstructure undergoes significant changes over the range of heat treatments, including an increase in microcracking up to 1100°C, and a subsequent healing of these microcracks at higher temperatures [72].

It is of interest to note that the internal friction shows a much greater variability than does the Young's modulus. It has been suggested that because these proppants are somewhat porous and made of ceramic, they may be absorbing water in certain cases, lowering their Q's.

This summary is sufficient to show the utility of RUS for the characterization of such novel materials as proppants, and provides the needed information to complete the present level of evaluation of the proppants as a solid thermal transfer medium in a solar receiver. However, because of the wealth of information supplied by high-quality resonance data, much more detailed analysis is possible. As a small example, one additional graph is considered, showing the size of the residual error in fitting the frequencies as a function of heat treatment (Fig. 43). One of the microstructural changes that is thought to take place in the Zirprop during extended heat treatments at 1100°C and above is a gradual crystallization of the amorphous glassy (SiO_2) matrix which surrounds the zirconia-rich phases [72]. One effect that this might have is to make the proppants less isotropic elastically, if the crystallites are not oriented in a sufficiently random fashion. Since the model used to analyze the proppants assumes that they <u>are</u> isotropic, one might expect that the agreement between theory and observation might get
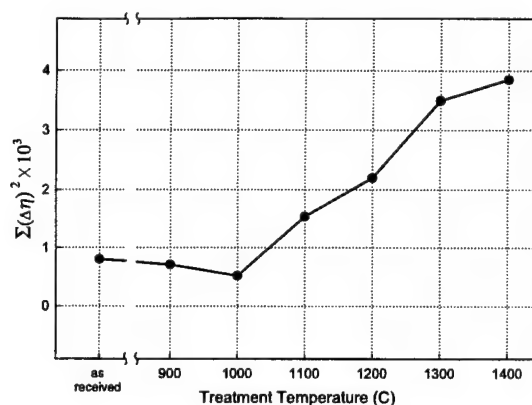
FIG. 43. The average residual error in fitting the normal mode frequencies of the proppants, for the various heat treatments.

worse at the higher temperature heat treatments, which is exactly what Fig. 43 shows. While this is not rigorous by any means, it does offer a hint of the extra information that comes packaged along with a RUS elastic-constant measurement.

V. INVESTIGATION OF QUASICRYSTALLINE AND CUBIC ALCULI

The last measurement presented in this paper, the measurement of isotropy and anisotropy in different phases of AlCuLi, demonstrates the use of RUS to probe structural differences in materials of which only very small samples are available. Here, in contrast to the last section, high precision is required, but absolute accuracy is unimportant. An icosahedral phase must be elastically isotropic (as discussed in Section II), but a cubic phase may be anisotropic; the ability to distinguish between the two phases with an elasticity measurement would be very useful in the study of alloys that have quasicrystalline phases as well as closely related crystalline phases.

A. Quasicrystals

One of the longest-standing assumptions in crystallography has been that a crystal may not have certain "forbidden" symmetries, such as an axis of fivefold rotational symmetry [73]. In two dimensions, the argument is that one cannot tile a plane with pentagons, without leaving gaps (as one can with triangles, squares, hexagons, *etc.*). In three dimensions, one cannot pack unit cells with icosahedral symmetry so they fill all space.

a. Penrose tilings At the heart of this argument lies the assumption that the packings consist of periodic arrangements of a single unit cell (or tile). Mathemeticians,
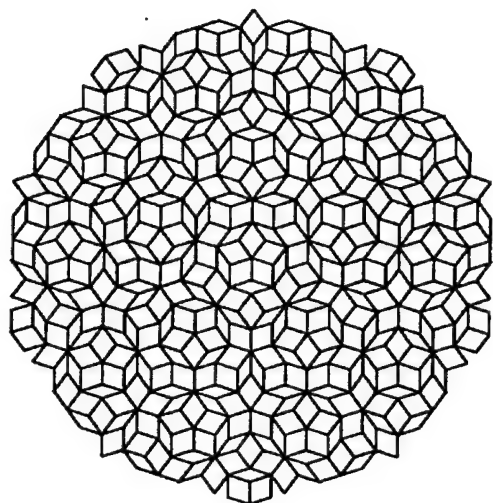
FIG. 44. A Penrose tiling with fivefold symmetry, comprised of "fat" and "skinny" rhombuses (from [76]).

FIG. 45. The electron diffraction pattern of Shechtmanite, the first known quasicrystalline alloy, along a fivefold axis (it appears tenfold symmetric; careful examination of the faint, apparently pentagonal patterns between each "spoke" show that they are distorted, and have mirror symmetry about the spokes).

on the other hand, have long had a fascination with so-called "quasiperiodic" tilings, ways of filling space with tiles of more than one shape in such a way that the pattern never repeats—yet is not random, but generated from some simple rules that guarantee long-range order. The long-range order may be expressed, for instance, as a Fourier transform of the lattice that has a small number of discrete frequency components, like a regular crystal lattice, only the frequency components are incommensurate, so the structure does not have translational periodicity. It may, however, have axes of rotational symmetry, including rotational symmetries that are classically "forbidden". The work of mathematician Roger Penrose on this subject culminated in 1974 with the now-famous "Penrose tilings" [74,75], quasiperiodic arrangements of two basic rhombus-shaped tiles, that have long-range fivefold rotational symmetry (see Fig. 44).

b. Icosahedral alloys These tilings remained primarily mathematical curiosities, with no connection to crystallography, until in 1982 Dany Shechtman [26] discovered an Al–Mn alloy that exhibited a fivefold electron diffraction pattern (Fig. 45). Soon other alloys were discovered with icosahedral and other forbidden symmetries, such as eightfold symmetry; some of the icosahedral alloys, such as one with approximate composition Al_6CuLi_3, allow stable grains of macroscopic size to be grown, so that facets are observable [79]. Figure 46 shows a photograph of some icosahedral grains of AlCuLi; the facets clearly resemble the Penrose tiles in Fig. 44. Levine and Steinhardt [80] had been coincidentally working on a theoretical model for an icosahedral solid with the structure of a three-dimensional Penrose tiling, when Shechtman's discovery was announced; they proposed that his AlMn alloy ("shechtmanite") might be a physical realization of such a structure. Such a solid would be crystallike but not periodic in structure, therefore not classically
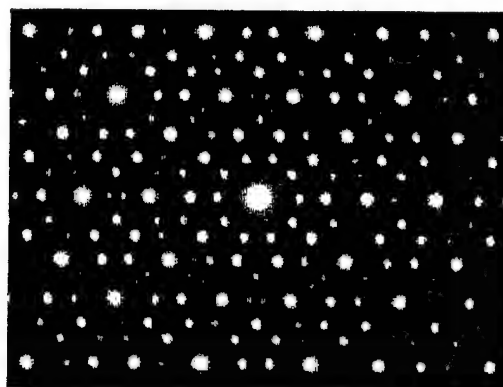
FIG. 46. Macroscopic ($\sim$ 1cm) grains of Al_6CuLi_3, exhibiting triacontahedral facets resembling Penrose tilings (from the Pechiney Research Center, France).

crystalline. Hence they coined the term "quasicrystal" to refer to solids with long-range, quasiperiodic order. The study of quasicrystals has since grown into a sizeable subbranch of materials physics, with books [81], congresses, and special sessions at American Physical Society meetings.

c. Unusual elastic properties One of the fascinating properties of icosahedral quasicrystals is that, unlike conventional crystals, they must be elastically isotropic, due to their "forbidden" symmetry (as shown in Section II). For conventional crystals with high symmetries (*e.g.* cubic crystals), many physical properties are isotropic, but the property of linear elasticity is fundamentally anisotropic; that is, the velocity of sound may be different in different directions. Thus it is interesting that icosahedral quasicrystals, having long-range order like conventional crystals, must be isotropic in sound propagation. Normally, substances that are elastically isotropic are amorphous, like glasses. Unlike disordered solids, however, quasicrystals may be *anisotropic* in the attenuation of sound and in the higher order elastic constants, even while they are fundamentally isotropic in linear elasticity [27,82].

Quasicrystals are further interesting in that by attaining an appropriate amount of a unique strain ("phason strain") [83], they may be transformed into conventional crystals (referred to as "periodic approximants") [84], thereby becoming elastically anisotropic. Measuring these properties experimentally has been challenging [85–87], because while conventional crystals are fundamentally anisotropic, their elastic constants may be numerically very close to those of an isotropic material, so that it is difficult to distinguish between intrinsically isotropic and anisotropic behavior in a measurement (recall the discussion of elastic tensors in Section II). Indeed, nearly isotropic behavior might be expected in the periodic approximants, because they are structurally very similar to the isotropic quasicrystals [88].

The following sections describe the use of resonant ultrasound spectroscopy to obtain high precision measurements of the elastic constants of both the quasicrystalline and a periodic approximant phase of AlCuLi which show, with a significant level of confidence, that the quasicrystalline phase is isotropic (less anisotropic than the most nearly isotropic conventional crystal by at least five standard deviations), while the periodic approximant is not.

B. The measurement of isotropy

Before presenting the details of the measurement, it is worthwhile to quantify the difficulty of determining whether or not a material is elastically isotropic. For this purpose, we consider cubic tungsten, which has the smallest anisotropy for a conventional crystal to be found in the literature [89,90]. The sound velocity in tungsten varies with direction by less than 0.5%; depending on the

orientations used in a particular experiment, the observable variation could be significantly smaller. To show that a quasicrystal is more isotropic than ordinary crystals, a conventional sound velocity measurement would have to probe all principal directions (which might require remounting transducers, possibly resulting in a loss of precision) with an overall resolution better than 0.5%. This is especially challenging considering the small size of most high-quality samples. Previous studies of quasicrystals [85–87] have found isotropy in sound propagation but only at the 1% level; considering the properties of tungsten and the possibilities for periodic approximants, it is apparent that more precise measurements are necessary. If a sufficient number of normal modes are used in a measurement, resonant ultrasound spectroscopy probes all principal directions in one measurement, while achieving precision sufficient both to show that the AlCuLi quasicrystal is at least an order of magnitude more isotropic than tungsten, and to quantify the anisotropy of a periodic approximant. First we shall discuss the notion of elastic anisotropy in terms of the elements of the elastic tensor.

As discussed in Section II, the elastic tensor c_{ij} for an isotropic solid has only two independent elements, related to a shear and a bulk modulus. By contrast, the most symmetric elastic tensor for a conventional crystal (cubic) has three independent constants, c_{11}, c_{12} and c_{44}. However, the form for the isotropic and cubic tensors are identical, except that for an isotropic solid, $c_{12} = c_{11} - 2c_{44}$. Zener [91] defined his anisotropy parameter A to be

$$A \equiv \frac{2c_{44}}{c_{11} - c_{12}},$$

which is unity for an isotropic solid. For nearly isotropic solids, it is therefore convenient to define an anisotropy parameter ϵ_z, in honor of Zener, as

$$\epsilon_z \equiv 1 - A = 1 - \frac{2c_{44}}{c_{11} - c_{12}}, \tag{65}$$

so that ϵ_z is zero for an isotropic solid[4]. For α–tungsten, ϵ_z is only 0.007 ± 0.002 [89,90]. Rather than attempt to measure sound velocities in a number of distinct directions, we seek to measure normal mode spectra of our samples, and fit the data to a model that allows 3 independent elastic constants (cubic symmetry). If the quasicrystal is indeed isotropic, the resulting value of ϵ_z calculated from the fitted values of c_{ij} should be significantly less than that of tungsten (and, it is hoped, the periodic approximants as well).

---

[4]This definition of anisotropy is obviously geared toward cubic solids. Chung and Buessem [90] have developed a scheme for attributing a single-valued anisotropy to other crystal classes.

1. The AlCuLi samples

Verifying small values of ϵ_z not only requires a precise measurement of the elastic constants, but also requires single crystal (or quasicrystal) samples of very high quality, since defects or grain boundaries could give rise to systematic errors, resulting in a spurious anisotropy result. For our measurement we used the AlCuLi system, because high-quality single crystals of both the quasicrystal and a periodic (cubic) approximant can be grown to millimeter size [92]. The cubic approximant, referred to as R-phase [93], is similar in structure, composition, and density to the quasicrystalline phase [88,94].

A 1 mm-thick disk of AlCuLi cut from an ingot of approximately 1 cm diameter, containing R-phase and quasicrystalline phase, was obtained from A. R. Kortan of AT&T Bell Laboratories. Two specimens, one of each phase, were cut from this disk with a diamond wire saw, and polished into rectangular parallelepipeds. At first, a few features (possibly fissures or grain boundaries) were observed on the sample surfaces. As a consequence, the specimens were painstakingly polished, examined, and repolished until no surface features were visible, which was a bit of a challenge. As anyone who has handled these materials is no doubt aware, they are extremely fragile and brittle, and a parallelepiped of such a material is very prone to having the corners break off (this is a strong argument in favor of using transducers such as the present thin-film PVDF type). This very brittleness appears to be another consequence of quasiperiodicity, because classic dislocations cannot propagate in a non-periodic lattice—and the defects unique to quasicrystals, such as the so-called "phasons" (reorderings of the tiling pattern that fill space but do not follow the long-range pattern generating rules) propagate only at the speed of atomic diffusion. Thus, quasicrystals cannot plastically deform in the conventional sense [83].

Care was taken to insure that the sample faces were flat, smooth, and perpendicular to within 0.5°. The finished parallelepipeds of cubic and quasicrystalline AlCuLi were each small enough to be placed entirely within a 1 mm^2 X-ray beam, and transmission Laue diffraction revealed that they were both single grains of excellent quality. A third parallelepiped, with a mass of only $\sim70\,\mu$g, was prepared from a separate sample of quasicrystalline AlCuLi for comparison. Laue photographs of this third specimen, however, showed that more than one grain may have been present. Henceforth these samples shall be referred to as QX1 (high quality quasicrystal), QX2 (lesser quality quasicrystal), and R (R-phase cubic approximant). The vital characteristics of each sample are summarized in Table XVIII. Diffraction photographs of each sample are shown in Fig. 47; the five-fold symmetry of QX1 is quite apparent, while that of QX2 is less so. The photo of R is along a twofold axis, and shows symmetry 2mm (but not fourfold symmetry). The R-phase of AlCuLi is a somewhat complicated struc-

TABLE XVIII. Dimensions, masses, and sample qualities of the three AlCuLi samples studied in this section. Dimensions are approximately ±0.003 mm, and masses are approximately ±0.0005 mg.

Label	Dimensions	Mass	Grains
QX1	$0.419\times0.427\times0.576$ mm^3	0.2397 mg	single
QX2	$0.241\times0.285\times0.389$ mm^3	0.0665 mg	multiple
R	$0.362\times0.729\times0.950$ mm^3	0.6268 mg	single

ture with a unit cell of 104 atoms, basically a decorated b.c.c. lattice of interpenetrating icosahedra and slightly distorted triacontahedra [94]. The R-phase is an example of a cubic substance without a fourfold axis of symmetry.

The diffraction photo of QX1 shows some smearing of the normally sharp diffraction spots that one sees in a transmission Laue photo of a crystal (such as the neighboring photo of R). This may be due to the presence of phason strains which are known to corrupt the AlCuLi structure [95]. Whether or not these defects affect the overall icosahedral symmetry may, in fact, be apparent if the anisotropy differs significantly from zero. Deviations from 5-fold symmetry may also be observed in the Al-Mn diffraction pattern shown in Fig. 45, by holding the page at a grazing angle and viewing along one of the "spokes"—the spots do not line up perfectly but have a certain amount of "zig-zagging". Lubensky *et al.* [95] have suggested that this is due to a phason strain "quenched" during crystal growth. They suggest that this strain is probably anisotropic, but add that studies of diffraction patterns alone make confirmation of this prediction difficult. This makes the present investigation all the more relevant; a small anisotropy might indicate the presence of anisotropic phason strain [83].

C. The measurements

The normal-mode frequencies of QX1, QX2, and R are measured by the method of Section III: each rectangular parallelepiped sample is held lightly at opposing corners between two broadband PVDF transducers, one a driver and the other a receiver; the driver frequency is swept and the response at the receiver is monitored with a phase-sensitive detector and digitized. An initial scan to locate the peaks is followed by a finer scan of each peak; each peak is then fit with a Lorentzian. Thirty resonances of QX1 were recorded, with somewhat fewer recorded for QX2 and R. Since individual normal modes may involve torsion, shear, dilatation, or a combination, along any axis, all principal directions are investigated in several ways with a single spectrum, if enough modes are used. It is of some interest to note that the typical Q's of the resonances are quite a bit lower than those observed for Si; rather than being in the range of 10^4, they were
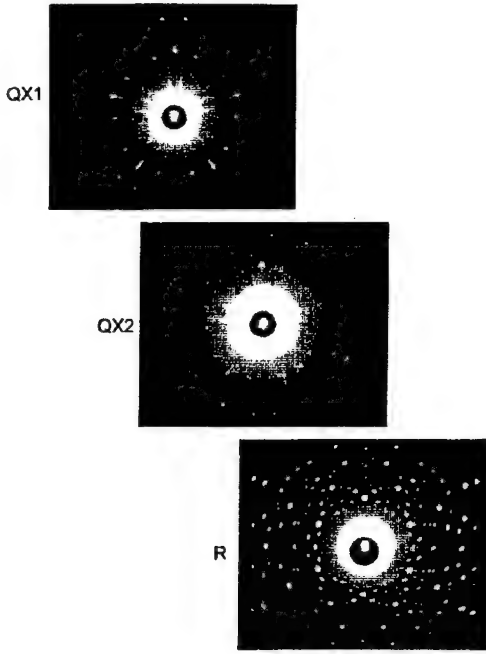
FIG. 47. Transmission Laue diffraction photos of the three AlCuLi samples described in the text. The two quasicrystal samples (QX1 and QX2) are photograhed along fivefold axes, and the cubic R phase is photographed along a twofold axis.

more in the range of 10^3. Whether this is related to the presence of defects in the samples is unknown.

We assume in our fitting procedure that all of our samples have at least cubic symmetry, so that there are at most three independent elastic constants. If the quasicrystal is isotropic and has only two independent constants, the value of ϵ_z from Eq. (65) will be correspondingly small. The frequencies in the measurement are determined with good precision and accuracy, so that the accuracy of the calculated elastic constants is limited by the accuracy with which the geometry of the sample is determined. The size of the sample may be taken as one physical dimension and two aspect ratios. Since we measure many more frequencies than elastic constants, the problem is overdetermined and the aspect ratios can be included as free parameters in the fit. Only a single dimension is required to determine the elastic constants, but in calculating the anisotropy parameter with a ratio of elastic constants, the dimension, as well as the mass of the sample, cancels out. Thus the random errors determined by our Monte Carlo simulations can be taken as the overall error in the measurement of the anisotropies.

Table XIX shows the results of fitting 30 modes of sample QX1. The fit appears to be quite good, with an rms error of only 0.08%; the anisotropy calculated from the resulting elastic constants is $\epsilon_z = -0.0024$, significantly smaller in magnitude than that of tungsten. However, an estimate of the measurement error from an examination of the error surface curvature (as described in Section

TABLE XIX. The observed and calculated frequencies, in MHz, for the 0.24 mg AlCuLi quasicrystal sample QX1, from a fit using all observed modes. The maximum order of the basis functions used in the calculations is 12.

	Mode	f_{obs}	f_{calc}	Δf	|% error|
1	EV-1	3.31323	3.30643	0.00680	0.205
2	EY-1	4.23613	4.23789	−0.00177	0.042
3	EX-1	4.26763	4.26636	0.00127	0.030
4	EV-2	4.89840	4.89171	0.00669	0.137
5	OY-1	5.28175	5.28267	−0.00092	0.017
6	OX-1	5.32980	5.33646	−0.00666	0.125
7	OD-1	5.44512	5.44834	−0.00323	0.059
8	OZ-1	5.96625	5.95830	0.00795	0.133
9	OZ-2	6.23313	6.24199	−0.00886	0.142
10	EZ-1	6.36354	6.36632	−0.00279	0.044
11	EY-2	6.38945	6.39185	−0.00240	0.038
12	OD-2	6.41163	6.41211	−0.00048	0.008
13	OZ-3	6.53294	6.53025	0.00269	0.041
14	EX-2	6.56425	6.56600	−0.00175	0.027
15	OX-2	6.95444	6.95330	0.00114	0.016
16	OD-3	———	7.00376	———	—
17	OY-2	7.09166	7.08674	0.00492	0.069
18	EZ-2	7.24058	7.23987	0.00070	0.010
19	OD-4	7.33420	7.33094	0.00326	0.044
20	EV-3	7.76685	7.77588	−0.00904	0.116
21	OD-5	7.87680	7.87674	0.00005	0.001
22	EZ-3	7.96638	7.96703	−0.00065	0.008
23	EY-3	8.00375	7.99584	0.00791	0.099
24	EX-3	8.02944	8.01923	0.01020	0.127
25	EX-4	8.25410	8.25852	−0.00442	0.053
26	EY-4	8.27553	8.28903	−0.01350	0.163
27	EZ-4	8.48225	8.47593	0.00632	0.075
28	OX-3	8.48225	8.48517	−0.00292	0.034
29	OY-3	8.52350	8.52733	−0.00383	0.045
30	EZ-5	8.60290	8.60911	−0.00621	0.072
31	OX-4	8.86694	8.86613	0.00080	0.009
				Avg.	0.08%

II) indicates that the confidence interval may be significantly smaller than 0.0024, so it seems worthwhile to consider possible sources of bias in the anisotropy determination. One interesting aspect of the fit is that the lowest frequency has the largest error (by almost 50%) of any mode. This would not be so interesting, except that it seems to be a consistent effect, observed in many RUS investigations [96]. The lowest mode is a torsional mode (recall the plot of mode EV-1 from Fig. 8); it therefore has a great deal of motion at the corners. If this mode is excited with a sizeable amplitude, it is reasonable to suppose that it may interact more strongly with the transducers than other modes, which may account for its (relatively) poor agreement. It is natural, then, to consider what the fit would look like if this one anomalous point were omitted.

In standard least-squares curvefitting, this sort of exclusion of anomalous or "outlier" points is done routinely,

but one hesitates to do it in the present context. For one thing, there is not an overwhelming wealth of data. Also, the "points" are not simply redundant random samplings of a single physical process, but rather, resonance frequencies that each represent a distinct physical process. However, we may justify excluding the lowest frequency from the fit on the following grounds:

- The lowest frequency is consistently observed to fit (relatively) poorly, and there is at least one plausible physical explanation (that it has the most interaction with the transducers).

- It is not uncommon to miss one or two modes out of thirty in a measurement, and still be able to fit the data successfully and find the elastic constants. Since the number of free parameters in the present fit is small (three elastic constants and two aspect ratios), one frequency can be safely omitted because there is enough redundancy in the data.

- The lowest frequency is a torsional mode, which depends almost entirely on the shear modulus (c_{44}). The shear modulus is typically the most well-determined of all the moduli, so this one frequency can be excluded.

If the fit is repeated, but without the lowest frequency, one finds predictably that the overall rms error decreases—and the anisotropy (magnitude) also decreases, to $\epsilon_z = -0.0016$ (see Table XX). This value for the anisotropy is most likely a more accurate value.

Table XXI shows the fit of the data obtained on the second quasicrystal sample, QX2. Notice that even though this sample has a mass of only 70 μg, a tiny fraction of the many milligrams of most samples in RUS measurements, the agreement between the measured and calculated frequencies is still on par with that of the larger samples. Here again, the lowest frequency had an anomalously bad fit and was omitted to avoid biasing the anisotropy results. Again, the anisotropy is considerably smaller than that of tungsten, and is found to be $\epsilon_z = 0.0011$. Table XXII shows the fit for the cubic approximant R; the anisotropy is found to be $\epsilon_z = 0.0096$; though small, it is comparable to that of tungsten and much larger than the two quasicrystal samples. Only twelve modes of R are measured and one may wonder if this is really enough data. There are several ways one might argue that it is: first, the determined anisotropy is much larger than the other two cases, and is therefore less sensitive to the amount of data. Second, by examining the matrix of frequency derivatives (Table XXIII), it would appear that the the dependence of the various modes on the free parameters is complete and independent enough to provide an accurate determination. This is confirmed if one examines the condition number of the design matrix after the singular value decomposition: the ratio of the extreme singular values is $s_{min}/s_{max} = 0.01$, a long way from being ill-conditioned.

TABLE XX. The observed and calculated frequencies, in MHz, for the 0.24 mg AlCuLi quasicrystal sample QX1, from a fit excluding the lowest observed mode.

	Mode	f_{obs}	f_{calc}	Δf	$|\%$ error$|$
1	EV-1	——	3.30479	——	——
2	EY-1	4.23612	4.23671	−0.00058	0.014
3	EX-1	4.26763	4.26524	0.00239	0.056
4	EV-2	4.89840	4.89116	0.00724	0.148
5	OY-1	5.28175	5.28101	0.00074	0.014
6	OX-1	5.32980	5.33494	−0.00514	0.096
7	OD-1	5.44512	5.44802	−0.00290	0.053
8	OZ-1	5.96625	5.95753	0.00872	0.146
9	OZ-2	6.23313	6.24089	−0.00776	0.124
10	EZ-1	6.36354	6.36749	−0.00396	0.062
11	EY-2	6.38945	6.39221	−0.00277	0.043
12	OD-2	6.41163	6.41310	−0.00147	0.023
13	OZ-3	6.53294	6.52729	0.00565	0.086
14	EX-2	6.56425	6.56684	−0.00259	0.039
15	OX-2	6.95444	6.95340	0.00104	0.015
16	OD-3	——	7.00526	——	——
17	OY-2	7.09166	7.08727	0.00439	0.062
18	EZ-2	7.24058	7.24088	−0.00030	0.004
19	OD-4	7.33420	7.33200	0.00220	0.030
20	EV-3	7.76685	7.77397	−0.00712	0.092
21	OD-5	7.87680	7.87835	−0.00155	0.020
22	EZ-3	7.96638	7.96736	−0.00098	0.012
23	EY-3	8.00375	7.99586	0.00789	0.099
24	EX-3	8.02944	8.01918	0.01026	0.128
25	EX-4	8.25410	8.25694	−0.00284	0.034
26	EY-4	8.27553	8.28727	−0.01172	0.142
27	EZ-4	8.48225	8.47622	0.00603	0.071
28	OX-3	8.48225	8.48429	−0.00204	0.024
29	OY-3	8.52350	8.52641	−0.00292	0.034
30	EZ-5	8.60290	8.60919	−0.00629	0.073
31	OX-4	8.86694	8.86356	0.00338	0.038
				Avg.	0.07%

TABLE XXI. The observed and calculated frequencies, in MHz, for the 66 μg AlCuLi quasicrystal sample (QX2), from a fit excluding the lowest observed mode.

	Mode	f_{obs}	f_{calc}	Δf	|% error|
1	EV-1	————	4.71210	————	——
2	EX-1	5.84360	5.84875	−0.00515	0.088
3	EY-1	6.21250	6.21127	0.00123	0.020
4	OX-1	7.71805	7.72498	−0.00693	0.090
5	EV-2	7.96998	7.96660	0.00337	0.042
6	OD-1	7.98782	7.98017	0.00765	0.096
7	OY-1	8.38935	8.39093	−0.00158	0.019
8	OZ-1	8.76000	8.74884	0.01116	0.127
9	EX-2	9.04020	9.04756	−0.00736	0.081
10	EZ-1	9.68615	9.68611	0.00004	0.000
11	OD-2	9.74250	9.74162	0.00088	0.009
12	OZ-2	9.75500	9.75252	0.00248	0.025
13	OZ-3	9.99745	10.00706	−0.00961	0.096
14	OY-2	10.06025	10.04509	0.01516	0.151
15	OD-3	10.85545	10.86949	−0.01404	0.129
16	EY-2	11.27615	11.27395	0.00220	0.020
17	OD-4	————	11.83692	————	——
18	OX-2	11.85815	11.85645	0.00170	0.014
				Avg.	0.07%

TABLE XXII. The observed and calculated frequencies, in MHz, for the 0.63 mg cubic AlCuLi sample (R).

	Mode	f_{obs}	f_{calc}	Δf	|% error|
1	EV−1	1.50698	1.50449	0.00249	0.165
2	EX−1	1.88084	1.88217	−0.00134	0.071
3	EY−1	2.54689	2.54605	0.00083	0.033
4	EX−2	2.87475	2.87417	0.00058	0.020
5	OZ−1	2.94790	2.94698	0.00092	0.031
6	OX−1	3.00810	3.01476	−0.00666	0.221
7	OD−1	3.21271	3.21352	−0.00082	0.025
8	OY−1	3.34405	3.34836	−0.00431	0.129
9	EZ−1	3.74133	3.74275	−0.00143	0.038
10	OY−2	3.78285	3.78415	−0.00130	0.034
11	OD−2	3.86068	3.85562	0.00505	0.131
12	EV−2	4.22269	4.21676	0.00593	0.140
				Avg.	0.11%

TABLE XXIII. The derivatives of frequency with respect to elastic constants and edge lengths, for the 0.63 mg cubic AlCuLi sample.

	Mode	f_{calc}	$\frac{\partial f_n}{\partial c_{11}}$	$\frac{\partial f_n}{\partial c_{12}}$	$\frac{\partial f_n}{\partial c_{44}}$	$\frac{\partial f_n}{\partial L_x}$	$\frac{\partial f_n}{\partial L_y}$
1	EV-1	1.5045	0.00	0.00	1.89	4.35	−0.36
2	EX-1	1.8822	0.89	−0.66	0.40	5.46	1.21
3	EY-1	2.5461	1.10	−0.77	0.74	3.46	2.83
4	EX-2	2.8742	1.17	−0.61	0.81	7.52	−3.63
5	OZ-1	2.9470	0.42	−0.29	2.76	7.35	−0.11
6	OX-1	3.0148	0.12	−0.07	3.52	4.12	−0.17
7	OD-1	3.2135	1.91	−1.68	0.00	4.36	1.74
8	OY-1	3.3484	1.07	−0.90	1.92	7.62	−1.81
9	EZ-1	3.7428	1.64	−1.19	1.04	5.03	−3.30
10	OY-2	3.7841	0.91	−0.30	2.45	6.86	1.79
11	OD-2	3.8556	2.14	−1.62	0.13	5.14	−1.35
12	EV-2	4.2168	0.72	−0.61	3.77	3.75	1.06

TABLE XXIV. The elastic properties of the three AlCuLi samples.

Label	c_{11}	c_{12}	c_{44}	ϵ_z
QX1	1.1214	0.3043	0.4092	−0.0016±0.0007
QX2	1.1470	0.3081	0.4190	0.0011±0.0013
R	1.1120	0.3109	0.3967	0.0095±0.0014

Perhaps the best way to assess the uncertainty in the determination of R's parameters is to calculate the confidence interval by use of "Monte Carlo" simulations (as discussed in Sections II and III). This is carried out for all three samples, and the results are presented in Table XXIV and Fig. 48.

The standard deviations (and the error bars in Fig. 48) reflect to some degree the sample quality and the number of data points; the error for the high quality quasicrystal (QX1) is concomitantly the smallest of the three. It is apparent that the R-phase is measurably anisotropic, while the quasicrystal samples may not be. The anisotropy of the R-phase is seen to be comparable to that of tungsten, and differs from zero by several standard deviations. The anisotropy of the high quality quasicrystal, with $|\epsilon|$ = 0.0016 ± 0.0007, is 8 standard deviations, and about a factor of 5, less anisotropic than tungsten. Hence the quasicrystal is significantly more isotropic than the most isotropic conventional crystal to be found in the literature.

D. Discussion

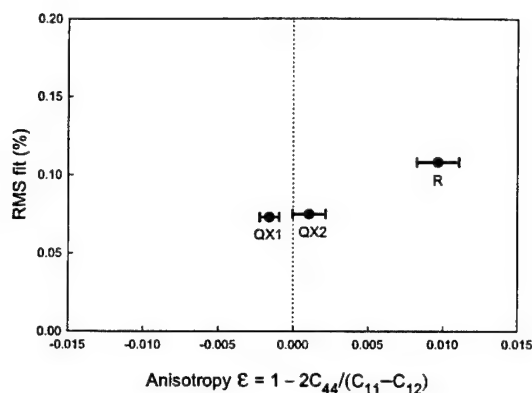Although the icosahedral AlCuLi quasicrystal has been shown to be significantly less anisotropic than any known

63

FIG. 48. The anisotropies and rms errors for the three Al-CuLi samples.

FIG. 49. A crystalline sample whose lattice is misaligned with its "object axes".

crystals, including the nearly isotropic R-phase approximant, the theory says it should be perfectly isotropic. There is still the interesting question of whether the defects in the AlCuLi structure are random or anisotropic, as discussed earlier, and also the question of whether "higher-order" approximant crystals, with even larger unit cells and more nearly icosahedral local symmetry than the R-phase, may be distinguished from true quasicrystals in an elasticity measurement. To answer these questions requires an uncommon amount of precision. While the present measurement indicates that RUS may be up to the task, it cannot answer it definitively, without more measurements (preferably on the reputedly perfect quasicrystal $Al_{65}Cu_{20}Fe_{15}$ [97]). The quasicrystal samples measured here appear to have an ever-so-slightly measureable anisotropy, based on the results shown in Fig. 48.

a. Bias due to sample preparation errors Another source of error that must be considered is if the actual shape of the sample differs in a systematic way from that assumed in the fitting program, nominally a rectangular parallelepiped. An inexact shape may result from the limits of our polishing technique and the small size of the samples, and shape anisotropy may appear as elastic anisotropy in the results of a fitting procedure that assumes an ideal shape. For a carefully shaped sample, the sides may differ from being mutually perpendicular by a few tenths of a degree, and the errors in c_{ij} may be a few tenths of a percent, sufficiently small for most purposes. However, the present measurement requires as little systematic error as possible, so the actual shape of QX1 was measured by first mounting the sample on a goniometer, and then using a laser beam reflecting from the polished sample faces to determine the angles between each side. A second-order frequency perturbation calculation using this more accurate shape is developed in detail in Section VI; however, the conclusion is that the small preparation errors in this sample are insufficient to bias the anisotropy result (see Section VI for a full treatment of this question).
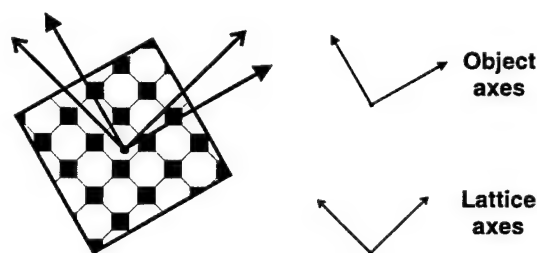
1. Other evidence of isotropy

There are other ways in which one can use RUS to explore the relative anisotropies of two materials. For instance, one may test the invariance of an isotropic tensor under rotation by running the fitting program multiple times for different rotations of the elastic constant matrix. The fit error for the crystalline R phase should show a clear dependence on orientation, while the quasicrystal should not.

a. Effects of misorientation It is worthwhile to recall that in the development of the variational principle for elastic solids, there are two distinct coordinate systems of importance: that of the *crystal lattice*, and that of the *object*. Normally, the equation of motion is expressed in coordinates that take advantage of some symmetries of the object. Ideally, these same symmetries are shared by the crystal lattice, and the two are aligned so that the object and lattice axes coincide, but it is not a necessary condition. The misalignment of the lattice may be accounted for by rotating the elastic constant matrix in its original tensor form c_{ijkl}. Fig. 49 shows a schematic representation of a case where the two coordinate systems are misaligned.

In fact, all three samples studied in this section are misoriented in this manner. When the samples were first prepared, attempts were made to orient them using reflection Laue photography. Possibly due to the tertiary structure, and the presence of soft elements like lithium in the alloys, the surfaces of the samples were essentially disordered (even after etching) and no coherent spot patterns could be produced. Therefore, the parallelepipeds were cut and polished with no knowledge of the lattice orientation, which therefore has an arbitrary relationship with the parallelepiped axes of each sample. Eventually, the orientations of the lattices with respect to the parallelepiped axes were obtained by means of transmission Laue photography, producing the photos shown earlier in the section (Fig. 47).

These orientation angles may be used to give the elastic constant tensor the appropriate rotation, so that the eigenvalue problem is solved in the correct coordinates. To do so, one must recall how the samples are oriented (see Section III). The samples are mounted on a goniometer, with sections that rotate about three initially per-

64

pendicular axes. In the present case, the polished parallelepiped samples may be mounted on the goniometer in such a way that these axes coincide with the parallelepiped axes. When the sample has been successfully oriented, the lattice axes will be in the original position of the parallelepiped (and goniometer) axes. Therefore, the rotations of the goniometer sections represent the rotation of the parallelepiped coordinate system away from the lattice. Because the vertical axis of the goniometer always remains in the same orientation, it is natural to represent this transformation as first a rotation of ψ about z, then a rotation of θ about y' (where y is the axis of the middle section of the goniometer), and finally a rotation of ϕ about x''. Then ψ, θ, and ϕ are the angles read directly off the bottom, middle, and top stages of the goniometer when the lattice is oriented with the X-ray beam.

A similar type of rotation applied to the elastic tensor in the forward calculation, however, represents a rotation of the *lattice* axes away from the *object* axes (the object axes being inherent in the expressions for the integrals representing the matrix elements, Γ_{mn} and E_{mn}, from (37)). In this case the axes of rotation are taken with respect to the lattice, and not the object. Rotations about these axes to create the proper misorientation of the lattice therefore represent the inverse of the previous case, when the axes of the object were rotated to determine the relative orientation of the lattice. Let α, β, and γ represent the rotations about these lattice axes; if the direction cosines of the rotation are given by a_{ij}, and the direction cosines of the goniometer rotations corresponding to ψ, θ, and ϕ are given by g_{ij}, then one has

$$a_{ij}(\alpha, \beta, \gamma) = g_{ji}(\psi, \theta, \phi).$$

Then the rotated elastic tensor is given by $c'_{ijkl} = a_{ij}a_{kl}a_{mn}a_{op}c_{mnop}$, as in Section II. The angles α, β, and γ do not have to be solved for explicitly, and in fact may not be unique. Since they represent rotations about the lattice, which in the present case is assumed to have cubic symmetry, one can use the symmetry properties of the cubic elastic tensor to find "principal values" (values between 0 and π) for the angles α, β, and γ. These are useful for graphing purposes, as will be explained.

b. Fit error versus rotation of elastic tensor If an object's elastic tensor is truly isotropic, then the previous discussion of elastic tensor rotation and lattice misorientation is irrelevant, since the elastic tensor is invariant under any rotation. If the tensor were slightly anisotropic, one might still expect convergence in the fitting procedure, but the overall fit error would theoretically be greater when the elastic tensor is rotated away from the true orientation of the lattice. Therefore, if one plots the fit error (the quantity F from (48)) versus rotations of the elastic tensor, one ought to see a clear dependence on orientation for the R-phase, but not the quasicrystal.

Figures 50 and 51 show such plots for the data on R
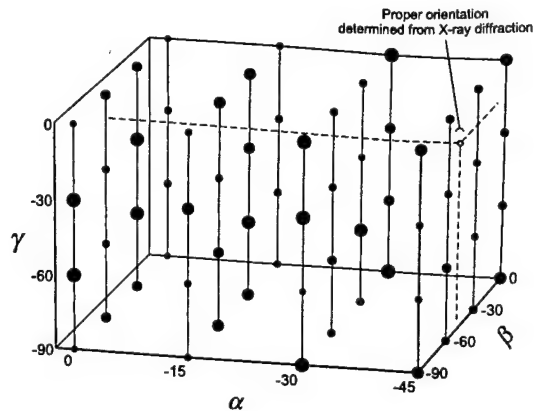
FIG. 50. The goodness-of-fit parameter F versus rotation of elastic tensor, for the R-cubic approximant sample of Al-CuLi. The relative size of F at various points is indicated by the diameter of the dot.
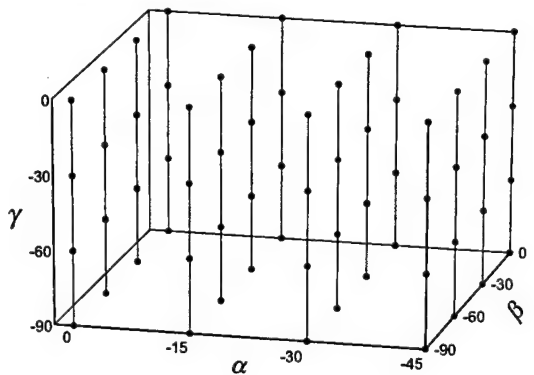
FIG. 51. The goodness-of-fit parameter F versus rotation of elastic tensor, for AlCuLi quasicrystal sample QX1. The relative size of F at various points is indicated by the diameter of the dot.

and QX1, respectively. The diameter of the dots represents the size of the fit error (arbitrary units), and one can see that the R-phase fit error has clear orientational dependence, while the quasicrystal shows none. The range of α, β, and γ used to produce the plots exploits the symmetries of the cubic elastic tensor, so all possible unique orientations are included in these volumes. Ideally, the fit error for R should show an overall minimum at the correct orientation, shown by the white dot (the corresponding α, β, and γ are the "principle values" mentioned above corresponding to the measured orientation angles). This is not obviously the case judging from the figure, which shows many apparent local maxima and minima. It would be of interest to produce some simulated graphs of this type by introducing controlled amounts of "noise" to some artificial "data", to find out what an ideal plot would look like and what the effects of small rms errors are on its form. A finer grid would no doubt help, as well.

65

c. Other investigations One other investigation [99] claims to have found isotropy in a quasicrystal at a significant level; in that paper, sound velocities along the twofold and fivefold directions were the same within 0.2%, which translates to an elastic anisotropy of about 0.4%, or 0.004. In addition, the shear wave velocity along the twofold direction was measured for a variety of orientations by changing the polarization vector of the transducer, and was found to be constant within 0.01%. Unfortunately, this does not provide very good evidence for isotropy. For one thing, the maximum variation in sound velocity may not occur in the specific directions measured. If a cubic crystal system is oriented with the twofold axes of an icosahedral quasicrystal, a fivefold axis is found along the ⟨530⟩ crystal direction. If the sound velocities of tungsten are evaluated along the ⟨100⟩ and ⟨530⟩ directions, one finds that the variation is only about 0.2%. The invariance of the shear velocity along ⟨100⟩ is meaningless because shear propagation is isotropic in the plane perpendicular to ⟨100⟩ for any cubic crystal.

The curious reader may also want to consider the actual method used to make such precise sound velocity measurements. To quote from [99]:

> The sample was cut with faces perpendicular to a twofold and a fivefold axis...The sample thicknesses were 1 cm and 0.5 cm for the twofold and fivefold axes, respectively. Ultrasonic measurements were made along two different axes, but in the same sample. Both longitudinal and shear velocities have been measured accurately by using a resonance method. A piezoelectric transducer is bonded on one face of the sample in order to excite ultrasonic standing waves between the bonded and the opposite flat parallel faces. *If the bonding is loose enough for the sample to be free of stress* [emphasis added], the resonance frequencies are given by
>
> $$f = n\frac{V}{2l},$$
>
> where V is the phase velocity of the wave...n is an integer, l the thickness of the sample. (from [99])

In other words, a transducer bonded to a face of a sample was coupled weakly enough to guarantee with precision a stress-free boundary, and the free resonances of an odd-shaped sample with an aspect ratio of 0.5 formed a harmonic series. The author finds this implausible, and so is unsure what to make of this measurement.

d. Absolute comparisons Since the focus of this experiment was on the measurement of anisotropy, no effort was made to establish firmly the absolute accuracy of the elastic constants determined. Still, it is useful to know how the present values compare to those of other investigators. Satish *et al.* [86] measured the Rayleigh wave velocity in an AlCuLi quasicrystal, while Reynolds *et al.* [85] measured the velocity of plane ultrasonic pulses. It is therefore convenient to calculate a Rayleigh wave velocity from the present data and from that of Reynolds *et al.*, and compare to the results of Satish. The Rayleigh wave velocity v_r is a root of the equation [98]: $r^3 - 8r^2 + (24 - 16g)r - 16(1 - g) = 0$, where $r = \frac{v_r}{v_s}$, v_s being the speed of shear waves, and $g = \frac{1 - 2\nu}{2(1 - \nu)}$, ν being Poisson's ratio.

Using the values of c_{ij} from Table XXIV, the Rayleigh wave velocity v_r in sample QX1 is predicted to be 3.79×10^5 cm/sec, while from Reynold's data v_r is predicted to be 3.49×10^5 cm/sec. The average velocity measured directly by Satish *et al.* was 3.66×10^5 cm/sec. The samples in all three cases were from different sources, and there is apparently a fair amount of variability in them.

E. Conclusions

The measurement of anisotropy in nearly isotropic substances is an experimental challenge, which requires the ability to probe material properties in many directions in as few measurements as possible. Resonant ultrasound spectroscopy appears to be ideally suited to this task, able to find elastic constants with relative accuracy in the tenths of percent or better.

In conclusion, the AlCuLi quasicrystal has been shown to be significantly more isotropic than conventional crystals, in accordance with theoretical predictions. The R-phase periodic approximant has been shown to possess an anisotropy which is very small, but readily measured with resonant ultrasound spectroscopy. In future research other quasicrystal alloys and their periodic approximants could be investigated, including studies of the temperature and pressure dependence of their elastic constants. The latter measurement might provide evidence of anisotropy in the higher-order elastic constants for the quasicrystal, as predicted by theory [27]. In addition, measurements on more "perfect" quasicrystals such as AlCuFe may confirm the small residual anisotropies observed in the present work as evidence of anisotropic phason strains in AlCuLi.

VI. EFFECTS OF SAMPLE PREPARATION ERRORS

One of the great advantages of a resonant technique such as RUS is that the coupling between the sample and the transducers can be made very weak, so that only properties of the sample are reflected in the measured resonance frequencies. However, as has been discussed in Section II, the frequencies alone cannot uniquely determine all the sample parameters at once; in addition, the accuracy in the determination of any given parameter is

improved if reliable knowledge about other parameters is available. Thus, for an accurate determination of elastic constants, it is important to have good knowledge of the sample density and geometry.

In most cases, the sample is assumed to be a perfect sphere or rectangular parallelepiped, so knowing the geometry is reduced to knowing the characteristic dimensions. Clearly, though, the geometry of an actual sample is likely to be more complicated, due to small errors in sample preparation. In previous research, these errors were ignored, on the basis that careful sample preparation should minimize such errors, and the effects of small geometric perturbations on the frequencies should be negligible; but the precise meaning of "negligible" has never been firmly established. Furthermore, in very precise measurements or measurements under high temperature or pressure [101], these effects may not be negligible at all.

A. Types of Preparation Errors

Unfortunately, it is not entirely straightforward to quantify the errors in sample preparation, or their effects. One may begin by considering different categories of preparation errors, and their relative importance. Since the work in this paper is primarily concerned with rectangular parallelepipeds, the most likely types of errors that may occur when cutting and polishing a sample into a rectangular parallelepiped are considered:

- *Surface Roughness.* Surface roughness may be effectively gauged by eye, under a microscope; also, the wavelengths of sound are so much longer than the scale of the surface roughness, which is assumed to be random, that the effects of each individual surface scratch or pit should essentially cancel out.

- *Broken or rounded corners and edges, rounded faces.* These are also easy to see (if not prevent); however, their presence may well lead to systematic errors in the frequencies. For instance, if one corner is broken but the others are intact, torsional modes may be affected more than dilatational modes (due to the loss of rotational inertia at that corner).

- *Non-perpendicular faces.* A systematic deviation such as a non-perpendicular side may well have a systematic effect on the frequencies; unlike the above items, these are very hard to detect visually, even under a microscope.

Of the three categories, non-perpendicular (or non-parallel) sides are potentially the most troublesome. They can be expected to be systematic in their effect on the frequencies, and yet are easily overlooked. A surface roughness of $\sim 1\,\mu$m on the surface of a 1 mm sample has a quite visible effect on the quality of reflected light from that surface; but a deviation of $\sim 1\mu$m/mm in parallelism

or perpendicularity, or even ten times that (about 0.5°) is rather difficult to see.

B. Skewed or tilted sides

For the rectangular parallelepiped samples so often used in RUS, it would appear useful to calculate the shifts in the natural frequencies, and the subsequent effects on the accuracy of a RUS measurement, that could result from sample sides that are slightly nonparallel or nonperpendicular.

1. Perturbation methods

One might first look for a perturbation theory to facilitate such a calculation; for instance, a first-order perturbation theory for elastic spheres was developed by geophysicist J. Woodhouse [61], [100] for use in analyzing the free vibrations of the spheroidal Earth. This was subsequently used by Oda *et al.* [101] when studying prepared spheres of anisotropic crystals, which tended to become aspherical under high pressures.

Woodhouse's theory can be understood reasonably well as follows: Consider the now familiar expression for the eigenfrequency of an elastic solid having elastic tensor c and volume V as a ratio of integrals (Rayleigh's principle):

$$\omega^2 = \frac{\displaystyle\int_V c_{ijkl} \frac{\partial \psi_i}{\partial x_j} \frac{\partial \psi_k}{\partial x_l} \, dV}{\displaystyle\int_V \rho \, \psi_i \psi_i \, dV} \ . \tag{66}$$

Now suppose that the surface is perturbed slightly by an amount $h(x,y,z)$, where h is everywhere normal to the unperturbed surface S. Then the volume becomes

$$V' = \int_V dV + \int_S h \, dS \ . \tag{67}$$

We assume that if the sample is of characteristic dimension l, then $h \ll l$ and for the lower eigenmodes, $h \ll \lambda$. Then to a first approximation, displacement and strain are constant in the perturbed region, such that

$$(\omega')^2 = (\omega + \delta\omega)^2 \simeq$$

$$\frac{\displaystyle\int_V c_{ijkl} \frac{\partial \psi_i}{\partial x_j} \frac{\partial \psi_k}{\partial x_l} \, dV + \int_S c_{ijkl} \frac{\partial \psi_i}{\partial x_j} \frac{\partial \psi_k}{\partial x_l} h \, dS}{\displaystyle\int_V \rho \, \psi_i \psi_i \, dV + \int_S \rho \, \psi_i \psi_i \, h \, dS} \ , \tag{68}$$

where ψ and its derivatives are evaluated on the *unperturbed* surface S.

Noting that $\int_V \rho\,\psi_i\psi_i\,dV \gg \int_S \rho\,\psi_i\psi_i\,h\,dS$, we can rewrite the denominator of (68) as

$$\int_V \rho\,\psi_i\psi_i\,dV + \int_S \rho\,\psi_i\psi_i\,h\,dS$$

$$= \int_V \rho\,\psi_i\psi_i\,dV \left[1 + \frac{\displaystyle\int_S \rho\,\psi_i\psi_i\,h\,dS}{\displaystyle\int_V \rho\,\psi_i\psi_i\,dV} \right]$$

$$= \int_V \rho\,\psi_i\psi_i\,dV\,(1 + \varepsilon)\,, \tag{69}$$

where $\varepsilon \ll 1$. Dividing both the numerator and denominator of Eq.(68) by $\int_V \rho\,\psi_i\psi_i\,dV$, and multiplying through by $(1+\varepsilon)$, we obtain

$$(\omega + \delta\omega)^2(1+\varepsilon) \simeq \frac{\displaystyle\int_V c_{ijkl}\frac{\partial\psi_i}{\partial x_j}\frac{\partial\psi_k}{\partial x_l}\,dV}{\displaystyle\int_V \rho\,\psi_i\psi_i\,dV}$$

$$+ \frac{\displaystyle\int_S c_{ijkl}\frac{\partial\psi_i}{\partial x_j}\frac{\partial\psi_k}{\partial x_l}\,h\,dS}{\displaystyle\int_V \rho\,\psi_i\psi_i\,dV}\,; \tag{70}$$

recognizing ω^2 on the right hand side, we obtain

$$\left(\omega^2 + 2\omega\delta\omega + (\delta\omega)^2\right)(1+\varepsilon)$$

$$\simeq \omega^2 + \frac{\displaystyle\int_S c_{ijkl}\frac{\partial\psi_i}{\partial x_j}\frac{\partial\psi_k}{\partial x_l}\,h\,dS}{\displaystyle\int_V \rho\,\psi_i\psi_i\,dV}\,. \tag{71}$$

To first order, then:

$$2\omega\delta\omega + \varepsilon\omega^2 \simeq \frac{\displaystyle\int_S c_{ijkl}\frac{\partial\psi_i}{\partial x_j}\frac{\partial\psi_k}{\partial x_l}\,h\,dS}{\displaystyle\int_V \rho\,\psi_i\psi_i\,dV}\,; \tag{72}$$

using $\varepsilon = \int_S \rho\,\psi_i\psi_i\,h\,dS / \int_V \rho\,\psi_i\psi_i\,dV$ from Eq.(69), we finally obtain:

$$2\omega\delta\omega \simeq \frac{\displaystyle\int_S \left(c_{ijkl}\frac{\partial\psi_i}{\partial x_j}\frac{\partial\psi_k}{\partial x_l} - \rho\omega^2\psi_i\psi_i\right)h\,dS}{\displaystyle\int_V \rho\,\psi_i\psi_i\,dV}\,. \tag{73}$$

This first-order perturbation theory allows one to conveniently estimate the perturbed eigenvalues in terms of the original eigenvalues and eigenfunctions.
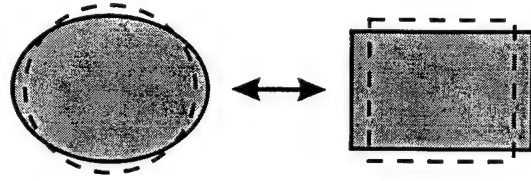
FIG. 52. Two analogous surface perturbations; on the left a sphere is perturbed into a spheroid, and on the right a box is elongated, changing its aspect ratio.
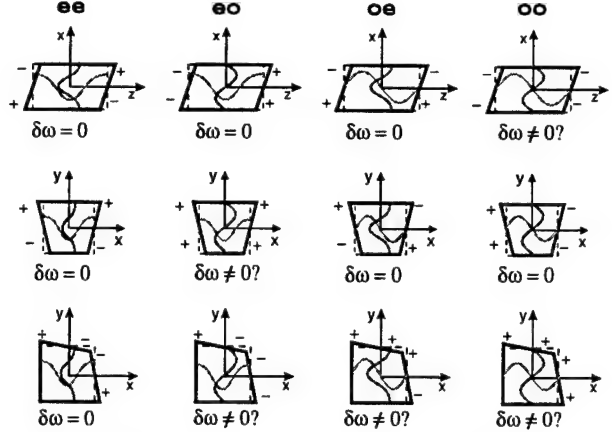
FIG. 53. Contributions to a first-order shift in natural resonance frequency of an elastic object due to several different types of boundary perturbations, as function of the parity of the bracketed terms in the numerator of (73) (which are then multiplied by the normal displacement h). The $+$ and $-$ symbols near the corners indicate the sign that the integral over that portion of the perturbed volume nearest the symbol will most likely have.

This method has been used with success by Woodhouse [61], Oda et al. [101] and others for aspherical corrections to nearly spherical samples; note that a change in asphericity of a spheroid may be considered analagous to a change in aspect ratio of a box (Fig. 52).

Whether tilted sides can be expected to produce first-order shifts in frequency may be addressed by considering the numerator of (73) for various cases. Fig. 53 shows that by considering the sign of h and the parity of $\frac{\partial\psi_i}{\partial x_j}\frac{\partial\psi_k}{\partial x_l}$ and/or $\rho\omega^2\psi_i\psi_i$ from (73), one might expect certain modes to exhibit first-order shifts in frequency, especially if two adjacent sides are tilted in opposite directions (a "kite" shape). Other modes, however, will have frequency shifts that are inherently second order, (for which the Woodhouse formula predicts $\delta\omega = 0$). If these latter shifts dominate for a particular case, then the forgoing analysis will, of course, be inadequate to assess the effects. A second-order perturbation theory could perhaps be applied; Morse [102] considered the problem of a membrane with a tilted edge, and found a stable second-order perturbation theory; however, the calculations are considerably more involved than those above.

If a change in aspect ratio (that leaves the volume

68
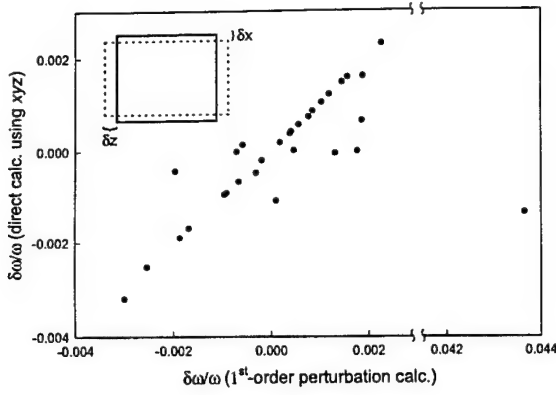
FIG. 54. The relative shifts $\delta\omega/\omega$ due to a change of 0.1% in aspect ratio of an elastic parallelepiped, calculated by both the xyz method directly and by a first-order perturbation theory due to Woodhouse. The elastic object is similar to a quasicrystal sample described in previous sections.

unchanged) is a first-order perturbation, we can calculate the shifts in ω both by Woodhouse's method and by our standard Rayleigh-Ritz forward calculation using the perturbed dimensions, thus checking the validity of the former for elastic boxes. If an elastic rectangular parallelepiped of nominal dimensions $2a$, $2b$ and $2c$ is perturbed by an amount δz in the z-direction, the adjusted z-dimension is $2c + 2\delta z$. To keep the volume constant, $ac = (c+\delta z)(a-\delta x)$, and it follows that $\delta x = a\delta z/(c+\delta z)$. Therefore, calculations using Eq.(37), first with dimensions a, c, then with $a - \delta x, c + \delta z$ to get the shifts $\delta\omega$, should agree with the $\delta\omega$ calculated with (73) using $+\delta z$ and $-\delta x$ as the surface perturbations.

Fig. 54 shows a comparison between these two approaches. Perhaps surprisingly, what works well for a spheroid does not work well for a block—many discrepancies are seen between the $\delta\omega$ calculated with the first-order approximation, and the presumably more accurate values obtained by subtracting one full forward calculation from another. Even without the one anomalously high error, the typical errors are probably too large to be suitable for RUS analysis.

2. Direct calculation with the Ritz method

There is, of course, another approach, which is to attempt to directly calculate the frequencies of the perturbed solid using Rayleigh-Ritz. There is no obvious barrier to doing so, and in particular the success of the "xyz algorithm" [103] in finding the normal modes of elastic solids for a great variety of shapes (as mentioned
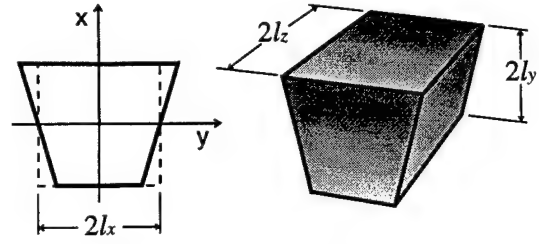
FIG. 55. A trapezium which is a slight perturbation away from a rectangular parallelepiped of dimensions $2l_x$, $2l_y$, $2l_z$. In the present orientation, the flared sides coincide with the lines $x = \pm(l_x + \alpha y)$ in the xy plane, where α is the tangent of the angle between the perturbed and unperturbed sides.

in Section II) seems to suggest itself as a starting point.[5]

One may imagine a rectangular parallelepiped, centered on the origin, perturbed into a trapezoidal prism as suggested in Fig. 55. Accordingly, in the Rayleigh-Ritz matrix eigenvalue equation (Eq.(37) from Section II),

$$\mathbf{\Gamma} \, \mathbf{a} = \omega^2 \, \mathbf{E} \mathbf{a} \, ,$$

the matrix elements are:

$$\Gamma_{mn} = \int_{-l_3}^{l_3} \int_{-l_2}^{l_2} \int_{-l_1-\alpha x_2}^{l_1+\alpha x_2} c_{ikjl} \frac{\partial}{\partial x_k} \left(x_1^{\,p_m} x_2^{\,q_m} x_3^{\,r_m} \right)$$

$$\frac{\partial}{\partial x_l} \left(x_1^{\,p_n} x_2^{\,q_n} x_3^{\,r_n} \right) \, dx_1 \, dx_2 \, dx_3 \qquad (74)$$

and

$$E_{mn} = \int_{-l_3}^{l_3} \int_{-l_2}^{l_2} \int_{-l_1-\alpha x_2}^{l_1+\alpha x_2}$$

$$\rho \left(x_1^{\,p_m+p_n} x_2^{\,q_m+q_n} x_3^{\,r_m+r_n} \right) \delta_{ij} \, dx_1 \, dx_2 \, dx_3 \, . \qquad (75)$$

The reader may recall from Section II that:

$$m, n \in 3N; \quad i, j = 1, 2, 3$$

and

$$\psi_i = \sum_{\mu=1}^{N} a_{\mu,i} \, \phi_\mu = \sum_{\mu=1}^{N} a_{\mu,i} \, x^{p_\mu} y^{q_\mu} z^{r_\mu}$$

where

$$p + q + r \le R, \quad N = (R+3)(R+2)(R+1)/6 \, .$$

---

[5]It is of interest to note that Oda *et al.* discovered the work of Visscher *et al.* featuring the "xyz algorithm" after the former had already worked out the first-order perturbation theory for an anisotropic spheroid; in their paper [101] Oda *et al.* compare frequencies of anisotropic spheroids calculated using the perturbation method versus xyz, and show that the two are in excellent agreement.

TABLE XXV. The properties of an elastic rectangular parallelepiped conjured up for study in the present and following sections. Its properties are made to be similar to those of a quasicrystal studied in Section V.

$c_{11} = 1.1$ Mbar	$2l_x = 0.4221$ mm	
$c_{12} = 0.3$ Mbar	$2l_y = 0.4221$ mm	$\rho = 2.359$ g/cc
$c_{44} = 0.4$ Mbar	$2l_z = 0.5761$ mm	

As in Section II, we prefer to use the scaled basis set,

$$\phi_{pqr} = \left(\frac{x}{l_x}\right)^p \left(\frac{y}{l_y}\right)^q \left(\frac{z}{l_z}\right)^r = \hat{x}^p \, \hat{y}^q \, \hat{z}^r \, .$$

It is evident from the simplicity of the basis set that both the Γ_{mn} and the E_{mn} integrals will have the form:

$$\int_V \phi(\hat{x}, \hat{y}, \hat{z}) \, dV = l_x l_y l_z \int_{-1}^{1} \int_{-1}^{1} \int_{-1-\varepsilon\hat{y}}^{1+\varepsilon\hat{y}} \hat{x}^p \, \hat{y}^q \, \hat{z}^r \, d\hat{x} \, d\hat{y} \, d\hat{z} \, ,$$

where $\varepsilon = \alpha(l_y/l_x)$.

Because the integration limits on $\hat{x}$ contain the tilt in the sides, the resulting expressions are more complex than those for a simple rectangular parallelepiped. It is found that:

$$\int_V \phi_{pqr}(\hat{x}, \hat{y}, \hat{z}) \, dV$$

$$= l_x l_y l_z \int_{-1}^{1} \int_{-1}^{1} \int_{-1-\varepsilon\hat{y}}^{1+\varepsilon\hat{y}} \hat{x}^p \, \hat{y}^q \, \hat{z}^r \, d\hat{x} \, d\hat{y} \, d\hat{z}$$

$$= \frac{8 \, l_x l_y l_z}{(p+1)(q+1)(r+1)}$$

$$\begin{bmatrix} 1 + \sum_{n=3,5,7}^{p+2} \binom{p+1}{n} \varepsilon^{n-1} & p,r,q \text{ even} \\ \sum_{n=2,4,6}^{p+2} \binom{p+1}{n} \varepsilon^{n-1} & p,r \text{ even}; q \text{ odd} \\ 0 & \text{otherwise.} \end{bmatrix} .$$

This does tend to "densen" the matrices a bit and worsen their conditioning; but with the scaled basis set (x/l_x etc.) and double precision, the matrices are still far from being singular, and a solution is readily obtained with the aid of a generalized eigensystem routine such as DSYGV in the ESSL library [104].

With an eye toward applying these sort of calculations to the quasicrystal measurement of Section V, it is useful to introduce a fictitious elastic object, very similar to the quasicrystal sample ("QX1"), that will then be used in the subsequent analyses. We consider an object with the properties given in Table XXV. All the proceeding figures of frequency shift versus angle and so on, show the properties of this object (perturbed in some specific way), unless otherwise specified.
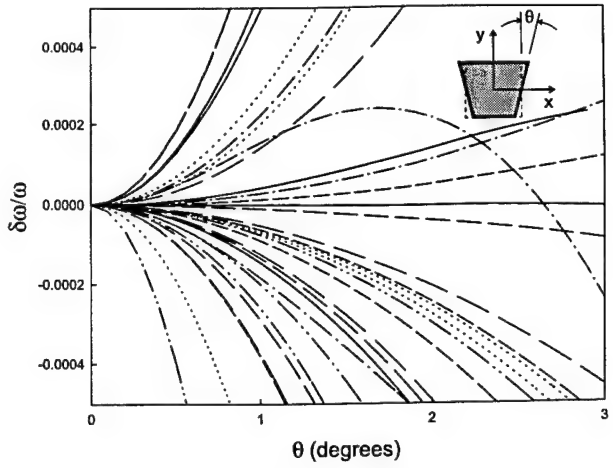
FIG. 56. Fractional frequency shifts for the lower normal mode resonances of an elastic trapezium, as a function of the angle as shown in the figure.

Figure 56 shows the frequency shifts of the lowest 30 modes versus tilt angle for the elastically isotropic sample of Table XXV; these modes all exhibit essentially quadratic behavior. Without similar calculations for comparison, alternate solutions are sought to verify that the above results are correct. One obvious option is to repeat the above calculation, but with a different coordinate system; for instance, the coordinates (or the object) from Fig. 55 could be rotated 45° about z so that the trapezium appears as four adjacent triangular prisms, one in each quadrant (see Fig. 57) (this only works if the sample is initially square, that is, the x and y dimensions are equal). This is equivalent to the previous case, as long as the nominal edge lengths are adjusted to keep the volume constant. If the sample is initially square, with $2l_x = 2l_y = 2l_0$, then its unperturbed volume is $8l_0^2 l_z$. This can be held constant by rescaling the x and y edge lengths as the angle changes, according to

$$l_x = l_y = l' \equiv \frac{2l_0 \tan(\pi/4 - \theta)}{1 + \tan(\pi/4 - \theta)} \, .$$

With $\beta = \tan(\pi/4 + \theta)$, it is found that:

$$\int_V \phi_{pqr}(\hat{x}, \hat{y}, \hat{z}) \, dV =$$

$$2 \frac{\left((-1)^p + \beta^{-(p+1)} - (-\beta)^{(q+1)} - (-\beta)^{(p+q+2)} \right) p! q!}{(p+q+2)! \, (r+1)}$$

$$\tag{76}$$

if r is even and zero otherwise.

This approach differs algorithmically from the former solution, but should produce nearly identical results numerically, if the method is correct. Figure 58 shows that the two solutions are in excellent agreement.

70
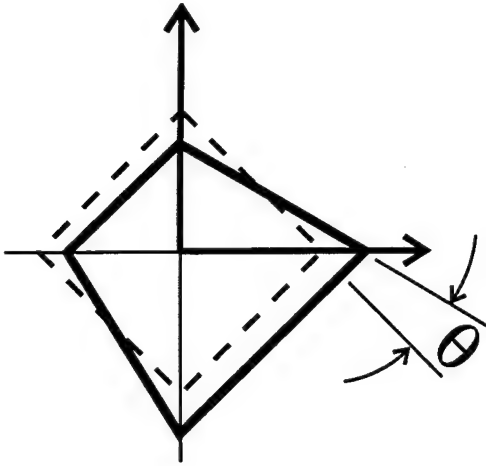
FIG. 57. A trapezium of the sort in Fig. 55, oriented so that the object forms 4 adjacent triangular prisms, one in each quadrant. The unperturbed parallelepiped must be square on end for this to work (without transforming the coordinates).
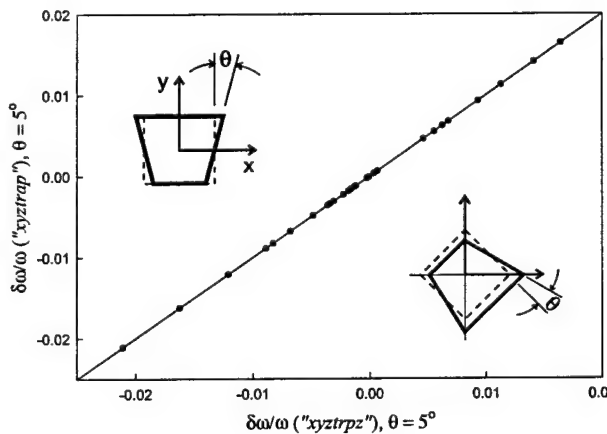
FIG. 58. A comparison between two calculations of the normal mode shifts of a perturbed elastic object, using the xyz method for two different orientations. The results from computer program **xyztrap** are associated with the vertical axis and the geometry shown in the upper left; program **xyztrpz** (**xyz** method for adjacent **tr**iangular **p**risms composing a trape**z**ium) is associated with the horizontal axis and the geometry shown in the lower right.
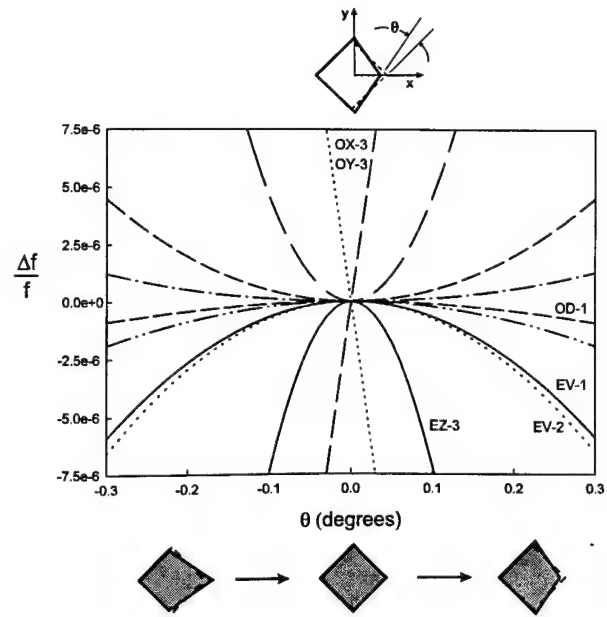
FIG. 59. Fractional frequency shifts for selected modes in the spectrum of a fictitious sample very similar to the quasicrystal sample of Section V, due to one type of surface perturbation away from an ideal rectangular parallelepiped. This is one type of perturbation the real sample was found, by optical measurements, to posess. Some of the modes that correspond uniquely with those of the unperturbed object are given. The two linear shifts are from an originally degenerate pair that has split.

With this assurance that the xyz method obtains the correct resonance frequency shifts due to tilted specimen sides, one can proceed to evaluate how these frequency shifts may affect a measurement. One may first examine the shifts in frequency caused by other types of perturbative surface tilts; Figs. 60 and 59 show some more examples. The perturbation in Fig. 59 is another example of sticking together triangular prisms, and as such only works for a square-ended sample. Again, the nominal dimension must be adjusted to keep the volume constant; if initially $l_x = l_y = l_0$, this is accomplished by defining a new edge length l' such that:

$$l' = l_0 \left(\frac{2\tan\theta}{\tan\theta + 1} \right).$$

Figure 61 shows a portion of the spectrum of the elastic object versus angle for the "kite" perturbation of Fig. 59. Since the changes in frequency are very small, only a small part of the spectrum is shown. This figure is included so one may observe the mode crossings, and at least one mode repulsion, in the spectrum.

Figure 59 in shows some shifts that are linear in θ as predicted in Fig. 53. For small angles, these first-order shifts will dominate. It is significant to note that the linear shifts in this figure (and all other linear shifts in the spectrum) come in symmetric (or properly, antisym-

71
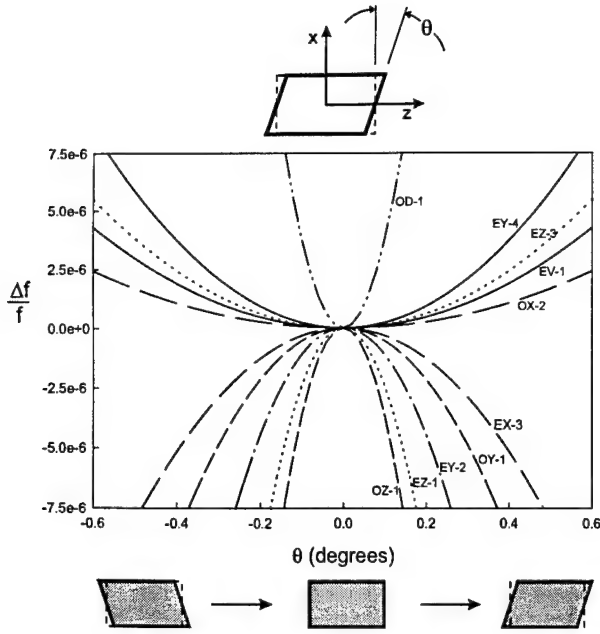
FIG. 60. Fractional frequency shifts for selected modes in the spectrum of a fictitious sample very similar to the quasicrystal sample of Section V, due to one type of surface perturbation away from an ideal rectangular parallelepiped. This is one type of perturbation the real sample was found, by optical measurements, to posess.
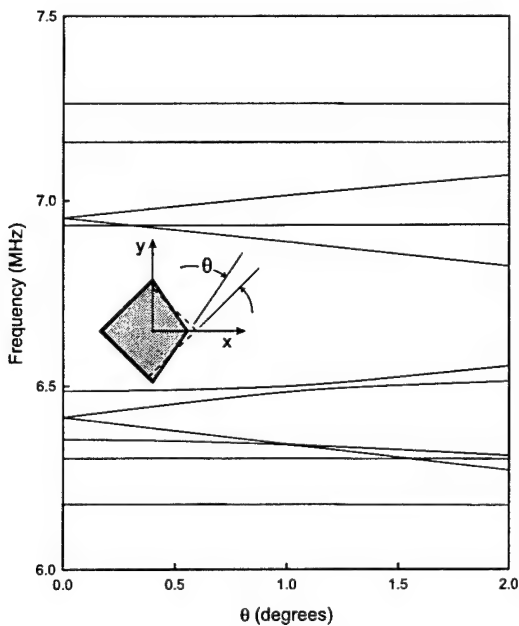
FIG. 61. A portion of the spectrum of a fictitious isotropic elastic object peturbed as shown in the figure, as a function of perturbation angle. Note the multiple mode crossings, and at least one prominent mode repulsion.
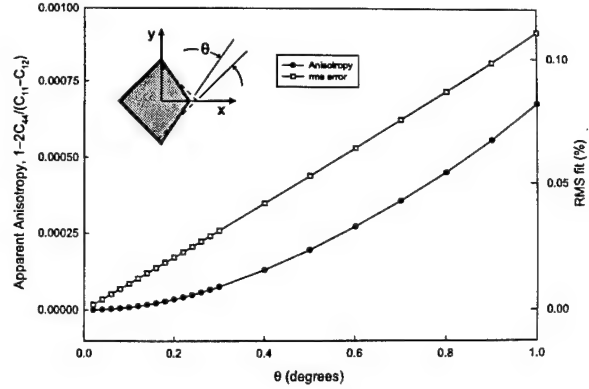
FIG. 62. The apparent elastic anisotropy implied by synthetic data generated by calculating the theoretical frequencies of an elastically isotropic object with a perturbed boundary, and fitting the data with a model that assumes the object is unperturbed. In this case, the object is a rectangular parallelepiped and the perturbation consists of "squashing" the object along the diagonal, as shown.

metric) pairs, from the splitting of degenerate modes (see also Fig. 61). Thus if such pairs of degenerate frequencies, split due to tilted sides, were observed in an actual measurement, the tilted sides would be well accounted for by averaging each pair (a common practice in any case).

The most immediately pertinent information gathered from these calculations is that tilts of a few tenths of a degree could produce frequency shifts in the tenths of a percent, which is significant (since the agreement between theoretical and experimental frequencies is typically 0.1% or better in a RUS measurement). To see how much these shifts might actually perturb an elastic constant determination, one may do the following:

1. Generate some synthetic data by calculating the frequencies of a fictitious, slightly perturbed sample whose elastic properties are known (or assumed).

2. With a search or minimization algorithm, fit the synthetic data, with the assumption that the sample is an unperturbed rectangular parallelepiped, and using the elastic properties of the sample from item 1 as the starting point in the search.

This enables at least a rough assessment of how the perturbed frequencies propagate through the inverse problem and consequently perturb the determined elastic constants, if at all. Figure 62 shows the result of this process for one type of perturbation, on the determination of the elastic anisotropy (a quantity relevant to quasicrystals, as seen in the previous section). Due to the numerous mode crossings in the spectrum, proper mode assignment is crucial when fitting the frequencies, as always. As one

72

FIG. 64. The trapezoid of Fig. 55, showing lines of constant η that include the perturbed boundaries as level surfaces.
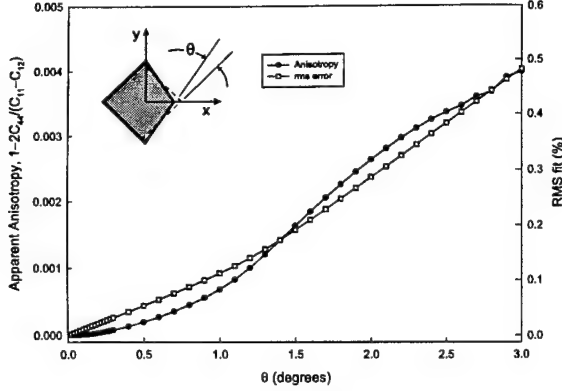
FIG. 63. The same as Fig. 62, for a larger range of perturbation angles.

might expect, as the "geometric anisotropy" increases, the apparent elastic anisotropy also increases.

The anisotropy and RMS error both increase monotonically, for the case considered here; in addition, the anisotropy curve appears quadratic, showing that even though some frequencies may vary as θ, the c_{ij} still vary as θ^2. This seems reasonable, since in general, frequency $\propto \sqrt{c_{ij}/\rho}$. The rms error, on the other hand, increases linearly.

If slightly larger angles are considered, up to 3°, an interesting thing happens. As shown in Fig. 63, the trends of both ϵ_z vs θ and rms vs θ change, perhaps due to mode repulsion in the spectrum (see Fig. 61).

A less obvious source of trouble in this process should be mentioned, if only briefly. While the elastic constants generally are proportional to θ^2, the edge lengths of a sample are proportional to θ. Edge lengths are typically included in RUS fits, as mentioned in Section I, because the frequencies can be measured to better precision than can the dimensions. However, allowing the geometry to vary while fitting the data does raise some interesting questions, and these questions are all the more pertinent if tilted sides are a possibility. It has been shown that even for so simple a system as a taut membrane, the shape cannot be deduced uniquely from the spectrum (see [105], [106]). It seems at least conceivable that for a sensitive measurement, if the shape is not known precisely, this lack of knowledge could lead to ambiguity in the final result.

3. Generalized method for arbitrary tilts in all 6 sides

When a real rectangular parallelepiped sample is considered, which may have arbitrary tilts in all six sides, the direct calculation with xyz becomes a bit unwieldy. All six planes which form the volume boundaries now depend on all three independent variables x, y, and z. One could try breaking up the volume into a number of separate integrals, but it is not clear that this would be at all straightforward.
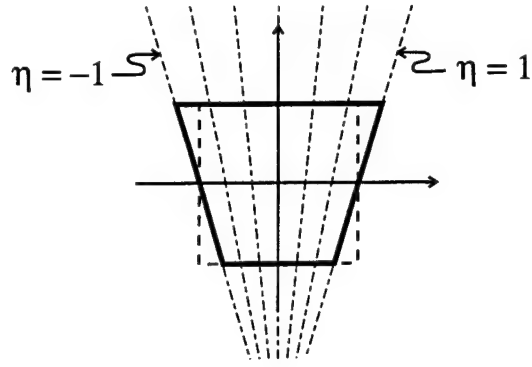
On the other hand, one may instead try using a transformed basis set that includes the perturbed boundaries as level surfaces. If we again consider the trapezoidal prism, we see that the tilted sides can be represented as $x/(l_x + \alpha y) = \pm 1$, or lines of constant η , where

$$\eta = \frac{x}{l_x + \alpha y} = \frac{(x/l_x)}{1 + \varepsilon(y/l_y)}$$

and

$$\varepsilon = \frac{\alpha l_y}{l_x} \tag{77}$$

The x-coordinate is replaced by a new coordinate η that "fans out", in a sense mapping the old coordinates on to the new shape (Fig. 64). Then the transformed coordinates are η, $\hat{y}$, and $\hat{z}$, where

$$x = \eta \, l_x \, [1 + \varepsilon(y/l_y)]$$
$$y = l_y \hat{y}$$
$$z = l_z \hat{z} \tag{78}$$

and

$$J\left(\frac{x,y,z}{\eta,\hat{y},\hat{z}}\right) = \begin{vmatrix} l_x\,[1 + \varepsilon(y/l_y)] & 0 & 0 \\ \dfrac{\eta l_x \varepsilon}{l_y} & l_y & 0 \\ 0 & 0 & l_z \end{vmatrix}. \tag{79}$$

A basis can then be chosen, where all the boundaries are level surfaces:

$$\phi_{pqr} = \eta^p \, \hat{y}^q \, \hat{z}^r = \left(\frac{(x/l_x)}{1 + \varepsilon(y/l_y)}\right)^p \left(\frac{y}{l_y}\right)^q \left(\frac{z}{l_z}\right)^r . \tag{80}$$

The simplicity of the integrals in the xyz algorithm is not preserved here; in particular, the Γ integrals must be evaluated case by case, with some approximation for
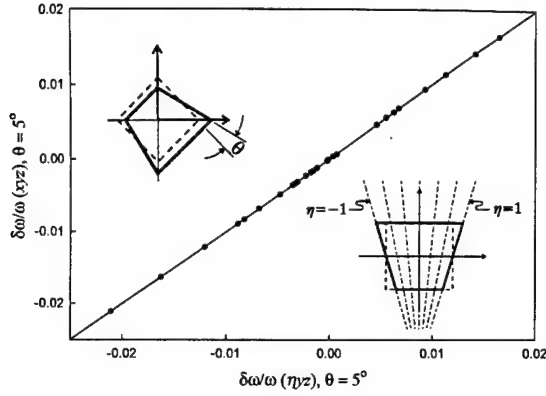
FIG. 65. Fractional frequency shifts, due to a trapezoidal perturbation of an originally square-ended elastic block, calculated using two different algorithms: the xyz basis set with the geometry shown in the upper left corner, and the ηyz basis set with the geometry shown in the lower right corner.

small angles included. However, matrix $\mathbf{E}$ is rather simple to compute. If we let $p_m + p_n = p$, $q_m + q_n = q$, and $r_m + r_n = r$, then

$$
\begin{aligned}
E_{mn} &= \int_{-l_z}^{l_z}\int_{-l_y}^{l_y}\int_{-l_x-\alpha y}^{l_x+\alpha y} \\
&\quad \left(\frac{(x/l_x)}{1+\varepsilon(y/l_y)}\right)^p \left(\frac{y}{l_y}\right)^q \left(\frac{z}{l_z}\right)^r \delta_{ij}\, dx\, dy\, dz \\
&= \int_{-1}^{1}\int_{-1}^{1}\int_{-1}^{1} \eta^p\, \hat{y}^q\, \hat{z}^r\, J\!\left(\frac{x,y,z}{\eta,\hat{y},\hat{z}}\right)\, d\eta\, d\hat{y}\, d\hat{z} \\
&= \int_{-1}^{1}\int_{-1}^{1}\int_{-1}^{1} \eta^p\, \hat{y}^q\, \hat{z}^r\, [1+\varepsilon\hat{y}]\, l_x l_y l_z\, d\eta\, d\hat{y}\, d\hat{z}\, .
\end{aligned}
\tag{81}
$$

With $V_0 = 8 l_x l_y l_z$, one obtains

$$
E_{mn} = \begin{cases}
\dfrac{V_0}{(p+1)(q+1)(r+1)} & p,q,r \text{ even} \\[2ex]
\dfrac{\varepsilon V_0}{(p+1)(q+2)(r+1)} & p,r \text{ even, } q \text{ odd} \\[2ex]
0 & \text{otherwise.}
\end{cases}
\tag{82}
$$

This is much simpler than the result obtained with the xyz basis set, and produces a better conditioned matrix.

The veracity of this approach can be substantiated to some degree by comparing frequency shifts calculated with the xyz method and the present method, which one might call the ηyz method; this is represented graphically in Fig. 65. Apparently the two are in excellent agreement.

It is possible to generalize the above method to apply to an arbitrary intersection of planes that is a small perturbation away from a rectangular paralellepiped. As an example, consider a trapezoidal prism whose sides tilt at
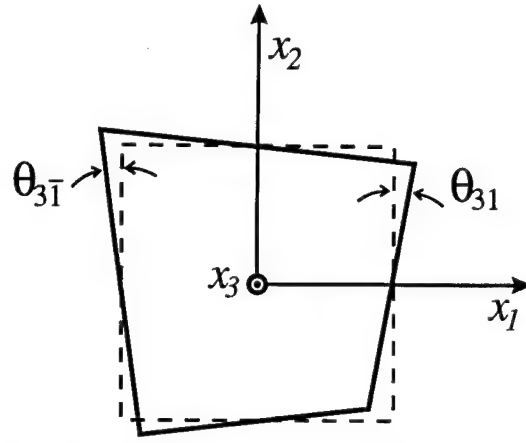
FIG. 66. A nearly rectangular quadrilateral, whose sides vary from square by arbitrary angles. This could represent the intersection of the $x_1 x_2$ plane with a nearly rectangular parallelepiped, whose sides tilt at arbitrary angles.

different angles. A coordinate that "splits the difference" can be obtained so that the sides are still level surfaces, e.g. $\phi_{pqr} = \xi^p\, \hat{y}^q\, \hat{z}^r$, where

$$
\xi = \frac{x - \dfrac{\alpha_1+\alpha_2}{2}y}{l_x + \dfrac{\alpha_1-\alpha_2}{2}y} = \frac{\hat{x} - \overline{\varepsilon}\hat{y}}{1 + (\varepsilon_1-\varepsilon_2)/2\,\hat{y}}\, ;
\tag{83}
$$

here $\varepsilon_i = \alpha_i(l_y/l_x)$, $\overline{\varepsilon} = (\varepsilon_1 + \varepsilon_2)/2$.

To extend this approach to an arbitrary intersection of planes, consider how one might measure the orientation of these planes experimentally. The method mentioned in Section V is fairly straightforward and repeatable; it consists of mounting a sample on a goniometer which is in turn mounted in a precision turntable, such as a machine shop dividing head that one might use for drilling a circular array of holes. A laser beam is reflected from the polished sample faces, as the sample is rotated in precise 90° increments. In this manner, the deviation of each side from perpendicularity in the plane of rotation is indicated by the horizontal deflection of the laser beam.

Fig. 66 shows a schematic view of a sample with arbitrarily tilted sides. Here we define the unperturbed dimensions so that the tilted sides intersect the middle of each unperturbed side. This simplifies the mathematics, although it does mean that the volume will change very slightly with angle. The volume change will be negligible for small angles, and can be accounted for in the inverse calculation by letting the edge lengths vary as free parameters (which is frequently done, as has been mentioned in earlier sections). These edge lengths are the ones that would in fact be measured, if one used pointed calipers at the center of each face, which is not unreasonable. If we suppose that we are measuring the deviation from perpendicularity of each side as mentioned above, then we can devise a sensible indexing scheme so that the equations of each plane can be represented in terms

74

of these angles. If we are looking down the x_3 axis as shown, and measuring the deflection of a beam incident along the x_1 axis, then the angle of deflection may be indexed as θ_{31}. Likewise, the angle of the side opposite, where the beam is coming from the $-x_1$ direction, may be indexed as $\theta_{3\bar{1}}$.

If we index the slope of each side in a given plane in a similar manner, i.e., $\tan\theta_{ij} = \Delta_{ij}$, then an equation for the plane containing the side nominally normal to x_1 is:

$$x_1 = -\Delta_{31}x_2 + \Delta_{21}x_3 + l_1$$

(the equations for all the sides can be found by solving a system of simultaneous equations, in a very obvious fashion). Let us further define $\alpha_{ij} = \pm\Delta_{ij}$, so that the equation of each plane can be written in the form

$$x_i = \alpha_{ki}x_j + \alpha_{ji}x_k + l_i\,;$$

the signs of the α_{ij} can be determined in a straightforward way from the equations of each plane. If, for instance, one defines a right-handed coordinate system as shown in Fig. 66, then the $\alpha_{ij} = \Delta_{ij}$, except:

$$
\begin{aligned}
\alpha_{31} &= -\Delta_{31}\\
\alpha_{3\bar{1}} &= -\Delta_{3\bar{1}}\\
\alpha_{12} &= -\Delta_{12}\\
\alpha_{1\bar{2}} &= -\Delta_{1\bar{2}}\\
\alpha_{23} &= -\Delta_{23}\\
\alpha_{2\bar{3}} &= -\Delta_{2\bar{3}}
\end{aligned}
\tag{84}
$$

With a derivation similar to that for the "ηyz" basis, a generalized coordinate that makes all six sides level surfaces is:

$$\eta_i = \frac{x_i - \left(\dfrac{\alpha_{ki}+\alpha_{k\bar{i}}}{2}\right)x_j - \left(\dfrac{\alpha_{ji}+\alpha_{j\bar{i}}}{2}\right)x_k}{l_i + \left(\dfrac{\alpha_{ki}-\alpha_{k\bar{i}}}{2}\right)x_j + \left(\dfrac{\alpha_{ji}-\alpha_{j\bar{i}}}{2}\right)x_k}\,. \tag{85}$$

With

$$a_{ij} = \frac{\alpha_{ki}+\alpha_{k\bar{i}}}{2} \quad\text{and}\quad d_{ij} = \frac{\alpha_{ki}-\alpha_{k\bar{i}}}{2},$$

we have

$$\eta_i = \frac{x_i - a_{ki}x_j - a_{ji}x_k}{l_i + d_{ki}x_j + d_{ji}x_k}\,. \tag{86}$$

The logical basis is then $\phi_{pqr} = \eta_1^p \eta_2^q \eta_3^r$, and the volume integrals for the matrix components will be similar in form to:

$$\int_V \phi\, dV = \int_{-1}^1 \int_{-1}^1 \int_{-1}^1 \eta_1^p \eta_2^q \eta_3^r\, J\!\left(\frac{x,y,z}{\eta_1,\eta_2,\eta_3}\right) d\eta_1\, d\eta_2\, d\eta_3$$

Since this method is intended for **nonparallelepiped** resonance, it could be referred to as the "*npr*" method.

Unlike the first example of a transformed coordinate, where only two opposite sides were tilted in only one plane, the Jacobian for the present case has many terms,

and the necessary volume integrals become quite complicated. To keep the number of terms manageable, all quantities may be kept to first order. This does necessitate discarding a large number of terms, so the result may not be accurate for any other than very small angles. However, if the "first-order" result is sensible, then more terms can be included to improve accuracy as needed.

The elements of $\boldsymbol\Gamma$ are found to be, to first order:

$$\frac{1}{8l_x l_y l_z}\int_V \frac{\partial\phi_u}{\partial x_i}\frac{\partial\phi_v}{\partial x_i} J\!\left(\frac{x_1,x_2,x_3}{\eta_1,\eta_2,\eta_3}\right) d\eta^3 \simeq$$

$$\left(\frac{l_j l_k}{l_i}\right) \left.\frac{p_{i_u} p_{i_v}}{(p_i-1)(p_j+1)(p_k+1)}\right|_{eee}$$

$$+ (d_{ik}l_i - d_{ki}l_k)\left(\frac{l_j^2}{l_i^2}\right)\left.\frac{p_{i_u}p_{i_v}}{(p_i-1)(p_j+2)(p_k+1)}\right|_{eoe}$$

$$+ (d_{ij}l_i - d_{ji}l_j)\left(\frac{l_k^2}{l_i^2}\right)\left.\frac{p_{i_u}p_{i_v}}{(p_i-1)(p_j+1)(p_k+2)}\right|_{eeo}$$

$$+ [d_{kj}l_k(p_{i_u}p_{i_v} - p_{i_u}p_{j_v} - p_{i_v}p_{j_u})$$

$$+ d_{jk}l_j(p_{i_u}p_{i_v} - p_{i_u}p_{k_v} - p_{i_v}p_{k_u})]\left.\frac{1}{p_i(p_j+1)(p_k+1)}\right|_{oee}$$

$$-a_{jk}l_j\left.\frac{p_{i_u}p_{k_v}+p_{i_v}p_{k_u}}{p_i(p_j+1)p_k}\right|_{oeo} - a_{kj}l_k\left.\frac{p_{i_u}p_{j_v}+p_{i_v}p_{j_u}}{p_i p_j(p_k+1)}\right|_{ooe}\;;$$

$$\tag{87}$$

and

$$\frac{1}{8l_x l_y l_z}\int_V \frac{\partial\phi_u}{\partial x_i}\frac{\partial\phi_v}{\partial x_j} J\!\left(\frac{x_1,x_2,x_3}{\eta_1,\eta_2,\eta_3}\right) d\eta^3 \simeq$$

$$\left.\frac{p_{i_u}p_{j_v}l_k}{p_i p_j(p_k+1)}\right|_{ooe}$$

$$+ \left[(p_{i_u}p_{j_v} - p_{i_u}p_{k_v})l_j d_{ik} - p_{i_u}p_{i_v}\frac{l_j l_k}{l_i}d_{ki}\right]$$

$$\left.\frac{1}{p_i(p_j+1)(p_k+1)}\right|_{oee}$$

$$+ \left[(p_{i_u}p_{j_v} - p_{k_u}p_{j_v})l_i d_{jk} - p_{j_u}p_{j_v}\frac{l_i l_k}{l_j}d_{kj}\right]$$

$$\left.\frac{1}{(p_i+1)p_j(p_k+1)}\right|_{eoe}$$
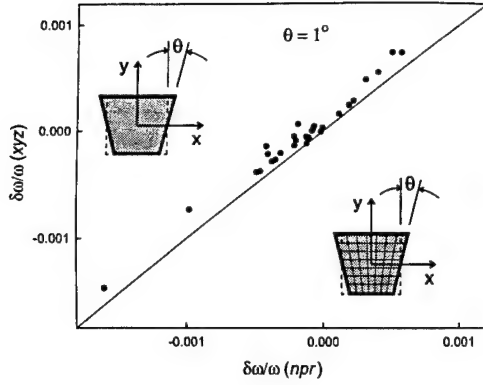
75

FIG. 67. Fractional frequency shifts due to the boundary perturbation shown, in the resonance spectrum of an elastic object, calculated by two methods: first, the xyz method (vertical axis); second, the more approximate (but more general) npr method (horizontal axis).

FIG. 68. Fractional frequency shifts due to the boundary perturbation shown, in the resonance spectrum of an elastic object, calculated by two methods: first, the xyz method (vertical axis); second, the more approximate (but more general) npr method (horizontal axis).

$$- \left[p_{i_u} p_{i_v} \frac{l_j l_k}{l_i} \frac{a_{ki}}{(p_i - 1)(p_j + 1)(p_k + 1)} \right.$$

$$\left. + p_{j_u} p_{j_v} \frac{l_i l_k}{l_j} \frac{a_{kj}}{(p_i + 1)(p_j - 1)(p_k + 1)} \right]_{eee}$$

$$- \frac{p_{i_u} p_{k_v} l_j a_{ik}}{p_i (p_j + 1) p_k} \bigg|_{oeo} - \frac{p_{j_v} p_{k_u} l_i a_{jk}}{(p_i + 1) p_j p_k} \bigg|_{eoo} . \quad (88)$$

The elements of **E** are simpler; it is found that

$$\frac{1}{8 l_x l_y l_z} \int_V \eta_1^{p_1} \eta_2^{p_2} \eta_3^{p_3} J\left(\frac{x_1, x_2, x_3}{\eta_1, \eta_2, \eta_3} \right) d\eta^3 \simeq$$

$$\left(\frac{1}{(p_1 + 1)(p_2 + 2)(p_3 + 3)} \bigg|_{eee} \right.$$

$$\left. + \frac{d_{kj}(l_i/l_j) + d_{jk}(l_i/l_k)}{(p_i + 2)(p_j + 1)(p_k + 1)} \bigg|_{oee} \right) \quad (89)$$

In the above formulas, the labels such as *eeo* or *oeo* refer to the parity of the basis functions; that is, if p_i is even, p_j is odd, and p_k is odd, then the only nonzero terms are those with the label *eoo*.

The accuracy of this very approximate method may be gauged by comparing it with the more accurate methods previously developed, for the simple cases already studied. Figures 67 and 68 show such comparisons for two cases.

The agreement between the two methods is not bad, at least for the larger frequency shifts (which should matter the most). Fig. 67 does show a curious bias, in that the $\delta\omega$ calculated with *npr* are uniformly low. This does not appear to be a problem, since the bias is not large
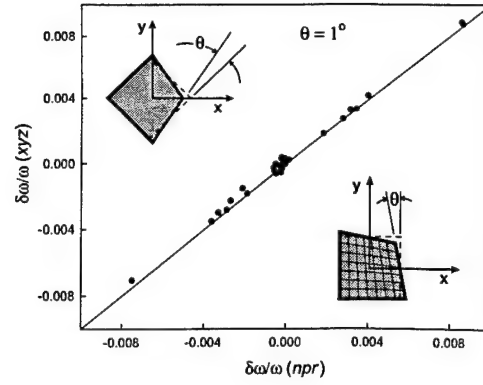
and the variance is reasonably small. All that will happen is that the frequencies will all go the right way, just not quite far enough. If one were to use this method to calculate frequency corrections for use in fitting RUS data, one might compensate for the bias by allowing the perturbation angle, or some related variable, to be a free parameter in the fit. Again we see (interpolating from Fig. 68) that angles of a few tenths of a degree, in the proper arrangement, can cause frequency shifts on the order of tenths of a percent.

4. An application

The quasicrystal measurement of Section V provides a possible test of the methods in section VI B 2. As described in Section V, the actual angles between sides of a quasicrystal specimen were measured optically.

Fig. 69 shows a schematic of the measurement setup (top view), where the sample is mounted on a goniometer, which is in turn mounted in a machine shop dividing head (such as one might use for drilling a precision circular array of holes). The dividing head is placed on one end of an optical bench, with a laser placed at the other end. A piece of thick posterboard with a sheet of centimeter graph paper affixed to it with spray adhesive is placed in front of the laser; a hole in the center of the board allows the beam to pass through and strike the sample, while the scattered beam can be observed on the graph paper. For small angles, the scale can be most easily calibrated by rotating the dividing head by some amount (say, a degree) and noting the horizontal diplacement of the spot. In this manner, the geometry of the sample in the plane of rotation can be readily measured. Typically, one would use one of the sides as a reference plane, us-

76
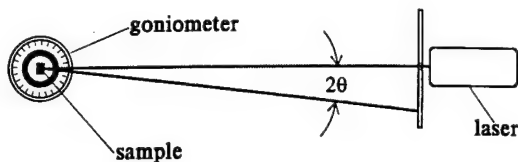
FIG. 69. A top view of the apparatus used to measure the geometry of a nominally rectangular parallelepiped sample. The sample is mounted on a goniometer, which is in turn mounted on a precision turntable (not shown). The laser-to-sample distance is about 8 feet. The calibration was: one degree of rotation of the turntable produced 6.5 cm of displacement on the scale placed in front of the laser.

TABLE XXVI. Angles of deviation from a rectangular parallelepiped, θ_{ij}, as defined in the text.

i\j	−3	−2	−3	0	1	2	3
1	0.26	-0.05	—	—	—	0.00	0.31
2	0.09	—	-0.11	—	0.00	—	0.12
3	—	-0.15	-0.17	—	0.00	-0.31	—

ing the goniometer to center the reflected spot from that side on the incident beam (thus indicating a "tilt" angle of 0°. The dividing head may subsequently be rotated in 90° increments, so that the deviations from perpendicularity of each side may be measured. The process is performed a total of three times, using three mutually perpendicular sample orientations to obtain two orthogonal tilt angles for each side (necessary for a complete description of the sample geometry). The dividing head used in the present work is accurate to better than 0.1°, so with a long enough optical "lever arm", the angles between the sides should be measurable at least within 0.1°. The limiting factor in the present measurement is that the sample is smaller than the laser spot (after the beam has traveled the approximately 8 feet from the laser to the sample), so the scattered spots are somewhat diffuse, with evidence of diffraction. Nevertheless, the angles are measured comfortably to better than 0.1°. The convention is used that a displacement left-of-center is positive (a counterclockwise angle).

The results of the measurement on the quasicrystal may be summarized as a "matrix" of angles (the θ_{ij} defined in the preceding section): where the angles are in degrees. Zero values indicate that the laser spot was set to zero horizontal deflection for reference, while ———— indicates a pair of indices for which no angle is defined under the current scheme. Obviously the particular indices associated with an angle will vary according to which sides are used for reference; here it is assumed that $l_1 = 0.426$ mm and $l_2 = 0.419$ mm.

It is rather difficult to form an idea of what the sample looks like from a matrix of numbers; Fig. 70 shows a somewhat simplified (and exaggerated) diagram of the sample geometry, featuring the two biggest perturbations. These perturbations resemble those studied; in
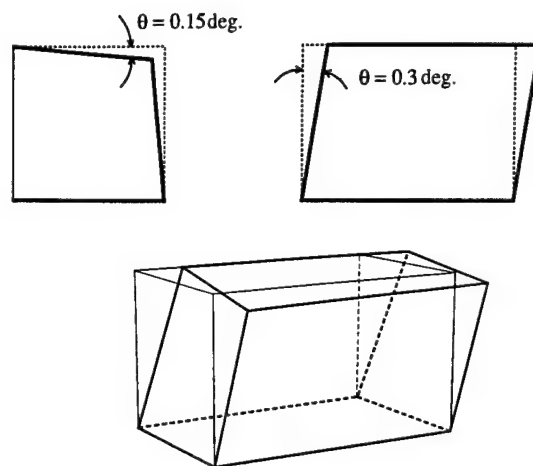
FIG. 70. The approximate geometry of the AlCuLi quasicrystal sample QX1 of Section V, as revealed by optical measurements.

particular, there is a perturbation similar to that of Fig. 62, with a characteristic angle of about 0.15°. We may modify our fitting program to use transformed coordinates based on this perturbed geometry in each forward calculation; or, given that the angles between the sides don't change, we may calculate fractional deviations once for each mode and subsequently adjust the modes in each forward calculation by multiplying each frequency by an appropriate coefficient.

From the analyses in the preceding sections, it was at first thought that the dominant shifts in frequency could be accounted for by approximating the sample as square on the end (it is nearly so already, within 2%) and including a "kite" perturbation of the type in Fig. 59, rather than using the more approximate npr method for the general case. Indeed, it seemed that some of the frequency shifts might be large enough to cause a statistically significant change in the rms error. Upon reflection, however, it was realized that there is no meaningful way to assign modes (or mode shifts) to the original sample, which is nondegenerate, from a square version used for computation. The reason is that when the square object is perturbed in such a way that the original symmetries are broken, the degeneracies split, and there is no way to know which member of the degenerate pair corresponds to which mode in the real, nondegenerate sample.

Subsequently, the npr method was used to calculate frequency corrections using the real sample dimensions and perturbation angles. It was found, however, that including such corrections produced no statistically significant change in either the anisotropy or the rms error; this was somewhat unexpected given the sizeable shifts ($\sim 0.1\%$) seen in the frequencies when the sample was approximated as shown in Fig. 70. It was not thought that the slight changes in angles or aspect ratios would make that much difference in the order of magnitude of the frequency shifts. However, Figures 71 and 72 confirm
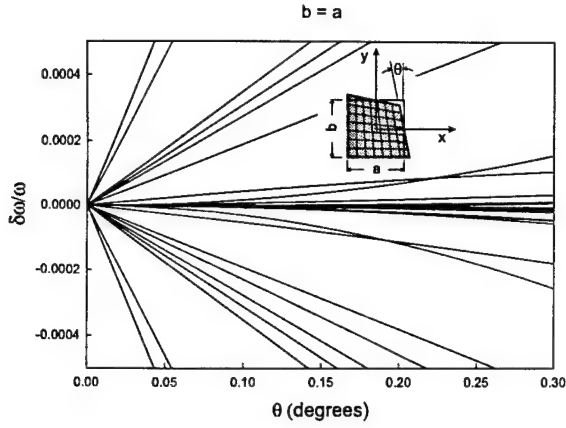
FIG. 71. The frequency shifts calculated by the *npr* method for the perturbation shown, as a function of perturbation angle, for the fictitious elastic object of the preceding sections (an object similar to the quasicrystal sample of Section V with the two shorter sides made equal, so that the end is square).

that a very small change in aspect ratio not only causes the frequency shifts to drop an order of magnitude, but also shows that the largest ones change from being linear to being quadratic.

As it turns out (and as many readers may be aware), it is in fact a well-known property of eigensystems in general that degenerate eigenvalues are often more strongly affected by perturbation than nondegenerate ones [107], [108]. As an example, consider the matrix

$$\mathbf{A} = \begin{bmatrix} 1 & 0 \\ 0 & 2 \end{bmatrix} + \varepsilon \begin{bmatrix} b_{11} & b_{12} \\ b_{21} & b_{22} \end{bmatrix} ;$$

the eigenvalues are perturbations of the nondegenerate eigenvalues of the first term in the sum, and are analytic functions of ε:

$$\lambda_1(\varepsilon) = 1 + \varepsilon\lambda_{11} + \varepsilon^2\lambda_{12} + \dots \quad (90)$$
$$\lambda_2(\varepsilon) = 2 + \varepsilon\lambda_{21} + \varepsilon^2\lambda_{22} + \dots$$

On the other hand, consider the following matrix $\mathbf{B}$, where

$$\mathbf{B} = \begin{bmatrix} 1 & 0 \\ 1 & 1 \end{bmatrix} + \begin{bmatrix} 0 & \varepsilon \\ 0 & 0 \end{bmatrix} ;$$

the eigenvalues are given by

$$\lambda_\pm(\varepsilon) = 1 \pm \sqrt{\varepsilon} .$$

Therefore, even in a simple 2×2 matrix, degenerate eigenvalues may be affected much more strongly by perturbation.

For a physical understanding of why the "kite" perturbation in particular exerts a strong influence on degenerate modes, one might suppose that it is related to
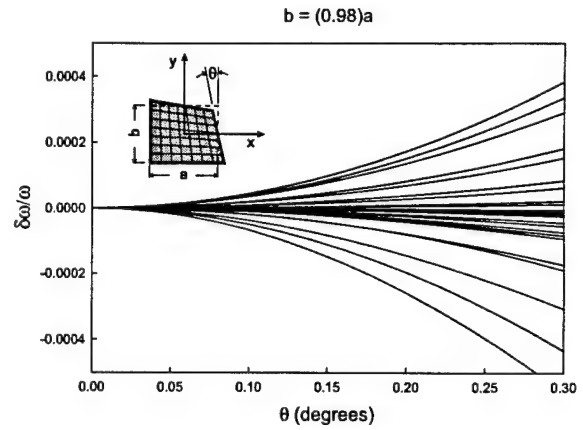
FIG. 72. The same as Fig. 71, except that the real sample's original dimensions are used.
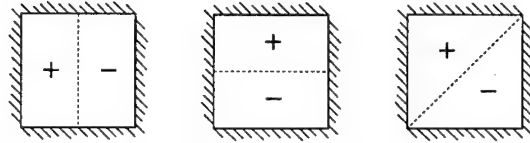
FIG. 73. Three possible degenerate modes of a square membrane; the one on the right is a linear combination of the first two (orthogonal) modes.

an important property of degenerate vibrating systems. Recall that a square membrane under tension, with all sides fixed, has many pairs of degenerate modes; since both eigenfunctions in a degenerate pair correspond to the same frequency, they can be linearly combined to produce different but equally valid eigenfunctions. There is no *a priori* way of choosing among them; if the wave equation is solved in one set of coordinates, one will obtain different functions that if the problem were solved in some other coordinates. Figure 73 shows one such example, where a mode with a nodal line across the diagonal is a linear combination of two modes with nodal lines parallel to the sides (the (1,2) and (2,1) modes). This problem is treated by Morse in his *Vibration and Sound* [109]. If a perturbation is introduced, however, then the situation changes. In particular, if a square membrane were perturbed in the manner of Fig. 59 (a "kite" shape), since that perturbation is symmetric about the diagonal it would cause the eigenfunctions to reflect that symmetry. The formerly degenerate (2,1) and (1,2) modes would be split in frequency, with each mode having one of the diagonals as its nodal line. One might suppose that in this case, the effect of the perturbation on the frequencies would be rather strong. If the square shape were relaxed even a little, so that the symmetry about the diagonal were broken by having the sides unequal in length, then perhaps the eigenfunctions would not align themselves as well with the perturbation, so the effect on the frequencies would be weaker.

78
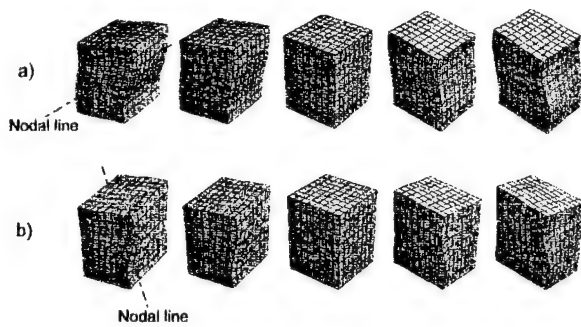
FIG. 74. Two equivalent degenerate shear eigenmodes of the isotropic elastic object considered elsewhere in this section. The figures may be viewed as animations by rapidly scanning back and forth.

The forgoing applies to vibrating elastic solids as well; Fig. 74 shows two equivalent degenerate shear modes of a vibrating elastic parallelepiped, which is square on the end; these are obtained by setting up the Rayleigh-Ritz integrals in different coordinates. Since the shifts in frequency due to the tilted sides are so small when the real quasicrystal's dimensions are used, it is concluded that the effect of the tilted sides is not sufficient to explain the residual anisotropy in the quasicrystal measurement.

C. Conclusions

Although the preceding work did not, as hoped, reduce the ambiguity in the quasicrystal measurement, several things of interest have been discovered in the process:

- Standard first-order perturbation theory is not especially accurate for vibrating elastic parallelepipeds (unlike elastic spheroids).

- Certain combinations of tilted sides can produce frequency shifts which are first-order in the tilt angle.

- The dominant shifts in frequency due to tilted sides can be adequately computed using a Rayleigh-Ritz algorithm similar to Visscher's xyz method, with appropriate coordinate transformations and approximations (the "npr" method).

- For samples whose sides are perpendicular within 0.5° and parallel within 0.3°, tilted sides should not normally be a problem in a RUS measurement, and these preparation limits are easily within reach, even for submillimeter samples. Of interest is the result that if opposite sides remain parallel (as in Fig. 60), they may be considerably skewed from perpendicular without causing noticeable frequency shifts. Frequency shifts are much larger for non-parallel sides. As has been mentioned before in Section III, it is somewhat difficult during sample

preparation to guarantee that sides are perfectly square, but making sides parallel is easier. This is good news for users of rectangular parallelepiped samples, in that the sample geometry criterion that is most critical is the easiest to accomplish.

- Factors other than geometric imperfections are contributing substantially to the residual error (error in fitting frequency data) in RUS measurements.

- Objects that have degenerate eigenfunctions are strongly affected by perturbations that break existing symmetries. This is of course not surprising; however, some of the effects of these broken symmetries could have interesting effects in RUS measurements. For instance, if a nominally rectangular parallelepiped sample were perturbed in such a way as to vibrate in the manner of Fig. 74(b) for the applicable shear modes, then one may notice that for these modes certain corners are very inactive. Thus there is a rigorous justification for measuring the sample several times, mounting it by different pairs of opposite corners, in order to ensure that all the modes are detected.

Though the work presented here is sufficient to give some idea of how sample preparation errors may affect RUS measurements, it is by no means exhaustive. If it is found, for instance, that samples under pressure deform significantly ($\sim 1°$), then if those samples already have modes that are close together, the effects of tilted sides may have to be considered when looking for small changes in the elastic constants. No effort has been made here to experimentally verify the accuracy of the above computations, or provide a rigorous justification for the results thus obtained; these might be worthwhile future undertakings.

A computer program that could be used to do the calculations in this section is listed in the Appendix; it is based on a simple, elegant program written by William Visscher of Los Alamos National Laboratories (see [103]).

[1] See, for instance, W. P. Mason, *Physical Acoustics and the Properties of Solids*, 369 (Van Nostrand, Princeton, 1948).

[2] See [47], and references therein.

[3] H. H. Demarest, J. Acoust. Soc. Am. **49**, 768 (1969).

[4] Y. Tatsumi and H. Ohsaki, in *Properties of Silicon*, 3 (INSPEC, 1988).

[5] A. G. Every and A. K. McCurdy, in *Landolt-Börnstein Tables, New Series, Group III (Crystal and Solid State Physics)* volume **29a**, edited by O. Madelung and D. F. Nelson (Springer-Verlag, Berlin, 1992)

[6] These "accepted values" are quoted by O. H. Nielsen in the reference work *Properties of Silicon*, 14 (INSPEC, 1988), as being the "most accurate"; they are attributed to J. J. Hall, Phys. Rev. **161**, 756 (1967).

[7] G. G. Bentle, J. Am. Ceram. Soc. **49**, 125 (1966).

[8] R. Truell, C. Elbaum, and B. Chick, *Ultrasonic Methods in Solid State Physics* (Academic Press, New York, 1969).

[9] Robert Hooke, *De potentia restutiva* (London, 1678).

[10] C. A. Coulomb, Histoire de l'Academie des Sciences, Year 1784, 229 (1787).

[11] Thomas Young, "Mathematical Elements of Natural Philosophy," Vol. II of Dr. Young's Lectures, Section IX, p. 46 (1807).

[12] J. M. Ide, Rev. Sci. Instr. **6**, 296 (1935).

[13] P. LeRolland and P. Sorin, Comptes rendus **176**, 536 (1933).

[14] R. D. Mindlin, J. Appl. Phys. **22**, 316 (1951).

[15] H. Ekstein and T. Schiffman, J. Appl. Phys. **27**, 405 (1956).

[16] R. D. Mindlin, "Simple modes of vibration of crystals," J. Appl. Phys. **27**, 1462 (1956).

[17] A. G. Every and W. Sachse, Ultrasonics **30**, 43 (1992).

[18] See, for instance: W. P. Mason, *Piezoelectric Crystals and Their Applications to Ultrasonics*, 446 (Van Nostrand, New York, 1950).

[19] See, for instance, C. Kittel, *Introduction to Solid State Physics*, 180 (John Wiley & Sons, New York, 1967).

[20] L. D. Landau and E. M. Lifshitz, *Theory of Elasticity* (Pergamon Press, Oxford, 1970).

[21] C. Zener, *Elasticity and Anelasticity of Metals* (University of Chicago Press, Chicago, 1948).

[22] H. Kolsky, *Stress Waves in Solids*, 131 (Dover, London 1963).

[23] Y. Sumino, I. Ohno, T. Goto, and M. Kumazawa, J. Phys. Earth **24**, 263, (1976).

[24] H. Oda, O. L. Anderson, and I. Suzuki, in the Proceeds of the 28th Annual Technical Meeting of the Society of Engineering Sciences, Nov. 6–8 1991.

[25] E. W. Christoffel, Annali Di Matematica Pura ed applicata, series II **8**, 193 (1877).

[26] D. Shechtman, I. Blech, D. Gratias, and J. W. Cahn, Phys. Rev. Lett. **53**, 1951 (1984).

[27] L. C. Chen, S. Ebalard, L. M. Goldman, W.l Ohashi, B. Park, and F. Spaepen, J. Appl. Phys. **60**, 2638 (1986).

[28] M. G. Lamé, *Leçons sur la Théorie Mathématique de l'Élasticité des corps Solides* (Gauthier-Villars, Paris, 1886).

[29] L. D. Landau and E. M. Lifshitz, *Mechanics*, chapter 10 (Pergamon Press, 1960).

[30] G. Arfken, *Mathematical Methods for Physicists*, 627 (Academic Press, Boston, 1985).

[31] Lord Rayleigh (J. W. S. Strutt), *Theory of Sound*, vol. 1, sec. 88 (Dover, New York, 1945).

[32] W. Ritz, "Über eine neue Methode zur Lösung gewisser Variationsprobleme der Mathematischen Physik", J. f. d. reine u. angew. Math. **135**, 1 (1909).

[33] B. L. Moiseiwitsch, *Variational Principles*, 153 (John Wiley & Sons, London, 1966).

[34] H. Ekstein and T. Schiffman, J. Appl. Phys. **27**, 405 (1956).

[35] Personal communication, 1996.

[36] R. Holland, J. Acoust. Soc. Am. **43**, 988 (1968).

[37] R. Courant and D. Hilbert, *Methods of Mathematical Physics*, 1st ed., 208 (Interscience, New York, 1953).

[38] R. Courant and D. Hilbert, *Methods of Mathematical Physics*, 1st ed., 209 (Interscience, New York, 1953).

[39] W. H. Press, S. A. Tuekolsky, W. T. Vetterling, and *Numerical Recipes*, 675 (Cambridge University Press, Cambridge, 1992).

[40] Ibid., p. 691

[41] A. Stekel, J. L. Sarrao, T. M. Bell, Ming Lei, R. G. Leisure, W. M. Visscher, and A. Migliori, J. Acoust. Soc. Am. **92**, 663 (1992).

[42] H. H. Demarest, J. Acoust. Soc. Am. **49**, 768 (1971).

[43] I. Ohno, J. Phys. Earth **24**, 355 (1976).

[44] I. Ohno, S. Yamamoto, O. L. Anderson, and J. Noda, J. Phys. Chem. Solids **47**, 1103 (1986).

[45] A. Migliori, J. L. Sarrao, W. M. Visscher, T. M. Bell, Ming Lei, Z. Fisk, and R. G. Leisure, Physica B **183**, 1 (1993).

[46] A. Migliori, personal communication, 1996.

[47] J. D. Maynard, J. Acoust. Soc. Am. **91**, 1754 (1992).

[48] *Handbook of Chemistry and Physics*, 67th ed., edited by R. C. Weast, M. J. Astle, and W. H. Berger (CRC Press, Boca Raton, 1986).

[49] J. L. Amoros, M. J. Buerger, and M. C. Amoros, The Laue Method (Academic Press, New York, 1975).

[50] South Bay Technologies, 1120 Via Callejon, San Clemente, CA 92627.

[51] KYNAR Piezo Film, Pennwalt Corporation, 900 First Avenue, P.O. Box C, King of Prussia, PA 19406, (215) 337–6710.

[52] H. R. Gallantree, the Marconi Review **45**, 49 (1982).

[53] T. M. Slawecki, Master's Thesis, Department of Physics, the Pennsylvania State University (1989).

[54] KYNAR Piezo Film Technical Manual, Pennwalt Corporation (see address in [51] above) 49 (1983).

[55] Chang Yu, Ph.D. thesis, Department of Physics, the Pennsylvania State University (1989).

[56] Wei-Li Lin, Ph.D. thesis, Department of Physics, the Pennsylvania State University (1995).

[57] See, for instance, C. E. Cooke, "Hydraulic Fracturing with a High-Strength Proppant," Society of Petroleum Engineers paper # SPE 6213 (presented at the 51st Annual Fall Technical Conference of the SPE, October 3–6, 1976).

[58] J. Martin and J. Vitko, Jr., "ASCUAS: A Solar Central Receiver Utilizing a Solid Thermal Carrier," SAND82-8203, Sandia National Laboratories, January 1982.

[59] J. R. Hellmann, M. O. Eatough, P. F. Hlava, and A. R. Mahoney, "Evaluation of Spherical Ceramic Particles for Solar Thermal Transfer Media," SAND86-0981, Sandia National Laboratories, January, 1987.

[60] Zirprop™ Z126, spheroidized fused zircon propduct by the SEPR division of the Quartz Products Corporation, Plainfield, NJ.

[61] J. H. Woodhouse and F. A. Dahlen, "The effect of a general aspherical perturbation on the free oscillations of the earth", Geophys. J. R. Astr. Soc. **53**, 335 (1978).

[62] E. Mochizuki, "The free oscillations of an anisotropic and heterogeneous Earth", Geophys. J. R. Astr. Soc. **86**, 167 (1986).

[63] d. Giardini, X.-D. Li, and J. H. Woodhouse, "Three-dimensional structure of the earth from splitting in free-oscillation spectra", Nature **325**, 405 (1987).

[64] H. Lamb, London Math. Soc. Proc. **13** (1882).

[65] P. Jaerisch, J. F. Math. (Crelle), **88** (1880).

[66] C. Chree, Cambridge Phil. Soc. Trans. **14** (1889).

[67] A. E. H. Love, *Treatise on the Mathematical Theory of Elasticity* (Cambridge University Press, Cambridge, 1927).

[68] Y. Satô and T. Usami, Geophys. Mag. (Japan Meteorological Society, Tokyo) **31**, 15 (1962).

[69] D. B. Fraser and R. C. Lecraw, "Novel method of measuring elastic and anelastic properties of solids", Rev. Sci. Instr. **35**, 1113 (1964).

[70] George Arfken, *Mathematical Methods for Physicists*, 3rd ed. (Academic Press, San Diego, 1985).

[71] E. Schreiber, O. L. Anderson, N. Soga, N. Warren, C. Sholtz, Science **167**, 732 (1970); E. Schreiber, O. L. Anderson, Science **168**, 1579 (1970).

[72] J. R. Hellmann, P. J. Jamnicky, D. L. Shelleman, P. S. Spoor, and J. D. Maynard, to be published.

[73] Almost any book on crystallography prior to 1985 will have some mention of the impossibility of fivefold rotational symmetry; see, for instance, C. Kittel, *Introduction to Solid State Physics*, 30 (John Wiley & Sons, New York, 1967).

[74] R. Penrose, Bull. Inst. Math. Appl. **10**, 266 (1974).

[75] M. Gardner, Sci. Am. **236**, 110 (1977).

[76] These pictures were obtained from the World-Wide Web site http://www.lassp.cornell.edu/lifshitz/quasicrystals.html

[77] D. Shechtman, I. Blech, D. Gratias, and J. W. Cahn, Phys. Rev. Lett. **53**, 1951 (1984)

[78] D. Levine and P. J. Steinhardt, Phys. Rev. Lett. **53**, 2477 (1984).

[79] B. Dubost, J. M. Lang, M. Tanaka, P. Sainfort, and M. Audier, Nature **324**, 48 (1986).

[80] D. Levine and P. J. Steinhardt, Phys. Rev. B **34**, 596 (1986).

[81] See, for instance, *Quasicrystals*, ed. by M. V. Jaric and S. Lunqvist (World Scientific, Singapore, 1990), and C. Janot, *Quasicrystals: a Primer* (Clarendon Press, Oxford, 1992).

[82] T. C. Lubensky, S. Ramanswamy, and J. Toner, Phys. Rev. B **32**, 7444 (1985).

[83] Per Bak, Phys. Rev. B **32**, 5764 (1985).

[84] A. Yamamoto, Phys. Rev. B **45**, 5217 (1992).

[85] G. A. M. Reynolds, B. Golding, A. R. Kortan, and J. M. Parsey, Jr., Phys. Rev. B **41**, 1194 (1990).

[86] S. Satish, A. Kulik, and G. Gremaud, Sol. St. Comm. **77**, 403 (1991).

[87] A. I. Goldman, C. Stassis, M. de Boissieu, R. Currat, C. Janot, R. Bellissent, H. Moudden, and F. W. Gayle, Phys. Rev. B **45**, 10280 (1992).

[88] C. L. Henley, Phys. Rev. B **43**, 993 (1991).

[89] F. H. Featherston and J. R. Neighbors, Phys. Rev. **130**, 1324 (1963).

[90] See D. H. Chung and W. R. Buessem, in *Anisotropy of Single-Crystal Refractory Compounds*, edited by F.W. Vahliek and S. A. Mersol (Plenum Press, New York, 1968) p. 217, and A. G. Every and A. K. McCurdy, in *Landolt-Börnstein Tables, New Series, Group III (Crystal and Solid State Physics)* volume **29a**, edited by O. Madelung and D. F. Nelson (Springer-Verlag, Berlin, 1992) p. 11. For the anisotropy of tungsten and its standard deviation, we use the average of the values in the literature. Published anisotropies for some crystals are smaller than that of tungsten, but the uncertainties in the elastic constants are either too large or are not given. We consider only crystals at standard temperature and pressure; other conditions are discussed in the conclusions of Section V.

[91] C. Zener, *Elasticity and Anelasticity of Metals*, 16 (University of Chicago Press, Chicago, 1948).

[92] A. R. Kortan, H. S. Chen, J. M. Parsey, and L. C. Kimerling, J. Mat. Sci. **24**, 1999 (1989).

[93] The R-phase was first described in a 1955 paper by H. K. Hardy and J. M. Silcock, in J. Inst. Metals **84**, 423 (1955). Interestingly, they also described the icosahedral (T_2) phase, but didn't know what to make of it, labeling it "structure undetermined"!

[94] C. Janot, *Quasicrystals: a Primer*, 166 (Oxford University Press, Oxford, 1992)

[95] T. C. Lubensky, Joshua E. S. Socolar, Paul J. Steinhardt, Peter A. Bancel, and Paul A. Heiney, Phys. Rev. Lett. **57**, 1440 (1986).

[96] The author has frequently encountered this effect in his own work, and has learned that it is commonly encountered by the Los Alamos researchers as well (A. Migliori, personal communication, 1994). Other than attending meetings where RUS data is presented, it is difficult for the outside observer to corroborate this since tables of frequencies are often not included in published reports on RUS measurements (one exception is Ref. [41]). Papers by Japanese investigators often *do* include such tables, but in these, the effect is not nearly so obvious. The reason seems to be that the Japanese use a much different (and perhaps cruder) transduction scheme than do their American counterparts, and there is much greater perturbation of the normal mode frequencies, resulting in larger errors for all modes. The lowest mode seems to fit anomalously badly only when the average rms error is around 0.1% or better.

[97] C. Janot, *Quasicrystals: a Primer*, 79 (Clarendon Press, Oxford, 1992).

[98] K. F. Graff, *Wave motion in elastic solids*, 325 (Ohio State University Press, Columbus, 1975).

[99] Y. Amazit, M. de Boissieu, and A. Zarembowitch, Europhys. Lett. **20**, 703 (1992).

[100] J. H. Woodhouse, Geophys. J. R. astr. Soc. **46**, 11 (1976).

[101] H. Oda, J. Hirao, I. Suzuki, W. M. Visscher, and O. L. Anderson, Geophys. J. Int. **118**, 555 (1994).

[102] P. M. Morse and H. Feshbach, *Methods of Theoretical Physics*, vol. 1 (McGraw-Hill, N.Y., 1953).

[103] W. M. Visscher, A. Migliori, T. M. Bell, and R. A. Reinert, J. Acoust. Soc. Am. **90**, 2154 (1991).

[104] International Business Machines Corporation, *Engineering and Scientific Subroutine Library*, Release 3 (I.B.M. Corp., 1988) 531.

[105] M. Kac, "Can one hear the shape of a drum?", Am. Math. Monthly **73**, 1 (1966).

[106] C. Gordon, D. L. Webb, and S. Wolpert, "One cannot hear the shape of a drum", Bull. Am. Math. Soc. **27**, 134 (1992).

[107] C. Eugene Wayne, personal communication, 1996.

[108] Tosio Kato, *Perturbation Theory for Linear Operators*, 2nd ed. (Springer-Verlag, New York, 1976).

[109] P. M. Morse, *Vibration and Sound* (American Institute of Physics, 1976) 181.

APPENDIX A: COMPUTER PROGRAMS

This Appendix contains some of the FORTRAN code used to obtain the results in the thesis. Programs included are:

xyztrap — Based on William Visscher's *xyz* algorithm, this program finds the normal mode frequencies of a trapezium.

npr— Loosely based on the *xyz* algorithm, this program uses a transformed basis set that includes tilted sides of an elastic block as level surfaces.

fumarp — Calculates the normal mode frequencies of a rectangular parallelepiped, and returns *Mathematica*-ready files plotting selected eigenfunctions.

lrnzmrq— A program for fitting phase-shifted Lorentzian resonance data with the Levenberg-Marquardt algorithm.

rprmrq — The program used to fit most of the RUS data in this work. Also included is a sample data file, the one corresponding to the 1 mg Si test sample.

These programs were originally written to run on the IBM 3270 mainframe, so they include some non-standard statements (such as "@PROCESS DC(BIG)") and references to ESSL subroutines, which are commonly available on these mainframes. Also, these programs make liberal use of Numerical Recipes subroutines [39] such as `svdcmp`, `mrqmin`, `mrqcof`, `covsrt`, and `shell`, which are not included if they can be taken verbatim from the source (converted to double precision where necessary). In addition, original subroutines that are shared by several programs are only included in one, to save space.

1. xyztrap

```
@PROCESS DC(BIG)
      Program xyztrap

      IMPLICIT real*8 (a-h,o-z)
      integer R,NN
      Parameter(R=252,NN=6,nof=31)
      real*8 w(R),dummy(1)
      real*8 wk1(R),cij(6,6),c(3,3,3,3),rho,d1,d2,d3,F
      COMMON/BIG/gamma(R,R),e(R,R)
      COMMON/TILT/tilt
      COMMON/PASCAL/P(30,30)
      integer lb(R),mb(R),nb(R),ic(R)
      integer neq(21),id(21,21)
      real*8 cf(21,21),cj(21),mass
      character*50 HEADER
400   FORMAT(A50)

      open(unit=7,file='/xyztrap dat',status='old')
      open(unit=8,file='/xyztrap out',status='unknown')

      read(7,400) HEADER
      read(7,*)numic
      do 11 i=1,numic
        read(7,*) cj(i),neq(i),(id(i,j),cf(i,j),j=1,neq(i))
11    continue
      read(7,*)d1,d2,d3
      read(7,*) rho
c     read(7,*) mass
      read(7,*)dtilt,ntilt1,ntilt2,nstep

      twopi = 2.d0*dacos(-1.d0)
      call pasc(NN)
```

83

```fortran
      call xuflow(0)

C--    rho=mass/(d1*d2*d3)
      E11=4.d+0/(D1*D1)
      E22=4.d+0/(D2*D2)
      E33=4.d+0/(D3*D3)
      E12=4.d+0/(D1*D2)
      E13=4.d+0/(D1*D3)
      E23=4.d+0/(D2*D3)
      call cjcij(cj,cij,neq,id,cf,numic)
      call cindex(cij,c,0)

      ig=0
      do 1 i=1,3
       do 2 l=1,NN+1
       do 2 m=1,NN+1
       do 2 n=1,NN+1
        if(l+m+n.gt.NN+3)go to 2
        ig=ig+1
        ic(ig)=i
        lb(ig)=l-1
        mb(ig)=m-1
        nb(ig)=n-1
2     continue
1     continue
      nr=ig

      DO 102 ITILT = NTILT1,NTILT2,NSTEP
       tilt=dtilt*dfloat(itilt)
       write(8,*)'tilt = ',tilt,'degrees'
      tilt=dtan(tilt*twopi/360.d+0)*d2/d1

      do 3 ig=1,nr
      do 3 jg=ig,nr
       i=ic(ig)
       j=ic(jg)
       ls=lb(ig)+lb(jg)
       ms=mb(ig)+mb(jg)
       ns=nb(ig)+nb(jg)
       gamma(ig,jg)=
     &   c(i,1,j,1)*dfloat(lb(ig)*lb(jg))*F(ls-2,ms,ns)*E11
     & +c(i,2,j,2)*dfloat(mb(ig)*mb(jg))*F(ls,ms-2,ns)*E22
     & +c(i,3,j,3)*dfloat(nb(ig)*nb(jg))*F(ls,ms,ns-2)*E33
     & +(c(i,1,j,2)*dfloat(lb(ig)*mb(jg))+c(i,2,j,1)*
     & dfloat(mb(ig)*lb(jg)))*F(ls-1,ms-1,ns)*E12
     & +(c(i,1,j,3)*dfloat(lb(ig)*nb(jg))+c(i,3,j,1)*
     & dfloat(nb(ig)*lb(jg)))*F(ls-1,ms,ns-1)*E13
     & +(c(i,2,j,3)*dfloat(mb(ig)*nb(jg))+c(i,3,j,2)*
     & dfloat(nb(ig)*mb(jg)))*F(ls,ms-1,ns-1)*E23
       gamma(jg,ig)=gamma(ig,jg)
       if(i.eq.j) e(ig,jg)=F(ls,ms,ns)
3     e(jg,ig)=e(ig,jg)

      call dsygv(0,gamma,nr,e,nr,w,dummy,1,R,wk1,R)

      do 4 i=1,nr
       if(w(i).gt.0)w(i)=dsqrt(w(i)/rho)/twopi
C      if(i.gt.6 .and. i.le.nof+6)write(8,402)i-6,',',w(i)
       if(i.gt.6 .and. i.le.nof+6)write(8,*)i-6,',',w(i)
C      if(i.gt.6)write(8,*)i-6,',',w(i)
```

```fortran
 4      continue
402     format(1X,I2,A1,F10.7)

        WRITE(8,*)' '
102     CONTINUE

        STOP
        END
c---------------
        Function F(ip,iq,ir)

        implicit real*8(a-h,o-z)
        COMMON/tilt/ tilt
        COMMON/pascal/p(30,30)
        integer ip,iq,ir
        real*8 F,fact

        F=0.d+0
        if(ip.lt.0 .or. iq.lt.0 .or. ir.lt.0)return
        if(mod(ip,2).ne.0)return
        if(mod(ir,2).ne.0)return

        ifac = ip+1
        do 10 m=1,ip+1
         if(mod(iq+m,2).eq.0)F=F+p(ip+1,m+1)*tilt**m/dfloat(iq+m+1)
         ifac=ifac*(ip+1-m)
         if(ifac.eq.0)goto 11
 10     continue
 11     if(mod(iq,2).eq.0)F = F + 1.d0/dfloat(iq + 1)
        F = F*1.d0/dfloat((ip+1)*(ir+1))
        return
        END


        Function fact(n)
        integer n
        real*8 fact

        fact = 1.0D+0
        if(n.lt.2)return
        do 10 i=1,n
         fact = fact*dfloat(n)
 10     continue
        return
        END

c---------------
        Subroutine pasc(NN)

        IMPLICIT real*8 (a-h,o-z)
        COMMON/PASCAL/p(30,30)
        Integer NN
        p(1,1)=1.d0
        p(1,2)=1.d0
        do 100 n=2,2*NN+1
         p(n,1)=1.d0
         p(n,n+1)=1.d0
         do 100 mu=2,n
          p(n,mu)=p(n-1,mu-1)+p(n-1,mu)
100     continue
```

85

```fortran
      return
      end

       SUBROUTINE cjcij(cj,cij,neq,id,cf,numic)
      integer neq(21),id(21,21),numic
      Real*8  cj(21),cf(21,21),cij(6,6)

      do 121 i=1,6
       do 111 j=1,6
         cij(i,j)=0.0d+00
111    continue
121   continue

      do 12 i=1,numic
        do 11 j=1,neq(i)
          i1=id(i,j)/10
          i2=id(i,j)-i1*10
          cij(i1,i2)=cij(i1,i2)+cj(i)*cf(i,j)
11      continue
12    continue
      do 14 i=1,6
       do 13 j=i,6
         cij(j,i)=cij(i,j)
13     continue
14    continue
      return
      END

      Subroutine cindex(cij,cijkl,job)
      Real*8 cij(6,6),cijkl(3,3,3,3)
      Integer ij(6,2)
      data (ij(i,1),i=1,6)/1,2,3,2,1,1/
      data (ij(i,2),i=1,6)/1,2,3,3,3,2/
      if(job.eq.0)then
        do 12 i=1,6
          do 11 j=1,6
            m=ij(i,1)
            n=ij(i,2)
            k=ij(j,1)
            l=ij(j,2)
            cijkl(m,n,k,l)=cij(i,j)
            cijkl(k,l,m,n)=cij(i,j)
            cijkl(n,m,k,l)=cij(i,j)
            cijkl(k,l,n,m)=cij(i,j)
            cijkl(m,n,l,k)=cij(i,j)
            cijkl(l,k,m,n)=cij(i,j)
            cijkl(n,m,l,k)=cij(i,j)
            cijkl(l,k,n,m)=cij(i,j)
11        continue
12      continue
      endif
      Return
      END
```

a. Data file `xyztrap.dat`

Here is a sample data file for use with the previous program. This file specifies the properties of the "fictitious elastic object" alluded to in the thesis and was used to generate the various plots in Section VI (as well as the eigenfunction plots in Fig. 8). The file contains a header, the number of independent constants, that same number of

consecutive lines specifying the elastic-constant Cij matrix, the edge lengths, and the density. The Cij matrix elements are specified in the following way: First, the value of one of the independent constants is given; next, the number of times it appears in the Cij matrix, and then, a list of the locations where it appears, with appropriate multipliers.

```
quasicrystal QX1 approximated for checking stuff  !  heading
3                                    ! { 3 independent constants }
1.100000, 3, 11,1., 22,1., 33,1.   ! { value (MBar), # of places it
0.300000, 3, 12,1., 13,1., 23,1.   ! appears in Cij, list of pairs
0.400000, 3, 44,1., 55,1., 66,1.   ! (indices ij, multiplier).}
0.0422100,0.0422100,0.057610       ! { edge lengths }
2.3590                             ! { density (g/cc) }
```

2. npr

```
@PROCESS DC(BIG)
      Program npr

      IMPLICIT real*8 (a-h,o-z)
      integer R,NN
      Parameter(R=660,NN=9,nof=31)
      real*8 w(R),dummy(1),f0(R)
      real*8 wk1(R),cij(6,6),c(3,3,3,3),rho,mass,FE,FG
      COMMON/BIG/gamma(R,R),e(R,R)
      real*8 slope(1:3,-3:3),L(3)
      COMMON/TILT/a(3,3),d(3,3)
      integer lb(R),mb(R),nb(R),ic(R),pu(3),pv(3),p(3)
      integer neq(21),id(21,21)
      real*8 cf(21,21),cj(21)
      character*50 HEADER
400   FORMAT(A50)

      open(unit=7,file='/npr1 dat',status='old')
c     open(unit=8,file='/npr1 out',status='unknown')
      OPEN(UNIT=8,FILE='/npr coef',    STATUS='UNKNOWN')

c     write(8,*)'Frequencies of perturbed llpiped, nn =', NN

      read(7,400) HEADER
      read(7,*)numic
      do 15 i=1,numic
        read(7,*) cj(i),neq(i),(id(i,j),cf(i,j),j=1,neq(i))
 15   continue
      read(7,*)l(1),l(2),l(3)

      twopi = 2.d0*dacos(-1.d0)

      read(7,*) rho
C     read(7,*) mass
C     rho=mass/(l(1)*l(2)*l(3))
      read(7,*) (inull, i=1,7)
      do 7 i=1,3
       read(7,*)inull,(slope(i,j),j=-3,3)
7     continue

      call xuflow(0)
      call cjcij(cj,cij,neq,id,cf,numic)
      call cindex(cij,c,0)

      ig=0
```

87

```fortran
      do 1 i=1,3
       do 2 il=1,NN+1
       do 2 im=1,NN+1
       do 2 in=1,NN+1
        if(il+im+in.gt.NN+3)go to 2
        ig=ig+1
        ic(ig)=i
        lb(ig)=il-1
        mb(ig)=im-1
        nb(ig)=in-1
2     continue
1     continue
      nr=ig

      DO 100 ITCODE = 0,1
      IF(itcode.eq.1)THEN
       slope(3,1) =-slope(3,1)
       slope(3,-1)=-slope(3,-1)
       slope(1,2) =-slope(1,2)
       slope(1,-2)=-slope(1,-2)
       slope(2,3) =-slope(2,3)
       slope(2,-3)=-slope(2,-3)
       do 9 i=1,3
        do 8 j=1,3
         if(i.ne.j)then
          a(i,j)=(dtan(slope(i,j)*twopi/360.d0)+
     &             dtan(slope(i,-j)*twopi/360.d0))/2.d0
          d(i,j)=(dtan(slope(i,j)*twopi/360.d0)-
     &             dtan(slope(i,-j)*twopi/360.d0))/2.d0
         endif
8      continue
9      continue
      ENDIF
      do 3 ig=1,nr
      do 3 jg=ig,nr
       e(ig,jg)=0.d+0
       i=ic(ig)
       j=ic(jg)
       pu(1)=lb(ig)
       pv(1)=lb(jg)
       pu(2)=mb(ig)
       pv(2)=mb(jg)
       pu(3)=nb(ig)
       pv(3)=nb(jg)
       p(1)=pu(1)+pv(1)
       p(2)=pu(2)+pv(2)
       p(3)=pu(3)+pv(3)
       gamma(ig,jg)=
     &   c(i,1,j,1)*FG(pu,pv,p,1,1,L)
     & +c(i,2,j,2)*FG(pu,pv,p,2,2,L)
     & +c(i,3,j,3)*FG(pu,pv,p,3,3,L)
     & +(c(i,1,j,2)*FG(pu,pv,p,1,2,L)+
     &   c(i,2,j,1)*FG(pu,pv,p,2,1,L))
     & +(c(i,1,j,3)*FG(pu,pv,p,1,3,L)+
     &   c(i,3,j,1)*FG(pu,pv,p,3,1,L))
     & +(c(i,2,j,3)*FG(pu,pv,p,2,3,L)+
     &   c(i,3,j,2)*FG(pu,pv,p,3,2,L))
       gamma(jg,ig)=gamma(ig,jg)
       if(i.eq.j) e(ig,jg)=FE(p,L)
3     e(jg,ig)=e(ig,jg)
```

```fortran
      call dsygv(0,gamma,R,e,R,w,dummy,1,nr,wk1,R)

      if(itcode.eq.0)then
       do 11 i = 1,nr
         if(w(i).gt.0.d0)w(i)=dsqrt(w(i)/rho)/twopi
         f0(i)=w(i)
         w(i)=0.0d0
 11    continue
      endif

100   CONTINUE


      do 4 i=7,nof+6
       if(w(i).gt.0)w(i)=dsqrt(w(i)/rho)/twopi
c      write(8,102)i-6,f0(i),w(i),(w(i)-f0(i))/f0(i)
       write(8,*)i-6,w(i)/f0(i)
 4    continue
102   format(1X,I4,2F11.7,1X,E13.5)

      STOP
      END


      Function FE(p,L)

      Implicit real*8 (a-h,o-z)
      integer p(3),i,j,k
      Real*8 FE,L(3)
      COMMON/tilt/a(3,3),d(3,3)

      FE=0.d+00
      ieven=0
      i = 1

      do 10 ip = 1,3
       if(mod(p(ip),2).ne.0)then
        i=ip
       else
        ieven = ieven + 1
       endif
10    continue
      if(ieven.lt.2)return
      j=2/i+i/3
      k=6-i-j
      if(ieven.eq.3)then
        FE = 1.d0/dfloat((p(i)+1)*(p(j)+1)*(p(k)+1))
       else
        FE = L(i)*(d(k,j)/L(j) + d(j,k)/L(k))/
     &             dfloat((p(i)+2)*(p(j)+1)*(p(k)+1))
      endif
      FE = FE*L(1)*L(2)*L(3)
      return
      END


      Function FG(pu,pv,p,ixu,ixv,L)

      implicit real*8 (a-h, o-z)
```

```fortran
      integer pu(3),pv(3),p(3),i,j,k,ixu,ixv,iparity(3)
      real*8 FG, L(3)
      character*3 parity
      COMMON/tilt/a(3,3),d(3,3)

      FG = 0.d+00
      i=ixu
      j=ixv
      if(ixu.eq.ixv)j = 2/i + i/3
      k=6-i-j
      iparity(1)=133
      iparity(2)=133
      iparity(3)=133
      if(mod(p(i),2).ne.0)iparity(1)=150
      if(mod(p(j),2).ne.0)iparity(2)=150
      if(mod(p(k),2).ne.0)iparity(3)=150

      parity = char(iparity(1))//char(iparity(2))//char(iparity(3))

      if(ixu.eq.ixv)then
        if(parity.eq.'eee')then
          idenom = (p(i)-1)*(p(j)+1)*(p(k)+1)
          if(idenom.le.0)return
          FG = (l(j)*l(k)/l(i))*dfloat(pu(i)*pv(i))/dfloat(idenom)
          return
        endif
        if(parity.eq.'eoe')then
          idenom = (p(i)-1)*(p(j)+2)*(p(k)+1)
          if(idenom.le.0)return
          FG = (d(i,k)*l(i)-d(k,i)*l(k))*(l(j)**2/l(i)**2)*
     &              dfloat(pu(i)*pv(i))/dfloat(idenom)
          return
        endif
        if(parity.eq.'eeo')then
          idenom = (p(i)-1)*(p(j)+1)*(p(k)+2)
          if(idenom.le.0)return
          FG = (d(i,j)*l(i)-d(j,i)*l(j))*(l(k)**2/l(i)**2)*
     &              dfloat(pu(i)*pv(i))/dfloat(idenom)
          return
        endif
        if(parity.eq.'oee')then
          idenom = p(i)*(p(j)+1)*(p(k)+1)
          if(idenom.le.0)return
          FG = (d(k,j)*l(k)*dfloat(pu(i)*pv(i)-
     &    pu(i)*pv(j)-pv(i)*pu(j))+
     &          d(j,k)*l(j)*dfloat(pu(i)*pv(i)-
     &    pu(i)*pv(k)-pv(i)*pu(k)))/dfloat(idenom)
          return
        endif
        if(parity.eq.'oeo')then
          idenom = p(i)*(p(j)+1)*p(k)
          if(idenom.le.0)return
          FG = - a(j,k)*l(j)*(pu(i)*pv(k)+pv(i)*pu(k))/dfloat(idenom)
          return
        endif
        if(parity.eq.'ooe')then
          idenom = p(i)*p(j)*(p(k)+1)
          if(idenom.le.0)return
          FG = - a(k,j)*l(k)*(pu(i)*pv(j)+pv(i)*pu(j))/dfloat(idenom)
          return
```

```fortran
          endif
        else
          if(parity.eq.'ooe')then
            idenom = p(i)*p(j)*(p(k)+1)
            if(idenom.le.0)return
            FG = dfloat(pu(i)*pv(j))*l(k)/dfloat(idenom)
            return
          endif
          if(parity.eq.'oee')then
            idenom = p(i)*(p(j)+1)*(p(k)+1)
            if(idenom.le.0)return
            FG = (dfloat(pu(i)*pv(j)-pu(i)*pv(k))*l(j)*d(i,k)-
     &        dfloat(pu(i)*pv(i))*l(j)*l(k)/l(i)*d(k,i))/dfloat(idenom)
            return
          endif
          if(parity.eq.'eoe')then
            idenom = (p(i)+1)*p(j)*(p(k)+1)
            if(idenom.le.0)return
            FG = (dfloat(pu(i)*pv(j)-pu(k)*pv(j))*l(i)*d(j,k)-
     &        dfloat(pu(j)*pv(j))*l(i)*l(k)/l(j)*d(k,j))/dfloat(idenom)
            return
          endif
          if(parity.eq.'eee')then
            idenom1 = (p(i)-1)*(p(j)+1)*(p(k)+1)
            idenom2 = (p(i)+1)*(p(j)-1)*(p(k)+1)
            if(idenom1.gt.0)FG =    - dfloat(pu(i)*pv(i))*l(j)*l(k)/l(i)*
     &                        a(k,i)/dfloat(idenom1)
            if(idenom2.gt.0)FG = FG - dfloat(pu(j)*pv(j))*l(i)*l(k)/l(j)*
     &                        a(k,j)/dfloat(idenom2)
            return
          endif
          if(parity.eq.'oeo')then
            idenom = p(i)*(p(j)+1)*p(k)
            if(idenom.le.0)return
            FG = - dfloat(pu(i)*pv(k))*l(j)*a(i,k)/dfloat(idenom)
            return
          endif
          if(parity.eq.'eoo')then
            idenom = (p(i)+1)*p(j)*p(k)
            if(idenom.le.0)return
            FG = - dfloat(pv(j)*pu(k))*l(i)*a(j,k)/dfloat(idenom)
            return
          endif
        endif

        return
        end
```

3. Data file npr.dat

The form of this data file is similar to that of xyztrap.dat, except that a matrix of tilt angles is given (as described in Section VI).

```
Sample QX1
3
1.100000, 3, 11,1., 22,1., 33,1.
0.300000, 3, 12,1., 13,1., 23,1.
0.400000, 3, 44,1., 55,1., 66,1.
0.0419200,0.0426700,0.0576100
```

2.3590

	-3	-2	-1	0	1	2	3
1	0.26	-0.05	0.	0.	0.	0.00	0.31
2	0.09	0.	-0.11	0.	0.00	0.	0.12
3	0.	-0.15	-0.17	0.	0.00	-0.31	0.

4. fumarp


```
@PROCESS DC(BIG)
c----------------------------------------------------------------


c    This program is used to plot the eigenfunctions of
c    elastic parallelepipeds, such as one might prepare for
c    a RUS measurement.  The sample parameters are read
c    from the data file 'rpma dat', and then the Rayleigh-
c    Ritz eigenvalue problem for the sample is solved using
c    a modified 'xyz' algorithm (see 'xyzrpr', 'xyzllogm',
c    etc.)  The lowest 50 frequencies are printed out, and
c    you are asked to choose among them for the corresponding
c    eigenfunctions to plot (you can ask for modes as high
c    as 99, but the frequencies above 50 are not printed).
c    FUMARP then uses the eigenvectors from the above solution
c    to caclculate the vertices of an 8X8 grid of rectangles
c    on three adjacent sample faces, and writes them out
c    as Mathematica 'Polygon[]' primitives.  Each eigenfunction
c    is written out as a separate file, according to
c    the mode number, i.e. 'EIGFUN01.MA' or 'EIGFUN10.MA'.
c    The files may be read directly into Mathematica and displayed
c    with Show[Graphics3D[ ]].
c
c    The 8X8 grid can be changed to a higher or lower
c    number by adjusting the parameter 'nsq'.  It may
c    be necessary to use a finer grid for higher modes (n > 15).
c
c -----------------------------------------------------
      Program fumarp

      IMPLICIT real*8 (a-h,o-z)
      integer R,RR,NN
      Parameter(R=858,RR=1716,NN=10)
      real*8 w(R)
      real*8 wk1(RR),cij(6,6),c(3,3,3,3),rho,d1,d2,d3,F
      COMMON/BIG/gamma(R,R),e(R,R)
      integer lb(R),mb(R),nb(R),ic(R)
      integer neq(21),id(21,21)
      real*8 cf(21,21),cj(21),mass
      character*50 HEADER
c----------------------------------------
      integer iw(100)
      parameter(nsq=16)
      real*8  x(nsq+1,nsq+1,3),x0(3),enorm(3)
      character*12 fname
      character*2  suffix
c----------------------------------------

400   FORMAT(A50)

      open(unit=7,file='/rpma dat',status='old')
```

```fortran
      read(7,400) HEADER
      read(7,*)numic
      do 11 i=1,numic
        read(7,*) cj(i),neq(i),(id(i,j),cf(i,j),j=1,neq(i))
 11   continue
      read(7,*)d1,d2,d3
      read(7,*) rho
c-------------------------------------
      TWOPI = 2.d0*DACOS(-1.d0)
c-------------------------------------

      E11=4.D0/(D1*D1)
      E22=4.D0/(D2*D2)
      E33=4.D0/(D3*D3)
      E23=4.D0/(D2*D3)
      E13=4.D0/(D1*D3)
      E12=4.D0/(D1*D2)

      enorm(1) = 3.*d1/(d1+d2+d3)
      enorm(2) = 3.*d2/(d1+d2+d3)
      enorm(3) = 3.*d3/(d1+d2+d3)

      call xuflow(0)

      call cjcij(cj,cij,neq,id,cf,numic)
      call cindex(cij,c,0)
      ig=0
      do 1 i=1,3
       do 2 l=1,NN+1
       do 2 m=1,NN+1
       do 2 n=1,NN+1
        if(l+m+n.gt.NN+3)go to 2
        ig=ig+1
        ic(ig)=i
        lb(ig)=l-1
        mb(ig)=m-1
        nb(ig)=n-1
 2     continue
 1    continue
      nr=ig
      do 3 ig=1,nr
      do 3 jg=ig,nr
       i=ic(ig)
       j=ic(jg)
       ls=lb(ig)+lb(jg)
       ms=mb(ig)+mb(jg)
       ns=nb(ig)+nb(jg)
       gamma(ig,jg)=
     &  c(i,1,j,1)*dfloat(lb(ig)*lb(jg))*F(ls-2,ms,ns)*E11
     & +c(i,2,j,2)*dfloat(mb(ig)*mb(jg))*F(ls,ms-2,ns)*E22
     & +c(i,3,j,3)*dfloat(nb(ig)*nb(jg))*F(ls,ms,ns-2)*E33
     & +(c(i,1,j,2)*dfloat(lb(ig)*mb(jg))+c(i,2,j,1)*
     & dfloat(mb(ig)*lb(jg)))*F(ls-1,ms-1,ns)*E12
     & +(c(i,1,j,3)*dfloat(lb(ig)*nb(jg))+c(i,3,j,1)*
     & dfloat(nb(ig)*lb(jg)))*F(ls-1,ms,ns-1)*E13
     & +(c(i,2,j,3)*dfloat(mb(ig)*nb(jg))+c(i,3,j,2)*
     & dfloat(nb(ig)*mb(jg)))*F(ls,ms-1,ns-1)*E23
       gamma(jg,ig)=gamma(ig,jg)
       if(i.eq.j) e(ig,jg)=F(ls,ms,ns)
```

```fortran
3       e(jg,ig)=e(ig,jg)

        call dsygv(1,gamma,nr,e,nr,w,gamma,R,R,wk1,RR)

        do 4 i=1,nr
         if(w(i).gt.0)w(i)=dsqrt(w(i)/rho)/twopi
4       continue
        print*,'frequencies of rect. parallelepiped:'
        print*, ' '
        print 101,(i-6, w(i), i=7,56)
101     format(5(2X,I2,1X,E11.5))

        write(6,*) 'How many eigenfunctions would you like to '
        write(6,*) 'calculate?'
        read(5,*) nfuns
        if(nfuns.eq.0)STOP
        write(6,*)'Enter what number eigenvalues correspond to the'
        write(6,*)'desired eigenfunctions, separated by commas. Use'
        write(6,*)'integers from 1 to 99, where 1 corresponds to the'
        write(6,*)'lowest non-zero eigenvalue.'
        read(5,*)(iw(i), i=1,nfuns)

        do 110 i = 1,nfuns
        write(6,*)'Enter scale factor for displacements (1 to 100'
        write(6,*)'as a percent of sample dimension).'
        read(5,*) scale
        scale = scale*2.d0*(d1*d2*d3)**0.6666666666
         if(iw(i).gt.99)goto 109
         if(iw(i).lt.10)fname = '/eigfun'//'0'//char(240+iw(i))//' ma'
         if(iw(i).ge.10)then
           idigi1 = iw(i)/10
           idigi2 = iw(i) - idigi1*10
           suffix = char(240+idigi1)//char(240+idigi2)
           fname =  '/eigfun'//suffix//' ma'
         endif
         open(unit=8, file = fname, status = 'unknown')

        write(8,430) '(*',HEADER,';'
        write(8,*) 'Plot of eigenfunction corresponding to'
        write(8,431) 'natural frequency',iw(i),',',w(iw(i)+6),'MHz,'
        write(8,*) 'to be displayed in Mathematica using'
        write(8,*) 'Show[Graphics3D[]].     *)'
430     Format(A2,3X,A50,A1)
431     Format(A17,1X,I2,A1,1X,F9.6,1X,A4)

        write(8,*) '{'

        do 150 iface = 1,3

        write(8,443) '(*  Face #',iface,'  *)'
443     Format(A10,I1,A4)

        iu = 3 - (iface/3)
        iv = 6 - iface - iu

        do 300 iui = 1, nsq + 1
         do 200 ivi = 1, nsq + 1
           x(iui,ivi,iface) = enorm(iface)
           x(iui,ivi,iu) = enorm(iu) -
     &        2.*enorm(iu)*dfloat(iui - 1)/dfloat(nsq)
```

```fortran
         x(iui,ivi,iv) = enorm(iv) -
     &       2.*enorm(iv)*dfloat(ivi - 1)/dfloat(nsq)
         x0(iface) = x(iui,ivi,iface)
         x0(iu)    = x(iui,ivi,iu)
         x0(iv)    = x(iui,ivi,iv)
         do 190 jg = 1,nr

          xbasis = 0.d0
          ybasis = 0.d0
          zbasis = 0.d0

          if(dabs(x0(1)).le.0.d-07 .and. lb(jg).eq.0) xbasis = 1.d0
          if(dabs(x0(2)).le.0.d-07 .and. mb(jg).eq.0) ybasis = 1.d0
          if(dabs(x0(3)).le.0.d-07 .and. nb(jg).eq.0) zbasis = 1.d0

          if(dabs(x0(1)).gt.0.d-07) xbasis = (x0(1)/enorm(1))**lb(jg)
          if(dabs(x0(2)).gt.0.d-07) ybasis = (x0(2)/enorm(2))**mb(jg)
          if(dabs(x0(3)).gt.0.d-07) zbasis = (x0(3)/enorm(3))**nb(jg)

          x(iui,ivi,ic(jg)) = x(iui,ivi,ic(jg)) +
     & gamma(jg,iw(i)+6)*xbasis*ybasis*zbasis*scale
190        continue

 200       continue
 300       continue

        do 301 j = 1,nsq
         do 201 k = 1,nsq


          write(8,444) 'Polygon[{{',
     &       x(j,k,1),',',x(j,k,2),',',x(j,k,3),'}',
     & ',{',x(j+1,k,1),',',x(j+1,k,2),',',x(j+1,k,3),'}',',,'
          if(iface.eq.3 .and. j.eq.nsq .and. k.eq.nsq)then
           write(8,445) '{',
     &       x(j+1,k+1,1),',',x(j+1,k+1,2),',',x(j+1,k+1,3),'}',
     & ',{',x(j,k+1,1),',',x(j,k+1,2),',',x(j,k+1,3),'}',
     & '}] '
          else
           write(8,445) '{',
     &       x(j+1,k+1,1),',',x(j+1,k+1,2),',',x(j+1,k+1,3),'}',
     & ',{',x(j,k+1,1),',',x(j,k+1,2),',',x(j,k+1,3),'}',
     & '}],'
          endif
444        Format(A10,3(F7.4,A1),A2,3(F7.4,A1),A1)
445        Format(5X,A1, 3(F7.4,A1),A2,3(F7.4,A1),A3)

 201       continue
 301       continue

 150       continue

        write(8,*) '}'

       close(8)

 109   continue
 110   continue

     STOP
```

```
      END


      DOUBLE PRECISION FUNCTION F(ip,iq,ir)
      F=0.00d+00
      if(ip.lt.0 .or. iq.lt.0 .or. ir.lt.0)return
      iodd=mod(ip,2)
      if(iodd.ne.0) return
      iodd=mod(iq,2)
      if(iodd.ne.0) return
      iodd=mod(ir,2)
      if(iodd.ne.0) return
       F=1.d+00/
     &  dfloat((ip+1)*(iq+1)*(ir+1))
      return
      end
```

The form for the data file rpma.dat is identical to the form of xyztrap.dat.

5. lrnzmrq


```
      Program lrnzmrq
```

```
c     This program fits data to a model of Lorenzian resonances
c  with arbitrary phase interfering with a frequency-dependent
c  background.  The method used is that of Marquart; initial guesses
c  for the parameters to be fit are read into array "a", and
c  corresponding elements in array "ia" are set to 1 if the
c  parameter is to be fit, 0 if it is to be held constant.  The
c  initial guesses for the fit are usually obtained by some sort
c  of visual curvefitting; the model used to fit the data is
c  chosen to be convenient for the above purpose.
c     The background (crosstalk) is assumed to
c  vary slowly compared to the resonance peaks, and is modeled
c  with a polynomial of the form
c
c        xtalk(f) = a0 + a1(f-fmid)/fmid + a2((f-fmid)/fmid)^2 ... ;
c
c  fmid is usually fixed to be the frequency in the middle of
c  the data file.  This way, the slope and the offset can be
c  adjusted independently when visually fitting the data.
c     The resonance peaks are modeled according to
c
c
c                   (f/f0)cos(phi) + Q(1-(f/f0)^2)sin(phi)
c     psi(f) = Amp -------------------------------------------
c                        (f/f0)^2 + Q^2(1-(f/f0)^2)^2
c
c    which is essentially the real or imaginary part of a
c    Lorenzian resonance with an arbitrary phase shift, such
c    as one might obtain from a phase-sensitive detector
c    like the PAR 5202 2-phase lockin amplifier.  Other detectors
c    may have slightly different outputs.
c
c    The matrix inversion for the least-squares problem
c    is done with singular value decomposition (SVD).
c    During each iteration, the program prints the
c    singular values and then the adjusted parameters. If
c    one of the singular values is zero, it means the fit
```

```fortran
c       depended on a parameter too weakly, and the program
c       has disabled fitting of that parameter to allow the other
c       parameters to be accurately determined.  This action can
c       be controlled by changing "wmax" in "invsvd".
c
c       If the program winds up disabling several parameters, often
c       it means that the initial guesses weren't good enough.  Good
c       initial guesses are crucial to successful fitting.
c
c       The use of the Marquardt method here is based on programs
c       from Numerical Recipes [W. H. Press, S. A. Teukolsky,
c       W. T. Vetterling, B. P. Flannery, 2nd ed. (Cambridge, 1992)],
c       in the section on nonlinear modeling (pg. 675, etc.).
c       Also, the SVD routine "svdcmp" on pg. 59 is used, and the
c       use of SVD in least-squares fitting described on pg. 670
c       is relevant.
c
c
        implicit real*8(a-h,o-z)
        Parameter(ma=25, nca=25, ndata=1001, maxpks = 4, itmax=40)
c         ma = max number of parameters; nca = max number of
c         free parameters; ndata=max number of data points,
c         maxpks = max number of resonance peaks in a record,
c        itmax = max number of iterations to achieve convergence.
        Parameter(iconv=2)
c         iconv = how many times least-squares should
c          decrease by a small amount before convergence is declared
        real*8 x(ndata), y(ndata), sig(ndata), alpha(nca,nca)
        real*8 covar(nca,nca), a(ma), Amp, f0, width, phase
        COMMON/MISC1/xmid,npks
        COMMON/MISC2/npts
        integer ia(ma)

        CALL XUFLOW(0)
        pi = dacos(-1.d0)

        open(unit=7, file = '/in dat', status='old')
        open(unit=8, file = '/in gss', status='old')
        open(unit=9, file = '/out prm', status='unknown')
c----------------------------------------------------
        read(8,*) a(1), a(2), a(3), a(4)
        npks=0
        do 1 i=1,maxpks
C        read(unit=8, fmt=*, end=2) Amp, f0, width, phase
         read(unit=8, fmt=*, end=2) Amp, f0, Q, phase
         if(Amp.ne.0.d0)then
          a(4*npks+5)=Amp
          a(4*npks+6)=f0
C         a(4*npks+7)=f0/width
          a(4*npks+7)=Q
          a(4*npks+8)=phase*pi/180.d0
          npks = npks+1
         endif
 1      continue
 2      do 3 i=1,ma
         if(a(i).ne.0d0)ia(i)=1
 3      continue
        npts = 0
c----------------------------------------------------
        READ(7,*) XMIN,XMAX,XSTEP,DRIVE
```

```fortran
      XMID = (XMAX+XMIN)/2.d0
      do 10 i=1,ndata
       read(unit=7,fmt=*,end=11) x(i), y(i)
       npts=npts+1
10    continue
11    chisq=1.0d6
      oldchi=1.0d6
      alamda=-1.d0
      oldlam=-1.d0
      monchi=0
      DO 100 ITCODE = 1, ITMAX
       if(monchi.le.iconv)then
         call mrqmin(x,y,sig,ndata,a,ia,ma,covar,alpha,nca,
     *                    chisq,alamda)
         PRINT*,'CHISQ=',CHISQ
         if(oldlam.gt.alamda   .and.
     &      (oldchi-chisq)/chisq.le.0.01d0)then
             monchi = monchi+1
         endif
         oldchi=chisq
         oldlam=alamda
       else
         call mrqmin(x,y,sig,ndata,a,ia,ma,covar,alpha,nca,
     *                    chisq,0.d0)
         write(9,*)'All parameters (xtalk, then Amp,f0,Q,phi(rad))'
         do 90 j=1,(npks+1)*4,4
          write(9,'(4F14.5)') a(j),a(j+1),a(j+2),a(j+3)
90       continue
         write(9,*)' '
         write(9,*)'-----Fitted parameters------'
         rmserr = dsqrt(chisq)/dfloat(npts)
         write(9,*)   'xtalk: (a0 + a1(f-fmid)/fmid + a2((f-fmid)/fmid)^2
     & ... )'
         write(9,'(1X,A8,E14.5,A8)')' fmid = ',xmid,' (fixed)'
         write(9,402)' a0 = ',a(1),' +-',dsqrt(covar(1,1))*
     *rmserr
         write(9,402)' a1 = ',a(2),' +-',dsqrt(covar(2,2))*
     *rmserr
       if(ia(3).ne.0)write(9,402)' a2 = ',a(3),' +-',dsqrt(covar(3,3))*
     *rmserr
       if(ia(4).ne.0)write(9,402)' a3 = ',a(4),' +-',dsqrt(covar(4,4))*
     *rmserr
         do 95 i=1,npks
          write(9,403)'Peak #',i,':'
          j=4*i
          write(9,404)' Amp = ',a(j+1),' +-',dsqrt(covar(j+1,j+1))*
     *rmserr
          write(9,404)' f0  = ',a(j+2),' +-',dsqrt(covar(j+2,j+2))*
     *rmserr
          write(9,404)' Q   = ',a(j+3),' +-',dsqrt(covar(j+3,j+3))*
     *rmserr
          write(9,404)' phi = ',a(j+4)*180.d0/pi,
     &            ' +-',dsqrt(covar(j+4,j+4))*(180.d0/pi)*rmserr
95       continue
402      FORMAT(1X,A6,E15.8,A3,E10.3)
403      FORMAT(1X,A6,I1,A1)
404      FORMAT(1X,A7,E15.8,A3,E10.3)
         STOP
       endif
100   CONTINUE
```

```fortran
      write(9,401)'no convergence in ',itmax,' iterations'
401   FORMAT(1X,A17,I3,A11)
      do 101 j=1,(npks+1)*4,4
        write(9,'(F14.5)') a(j),a(j+1),a(j+2),a(j+3)
101   continue

      STOP
      END

      subroutine mrqmin(x,y,sig,ndata,a,ia,ma,covar,alpha,nca,
     *                   chisq,alamda)
      IMPLICIT real*8(a-h,o-z)
      parameter (MMAX=25)

      integer ma,nca,ndata,ia(ma)
      real*8 alamda,chisq,a(ma),alpha(nca,nca),covar(nca,nca),
     *      sig(ndata),x(ndata),y(ndata)

      integer j,k,l,m,mfit
      real*8 ochisq,atry(MMAX),beta(MMAX),da(MMAX)

      SAVE ochisq,atry,beta,da,mfit
      if(alamda.lt.0.d+0)then
        mfit = 0
        do 11 j=1,ma
          if(ia(j).ne.0) mfit=mfit+1
11      continue
        alamda=0.1d-2
        call mrqcof(x,y,sig,ndata,a,ia,ma,alpha,beta,nca,chisq)
        ochisq=chisq
        do 12 j=1,ma
          atry(j)=a(j)
12      continue
      endif
      j=0
      do 14 l=1,ma
        if(ia(l).ne.0) then
          j=j+1
          k=0
          do 13  m=1,ma
            if(ia(m).ne.0)then
              k=k+1
              covar(j,k)=alpha(j,k)
            endif
13        continue
          covar(j,j)=alpha(j,j)*(1.d0+alamda)
          da(j)=beta(j)
        endif
14    continue
      call invsvd(covar,mfit,nca,da)
      if(alamda.eq.0)then
        call covsrt(covar,nca,ma,ia,mfit)
        return
      endif
      j=0
      do 15 l=1,ma
        if(ia(l).ne.0)then
          j=j+1
          atry(l)=a(l)+da(j)
```

```fortran
               WRITE(6,*) A(L),DA(J),ATRY(L)
            endif
  15     continue

         call mrqcof(x,y,sig,ndata,atry,ia,ma,covar,da,nca,chisq)
         if(chisq.lt.ochisq)then
            alamda=0.1d0*alamda
            ochisq=chisq
            j=0
            do 17 l=1,ma
               if(ia(l).ne.0)then
                   j=j+1
                   k=0
                   do 16 m=1,ma
                      if(ia(m).ne.0)then
                          k=k+1
                          alpha(j,k)=covar(j,k)
                      endif
  16               continue
                   beta(j)=da(j)
                   a(l)=atry(l)
               endif
  17        continue
         else
            alamda=10.d+0*alamda
            chisq=ochisq
         endif
         PRINT*,'alamda = ', alamda
         return
         END
C
         subroutine mrqcof(x,y,sig,ndata,a,ia,ma,alpha,beta,nca,
     &              chisq)
         IMPLICIT real*8(a-h,o-z)
         integer ma,nca,ndata,ia(ma)
         real*8 chisq,a(ma),alpha(nca,nca),beta(ma),sig(ndata),x(ndata),
     *          y(ndata)
         parameter (MMAX=25)
         COMMON/MISC2/npts
         integer mfit,i,j,k,l,m
         real*8 dy,sig2i,wt,ymod,dyda(MMAX)

         mfit = 0
         do 11 j=1,ma
            if(ia(j).ne.0)then
                mfit=mfit+1
            endif
  11     continue
         do 13 j=1,mfit
            do 12 k=1,j
                alpha(j,k)=0.d+0
  12        continue
            beta(j)=0.d+0
  13     continue
         chisq=0.d+0
         do 16 i=1,npts
            call lrzn(x(i),a,ymod,dyda,ma)
c-------------------------------------
         SIG(I)=1.d+0
c-------------------------------------
```

```fortran
c         sig2i=1.d+0/(sig(i)*sig(i))
          SIG2I=1.d0/Y(I)*Y(I)
          dy=(y(i)-ymod)
          j=0
          do 15 l=1,ma
              if(ia(l).ne.0)then
                  j=j+1
                  wt=dyda(l)*sig2i
c                 WT=1.d0/dyda(l)
                  k=0
                  do 14 m=1,l
                      if(ia(m).ne.0)then
                          k=k+1
                          alpha(j,k)=alpha(j,k)+wt*dyda(m)
                      endif
14                continue
                  beta(j)=beta(j)+dy*wt
              endif
15        continue
          chisq=chisq+dy*dy*sig2i
16    continue
      do 18 j=2,mfit
          do 17 k=1,j-1
              alpha(k,j)=alpha(j,k)
17        continue
18    continue
      return
      END

      SUBROUTINE covsrt(covar,npc,ma,ia,mfit)
      IMPLICIT real*8(a-h,o-z)
      INTEGER ma,mfit,npc,ia(ma)
      REAL*8 covar(npc,npc)
c     INTEGER i,j,k
      REAL*8 swap
      do 12 i=mfit+1,ma
          do 11 j=1,i
              covar(i,j)=0.d+0
              covar(j,i)=0.d+0
11        continue
12    continue
      k=mfit
      do 15 j=ma,1,-1
          if(ia(j).ne.0)then
              do 13 i=1,ma
                  swap=covar(i,k)
                  covar(i,k)=covar(i,j)
                  covar(i,j)=swap
13            continue
              do 14 i=1,ma
                  swap=covar(k,i)
                  covar(k,i)=covar(j,i)
                  covar(j,i)=swap
14            continue
              k=k-1
          endif
15    continue
      return
      END
```

```fortran
      SUBROUTINE invsvd(a,n,np,b)
      IMPLICIT real*8 (a-h,o-z)
      PARAMETER(MMAX=25)
      REAL*8   a(np,np),b(np),x(MMAX)
      REAL*8   ainv(MMAX,MMAX),w(MMAX),t1(MMAX,MMAX),v(MMAX,MMAX)

      call svdcmp(a,n,n,np,np,w,v)

      wmax=0.0d+00
      do 100 j=1,n
        if(w(j).gt.wmax) wmax=w(j)
100   continue
      wmin=wmax*1.d-14
      do 110 j=1,n
        if(w(j).lt.wmin) w(j)=0.0d+00
        write(6,*) w(j)
110   continue
c

      do 12 i=1,n
       do 11 j=1,n
         if(w(j).ne.0.d+00)then
          t1(i,j)=v(i,j)/w(j)
         else
          t1(i,j)=0.d+00
         endif
11       continue
12     continue

      do 15 i=1,n
       do 14 j=1,n
        ainv(i,j)=0.d+00
        do 13 k=1,n
          ainv(i,j)=ainv(i,j)+t1(i,k)*a(j,k)
13        continue
14      continue
15     continue

      do 17 i=1,n
       x(i)=0.d+0
       do 16 j=1,n
          x(i)=x(i)+ainv(i,j)*b(j)
16      continue
17     continue

      do 19 i=1,n
       b(i)=x(i)
       do 18 j=1,n
        a(i,j)=ainv(i,j)
18      continue
19    continue

      return
      END


      Subroutine lrzn(x,a,y,dyda,ma)
      implicit real*8 (a-h, o-z)
      real*8 x,y,a(ma),dyda(ma),num,den
```

```
      real*8 a0,a1,a2,a3,Amp,x0,Q,phi
      COMMON/MISC1/xmid,npks

      a0=a(1)
      a1=a(2)
      a2=a(3)
      a3=a(4)

      y  =  a0 + a1*(x-xmid)/xmid + a2*((x-xmid)/xmid)**2 +
     &                a3*((x-xmid)/xmid)**2

      dyda(1) = 1.d0
      dyda(2) =(x-xmid)/xmid
      dyda(3) =((x-xmid)/xmid)**2
      dyda(4) =((x-xmid)/xmid)**3

      DO 100 i=1,npks
       Amp=a(4*i+1)
       x0 =a(4*i+2)
       Q  =a(4*i+3)
       phi=a(4*i+4)
       num = (x/x0)*dcos(phi) + (1.d0 - (x/x0)**2)*Q*dsin(phi)
       den = (x/x0)**2 + (1.d0 - (x/x0)**2)**2*Q**2

      y = y + Amp*num/den

      dyda(4*i+1) = num/den

      dyda(4*i+2) = Amp*(x/x0**2)*(
     &        (2.d0*(x/x0)*Q*dsin(phi) - dcos(phi))/den -
     &    num*(x/x0)*(4.d0*(1.d0-(x/x0)**2)*Q**2 - 2.d0)/den**2 )

      dyda(4*i+3) = Amp*( (1.d0 - (x/x0)**2)*dsin(phi)/den -
     &                num*2*Q*(1.d0-(x/x0)**2)**2/den**2 )

      dyda(4*i+4) = Amp*( (1.d0-(x/x0)**2)*Q*dcos(phi) -
     &    (x/x0)*dsin(phi) )/den

100   CONTINUE

      return
      END
```

6. Data file in.gss

This file contains first the background parameters (slope, offset, *etc.*), and then guesses for the amplitude, frequency, peakwidth, and phase of the resonance peaks. The particular values in this file correspond to the crosstalk features shown in Fig. 36.

```
-0.020    0.15        0.0     0.00
 0.120    3750000.0   18.0    48.7
 0.420    4260000.0   20.0    123.0
 0.000    0000000.0   00.0    00.0
 0.000    0000000.0   00.0    00.0
```

7. rprmrq

```
      PROGRAM rprmrq
```

```
C
C  This program finds elastic constants from frequency data,
C mass, and initial guesses for lengths and elastic constants
C of a rectangular parallelepiped sample; the RPR in RPRMRQ
C stands for Rectangular Parallelepiped Resonance (coined by Ohno).
C  The Levenberg-Marquart method (the ''MRQ'' in RPRMRQ) is used to
C minimize the least-squares between the observed normal mode
C frequencies and those calculated from the current parameter set.
C The program looks for 2 data files: one contains the data
C (elastic constants, mass, edge lengths, resonance frequencies)
C called RPRMRQ.DAT, and a file containing a list of basis function
C (Legendre polynomial) indices, called RPRMRQ.INDEX .  RPRMRQ.INDEX
C is set up according to the precision (hence number of basis functions)
C that one wishes, and the crystal symmetry of the sample.  This in
C turn determines the size and number of matrix blocks that
C will be processed in calculating the frequencies.
C
C  To keep the program general, the setting up of the basis functions
C has been left up to the user.  However, the subroutine(s) ORTHIDX, etc.
C can set the index list up for you, for some special cases.  At this
C time they include:
C
C * Orthorhombic(incl. hexagonal, cubic, isotropic, etc.)
C(* Trigonal, e.g. alpha-quartz (first dim. in data file is X-dir))not yet
C(* Triclinic (most general symmetry---only two matrix blocks)) not yet
C
C   The symmetry is indicated by a 5-letter string in the second
C line in the data file RPRMRQ.DAT; "ORTHO"=orthorhombic,
C ("TRICL" will equal triclinic, "TRIGO" will = trigonal).
C
C   To allow the user to conserve virtual memory, the subroutine
C that calculates the frequencies (FREQ) defines a number of
C parameters for matrix dimensions, that depend on the crystal
C symmetry and number of basis functions.   Thus one must specify
C these differently for each case.  A fairly comprehensive list
C for the special cases listed above is included, so the user
C can simply "uncomment" the one desired.  If memory is not a
C problem, then one may go to the bottom entry in the TRICLINIC
C list, which will always provide enough space for the other cases.
C
C  For different symmetries, the mode labels will also be
C different; the character array MODEGRP may be set up any
C way one wishes (unless one desires mode labels of more than
C two characters, in which case other modifications are required).
C Again, a sequence of DATA statements has been included to cover
C some special cases.
C
      implicit real*8 (a-h,o-z)
      Parameter (maxfp=27,itmax=15,mdata=100,EPS=1.d-09,mconv=2)

C  maxfp=maximum number of free parameters.  For an orthorhombic
C  crystal with 9 independent elastic constants,
C  maxfp = 9 + 3 edge lengths + 3 Euler
C  angles = 15.  For triclinic crystal, maxfp could be as high as 27.
C  mconv is a convergence criterion (the number of times the
C  least squares must decrease by a negligible amount before
C  the fit is accepted).
C
C  NN is the maximum order of the basis function used in the matrix
C  approximation of the Lagrangian (in this case, Legendre polynomials  ,
```

```
C since the sample is a rectangular parallelepiped).  IR is the subsequent
C dimension of the largest matrix block in the block-diagonalized matrix.
C     IPACK is the size of a 1-dim "symmetry storage" matrix that is
C     equivalent to the square IRXIR matrix.  IPACK=IR(IR+1)/2
C
C     These parameters are defined in the subroutine "freq".

      real*8 a(maxfp),fcalc(mdata),ftemp(mdata)
      real*8 dfda(mdata,maxfp),temp,h,chitemp,sig(mdata),mass
      integer neq(21),id(21,21),ia(maxfp)
      real*8 cf(21,21),FOBSA(MDATA),tempdf(maxfp)
      real*8 covar(maxfp,maxfp),alpha(maxfp,maxfp),chisq,alamda
      character HEADER*50, modegrp(8)*2, fmode*5, mstring*2
      character symstrg*5, chdfda(maxfp)*4
      COMMON/symm/isymm
      COMMON/limits/fmin,fmax,iflag
      COMMON/modes1/obsarr(8,mdata),fobs(mdata)
      COMMON/modes2/modeid(mdata,2)

c----------for orthorhombic crystals--------------------
      DATA modegrp/'OD','EX','EY','EZ','OX','OY','OZ','EV'/
c-------------------------------------------------------

400   FORMAT(A50)
      open(unit=7,file='/rprmrq dat',status='old')
      open(unit=8,file='/rprmrq fit',status='unknown')
      read(7,400)HEADER
c------------------------------------------------------------
      read(7,'(A5)')symstrg
      isymm = 0
      IF(symstrg.eq.'ortho')isymm = 1
c------------------------------------------------------------
      read(7,*)numic
      do  7 i=1,numic
        read(7,*) a(i),neq(i),(id(i,j),cf(i,j),j=1,neq(i)),ia(i)
  7   continue
      read(7,*)a(numic+1),a(numic+2),a(numic+3),
     &    ia(numic+1),ia(numic+2),ia(numic+3)
C     read(7,*) rho
      read(7,*) mass,rhoref
      read(7,*)job
      iflag = 0
      read(7,*)fmin,fmax
      read(7,*)nof

      IF(NOF.gt.0)THEN
       do 14 i=1,nof
        IF(job.eq.30)read(7,*)j,fobsa(j)
        IF(job.ne.30)THEN
         read(7,'(A5,1X,F9.6)') fmode, fo
         do 13 k=1,8
           if(fmode(1:2).eq.modegrp(k))then
             imode = k
             jmode = (ichar(fmode(4:4)) - 240)*10 +
     &                  ichar(fmode(5:5)) - 240
             obsarr(imode,jmode) = fo
           endif
 13      continue
        ENDIF
 14    continue
```

```fortran
        ENDIF

        iflag=-1
        if(job.eq.40)goto 141
        if(mod(job,10).eq.0)goto 20

141     continue

        IF(rhoref.ne.0.d0)THEN
          volume = 1000.d0*mass/rhoref
          ivolflag = 0
        ENDIF
        chitemp=1000.d+00
        iconv=0
145     almtemp=1.d-3
        do 18 itcode=1,itmax
C         mass=rho*a(numic+1)*a(numic+2)*a(numic+3)/1000.d+00
          call freq(a,mass,neq,id,cf,numic,maxfp,mdata,fcalc,sig)
          do 16 j=1,numic+6
            if(ia(j).ne.0)then
                temp=a(j)
                h=EPS*dabs(temp)
                if(h.eq.0.d+00)h=EPS
                a(j)=temp+h
                h=a(j)-temp
                call freq(a,mass,neq,id,cf,numic,maxfp,mdata,ftemp,sig)
                a(j)=temp
                do 15 i=1,mdata
                 dfda(i,j)=(ftemp(i)-fcalc(i))/h
15              continue
            else
                do 151 i=1,mdata
                    dfda(i,j)=0.0d+00
151             continue
            endif
16        continue

          IF(JOB.EQ.40)GOTO 20

          almtemp=alamda
          if(itcode.eq.1)alamda=-1.d+00
          call mrqnmin(fobs,fcalc,dfda,sig,mdata,a,ia,maxfp,covar,
     &   alpha,maxfp,chisq,alamda,
     &   mass,neq,id,cf,numic)
          write(6,'(1X,A8,1X,E7.1)')'alamda =', alamda
c----------------------
C         anisot = 2*a(3)/(a(1) - a(2)) - 1.d0
C         write(6,'(1X,A13,F9.6)') 'anisotropy = ',anisot
c----------------------
          if(dabs(chitemp-chisq)/chisq.le.1.d-03 .and.
     &        almtemp.gt.alamda)iconv=iconv+1
          WRITE(6,'(A9,I1)')' iconv = ',ICONV
          if(chisq.lt.chitemp)chitemp=chisq
          if(iconv.eq.mconv)go to 19
18      continue

        write(6,*)'No convergence in',itmax,'iterations.'
C       STOP
19      IF(rhoref.ne.0.d0 .and. ivolflag.eq.0)THEN
            dimcorr =
```

```fortran
     &      (a(numic+1)*a(numic+2)*a(numic+3)/volume)**(1.d0/3.d0)
            do 142 icorr=1,numic
              a(icorr)=a(icorr)*dimcorr
142         continue
            a(numic+1) = a(numic+1)/dimcorr
            a(numic+2) = a(numic+2)/dimcorr
            a(numic+3) = a(numic+3)/dimcorr
            iconv = iconv -1
            ivolflag = 1
            GOTO 145
      ENDIF
      call mrqnmin(fobs,fcalc,dfda,sig,mdata,a,ia,maxfp,covar,
     &                  alpha,maxfp,chisq,0.d+0,
     &                  mass,neq,id,cf,numic)
      DATERR=DSQRT(CHISQ/DFLOAT(NOF))
 20   call freq(a,mass,neq,id,cf,numic,maxfp,mdata,fcalc,sig)
      do 30 i=1,mdata
        if(fcalc(i).ne.0)maxif = i
30    continue
c-----------------------------------------------
      anisot =  2.d0*a(3)/(a(1)-a(2)) - 1.d0
c-----------------------------------------------
      IF(JOB.GT.10)THEN
       call rprshell(mdata,maxif,fcalc,fobs,modeid,dfda,maxfp)
      ENDIF
      IF(JOB.EQ.30)THEN
       OPEN(unit=10,file='/modelist out',status='unknown')
       WRITE(10,*)'Observed frequencies assigned to modes in order'
       DO 120 I=1,mdata
         if(modeid(i,2).le.9)mstring = '0'//char(240+modeid(i,2))
         if(modeid(i,2).gt.9)mstring = char(240+modeid(i,2)/10)//
     &                  char(240+mod(modeid(i,2),10))
         if(fcalc(i).ne.0.d0)write(10,
     &  '(A2,A1,A2,2X,F8.6)') modegrp(modeid(i,1)),'-',mstring,
     &            fobsa(i)
120    CONTINUE
      ENDIF
c-----------------------------------------------
      write(8,*)'Observed and Caculated Frequencies,'
      write(8,*)'and their Differences (in MHz).'
      write(8,*)' '
      write(8,*)' mode            fobs          fcalc       fobs-fcalc
     & %err'
      write(8,*)' '
      DO 21 I=1,maxif
       if(modeid(i,2).le.9)mstring = '0'//char(240+modeid(i,2))
       if(modeid(i,2).gt.9)mstring = char(240+modeid(i,2)/10)//
     &                  char(240+mod(modeid(i,2),10))
       if(fobs(i).gt.0.0d0)then
         write(8,401)i,modegrp(modeid(i,1)),'-',mstring,
     &   fobs(i),fcalc(i),fobs(i)-fcalc(i),
     &         1.D+02*dabs((fobs(i)-fcalc(i))/fobs(i))
        else
         write(8,401)i,modegrp(modeid(i,1)),'-',mstring,
     &   1000.,fcalc(i), 1000., 1000.
       endif
21    CONTINUE
      write(8,*)' '
      write(8,'(1X,A8,E9.3)')'CHISQ = ',chisq
      write(8,408)'AVGFIT = ',DATERR*1.D+2,'%'
```

```fortran
      write(8,*)' '
      write(8,*)' '
      write(8,*)'Results of Fitted Parameters'
      write(8,*)' '

      ifit=0
      do 22 i=1,numic
        if(ia(i).ne.0)then
           ifit=ifit+1
           write(8,402)'C',id(i,1),'=',a(i),
     &      '+-',dsqrt(covar(ifit,ifit))*DATERR
        else
           write(8,403)'C',id(i,1),'=',a(i),'*'
        endif
 22   continue
      do 23 i=1,3
        if(ia(numic+i).ne.0)then
           ifit=ifit+1
           write(8,404)'L',i,'=',a(numic+i),
     &      '+-',dsqrt(covar(ifit,ifit))*DATERR
        else
           write(8,405)'L',i,'=',a(numic+i),'*'
        endif
 23   continue
      write(8,*)' '
      write(8,'(1X,A13,E10.3)')'Anisotropy = ', anisot
c------------------------------------
 
      write(8,*)' '
      write(8,*)'* = held fixed'
      write(8,*)' '
      write(8,'(A7,E11.5,A3)')'mass = ',mass*1000.,' mg'
      if(rhoref.ne.0.d0)write(8,'(A7,F7.4,A5)')'rho  = ',rhoref,' g/cc'

      close(8)
      open(unit=8, file='/rprdfda out', status='unknown')
      write(8,*)'Derivatives of frequencies with respect to'
      write(8,*)'free parameters:'
      write(8,*)' '
      write(8,*)' '
      ifit=0
      do 40 i=1,numic
        if(ia(i).ne.0)then
           ifit=ifit+1
           chdfda(ifit)='dC'//char(240+id(i,1)/10)//
     &     char(240+mod(id(i,1),10))
        endif
 40   continue
      do 41 i=1,3
        if(ia(numic+i).ne.0)then
           ifit=ifit+1
           chdfda(ifit)='dL'//char(240+i)//' '
        endif
 41   continue
      write(8,*)'                       ', ('dfn   ', i=1,ifit)
      write(8,*)'                       ', ('---- ', i=1,ifit)
      write(8,410)'  n  mode fcalc(n)  ', (chdfda(i), i=1,ifit)
      write(8,*)' '
      do 43 i=1,maxif
       if(modeid(i,2).le.9)mstring = '0'//char(240+modeid(i,2))
```

```fortran
           if(modeid(i,2).gt.9)mstring = char(240+modeid(i,2)/10)//
     &                    char(240+mod(modeid(i,2),10))
          itemp=0
          do 42 iai = 1,maxfp
            if(ia(iai).ne.0)then
              itemp=itemp+1
              tempdf(itemp)=dfda(i,iai)
            endif
42        continue
          write(8,411)i,modegrp(modeid(i,1)),'-',mstring,
     &         fcalc(i),(tempdf(j),j=1,ifit)
43     continue

401   Format(1X,I2,1X,A2,A1,A2,3X,F10.7,5X,F10.7,5X,F10.7,5X,F6.4)
402   Format(1X,A1,I2,4X,A1,1X,F9.6,A2,F8.6)
403   Format(1X,A1,I2,4X,A1,1X,F9.6,1X,A1)
404   Format(1X,A1,I1,5X,A1,1X,F9.6,A2,F8.6)
405   Format(1X,A1,I1,5X,A1,1X,F9.6,1X,A1)
406   Format(1X,A5,I1,1X,A1,1X,F9.6,A2,F8.6)
407   Format(1X,A5,I1,1X,A1,1X,F9.6,1X,A1)
408   Format(1X,A7,F5.3,A1)
409   Format(5X,A7,F7.5,A3)
410   Format(A19,11(A4,2X))
411   Format(1X,I2,1X,A2,A1,A2,2X,F6.4,11F6.2)

      STOP
      END




      SUBROUTINE freq(a,mass,neq,id,cf,numic,maxfp,mdata,fcalc,sig)
      IMPLICIT real*8(a-h,o-z)
C-------For orthorhombic crystals-----------------------------
C     Parameter (NN=06,IR=40,IRMAX=252,IPACK=820,NDATA=100)
C     Parameter (NN=07,IR=60,IRMAX=360,IPACK=1830,NDATA=100)
C     Parameter (NN=08,IR=75,IRMAX=495,IPACK=2850,NDATA=100)
C     Parameter (NN=09,IR=105,IRMAX=660,IPACK=5565,NDATA=100)
C     Parameter (NN=10,IR=126,IRMAX=858,IPACK=8001,NDATA=100)
C     Parameter (NN=11,IR=168,IRMAX=1092,IPACK=14196,NDATA=100)
      Parameter (NN=12,IR=200,IRMAX=1365,IPACK=20100,NDATA=100)
C     Parameter (NN=14,IR=288,IRMAX=2040,IPACK=41616,NDATA=100)
C------------------------------------------------------------
      PARAMETER (ETOL = 1.0d-04)
      real*8 sig(mdata)
      real*8 a(maxfp),mass,fcalc(mdata),emax,emin
      integer maxfp,neq(21),id(21,21),numic
      real*8 cj(21),cij(6,6),c(3,3,3,3)
      real*8 el(3),cf(21,21)
      real*8 gamma(IPACK),e(IR),z(IR,IR),wk(IR)
      real*8 evcof(0:NN,0:NN),oddcof(0:NN,0:NN)
      integer ier,icount,lmni(IRMAX,4),mxsz(8),nmxblk
      COMMON/limits/fmin,fmax,iflag
      COMMON/modes1/obsarr(8,ndata),fobs(ndata)
      COMMON/modes2/modeid(ndata,2)

      save lmni,nmxblk,mxsz,evcof,oddcof
      call xuflow(0)
      twopi = 2.d0*dacos(-1.d0)

      if(iflag.eq.-1)then
         call matcof(NN,IRMAX,lmni,nmxblk,mxsz,evcof,oddcof)
```

```
            iflag = 1
          endif

          icount=0
          do 9 i=1,mdata
            fcalc(i)=0.d0
            fobs(i) =0.d0
            modeid(i,1)=0
            modeid(i,2)=0
            sig(i) = 1.d0
    9     continue
          emax=((twopi*fmax)**2)*mass*1.0d+01
          emin=((twopi*fmin)**2)*mass*1.0d+01
          do 12 i=1,numic
            cj(i)=a(i)
   12     continue
          do 13 i=1,3
            el(i)=a(numic+i)
   13     continue
          call cjcij(cj,cij,neq,id,cf,numic)
          call cindex(cij,c,0)
          do 171 mxno=1,nmxblk
            imode = 0
            call matrix(c,mass,el,IRMAX,IPACK,NN,evcof,oddcof,
     &    nmxblk,mxno,mxsz,lmni,gamma,IR)
            call dspev(20,gamma,e,dummy,1,IR,wk,IR)

            DO 17 i=1,IR
C   The first 6 eigenvalues are always zero, corresponding to
C  three translations and three rotations.
            if(e(i).gt.ETOL)imode = imode+1
            if(e(i).gt.emin .and. e(i).le.emax .and.
     &              icount.le.mdata)then
              icount = icount+1
              fcalc(icount)=dsqrt(e(i)/(mass*1.0d+01))/twopi
              fobs(icount) = obsarr(mxno,imode)
              if(fobs(icount).gt.0.d0)sig(icount)=fobs(icount)
              modeid(icount,1)=mxno
              modeid(icount,2)=imode
            endif
   17     continue
  171   continue

        return
        END
c-------------

        SUBROUTINE rprshell(nmax,n,a,B,IB,dfda,maxfp)
        INTEGER nmax,n,i,j,inc,IB(NMAX,2),IV1,IV2
        REAL*8 a(nmax),B(NMAX),DFDA(nmax,maxfp),v,VB,vdf(30)
        inc=1
    1   inc=3*inc+1
        if(inc.le.n)goto 1
    2   continue
          inc=inc/3
          do 11 i=inc+1,n
            v=a(i)
            VB=B(i)
            IV1=IB(i,1)
            IV2=IB(i,2)
```

```fortran
            DO 25 ia=1,maxfp
              VDF(ia)=dfda(i,ia)
 25         CONTINUE
            j=i
 3          if(a(j-inc).gt.v)then
                a(j)=a(j-inc)
                B(j)=B(j-inc)
                IB(j,1)=IB(j-inc,1)
                IB(j,2)=IB(j-inc,2)
                DO 35 ia=1,maxfp
                  DFDA(j,ia)=DFDA(j-inc,ia)
 35             CONTINUE
                j=j-inc
                if(j.le.inc)goto 4
            goto 3
            endif
 4          a(j)=v
            B(j)=VB
            IB(j,1)=IV1
            IB(j,2)=IV2
            DO 45 ia=1,maxfp
              DFDA(j,ia)=VDF(ia)
 45         CONTINUE
 11     continue
      if(inc.gt.1)goto 2
      return
      END

      Subroutine matrix(c,mass,EL,IRMAX,IPACK,NN,evcof,oddcof,
     & nmxblk,mxno,mxsz,lmni,gamma,IR)
      implicit real*8(a-h,o-z)
      Parameter(IRBIG=1000)
      integer NN,IRMAX,IPACK,IR
      real*8 gamma(IPACK)
      real*8 mass,EL(3),HL(3),c(3,3,3,3),gtemp
      real*8 delta,evcof(0:NN,0:NN),oddcof(0:NN,0:NN)
      integer lmn(IRBIG,3),ic(IRBIG),lmni(IRMAX,4),mxsz(8)

      DO 1 I=1,IR
       LMN(I,1)=0
       LMN(I,2)=0
       LMN(I,3)=0
       IC(I)=0
       DO 1 J=I,IR
        GAMMA(I+J*(J-1)/2)=0.d0
 1    CONTINUE

      do 10 i=1,3
        HL(i)=EL(i)*0.5d+00
 10   continue

      do 21 i=1,mxno
        imin=1
        if(mxno.ne.1)then
          do 20 j=1,mxno-1
             imin=imin+mxsz(j)
 20       continue
        endif
 21   continue
      ig=0
```

```fortran
      do 2 i=imin,imin+mxsz(mxno)-1
       ig=ig+1
       ic(ig)=lmni(i,4)
       lmn(ig,1)=lmni(i,1)
       lmn(ig,2)=lmni(i,2)
       lmn(ig,3)=lmni(i,3)
   2    continue
      do 5 ig=1,mxsz(mxno)
      do 5 jg=ig,mxsz(mxno)
       gtemp=0.0d+00
       i=ic(ig)
       j=ic(jg)
       do 4 k=1,3
        do 3 l=1,3

         delta=0.1d+01
         do 11 ii=1,3
          if(ii.ne.k .and. ii.ne.l)then
           if(lmn(ig,ii).ne.lmn(jg,ii))delta=0.0d+00
          endif
  11      continue

         if(k.eq.l)then
          gtemp = gtemp + (c(i,k,j,k)/(HL(k)*HL(k)))*
     *                   delta*evcof(lmn(ig,k),lmn(jg,k))
         else
          gtemp = gtemp + (c(i,k,j,l)/(HL(k)*HL(l)))*delta*
     *         oddcof(lmn(ig,k),lmn(jg,k))*oddcof(lmn(jg,l),lmn(ig,l))
         endif
   3     continue
   4    continue
      gamma(ig+jg*(jg-1)/2)=8.0d+00*HL(1)*HL(2)*HL(3)*gtemp
   5  continue
      return
      END

      Subroutine matcof(NN,IRMAX,lmni,nmxblk,mxsz,evcof,oddcof)
      implicit real*8(a-h,o-z)
      integer NN,IRMAX
      real*8 evcof(0:NN,0:NN),oddcof(0:NN,0:NN)
      integer lmni(IRMAX,4),mxsz(8)
      COMMON/symm/isymm

C------------------------------------------------------
      IF(isymm.eq.1)CALL ORTHIDX(NN)
C------------------------------------------------------
      OPEN(unit=9,file='/rprmrq index',status='old')
      read(9,*) nmxblk

      jcount=0
      do 172 i=1,nmxblk
         read(9,*)mxsz(i)
         do 171 j=jcount+1,jcount+mxsz(i)
            read(9,*) (lmni(j,k),k=1,4)
 171     continue
         jcount=jcount+mxsz(i)
 172  continue

      do 4 ilmda=0,NN
        do 3 ixi=0,NN
```

```fortran
              evcof(ilmda,ixi)=0.0d+00
              oddcof(ilmda,ixi)=0.0d+00
              root=dsqrt(dfloat((2*ilmda + 1)*(2*ixi + 1)))
              parity=1
              do 11 i=1,NN
               if(ilmda+ixi.eq.2*i)parity=0
               if(2*i.gt.ilmda+ixi)goto12
11            continue
12            nmin=ilmda
              if(ixi.lt.ilmda)nmin=ixi
              factor=dfloat(nmin*(nmin+1))/2.0d+00
              if(ilmda.gt.ixi .and. parity.eq.1)oddcof(ilmda,ixi)=root
              if(parity.eq.0)evcof(ilmda,ixi)=root*factor
3          continue
4       continue

        return
        END


        SUBROUTINE orthidx(N)
        integer ix(8),lmn(4,10000)
        open(unit=9,file='/rprmrq index',status='unknown')

C       in the following function calls,
C       1,0,0 = odd,even,even etc. (basis function parity)

c dilatation
        ixglob=1
        ix(1)=0
        call evodd(N,lmn,ixglob,1,ix,1,0,0,1)
        call evodd(N,lmn,ixglob,1,ix,0,1,0,2)
        call evodd(N,lmn,ixglob,1,ix,0,0,1,3)
c flexure1
        ix(2)=0
        call evodd(N,lmn,ixglob,2,ix,0,0,0,1)
        call evodd(N,lmn,ixglob,2,ix,1,1,0,2)
        call evodd(N,lmn,ixglob,2,ix,1,0,1,3)
c flexure2
        ix(3)=0
        call evodd(N,lmn,ixglob,3,ix,1,1,0,1)
        call evodd(N,lmn,ixglob,3,ix,0,0,0,2)
        call evodd(N,lmn,ixglob,3,ix,0,1,1,3)
c flexure3
        ix(4)=0
        call evodd(N,lmn,ixglob,4,ix,1,0,1,1)
        call evodd(N,lmn,ixglob,4,ix,0,1,1,2)
        call evodd(N,lmn,ixglob,4,ix,0,0,0,3)
c shear1
        ix(5)=0
        call evodd(N,lmn,ixglob,5,ix,1,1,1,1)
        call evodd(N,lmn,ixglob,5,ix,0,0,1,2)
        call evodd(N,lmn,ixglob,5,ix,0,1,0,3)
c shear2
        ix(6)=0
        call evodd(N,lmn,ixglob,6,ix,0,0,1,1)
        call evodd(N,lmn,ixglob,6,ix,1,1,1,2)
        call evodd(N,lmn,ixglob,6,ix,1,0,0,3)
c shear3
        ix(7)=0
```

```
          call evodd(N,lmn,ixglob,7,ix,0,1,0,1)
          call evodd(N,lmn,ixglob,7,ix,1,0,0,2)
          call evodd(N,lmn,ixglob,7,ix,1,1,1,3)
c torsion
          ix(8)=0
          call evodd(N,lmn,ixglob,8,ix,0,1,1,1)
          call evodd(N,lmn,ixglob,8,ix,1,0,1,2)
          call evodd(N,lmn,ixglob,8,ix,1,1,0,3)

          WRITE(9,*)' 8,'

          ig=1
          do 6 j=1,8
           write(9,100)ix(j)
           do 5 i=1,ix(j)
            write(9,200)lmn(1,ig),lmn(2,ig),lmn(3,ig),lmn(4,ig)
            ig=ig+1
5          continue
6          continue
          CLOSE(9)

100       format(i4,',')
200       format(i4,',',i4,',',i4,',',i4)
          return
          END

          Subroutine evodd(NN,lmn,ixglob,iblk,ix,il,im,in,ie)
          integer lmn(4,10000),ix(8)
          do 3 l=il,NN,2
           do 2 m=im,NN,2
            do 1 n=in,NN,2
              if(l+m+n.le.NN)then
                lmn(1,ixglob)=l
                lmn(2,ixglob)=m
                lmn(3,ixglob)=n
                lmn(4,ixglob)=ie
                ix(iblk)=ix(iblk)+1
                ixglob=ixglob+1
              endif
1           continue
2          continue
3         continue
          return
          end


          SUBROUTINE mrqnmin(y,ymod,dyda,sig,ndata,a,ia,ma,
     &                       covar,alpha,nca,chisq,alamda,
     &                       mass,neq,id,cf,numic)

C         mrqNmin and its companion, mrqNcof, are adapted from the
C Numerical Recipes routines mrqmin and mrqcof.  The N indicates
C that these routines are for use with a model function whose
C numeric value for a given parameter set can be calculated, but
C cannot be expressed in 'closed form' (e.g. the Lagrangian integral
C used in RUS), and whose derivatives must be calculated using
C differences, since they are not known analytically.
C
          IMPLICIT REAL*8 (a-h,o-z)
          PARAMETER (MMAX=27)
```

```fortran
      COMMON/modes/modeid(2,100),fmodeid(100)

      integer ma,nca,ndata,ia(ma),neq(21),id(21,21)
      real*8 alamda,chisq,a(ma),alpha(nca,nca),covar(nca,nca),
     &       sig(ndata),y(ndata),ymod(ndata),dyda(ndata,nca),
     &       cf(21,21),mass

      integer j,k,l,m,mfit
      real*8 ochisq,atry(MMAX),beta(MMAX),da(MMAX)

      save ochisq,atry,beta,da,mfit

      if(alamda.lt.0.d+0)then
        mfit = 0
        do 11 j=1,ma
           if(ia(j).ne.0) mfit=mfit+1
11      continue
        alamda=1.0D-3
        call mrqncof(y,ymod,dyda,sig,ndata,a,ia,ma,alpha,beta,nca,chisq)
        flag=1
        ochisq=chisq
        do 12 j=1,ma
           atry(j)=a(j)
12      continue
      endif
      j=0
      do 14 l=1,ma
         if(ia(l).ne.0) then
            j=j+1
            k=0
            do 13  m=1,ma
              if(ia(m).ne.0)then
                 k=k+1
                 covar(j,k)=alpha(j,k)
              endif
13          continue
            covar(j,j)=alpha(j,j)*(1.d+00+alamda)
            da(j)=beta(j)
         endif
14    continue
      call invsvd(covar,mfit,nca,da)
      if(alamda.eq.0)then
        call covsrt(covar,nca,ma,ia,mfit)
        return
      endif
      j=0
      WRITE(6,*)'Parameters (old value, new value, difference)'
      do 15 l=1,ma
        if(ia(l).ne.0)then
           j=j+1
           atry(l)=a(l)+da(j)
           WRITE(6,'(3E15.6)') A(L),ATRY(L),DA(J)
        endif
15    continue
      call freq(atry,mass,neq,id,cf,numic,ma,ndata,ymod,sig)
      call mrqncof(y,ymod,dyda,sig,ndata,atry,ia,ma,covar,da,nca,chisq)
      if(chisq.lt.ochisq)then
         alamda=0.1d+00*alamda
         ochisq=chisq
         j=0
```

115

```fortran
            do 17 l=1,ma
               if(ia(l).ne.0)then
                  j=j+1
                  k=0
                  do 16 m=1,ma
                     if(ia(m).ne.0)then
                        k=k+1
                        alpha(j,k)=covar(j,k)
                     endif
16                continue
                  beta(j)=da(j)
                  a(l)=atry(l)
               endif
17          continue
         else
            alamda=1.0D+01*alamda
            chisq=ochisq
         endif
         return
         END
C
         SUBROUTINE mrqncof(y,ymod,dyda,sig,ndata,a,ia,ma,alpha,beta,
      &                    nalp,chisq)
         IMPLICIT REAL*8 (a-h,o-z)
         COMMON/modes/modeid(2,100),fmodeid(100)
         integer ma,nalp,ndata,ia(ma)
         real*8  chisq,a(ma),alpha(nalp,nalp),beta(ma),sig(ndata),
      *          y(ndata)
         parameter (MMAX=27)
         integer mfit,i,j,k,l
         real*8 dy,sig2i,wt,ymod(ndata),dyda(ndata,nalp)
         mfit = 0
         do 11 j=1,ma
            if(ia(j).ne.0)then
               mfit=mfit+1
            endif
11       continue
         do 13 j=1,mfit
            do 12 k=1,j
               alpha(j,k)=0.d+00
12          continue
            beta(j)=0.d+00
13       continue
         chisq=0.d+00
         do 16 i=1,ndata
            if(y(i).ge.1.d-05)then
               sig2i=1.d+00/(sig(i)*sig(i))
               dy=y(i)-ymod(i)
            else
               sig2i=0.d0
               dy=0.0d+00
            endif
            j=0
            do 15 l=1,ma
               if(ia(l).ne.0)then
                  j=j+1
                  wt=dyda(i,l)*sig2i
                  k=0
                  do 14 m=1,l
                     if(ia(m).ne.0)then
```

```
                        k=k+1
                        alpha(j,k)=alpha(j,k)+wt*dyda(i,m)
                     endif
14                 continue
                   beta(j)=beta(j)+dy*wt
               endif
15       continue
         chisq=chisq+dy*dy*sig2i
16   continue
     do 18 j=2,mfit
        do 17 k=1,j-1
           alpha(k,j)=alpha(j,k)
17      continue
18   continue
     write(6,'(A9,E12.5)')' chisq = ',chisq
     return
     END

     SUBROUTINE covsrt(covar,npc,ma,ia,mfit)
     IMPLICIT REAL*8 (a-h,o-z)
     INTEGER ma,mfit,npc,ia(ma)
     REAL*8 covar(npc,npc)
c    INTEGER i,j,k
     REAL*8 swap
     do 12 i=mfit+1,ma
        do 11 j=1,i
           covar(i,j)=0.d+00
           covar(j,i)=0.d+00
11      continue
12   continue
     k=mfit
     do 15 j=ma,1,-1
        if(ia(j).ne.0)then
            do 13 i=1,ma
               swap=covar(i,k)
               covar(i,k)=covar(i,j)
               covar(i,j)=swap
13          continue
            do 14 i=1,ma
               swap=covar(k,i)
               covar(k,i)=covar(j,i)
               covar(j,i)=swap
14          continue
            k=k-1
        endif
15   continue
     return
     END




     SUBROUTINE invsvd(a,n,np,b)
     IMPLICIT real*8 (a-h,o-z)
     PARAMETER(MMAX=27)
     REAL*8  a(np,np),b(np),x(MMAX)
     REAL*8  ainv(MMAX,MMAX),w(MMAX),t1(MMAX,MMAX),v(MMAX,MMAX)

     call svdcmp(a,n,n,np,np,w,v)
c                   ''svdcmp'' is the Numerical Recipes
c                   singular value decomposition subroutine.
```

```
      wmax=0.0d+00
      write(6,*)'Singular values from SVD:'
      do 100 j=1,n
        write(6,'(I2,1X,E13.5)')j, w(j)
        if(w(j).gt.wmax) wmax=w(j)
100   continue
      wmin=wmax*1.d-8
      do 110 j=1,n
        if(w(j).lt.wmin) w(j)=0.0d+00
110   continue
       do 12 i=1,n
        do 11 j=1,n
          if(w(j).ne.0.d+00)then
           t1(i,j)=v(i,j)/w(j)
          else
           t1(i,j)=0.d+00
          endif
11      continue
12      continue
       do 15 i=1,n
        do 14 j=1,n
         ainv(i,j)=0.d+00
          do 13 k=1,n
           ainv(i,j)=ainv(i,j)+t1(i,k)*a(j,k)
13        continue
14        continue
15      continue
       do 17 i=1,n
        x(i)=0.d+0
         do 16 j=1,n
            x(i)=x(i)+ainv(i,j)*b(j)
16       continue
17       continue
       do 19 i=1,n
        b(i)=x(i)
         do 18 j=1,n
          a(i,j)=ainv(i,j)
18        continue
19      continue
       return
       END
```

8. Sample data file rprmrq.dat

Here is a sample data file for use with the above program. It contains the data on the 1 mg Si test sample studied in Section III.

The program returns various things depending on the job code. Job code of 0 gives only one forward calculation, and the frequencies are unsorted (*i.e.* are grouped in blocks as they were calculated). Job code 1 performs a Levenberg-Marquardt fit of the resonance data, using the properties in the data file as a starting point. Again, in the final output, the calculated and measured frequencies are unsorted. Job codes 20 and 21 perform the same operations as 0 and 1, but the frequencies are put in ascending order in the final printout.

```
si<001>, from moises levy at uwm      ! {header}
orthorhombic                          ! {elastic symmetry}
3                                     ! {# of independent constants
1.650000, 3, 11,1., 22,1., 33,1.,   1 !  value (MBar), # of places in Cij
0.630001, 3, 12,1., 13,1., 23,1.,   1 ! matrix, indices ij, multipliers,
0.7900000,3, 44,1., 55,1., 66,1.,   1 ! flag (whether to include in fit)}
0.93055000,0.6875000, 0.6375000,0,1,1 !  edge lengths, flags
```

118

```
0.000963100,2.329d0                        ! mass (g), density (g/cc)
21                      ! job code
0.001,7.20              ! lower and upper cutoff frequencies (MHz)
32                      ! Number of resonance frequency data
EV-01  2.841887         ! Data points: mode label, frequency (MHz)
EZ-01  3.053338
EY-01  3.144748
OD-01  3.817882
EV-02  4.320650
OZ-01  4.444650
OD-02  4.538775
OY-01  4.575675
EX-01  4.620875
EZ-02  4.699700
OX-01  4.736975
OD-03  0.000000
EY-02  5.240553
OY-02  5.242106
OX-02  5.452744
OD-04  5.546350
OZ-02  5.559250
OX-03  5.600075
EX-02  5.649625
EX-03  5.737384
OD-05  5.811843
EZ-03  6.139875
EY-03  6.163125
EX-04  6.289825
EX-05  6.479125
EV-03  6.647013
OZ-03  6.696163
EY-04  6.707669
OY-03  6.744150
EZ-04  0.000000
OD-06  7.118000
OY-04  7.159500
```